

Hydrothermal Oxidation of Simple Organic Compounds

by
Brian D. Phenix

B.S. Chemical Engineering
Rensselaer Polytechnic Institute, 1987

Masters of Chemical Engineering
North Carolina State University, 1990

SUBMITTED TO THE DEPARTMENT OF CHEMICAL ENGINEERING IN PARTIAL
FULFILLMENT OF THE REQUIREMENTS FOR THE DEGREE OF

DOCTOR OF PHILOSOPHY IN CHEMICAL ENGINEERING AT THE
MASSACHUSETTS INSTITUTE OF TECHNOLOGY

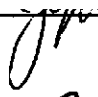
FEBRUARY 1998

© 1998 Massachusetts Institute of Technology
All rights reserved


Signature of Author:

Department of Chemical Engineering
September 25, 1997

Certified by:


Professor J.W. Tester
Thesis Supervisor

Certified by:


Professor J.B. Howard
Thesis Supervisor

Accepted by:

Professor R.E. Cohen
St. Laurent Professor of Chemical Engineering
Chairman, Committee for Graduate Students

Hydrothermal Oxidation of Simple Organic Compounds

by
Brian D. Phenix

Submitted to the Department of Chemical Engineering on
September 25, 1997 in partial fulfillment of the requirements for the
degree of Doctor of Philosophy in Chemical Engineering

ABSTRACT

Supercritical water oxidation (SCWO) is a thermally-based waste treatment process in which aqueous organic waste is oxidized at temperatures and pressures above the critical-point of water. This thesis concerns the identification and characterization of the chemical and physical processes which govern waste destruction in the supercritical water oxidation process. To gain a better understanding of the process, experimental data were collected over a range of industrially-relevant operating conditions. In addition, detailed kinetic models were developed which describe the oxidation process at the elementary reaction level.

Specifically, the kinetics of methanol oxidation in supercritical water were studied in an isothermal, isobaric, tubular flow reactor over a temperature range of 400 to 550°C, a pressure range of 246 to 269 bar, and fuel-equivalence ratio range of 0.5 to 4.5. Initial methanol concentrations at the inlet of the reactor were varied from 0.011 to 0.39 wt%. Over conditions explored in the study, the rate of methanol oxidation was found to be globally first-order in methanol concentration and independent of oxygen feed concentration below fuel-equivalence ratios of 1. Substoichiometric oxygen-to-organic molar feed ratios depressed the direct oxidation of methanol and CO to CO₂ and promoted the production of H₂ via the water-gas shift reaction. Reaction at fuel-lean conditions resulted in higher conversion of methanol to CO and CO₂ and a reduction in H₂ formation due to direct oxidation with the excess oxygen. Apparent induction, or lag, times previously attributed to purely kinetic phenomena were shown to be influenced by the geometry and flow conditions within the mixing tee located at the head of the reactor. Redesign of the tee resulted in an 83% reduction in the apparent induction time. In addition, a direct comparison of methanol oxidation kinetics was made using dissolved oxygen and hydrogen peroxide as oxidants. Using hydrogen peroxide feed concentrations which yielded stoichiometrically-equivalent amounts of dissolved oxygen upon decomposition, the rates of methanol conversion were found to be identical using the two oxidants. Moreover, the time-dependent concentrations of carbon monoxide, carbon dioxide, and hydrogen resulting from the oxidation process were demonstrated to be the same

for both oxidants. In an effort to address the scalability of the bench-scale data taken in this thesis, a collaborative research program was begun with the Combustion Research Facility at Sandia National Laboratory (SNL). Using the larger reactor at SNL, a series of joint methanol oxidation experiments were undertaken over a temperature range of 420 to 500 °C and feed concentrations of 0.011 to 0.39 wt%. Over the range of conditions explored, the rates of methanol oxidation in the MIT and Sandia reactor systems were found to be comparable. The best agreement was found at low methanol feed concentrations (0.011 and 0.056 wt%). Comparison of rate data at higher feed concentrations was complicated by the scatter in the Sandia data and the possibility of non-isothermal operation due to the reaction exotherm. In addition, the reaction of methanol due to hydrolysis or pyrolysis pathways was found to be negligible at the conditions studied. Preliminary experiments utilizing reactors with high surface-to-volume ratios were seen to exhibit a marked decrease in oxidation rate when compared to those conducted in low S/V reactors.

Monte Carlo simulation and the Deterministically Equivalent Modeling Method (DEMM) were used in a combined sensitivity/uncertainty/reaction path analysis of a reduced high-pressure mechanism for hydrogen oxidation in supercritical water. Both methods yielded identical predictions of species concentration profiles and their time-dependent probability distributions. Further, both analyses reveal that there is considerable uncertainty in the predicted species concentration profiles arising from the uncertainties in the forward rate constants and species enthalpies of formation. The model predictions were found to be highly sensitive to two relatively uncertain parameters: the ΔH_f° of HO_2 radical and the rate constant for H_2O_2 dissociation. The MC simulation work also demonstrated that the impact of real-gas corrections on the predicted species profiles is minimal when compared to the parametric uncertainty inherent in the mechanism itself. Lastly, the DEMM and Monte Carlo approaches differed substantially in the amount of computation time necessary to carry out the uncertainty analysis with DEMM resulting in a two order of magnitude reduction in the required number of model solutions.

Thesis supervisors: Jefferson W. Tester
Hermann P. Meissner Professor of Chemical Engineering
Director, MIT Energy Laboratory

Jack. B. Howard
Hoyt C. Hottel Professor of Chemical Engineering

ACKNOWLEDGMENTS

All good things must come to an end and so it is with my time at MIT. The completion of this thesis was made possible, and enjoyable, by the contributions of a great number of people. While it would be difficult to name them all, the following deserve special mention:

My advisors, Jeff Tester and Jack Howard for their guidance, enthusiasm, and constructive contributions throughout the course of my thesis work at MIT. I owe them both a debt of thanks for providing me with a terrific research environment, boundless (almost) resources, and the freedom to carry out a line of research largely of my own choosing. They more than kept their part of the bargain. I only hope I fulfilled mine.

Members of my thesis committee: Dr. Ken Smith for more than a few late afternoon conversations about puzzling data, future experiments, and my overriding inclination to employ empiricism at the expense of analysis; Dr. Bill Peters for his much needed, and often thought provoking, perspective as a physical chemist; and Dr. K.C. Swallow for keeping me honest in all things relating to analytical instrumentation. I will never again call an analytical instrument a "machine."

Thanks also go to my fellow labmates on the 5th (and ultimately, 0th) floor of Bldg. 66: Joanna DiNaro, Matt DiPippo, Mike Kutney, Russ Lachance, Phil Marrone, Josh Taylor, and Randy Weinstein. Graduate life at MIT would have been a lot less enjoyable without the hiking, rafting, skiing, biking, grilling, and other activities that occupied Group Tester outside of the lab. I am particularly indebted to Joanna for her role in our Herculean move to the basement, and for her contribution to virtually every experimental and computational aspect of this thesis. I wish her the best in her (hopefully brief) role as a senior researcher.

Group Tester aside, I should acknowledge the contributions of other friends scattered throughout the campus. Thanks go to Menner Tatang for his tireless help in helping me understand and implement the DEMM methodology described in Chapter 5 (particularly in its early "manual" stage of development). I'd also like to thank Professor Gregory McRae for his support and enthusiasm for the uncertainty analysis work. Thanks also go to Marc Hodes for constantly reminding me just how little I know about heat transfer, mechanical engineering, and running up bills at wildly expensive restaurants. I am also indebted to Joe Marr, Rick Holgate, and Rich Shandross for their help in getting me up to speed at falloff calculations, kinetic modeling, and understanding the impenetrable mass of FORTRAN code known as CHEMKIN. I'd also like to thank Dave Kronholm for more than a few extended conversations about uncertainty analysis and combustion modeling.

Outside of MIT, I have Steve Rice and Russ Hanush at Sandia National Laboratory to thank for their contribution to our joint research effort on methanol oxidation. I am also grateful for their hospitality during my stays in Livermore.

Going way back, I'd also like to thank Glenn Hong, Alan Bourhis, Bill Killilea, and Dave Ordway of what was then MODAR for their help during a few late night trips to Natick.

TABLE OF CONTENTS

Chapter 1: Introduction and background	16
1. 1 Introduction to the SCWO process.....	16
1.2 Properties of supercritical water	19
1.2.1 Thermodynamic properties.....	19
1.2.2 Solvent properties	20
1.3 Previous experimental work.....	23
1.3.1 Hydrolysis and pyrolysis.....	24
1.3.2 Oxidation reactions.....	29
1.4 Previous kinetic modeling work.....	31
Chapter 2: Research Objectives.....	43
Chapter 3: Experimental apparatus and methods.....	45
3.1 Description of experimental apparatus	45
3.1.1 Feed system	58
3.1.1.1 Organic feed system.....	58
3.1.1.2 Oxidant feed system.....	59
3.1.1.3 Oxidant and organic feed delivery	64
3.1.2 Preheat system	66
3.1.2.1 Sandbath preheating system.....	66
3.1.2.2 Firerod preheating system.....	67
3.1.2.3 Direct ohmic preheating (DOH) system	69
3.1.3 Reactor system.....	71
3.1.3.1 Mixing tee and reactor design.....	72
3.1.4 Downstream processing.....	81
3.2 Analytical methods.....	83
3.2.1 Feed analysis.....	83
3.2.1.1 Organic feed analysis	83
3.2.1.2 Oxidant feed analysis.....	84
3.2.2 Effluent analysis	85
3.2.2.1 Vapor effluent analysis	85
3.2.2.2 Liquid effluent analysis.....	86

3.3 Data reduction and analysis	87
3.3.1 Temperature measurement and data logging	87
3.3.2 Carbon balance closure.....	87
3.3.3 Reported experimental uncertainties	88
3.3.4 Data analysis program	89
3.4 System safety	90
3.4.1 Feed delivery of gaseous oxidants and organics.....	90
3.4.2 System overpressure	91
3.4.3 Saturator overpressure	91
3.4.4 Direct ohmic heating system	91
3.4.5 Nuisance dust and vapor handling systems	92
Chapter 4: Experimental studies of methanol oxidation.....	93
4.1 Mixing studies	94
4.2 Oxidant comparison studies	101
4.2.1 Kinetics of hydrogen peroxide decomposition	103
4.2.2 Oxygen evolution control experiments.....	105
4.2.3 Direct comparison of oxidation kinetics using oxygen and hydrogen peroxide..	107
4.3 Effect of fuel equivalence ratio	114
4.4 Inter-laboratory comparison of SCWO kinetics	121
4.4.1 Methanol hydrolysis/pyrolysis experiments	124
4.4.2 Joint MIT/Sandia methanol oxidation experiments	126
4.4.2.1 Temperature dependence of oxidation.....	127
4.4.2.2 Feed concentration dependence of oxidation.....	132
4.5 Effect of surface-to-volume ratio	137
Chapter 5: Kinetic modeling of supercritical water oxidation	141
5.1 Background and motivation	141
5.2 Theoretical treatment of SCWO kinetics	145
5.3 Application of uncertainty analysis to kinetic modeling	147
5.5 Discussion of modeling results.....	157

Chapter 6: Conclusions	167
Chapter 7: Recommendations	170
7.1 Examination of reactor surface effects	170
7.2 Extension of feed mixing studies	171
7.3 <i>In-situ</i> spectroscopic investigation of elementary reaction events in supercritical water	172
Chapter 8: Appendices	173
8.6 Program for Monte Carlo simulation of hydrogen oxidation	173
8.1 Operating instructions for bench-scale tubular reactor.....	174
8.2 Feed pump calibrations	184
8.2.1 High suction-side pressure calibration of organic-side Rainin SD-200 pump	184
8.2.2 Low suction-side pressure calibration of organic-side Rainin SD-200 pump.....	188
8.2.3 High suction-side pressure calibration of oxygen-side Rainin SD-200 pump.....	192
8.2.4 Low suction-side pressure calibration of oxygen-side Rainin SD-200 pump	197
8.3 Details of analytical methods	199
8.3.1 Liquid feed and effluent analysis.....	199
8.3.2 Vapor effluent analysis of light gases.....	205
8.3.3 Vapor effluent analysis of hydrogen.....	211
8.4 Summary of tubular reactor geometries	215
8.5 Summary of design changes to bench-scale reactor system.....	217
8.6 FORTRAN program for Monte Carlo simulation.....	218
Chapter 9: References	223

LIST OF FIGURES

Figure 1.1	Static dielectric constant and ion product of pure water as a function of temperature and pressure.	22
Figure 1.2	Hard-sphere collision frequency of water with itself as a function of temperature and pressure.	39
Figure 3.1	Schematic of bench-scale apparatus with sandbath preheating system.	47
Figure 3.2	Schematic of bench-scale apparatus with Firerod preheating system.	50
Figure 3.3	Schematic of bench-scale apparatus with Direct Ohmic Heating (DOH) preheating system.	53
Figure 3.4	Piping and materials of construction diagram for bench-scale reactor apparatus.	56
Figure 3.5	Oxygen solubility in water as a function of pressure at 25 °C.	62
Figure 3.6	Schematic and nomenclature for 90° mixing tee.	74
Figure 3.7	Schematics of opposed-flow and side-entry mixing tees.	79
Figure 4.1	Methanol conversion as a function of time using mixing tees 2a and 2b of Figure 4.2. $T=500^{\circ}\text{C}$ and $P=246$ bar.	96
Figure 4.2	Schematics of opposed-flow and side-entry mixing tees.	97
Figure 4.3	Assumed first-order plots of $\ln(1-X)$ vs. time for the methanol data taken using tees 2a and 2b of Figure 4.2. $T=500^{\circ}\text{C}$ and $P=246$ bar.	98
Figure 4.4	Comparison of the opposed-flow and side-entry mixing tees depicted in Figure 4.2. $T=500^{\circ}\text{C}$ and $P=246$ bar.	100
Figure 4.5	Comparison of methanol conversion as a function of time using dissolved oxygen and hydrogen peroxide as oxidants. $T=500^{\circ}\text{C}$, $P=246$ bar, $[\text{MeOH}]_0=0.069$ wt%, $\phi=1.5$.	108
Figure 4.6	Species concentrations as a function of time resulting from the oxidation	

	of methanol using dissolved oxygen as the oxidant. $T=500^{\circ}\text{C}$, $P=246$ bar, $[\text{MeOH}]_0=0.069$ wt%, $\phi=1.5$.	109
Figure 4.7	Species concentrations as a function of time resulting from the oxidation of methanol using hydrogen peroxide as the oxidant. $T=500^{\circ}\text{C}$, $P=246$ bar, $[\text{MeOH}]_0=0.069$ wt%, $\phi=1.5$.	110
Figure 4.8	Comparison of methanol and carbon monoxide concentrations as a function of time using both dissolved oxygen and hydrogen peroxide as oxidants. $T=500^{\circ}\text{C}$, $P=246$ bar, $[\text{MeOH}]_0=0.069$ wt%, $\phi=1.5$.	112
Figure 4.9	Comparison of carbon dioxide and hydrogen concentrations as a function of time using both dissolved oxygen and hydrogen peroxide as oxidants. $T=500^{\circ}\text{C}$, $P=246$ bar, $[\text{MeOH}]_0=0.069$ wt%, $\phi=1.5$.	113
Figure 4.10	Comparison of oxygen concentrations as a function of time using both dissolved oxygen and hydrogen peroxide as oxidants. $T=500^{\circ}\text{C}$, $P=246$ bar, $[\text{MeOH}]_0=0.069$ wt%, $\phi=1.5$.	114
Figure 4.11	Methanol conversion at 5 and 7 seconds as a function of fuel-equivalence ratio. $T=500^{\circ}\text{C}$, $P=246$ bar, $[\text{MeOH}]_0=0.069$ wt%.	116
Figure 4.12	Methanol conversion as a function of time at fuel-equivalence ratios of 0.85, 1.7, and 3.4.	117
Figure 4.13	Carbon monoxide, carbon dioxide, and hydrogen molar yields as a function of fuel-equivalence ratio at 5 seconds. $T=500^{\circ}\text{C}$, $P=246$ bar, $[\text{MeOH}]_0=0.069$ wt%.	118
Figure 4.14	Carbon monoxide, carbon dioxide, and hydrogen molar yields as a function of fuel-equivalence ratio at 5 seconds. $T=500^{\circ}\text{C}$, $P=246$ bar, $[\text{MeOH}]_0=0.069$ wt%.	119
Figure 4.15	Comparison of MIT and Sandia apparent, first-order rate constants as a function of temperature for methanol oxidation.	123
Figure 4.16	Schematic of Sandia supercritical water oxidation flow reactor.	125
Figure 4.17	Comparison of MIT and Sandia apparent, first-order rate constants as a function of temperature at a methanol feed concentration of 0.011 wt%.	128

Figure 4.18	Comparison of MIT and Sandia apparent, first-order rate constants as a function of temperature at a methanol feed concentration of 0.056 wt%.	129
Figure 4.19	Comparison of MIT and Sandia apparent, first-order rate constants as a function of temperature at a methanol feed concentration of 0.39 wt%.	130
Figure 4.20	MIT apparent, first-order rate constants as a function of temperature and methanol feed concentration.	133
Figure 4.21	Sandia apparent, first-order rate constants as a function of temperature and methanol feed concentration.	134
Figure 4.22	Comparison of apparent, first-order rate constants for methanol oxidation using two different surface-to-volume ratio reactors.	139
Figure 5.1	Flowsheet for Monte Carlo simulation of reduced hydrogen oxidation mechanism.	152
Figure 5.2	Flowsheet for DEMM analysis of reduced hydrogen oxidation mechanism.	154
Figure 5.3	Comparison of predicted H ₂ and O ₂ species concentrations from the full and reduced reaction mechanisms at: $T= 550\text{ }^{\circ}\text{C}$, $P= 246\text{ bar}$.	156
Figure 5.4	Sampled log-normal forward rate constant distributions for the reactions: $\text{H}_2+\text{OH}=\text{H}_2\text{O}+\text{H}$, and $\text{H}_2\text{O}_2=2\text{OH}$.	158
Figure 5.5	H ₂ and O ₂ concentration probability distributions as a function of time resulting from Monte Carlo simulation of the reduced hydrogen oxidation mechanism at: $T= 550\text{ }^{\circ}\text{C}$, $P= 246\text{ bar}$.	159
Figure 5.6	Hydrogen concentration probability distribution at 1.5, 2.5, and 5.0 seconds at: $T= 550\text{ }^{\circ}\text{C}$, $P= 246\text{ bar}$.	162
Figure 5.7	Uncertainty in predicted H ₂ concentrations resulting from: uncertainty in the k_f of the H ₂ O ₂ dissociation reaction, and uncertainty in the standard-state heat of formation of HO ₂ radical.	164
Figure 5.8	The effect of real-gas corrections on the H ₂ concentration predicted by the reduced hydrogen oxidation mechanism. Reaction conditions: $T= 582\text{ }^{\circ}\text{C}$, $P= 246\text{ bar}$.	166

LIST OF TABLES

Table 1.1	Static dielectric constants for supercritical water and some common organic solvents.	23
Table 3.1	Chronology of Reactor System Configurations.	57
Table 3.2	Summary of Mixing Tee Configurations and Flow Conditions.	78
Table 3.3	Summary of Measurement Uncertainty and Observed Experimental Variability.	90
Table 4.1	Estimate of hydrogen peroxide conversion in immersed section of oxidant preheating line.	105
Table 4.2	Results of oxygen evolution experiments using hydrogen peroxide feed solutions.	106
Table 4.3	Hydrolysis/pyrolysis control experiments for joint MIT/Sandia kinetic study.	126
Table 4.4	Summary of MIT/Sandia methanol oxidation experiments.	127
Table 4.5	Estimated adiabatic temperature rise for reactions R4.1 and R4.2 as a function of methanol feed concentration.	136
Table 5.1	Size comparison of several representative low-pressure oxidation mechanisms.	142
Table 5.2	Chemical kinetic mechanism for the high-pressure oxidation of hydrogen.	148
Table 5.3	Mean values and standard deviations for species standard-state enthalpies of formation.	150
Table 5.4	Reduced high-pressure hydrogen oxidation mechanism with reported uncertainty factors.	150

NOMENCLATURE
Variables:

$C_{p,i}^{\circ}$	standard-state constant pressure heat capacity of species i (J/mol K)
C_p	constant pressure heat capacity (J/mol K)
$\Delta C_{p,j}^{\circ}$	standard-state constant pressure heat capacity change for reaction j (J/mol K)
C_{MeOH}	concentration of methanol (mol/cm ³)
$C_{MeOH,0}$	initial concentration of methanol (mol/cm ³)
d_j	mixing tee branch diameter (cm)
D_R	reactor inner diameter (cm)
e_i	atomic charge of the i th hydrogen in a molecule
\hat{f}_i	mixture fugacity of species i (bar)
f_i°	standard-state fugacity of species i (bar)
$\Delta G_{rx,j}^{\circ}$	standard-state Gibbs-free-energy change for reaction j (J/mol)
h	Planck's constant (J•s)
$\Delta H_{f,i}^{\circ}$	standard-state heat of formation for species i (J/mol)
ΔH_R	enthalpy change of reaction (J/mol)
H_{i,H_2O}	Henry's law constant for species i in water (bar)
k_{app}	apparent first-order rate constant (1/s)
k_b	Boltzmann's constant (J/K)
$k_{f,j}$	forward rate constant for reaction j
k_h	first-order homogeneous rate constant (1/s) (Chapter 4)
$k_{r,j}$	reverse rate constant for reaction j
k_w	first-order heterogeneous rate constant (cm/s) (Chapter 4)
$K_{a,j}$	activity-based equilibrium constant for reaction j
$K_{c,j}$	concentration-based equilibrium constant for reaction j (mol/l) ^{ν_i}
\dot{m}	mass flowrate (g/s)

$N_{Re,j}$	mixing tee branch Reynolds number
P	pressure (bar)
P_c	critical pressure (bar)
r_{MeOH}	rate of reaction for methanol ($\text{mol}/\text{cm}^3 \text{ s}$)
R	gas constant ($\text{J}/\text{mol K}$)
S_i°	standard-state entropy for species i ($\text{J}/\text{mol K}$)
T	temperature (K)
T_c	critical temperature (K)
T_{sb}	sandbath temperature (K)
T°	standard-state temperature (K)
U_i	overall heat transfer coefficient based on internal surface area of reactor
UF_j	multiplicative uncertainty factor for the forward rate constant of reaction j
v_j	velocity in mixing tee branch (cm/s)
\bar{v}_i^∞	partial molar volume at infinite dilution of species i in water (cm^3/mol)
V_R	velocity in reactor (cm/s)
V_c	critical volume (cm^3/mol)
x_i	mole fraction of species i
X	conversion
z	axial distance down reactor (cm)
Z	mixture compressibility factor ($P\bar{V}/NRT$)

Greek variables:

$\nu_{i,j}$	stoichiometric coefficient of species i in reaction j
ν_j	net change in moles for reaction j ; $\nu_j = \sum_i \nu_{i,j}$
$\hat{\phi}_i$	mixture fugacity coefficient for species i
ϕ_i	pure component fugacity coefficient for species i
μ_i	chemical potential of species i (J/mol)

-
- ρ density (g/cm^3)
 σ_i^{HS} hard-sphere collision diameter (\AA)
 ω_i accentric factor
 $\bar{\omega}_{i,j}^{HS}$ hard-sphere collision frequency (sec^{-1})

Symbols:

- A reactant molecule
 M bath gas molecule

Subscripts and superscripts:

- i species i
 j reaction j
 \circ standard-state
 $*$ excited state
 \ddagger transition state

Chapter 1:

Introduction and background

1.1 INTRODUCTION TO THE SCWO PROCESS

Supercritical water oxidation (SCWO) is a thermally-based waste treatment process in which aqueous organic waste is oxidized, with air or oxygen, at temperatures and pressures above the critical-point of water. Originally proposed by Modell in the late 1970's, SCWO has become the subject of considerable academic, industrial, and government research. It has been shown to provide rapid and near-complete destruction of a broad spectrum of organic wastes, including aromatics and chlorinated hydrocarbons (Thomason and Modell, 1984; Staszak *et. al*, 1987; Modell, 1989; Swallow *et. al*, 1989; Thomason *et. al*, 1990), fermentation wastes (Johnston *et. al*, 1988), pulp mill sludges (Modell, 1990; Modell *et. al*, 1992), propellants (Beulow, 1990; Beulow, 1992; Downey *et. al*, 1995; Spritzer *et. al*, 1995); military smokes and dyes (Robinson, 1992; Rice *et. al*, 1994); and surrogate DOE waste mixtures (Bramlette *et. al*, 1990). A recent National Research Council report (NRC, 1993) identified SCWO as a promising alternative technology to the incineration process currently being developed by the U.S. Army for the destruction of the nation's unitary chemical weapons stockpile. Preliminary research into this application of SCWO technology has been carried out at the laboratory scale with live agents, and testing of a transportable 1,500 gpd pilot plant is currently underway using chemical agent simulants (Downey *et. al*, 1995; Spritzer *et. al*, 1995). Efforts are also underway for developing compact SCWO units for the shipboard destruction of U.S. Navy hazardous wastes (Kirts, 1995).

In the SCWO process, aqueous waste is brought into contact with an oxidant, typically oxygen, at temperatures of 400°-650°C and pressures above 221 bar. At these conditions, the resulting water/oxygen/organic mixture is a single fluid phase, and oxidation is initiated spontaneously. Organics in the waste stream are oxidized to lower molecular weight

compounds, and, ultimately, to carbon dioxide and water. There is virtually no NO_x formation in the process due to its relatively low operating temperature. Instead, the presence of nitrogen, either from air or fuel-bound, results in the formation of molecular nitrogen and N_2O . Heteroatoms, such as chlorine, sulfur, and phosphorous, are converted to their corresponding acids (*e.g.*, HCl , H_2SO_4 , etc.). If cations are present in the waste stream, either naturally or as the result of addition to the feed, the presence of heteroatoms results in the formation of inorganic salts (*e.g.*, NaCl , Na_2SO_4 , etc.). These salts have extremely low solubilities in supercritical water (Armellini, 1993), and, as a consequence, they precipitate out of the reaction medium. The formation of salts and their acid precursors from fuel-bound heteroatoms poses the most significant obstacle to commercial implementation of SCWO technology. It does so in two ways: first, by creating an extremely aggressive and corrosive process environment which is incompatible with the majority of engineering materials of construction; and second, by requiring complex system designs to manage the formation and egress of salt from the reactor.

In an industrial setting, the effectiveness of the oxidation process is commonly measured by the percent conversion of the organic feed or, more stringently, as the percent of organic carbon converted to carbon dioxide. Regardless of which definition is used, the destruction efficiency in a SCWO reactor is a function of the concentration and chemical composition of the waste stream, the oxidant feed concentration, and the reactor operating conditions. Reported destruction efficiencies of representative hydrocarbons like benzene, methyl ethyl ketone, and *o*-xylene range from 99.9% ($400^\circ\text{-}500^\circ\text{C}$, $t = 5$ min.) to greater than 99.9999% ($600^\circ\text{-}650^\circ\text{C}$, $t < 1$ min.) (Modell, 1989). It is important to emphasize that these efficiencies, while illustrative of SCWO performance, are not universal. The successful operation of an industrial SCWO system requires the determination of the operating conditions (temperature, residence times, etc.) necessary to attain the desired degree of destruction, and these conditions will vary based on the feed composition and concentration.

The selection of a waste treatment method is dependent on the nature and composition of the waste stream, its volume and frequency, the degree of remediation required, and local

and national regulatory laws. SCWO is typically targeted at waste streams containing approximately 1–20 wt% organic, although higher and lower concentrations can be accommodated through blending. At the lower end of the concentration range (< 1-2 wt%), SCWO competes with traditional activated-carbon and biological treatment methods. At higher concentrations (>20 wt%), it competes with conventional incineration technology. For wastes with low to moderate heating values (350-2,000 Btu/lb, ca. 1-20 wt% organic), SCWO has been estimated to be more cost effective than the other three treatment methods mentioned (Thomason and Modell, 1984). Estimates of this kind should be viewed with caution, however, given the uncertain and evolving nature of the technology and the scale at which it is currently practiced. A more complete discussion of SCWO economics can be found in papers by Thomason and Modell (1984), and Modell (1989). Broader reviews of SCWO technology, basic research, and commercial activity are available in reports by Tester, *et al.* (1991), Moore and Simpson (1993), and Barnes, *et al.* (1993).

The brief description of the SCWO process given above serves to introduce the subject of this thesis: the characterization of the chemical and physical processes which govern waste destruction in the supercritical water oxidation process. In the remaining sections of this chapter, we begin the characterization process by briefly reviewing the thermodynamic and solvent properties of supercritical water and their potential to influence chemical kinetic events and pathways. In sections 1.2.2 and 1.2.3 we discuss previous experimental and kinetic modeling studies of reactions in supercritical water. The discussion is not intended to catalog and describe the entire SCWO kinetics literature, but rather to highlight key findings and to motivate the course of study taken in this thesis by identifying areas which may benefit from further research. The specific research objectives of this thesis are stated in Chapter 2. Chapter 3 contains a detailed description of the experimental equipment, instruments, and methods used to acquire the data for the stated line of research. The results of the experimental effort are presented in Chapter 4. As outlined in Chapter 2, the bulk of the experimental work centers on understanding the kinetics of methanol oxidation in supercritical water, including the effects of oxidant type, fuel-equivalence ratio, reactor scale, and feed mixing on the rate

and extent of oxidation. The kinetic modeling component of this thesis is described in Chapter 5. It is primarily concerned with quantifying the predictive capability of elementary reaction mechanisms used in the modeling of SCWO oxidation processes. The essential findings of Chapters 4 and 5 are summarized briefly in Chapter 6, while recommendations for future research in the area are presented in Chapter 7.

1.2 PROPERTIES OF SUPERCRITICAL WATER

1.2.1 Thermodynamic properties

Water and aqueous solutions are one of the most extensively investigated classes of fluids. A tremendous amount of information has been published describing their phase behavior and physicochemical properties at low to moderate temperatures and pressures. However, much less is known about the properties of these fluids at the conditions of interest in the SCWO process. This is particularly true in regard to the thermodynamic and solvent properties of supercritical fluid mixtures. In the following section we describe the thermodynamic and solvent properties of pure water at supercritical conditions. These properties are markedly different from those of ambient water, and their description provides a starting point for understanding supercritical water's behavior as a reaction medium.

The thermodynamic and transport properties of pure water in the supercritical region have been compiled and reviewed by Franck (1970; 1976; 1983; 1987). Pure water is considered supercritical if its temperature and pressure exceed 374.2 °C and 221.1 bar (Simmrock *et. al*, 1986). Typical SCWO operating conditions (240-260 bar and 500-650°C) occupy a small fraction of the supercritical region and lie in the expanded, low-density portion of the T - ρ phase diagram. In the vicinity of the critical point, the fluid density changes rapidly with small changes in temperature and pressure. Close examination of a Mollier diagram (Haar *et. al*, 1984) reveals that the density of water varies from 0.065 to 0.10 g/cm³ over the range of reaction conditions typically employed in SCWO. This limited density range, however, is not representative of the entire density range encountered in an operating reactor system. Subcritical and near-critical conditions exist both before and after the reactor in the

preheat and let-down heat-exchangers. As a result, process streams undergo large density variations during the course of passing to and from supercritical reaction conditions. Density variations of this kind are potentially important, since, as will be discussed shortly, solvent properties such as the dielectric constant are a strong function of density (Franck, 1976).

1.2.2 Solvent properties

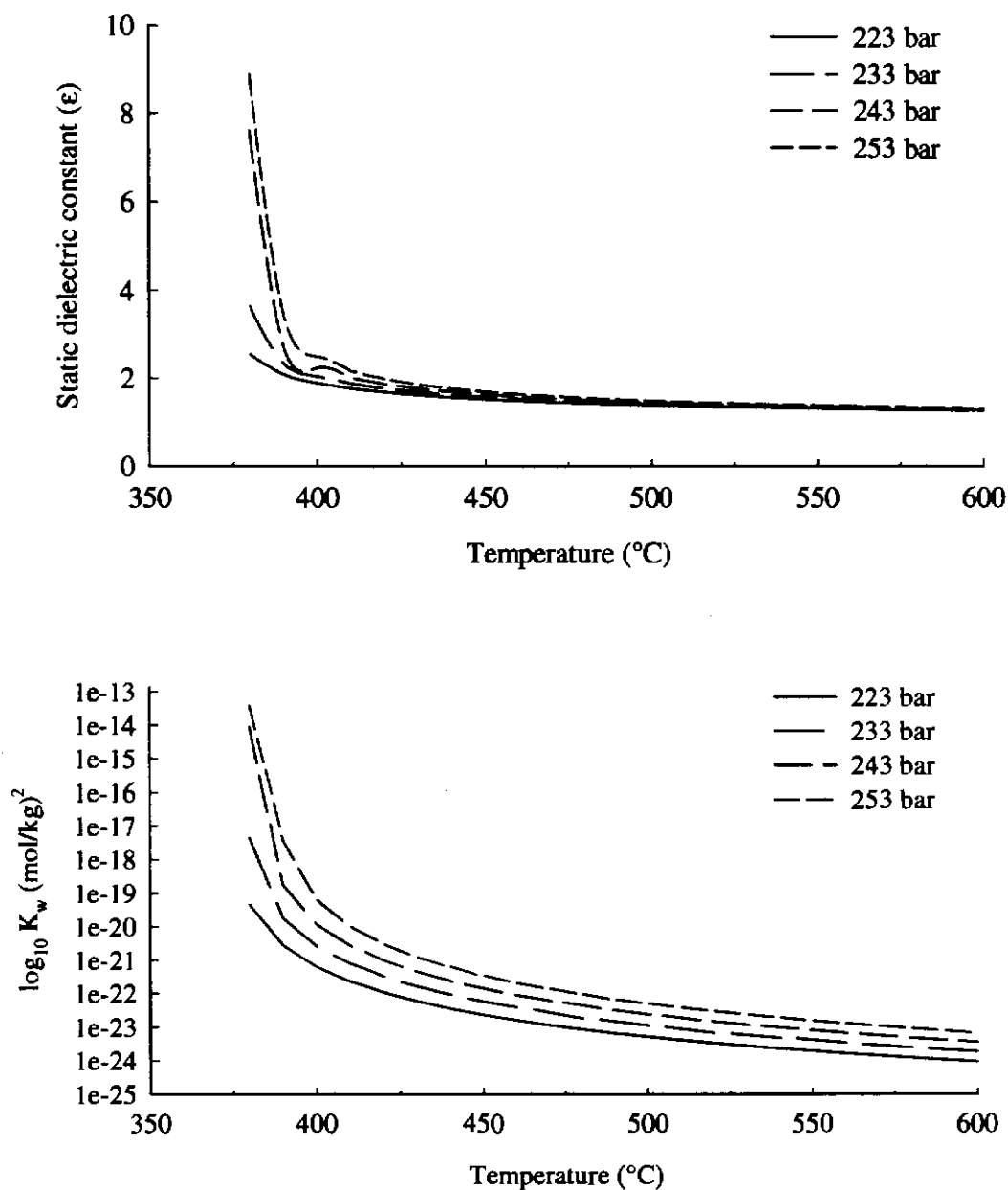
Our interest in water's solvent properties is motivated by both experimental and modeling considerations. Experimentally, we would like to understand how solvent properties influence the reaction rates and product spectra in SCWO reactor systems. From a modeling standpoint, we would like to be able to describe, either at a continuum or molecular level, how solvent-related phenomena impact elementary reaction events. Unfortunately, continuum descriptions of reaction rates in solution have long been recognized as being both unrealistic and inaccurate (Hynes, 1985; Hynes, 1985); and, as yet, there is no detailed description of the structure, dynamics, and molecular interactions of supercritical water mixtures. Nor is there a generalized, quantitative means of calculating the effect solvation phenomena have on chemical reaction rates (Truhlar *et. al*, 1983; Hynes, 1985; Hynes, 1985; Ladanyi and Hynes, 1986). These issues will be addressed in greater depth in Section 1.4.

For the vast majority of reactions, the solvent properties of the reaction medium are important in determining which kinetic pathways are accessible to the reactants. The degree to which a solvent is capable of supporting a given reaction pathway directly influences the observed reaction rate, product selectivity, and equilibrium composition. Unlike the relatively narrow range of solvent properties exhibited by most pure solvents at ambient conditions, supercritical water's solvent properties vary continuously, and sometimes dramatically, as a function of temperature and pressure in the supercritical region. These changes in solvent properties influence which kinetic pathways are active at supercritical conditions. The consequence of changes in solvent-solvent interactions can be seen in changes in properties like the ionic dissociation constant and the static dielectric constant. Both quantities are shown in Figure 1.1 as a function of temperature and pressure over the SCWO operating range. The values shown were calculated using the empirical correlations of Uematsu and Franck (1980)

and Marshall and Franck (1981) and are based on critical assessments of existing experimental data.

The dielectric constant of a solvent provides information on its ability to solvate ions, and, hence, support ionic reactions. For hydrogen bonding fluids, it can also be a crude measure of the extent of local solvent structure at the molecular level. The departure of the static dielectric constant of a medium from 1.0 arises from two sources: the presence of permanent dipole moments and the induction of dipole moments due to the presence of an electric field (electronic polarization). For fluids comprised of molecules with low polarizabilities and strong permanent dipole moments, like water, the former contribution is dominant. The term “static” in “static dielectric constant” refers to dielectric constants measured under low frequency and moderate intensity electric fields. Under these conditions, permanent dipoles contribute fully to the net polarization (due to the low applied frequencies), and the magnitudes of the induced dipoles are proportional to the applied field (due to its low intensity).

As seen in Figure 1.1, the static dielectric constant of water drops from its room temperature value of 78.5 to about 4 to 10 in the near-critical region, and, finally, to a value of around 1.2 at 450°C and above. Table 1.1 presents values for the static dielectric constants of several well-known organic liquids at ambient conditions for comparison. The dramatic decrease in water’s static dielectric constant at supercritical conditions is consistent with the current understanding of the character of hydrogen bonding in supercritical water (Gorbaty and Kalinichev, 1995). As temperature is increased, the kinetic energy of the water molecules becomes sufficiently high to significantly weaken the strength and cohesiveness of the hydrogen bond network. This attenuation in hydrogen bonding decreases the net orientation of the permanent dipoles and causes a corresponding decrease in the dielectric constant.

**Figure 1.1**

Static dielectric constant, ϵ , and ion product, K_w , of pure water as a function of temperature and pressure. Values calculated from empirical correlations of Uematsu and Franck (1980) and Marshall and Franck (1981).

The impact this decrease has on water's ability to solvate ions is reflected in the lower graph of Figure 1.1. As shown, the value of the ionic dissociation constant of water over the SCWO temperature and pressure range is approximately 8 to 10 orders of magnitude lower than that of liquid water at ambient conditions. The impact the changes in dielectric constant and ionic dissociation constant have on chemical kinetics is described in the next section.

TABLE 1.1
Static dielectric constants for supercritical water and some common organic solvents

Fluid	Dielectric constant
Liquid water (25°C)	78.5
Methanol (25°C)	32.6
Phenol (25°C)	9.8
Near-critical water (375-400°C, > 24 MPa)	4-10
Benzene (25°C)	2.3
n-Nonane (25°C)	1.9
Supercritical water (450-600°C, > 24 MPa)	1.2

1.3 PREVIOUS EXPERIMENTAL WORK

Chemical reactions in near-critical and supercritical water have been the subject of experimental investigation since the inception of the SCWO process in the late 1970's. As a result, a substantial amount of kinetic information has accumulated describing organic reactions in these environments. More complete reviews of supercritical water kinetics research can be found in papers by Moore and Simpson (1993) and Tester, *et al.* (1991).

Although oxidation reactions have been the primary focus of earlier studies at MIT, reactions in supercritical water are not limited to oxidation. In fact, the existing body of kinetic literature shows that water near or above its critical point is capable of supporting a wide array of reaction chemistries—including hydrolysis, pyrolysis, dehydration, and oxidation. The ability of water to support such seemingly disparate mechanisms (ionic and free-radical) is a direct result of its unique solvent properties at supercritical conditions and the tremendous changes which can occur in these properties in the critical region. The solvent

properties of supercritical water and their dependence on temperature and density were discussed in the previous section, and they provide a useful framework in which to interpret the kinetic behavior described below. In the following two sections (1.3.1 and 1.3.2), we review several previous studies of chemical reactions in supercritical water. Emphasis in the review is placed on the experimental methods used, the observed influence of operating conditions on reaction rates and selectivities, and the extent to which important experimental issues (control experiments, mass balance closures, error estimates) were addressed.

1.3.1 Hydrolysis and pyrolysis

The hydrolysis and pyrolysis of organic molecules in supercritical water have been studied by a number of investigators. As a general class, hydrolysis reactions involve the cleavage of a molecule by water. They typically proceed via S_N1 or S_N2 mechanisms with the selectivity to either pathway being dependent on the solvent properties of the reaction medium and the structure of the molecule. For simple molecules containing a limited number of bonds susceptible to hydrolysis, both mechanisms result in highly specific product spectra. The product spectra of pyrolysis reactions, on the other hand, can either be narrow or broad, depending on the number and strength of thermally labile bonds in the molecule. Pyrolysis involves the thermal degradation of molecules at elevated temperatures and is typically investigated under gas-phase conditions. In dense reaction media, such as supercritical water, the pyrolysis process may be influenced by the surrounding solvent. Neither hydrolysis nor pyrolysis require the presence of oxygen to proceed.

The majority of hydrolysis and pyrolysis studies have focused on reactions involving ethers and monosaccharides. They include glucose (Amin *et. al.*, 1975; Woerner, 1976; Whitlock, 1978), diphenylether (Kersten, 1991), 2-methoxynaphthalene (Baur, 1991), benzylphenylamine (Abraham and Klein, 1985; Townsend *et. al.*, 1988), o-methoxyphenol (Lawson and Klein, 1985; Townsend *et. al.*, 1988; Huppert *et. al.*, 1989; Klein *et. al.*, 1990), dibenzylether (Townsend and Klein, 1985; Townsend *et. al.*, 1988; Klein *et. al.*, 1990), and phenethyl phenyl ether (Townsend *et. al.*, 1988; Klein *et. al.*, 1990). Key findings from these studies are presented below.

Kersten (1991) investigated the parallel hydrolysis and pyrolysis of diphenylether (DPE) in a batch reactor at temperatures of 415, 430 and 480°C and densities ranging from 0.294 to 0.460 g/cm³. These temperatures and densities correspond to an experimental pressure range of 352 to 702 atm--values far above the 230 to 240 atm conditions employed in the commercial application of SCWO technology. Water/DPE solutions were prepared by directly weighing in both components into a 256 ml reaction bomb. The reaction vessel was then closed, blanketed with nitrogen, and brought to reaction temperature in a furnace over a period of approximately one hour. The effectiveness of the nitrogen blanketing procedure in reducing the initial oxygen concentration is unclear, since dissolved O₂ levels in the reactor were not measured prior to heatup. As a consequence, little can be said about the extent to which oxidation may have contributed to overall conversion of DPE. Reaction times of 4-5 hours were needed to achieve measurable conversions. Product analysis was performed by gas chromatography and was limited to quantifying the concentrations of DPE and phenol (the product of hydrolysis). As a result of the limited effluent analysis, carbon balance closures were not reported. Additionally, no attempt was made to estimate the uncertainties in any of the measured values or experimental variables.

Overall conversions were based on DPE disappearance. Conversion of DPE via the hydrolysis pathway was based on phenol appearance and the stoichiometry of the hydrolysis reaction (1 mol DPE --> 2 mols phenol). In a set of 10 experiments, the selectivity to the hydrolysis pathway (defined as $S_{hyd} = X_{hyd}/X_{overall}$) was found to increase with increasing density. At a fixed temperature of 480°C and densities between 0.296-0.460 g/cm³ (corresponding to an estimated ϵ range of 4.1-7.7), the hydrolysis selectivity increased with increasing density from 0.27% to 51.0%. No attempt was made to see if the change in X_{hyd} , or equivalently k_{hyd} , with dielectric constant was consistent with a simple continuum dielectric description of the reaction (e.g., using the Kirkwood equation). Nor was any effort made to confirm that the change in selectivity with density was solely due to the decreasing contribution of a pyrolysis pathway. This shortcoming, coupled with the other experimental problems described above, makes it difficult to use Kersten's findings to draw any

conclusions about hydrolysis and pyrolysis reactions which may occur in the SCWO operating range. The findings do, however, suggest that both pathways are present at supercritical conditions and that they can act in parallel in the destruction of a molecule.

More complete studies of hydrolysis and pyrolysis reactions in SCW have been carried out at the University of Delaware (Abraham and Klein, 1985; Lawson and Klein, 1985; Townsend and Klein, 1985; Abraham and Klein, 1987; Townsend *et. al.*, 1988; Huppert *et. al.*, 1989; Klein *et. al.*, 1990). Using *o*-methoxyphenol (*o*MP), benzylphenylamine (BPA), dibenzylether (DBE), phenethylphenyl ether (PPE), and benzylphenyl ether (BPE) as model compounds, researchers conducted a series of pyrolysis experiments in the absence and presence of supercritical water. Experiments were conducted batchwise in reactors whose total volume was 0.65 cm³. Reactants--either the neat compound or a compound/water mixture--were weighed directly in the reactor, which was then sealed and immersed in a constant-temperature sandbath. No effort was made to reduce or eliminate initial oxygen concentrations in the reactor. After a predetermined reaction time (5-90 min), the reactor was removed, quenched under running water, and opened. The contents of the reactor were then extracted in acetone and analyzed using a gas chromatograph equipped with a flame ionization detector (FID). Unlike the Kersten study, product analysis was not restricted to reactants and hydrolysis products. Product identification was determined by comparing the retention times of unknown compounds to those of known chemical standards. No effort was made to analyze the contents of the reactor for oxygen or other permanent gases.

In all compounds studied, parallel hydrolysis and pyrolysis pathways were observed. In the case of *o*-methoxyphenol (*o*-MP), the major products of neat pyrolysis at 383°C were catechol, phenol, *o*-cresol, and char. Char formation prevented the determination of carbon balance closures. The conversion of *o*-MP via neat pyrolysis reached a value of 87% over a period 90 minutes. In the presence of water at 383°C and $\rho = 0.51 \text{ g/cm}^3$ ($P=24.3 \text{ MPa}$, $\epsilon=10.3$), no char formation was observed, and the major reaction products were catechol and methanol. Only trace levels of phenol and *o*-cresol were detected. As in the Kersten study, the selectivity to hydrolysis products (catechol and methanol) was found to increase with

increasing water density. Similar trends in selectivity were observed for the other ether compounds studied. In general, it was found that neat reactions lead to a pyrolysis product spectrum, and the addition of water at progressively higher densities alters that spectrum toward hydrolysis products. The rate of reaction along the hydrolysis pathway was found to increase with increasing density--due to mass action and, possibly, solvation effects.

For dibenzylether (DBE) and phenethylphenyl ether (PPE), several interesting experiments were carried out to probe the role of water in the hydrolysis pathway. These additional experiments included runs at varying water densities, runs in $H_2^{16}O/H_2^{18}O$ mixtures, and runs in dilute salt solutions. As found with the other ether compounds, the selectivity toward hydrolysis products increased with increasing water concentration. The dependence of S_{hyd} on density was found to be non-linear and not in accord with the simple functional behavior expected from first order, parallel reactions with constant rate coefficients:

$$S_{hyd} = \frac{k_{hyd}\rho_{H_2O}}{(k_{pyr} + k_{hyd}\rho_{H_2O})} \quad (1.1)$$

This suggests either that hydrolysis is greater than first order in water density or that k_{hyd} increases with water density (possibly as a result of solvent properties that change with density). The difficulty in discriminating between the two alternatives lies in the fact that the classic test of reaction order would require that the water concentration be varied without changing any other variables. However, changes in density at supercritical conditions result in changes in solvent properties. The reaction order with respect to water was found by carrying out a series of experiments in which the total water concentration was held constant but the fraction of water containing an ^{18}O label was varied. This approach held solvent properties essentially constant while allowing assessment of reaction stoichiometry. In both DBE and PPE hydrolysis experiments, ^{18}O was found incorporated in the products of hydrolysis. For DBE hydrolysis, the order of reaction with respect to water was estimated by calculating the

fraction of benzyl alcohol (the hydrolysis product) containing the isotope label. Writing the rate equations for hydrolysis:

$$r_{18} = k_{hyd} [DBE] [H_2^{18}O]^\alpha \quad (1.2)$$

$$r_{total} = k_{hyd} [DBE] [H_2O_{total}]^\alpha \quad (1.3)$$

we see that a plot of $\ln(r_{18}/r_{total})$ vs. $\ln(H_2^{18}O/H_2O_{total})$ should have a slope equal to α . Using rate data obtained at varying isotope label fractions, the value of α was found to be 1.03. This suggests that DBE hydrolysis is first order in water and that the nonlinear dependence of selectivity on density is due to a solvent effect. For an ionic reaction in a dielectric field of ϵ , the Kirkwood equation (Moore and Pearson, 1981) predicts the following functional dependence of k_{hyd} on ϵ :

$$\ln k_{hyd} = \ln k_o - \left(\frac{\epsilon - 1}{\epsilon} \right) \frac{C}{4\pi\epsilon_o RT} \quad (1.4)$$

where k_o is the rate constant in a medium of $\epsilon = 1.0$, and C is a constant representing the change in charge distribution in going from reactants to the transition state complex. Equation (1.4) arises from the application of transition state theory where ΔG^\ddagger , the Gibb's free energy change between reactants and the transition state, is determined using a simple electrostatic model. For reactions with transition states which are more polar than the reactants, C is less than zero, and the rate constant increases with increasing values of ϵ . Using this formalism, the authors constructed plots of $\ln(k_{hyd})$ vs. $(\epsilon - 1/\epsilon)$ for DBE and PPE hydrolysis. The plots were found to be linear with positive slopes. Additional hydrolysis experiments in dilute (0.002-0.71 mmol/cm³) NaCl solutions at constant water density ($\rho = 0.447$) revealed that the addition of salt increased the rate of hydrolysis. No new reaction products were found upon addition of the salt. Using these and several other experimental observations, the authors postulated that the hydrolysis of ethers under the conditions studied occurs via a S_N2 mechanism with water acting as the nucleophile. Evidence of an S_N1 mechanism was not

supported by the observed, non-zero dependence of the hydrolysis rate on water concentration, and OH^- was rejected as a candidate nucleophile due to the low value of K_w over the experimental range of temperature and density. A complete discussion can be found in Klein, *et al.*, (1990).

The importance of these studies to the current study of methanol oxidation is two-fold. First, they clearly demonstrate that for certain classes of compounds hydrolysis and pyrolysis pathways can play an active role at SCWO conditions. If active, they provide additional kinetic pathways which can act in parallel to oxidation. Thus, any attempt to obtain kinetic data which is solely the result of oxidation must first be preceded by a series of control experiments in which the presence or absence of these additional pathways is determined. Secondly, if either pathway is found to contribute significantly to the overall conversion, the work described above provides an initial framework in which to interpret the observed kinetic behavior.

1.3.2 Oxidation reactions

Oxidation is, by far, the most extensively studied class of reaction in supercritical water. The earliest experimental studies were made by Modell and coworkers and focused on defining reactor operating conditions which resulted in the complete oxidation of candidate waste compounds and mixtures. This work, like much of the industrial work which followed (Timberlake *et. al.*, 1982; Hong *et. al.*, 1987; Johnston *et. al.*, 1988; Killilea and Swallow, 1992) was motivated by the need to demonstrate the high destruction efficiency of the SCWO process and to establish it as a viable, commercial alternative to other treatment technologies. In this regard, these studies were, and continue to be, extremely effective. They also have proved to be one of the few sources of information on the oxidation of complex waste mixtures. Their use as a source of detailed kinetic rate data, however, is limited by the fact that the majority of the reported experiments focused on attaining high conversions (>99.9%) rather than explicitly determining reaction rates as a function of temperature, pressure, residence time, etc..

The primary source of detailed oxidation data is university and government research laboratories. Reviews by Tester, *et al.*(1991) and Gloyna and Li (1995) provide comprehensive summaries of recent research activity on the destruction of simple organic compounds and mixtures. In many studies of SCWO oxidation, kinetic information is correlated in the form of a regressed, global rate expression whose functional form follows an assumed first-order relationship:

$$\frac{d[C]}{dt} = A \exp(-E_a / RT) [C]^a [O_2]^b. \quad (1.5)$$

It is important to note, though, that the methods and algorithms used to regress the kinetic and reaction order parameters vary from investigator to investigator, and, in some cases, the published global rate expressions do not adequately represent the data from which they were derived. Critical comparisons of studies involving the same compound should therefore be based on raw data not correlations to the data. Further discussion of the use of equations like the one shown in Equation (1.5) to determine reaction orders is given in Section 4.3.

In studies involving hydrogen, carbon monoxide, acetic acid, and methylene chloride, researchers at MIT observed pronounced induction periods prior to the start of reaction (Holgate, 1993; Meyer, 1993). The induction periods were approximately 1 to 3 seconds in length and were estimated by extrapolating the experimental concentration profiles back to the starting feed concentrations. The duration of the induction delays were comparable to those predicted by combustion models and were taken to be indicative of a free-radical oxidation mechanism. The precise values of the induction times are difficult to gauge since the data do not extend into the induction period itself. The lack of data at very short (< 3 seconds) residence times is a result of the flowrate limitations of the MIT feed system at the time the data were taken. Elimination of this shortcoming in this work should allow more unequivocal determination of induction times and their dependence on feed concentrations and reactor operating conditions.

1.4 PREVIOUS KINETIC MODELING WORK

As discussed above, many kinetic studies in SCW attempt to correlate observed kinetic behavior in terms of a power-law rate expression. Provided the resulting rate expression adequately describes the data from which it was derived, such global models can be quite useful for engineering design calculations. However, their global nature generally restricts their use to the range of concentrations and operating conditions over which they were fit. For example, rate expressions based on pure component oxidation data can not be reliably used to predict the kinetic behavior of mixtures. Nor can rate expressions developed at low to moderate conversions be accurately used to determine the residence times required to achieve extremely high conversions (e.g., 99.999%). Global models fail to be completely satisfactory, in part, because they contain no mechanistic detail. The power-law and Arrhenius parameters on which they depend are fit constants with little connection to underlying elementary rate processes. As a result, global rate expressions fail to capture the essential kinetic features of a mechanism and offer limited insight into the complex rate processes responsible for oxidation.

The lack of a mechanistic description of SCWO reactions has prompted interest in the development of detailed kinetic models which describe oxidation at the elementary reaction level. Past efforts by researchers at MIT and a number of national laboratories have resulted in the development of such models for simple compounds like hydrogen (Holgate and Tester, 1993; Paterson *et. al*, 1993; Holgate and Tester, 1994; Brock and Savage, 1995; Dagaut *et. al*, 1995; Alkam *et. al*, 1996), carbon monoxide (Holgate and Tester, 1994; Brock and Savage, 1995; Dagaut *et. al*, 1995), methane (Webley and Tester, 1991; Brock and Savage, 1995; Dagaut *et. al*, 1995) and methanol (Webley and Tester, 1989; Butler *et. al*, 1991; Butler *et. al*, 1991; Schmitt *et. al*, 1991; Brock and Savage, 1995; Alkam *et. al*, 1996; Dagaut *et. al*, 1996). These mechanisms have been incorporated into one-dimensional, isobaric flow models with either isothermal or imposed axial temperature profiles, and the resulting plug-flow reactor models have been compared, with varying degrees of success, to experimentally-measured, stable species concentration profiles. In all cases, the starting point for model development was a validated gas-phase, free-radical oxidation mechanism. The mechanisms were then

modified in an effort to adapt them to the high pressure conditions of the SCWO process. The following paragraphs describe the adaptation procedures used and the assumptions associated with each.

A gas-phase chemical kinetic mechanism is comprised of a set of reversible elementary reactions, a set of forward rate constants, and a set of thermochemistry values (ΔH_f^0 , ΔS_f^0 and $C_p^o = f(T)$) for each reacting species. Expressions for the forward rate constants are typically provided in Arrhenius or Arrhenius-like form and contain two to three parameters. Values for the reverse rate constants are calculated from the supplied forward rate constants, k_f , and the concentration-based equilibrium constants, K_c , for each reaction:

$$k_r = k_f / K_c \quad (1.6)$$

K_c , in turn, is related to the activity-based equilibrium constant, $K_{a,j}$, by:

$$K_c = K_a \left(\frac{ZRT}{f_i^o} \right)^{-\sum_i \nu_i} \left(\prod_i \hat{\phi}_i^{-\nu_i} \right) \quad (1.7)$$

where R is the gas constant, T is the temperature in K, f_i^o is the fugacity of pure component i in its standard state, ν_i is the stoichiometric coefficient of species i , $\hat{\phi}_i$ is the fugacity coefficient of component i in the mixture, and Z is the mixture compressibility factor. By definition, K_a can be expressed in terms of the standard-state Gibbs-free-energy change of reaction via

$$K_a = \exp(-\Delta G_R^0 / RT). \quad (1.8)$$

The temperature dependence of $\Delta G_R^o(T)$ is found using the integrated form of the Gibbs-Helmholtz equation (Tester and Modell, 1997):

$$\frac{\Delta G_R^o(T)}{T} = \frac{\Delta G_R^o(T^o)}{T^o} + \int_{T^o}^T \left\{ \frac{-\Delta H_R^o(T^o)}{T^2} - \frac{1}{T^2} \int_{T^o}^T \Delta C_p^o dT \right\} dT \quad (1.9)$$

The standard-state Gibbs free energy, enthalpy, and heat capacity changes of reaction in equation (1.9) are calculated using the stoichiometric coefficients and standard-state thermochemistry values for each species involved in the reaction:

$$\Delta G_R^o(T^o) = \sum_i \nu_i \Delta G_{f,i}^o(T^o) \quad (1.10)$$

$$\Delta H_R^o(T^o) = \sum_i \nu_i \Delta H_{f,i}^o(T^o) \quad (1.11)$$

$$\Delta C_p^o(T) = \left(\sum_i \nu_i a_i \right) + \left(\sum_i \nu_i b_i \right) T + \left(\sum_i \nu_i c_i \right) T^2 + \left(\sum_i \nu_i d_i \right) T^3 + \left(\sum_i \nu_i e_i \right) T^4 \quad (1.12)$$

The a_i , b_i , c_i , d_i , and e_i parameters in equation (1.12) arise from the following commonly used polynomial form for the constant-pressure heat capacity of an ideal gas:

$$C_{p,i}^o(T) = a_i + b_i T + c_i T^2 + d_i T^3 + e_i T^4 \quad (1.13)$$

In the gas-phase at low to moderate pressures, the compressibility factor and mixture fugacity coefficients in equation (1.7) can, to a good approximation, be set equal to one. Equations (1.6) to (1.13) can then be used to calculate the reverse rate constant for each elementary reaction using the forward rate constants and species thermochemistry supplied with reaction mechanism. This kinetic information, when coupled with the appropriate species and energy conservation equations, allows for the complete description of the temporal and spatial behavior of the reacting system. For an isothermal tubular reactor which is well approximated by the plug-flow idealization, the conservation equations reduce to a simple set of coupled, first-order differential equations which can be solved by a variety of numerical integration schemes. The process of calculating the reverse rate constants and solving the plug-flow species conservation equations has been automated by Kee, *et al.* (1989). The resulting kinetics software, CHEMKIN-II, is widely used in atmospheric and combustion modeling research.

At the elevated pressures of the SCWO process, however, the aforementioned simplifying assumptions regarding the compressibility factor and mixture fugacity coefficients

are not likely to be valid, and researchers are faced with the problem of how to estimate these quantities. To date, two approaches have been taken. The first attempts to estimate these nonideal contributions through the use of a classical thermodynamic (*PVTN*) equation of state. However, an accurate thermodynamic description of the multi-component, supercritical reaction medium requires data to specify the pure-component and interaction parameters for stable *and* unstable species. Given the limited mixture data available for stable species in supercritical water and the complete absence of such data for unstable, free-radical intermediates, accounting for solution-phase non-idealities via a classical equation of state is subject to considerable uncertainty. In principle, critical parameters for unstable, free-radical intermediates and binary interaction parameters for stable and unstable species are needed. In practice, pure component radical species critical properties are estimated using group contribution methods, while binary interaction parameters are frequently set to zero because of the lack of data available for estimating them.

The second approach, relies on the fact that the modeled reaction medium is a likely to be dilute (< 1wt% organic for most laboratory studies). As a result, the mixture compressibility factor in equation (1.7) can be adequately approximated by the compressibility factor of pure water. Fugacity coefficients are handled in a straightforward, though nonrigorous, way: due to lack of data, they are set equal to one. The error introduced by the latter assumption is difficult to gauge since few estimates of fugacity coefficients have been made for compounds in SCW, and extension of the estimation formalism to unstable species is subject to considerable uncertainty. In cases where mixture data are available, reliable estimates for stable species can be made. For example, Webley (1989) calculated the fugacity coefficients of carbon dioxide, hydrogen, methane, and oxygen in supercritical water using the Christoforakos-Franck equation of state (1986). Mixture parameters were fit to binary PVT data in the temperature and pressure range of 400°-700°C and 230-260 bar. At temperatures above 600°C, the fugacity coefficients of the four compounds were found to lie between 0.7 and 1.2. As the temperature was lowered below 600°C and the critical point was approached, they rose to values of 2.0-4.0 and higher.

From a strict theoretical standpoint, the inclusion of nonideal effects in the calculation of the reverse rate constant (as in the one approach described above) precludes the use of gas-phase rate constants in the forward direction. That is to say, it is not theoretically consistent to argue that the reverse rate constant is influenced by nonideal effects while the forward rate constant is well represented by calculated or experimental gas-phase rate constants. In addition, agreement between model prediction and experiment can not be used to “prove” that a particular mechanism or modeling method is fundamentally correct. As has been pointed out by many authors of kinetics texts, a variety of kinetic mechanisms, each with their own different set of reactions or underlying assumptions, may give rise to the same overall kinetic behavior (i.e., dependence of temperatures, reactant concentrations, etc.). In the case of large elementary reaction models, there is not a one-to-one correspondence between a given set of rate parameters and the predicted rate of reaction. As a result, the rate data may be equally well-represented by more than one reaction model.

In addition to the compressibility and fugacity coefficient modifications described above, several other changes are made to gas-phase mechanisms in an effort to adapt them to the SCWO environment. One of the most important is the pressure correction of unimolecular dissociation (or recombination) reaction rate constants. The dependence of these rate constants on pressure can be qualitatively described by (1) a *high-pressure limit*, where the rate coefficient is independent of pressure, (2) a *low-pressure limit*, where the rate coefficient is proportional to pressure, and (3) a *fall-off regime*, where the transition is made from one limit to the other. The dependence of the rate constant on pressure between the upper and lower limits is a complex function of molecular and collisional properties, and its accurate description requires the use of statistical unimolecular rate theories, of which RRKM is an example. The following paragraphs briefly describe the basic assumptions of these rate theories and their applicability to unimolecular reactions occurring under SCWO conditions.

All modern theories for treating unimolecular dynamics in the gas phase (RRKM, SACM, and PST)¹ have as their starting point the basic two-step mechanism proposed by Lindemann in 1922 (Lindemann, 1922):



where A is a reactant, M is a bath gas molecule, and the asterisk denotes internal excitation. The separation of the collisional activation/deactivation process (1.14) from the subsequent reaction step (1.15) leads to the well-known pressure dependence and fall-off behavior outlined above. The Lindemann treatment implicitly requires that the timescales for reaction and collisional energy transfer be well separated and that collisions not interfere with A^* molecules in the process of reacting. The separation of timescales is well-founded in the gas-phase where the duration of the collisional activation and deactivation steps (on the order of 10^{-13} sec) is much shorter than the lifetime of an excited A^* molecule (typically 10^{-9} sec or greater) (Gilbert and Smith, 1990). Thus, the collisions of (1.14) occur essentially instantaneously relative to the reaction step of (1.15), making it possible to separate the theoretical treatment of the two processes. Such a separation means that we only need to consider the A^* molecule in isolation when developing a suitable rate theory for excited species. The bath gas, or reaction medium, is assumed not to be involved in the reaction event. This assumption is vital to the implementation of all gas-phase, statistical rate theories (which deal exclusively with the description of the reaction event in (1.15)). The assumption will be valid so long as the collision frequency in the medium is not so high that there is a significant probability of collisions occurring with an excited molecule in the process of reacting. At low to moderate pressures, the probability of such collisions is quite low (Gilbert and Smith,

¹ RRKM: Rice-Ramsperger-Kassel-Marcus
SACM: Statistical Adiabatic Channel Model
PST: Phase Space Theory

1990). At higher pressures (approximately 10^2 - 10^3 atm), however, the collision frequency may become so high that collisions do interfere with reactions. Under such conditions, it is necessary to consider the effect of the surrounding reaction medium on the microscopic reaction event. The theoretical treatment of systems of this kind requires a statistical mechanical description of the bath gas (perhaps now better referred to as a solvent). More importantly, it also requires a theoretical means of relating the rate constant to the static and dynamic solvent properties which result from such a description. Treatments of this kind are quite complex and, owing to the shortcomings in the current statistical mechanical descriptions of liquids and the lack of adequate solution-phase rate theories, they are far from quantitative.

Based on the above discussion, it should be clear that the use of gas-phase rate theories to describe unimolecular dynamics is dependent on the assumption that the reaction medium does not appreciably interfere with reaction events. Determining the precise conditions at which this assumption breaks down is difficult. The simplest approach is to employ elementary gas-kinetic theory to estimate the hard-sphere collision frequency in the medium and compare the resulting frequencies with representative reaction timescales. This approach is admittedly crude since (1) the hard-sphere model is an extremely primitive description of the interaction potential and (2) the notion of "collision frequencies" is inherently a gas-phase concept. The resulting collision frequencies, therefore, are unlikely to be quantitatively accurate. They do, however, provide a convenient, zeroth-order means of comparing collision rates at ambient and elevated pressures. Figure 1.2 presents the hard-sphere collision frequency of pure supercritical water at sub-ambient, ambient, and supercritical pressures. The frequencies were calculated via the hard-sphere, gas-kinetic expression (Moore and Pearson, 1981):

$$\omega_{H_2O-H_2O}^{HS} = \frac{1}{2} \left(\frac{16kT}{\pi m_{H_2O}} \right)^{1/2} \pi d_{H_2O}^2 [M_{H_2O}] \quad (1.16)$$

where M_{H_2O} is the number of water molecules per unit volume and d_{H_2O} is the hard-sphere diameter. The value for hard-sphere diameter was estimated as:

$$d_{H_2O} = \sigma_{H_2O}^{HS} \quad (1.17)$$

where σ_{H_2O} was taken to be equal to 2.641 Å (Reid *et. al*, 1987). The water density was calculated using the IAPS equation of state for pure water developed by Kesten and Sengers (1986). As shown, the hard-sphere collision frequencies at supercritical conditions are 2.5-3.5 orders of magnitude higher than at typical gas-phase reaction conditions and they approach the 10^{13} sec^{-1} value normally associated with liquids (Moore and Pearson, 1981; Steinfeld *et. al*, 1989). Use of a slightly more realistic, but still quite approximate, interaction potential such as the Leonard-Jones model results in collision frequencies which are 1.45-1.78 times higher than the hard-sphere values shown.

A more accurate assessment of the possible breakdown of gas-phase rate theories at SCWO conditions will likely arise from spectroscopic studies in supercritical water. Such studies may involve either static measurements of the local SCW environment using solvachromic probe molecules or time-resolved investigations of isolated unimolecular rate processes at SCW conditions. To date, these kinds of investigations in supercritical mediums have been restricted to fluids with low critical temperatures and pressures--such as carbon dioxide, ethane, propane, n-butane, ethylene, and fluoroform (Gehrke *et. al*, 1990; Schroeder *et. al*, 1990; Brennecke, 1993). Their extension to supercritical water conditions poses a number of technical challenges and is an active area of research within the SCWO community. The potential impact of spectroscopic information on current modeling approaches is enormous. Work in other supercritical fluids like carbon dioxide and ethane has revealed the presence of significant local density and composition enhancements around solute molecules in solution (Brennecke, 1993). Effects of this kind are not incorporated into existing kinetic models, nor are they likely to be adequately described by the equation-of-state approach outlined earlier. In addition, comparison of experimental supercritical rate constants with calculated and measured high-pressure, gas-phase rate constants has shown large (greater than one order of

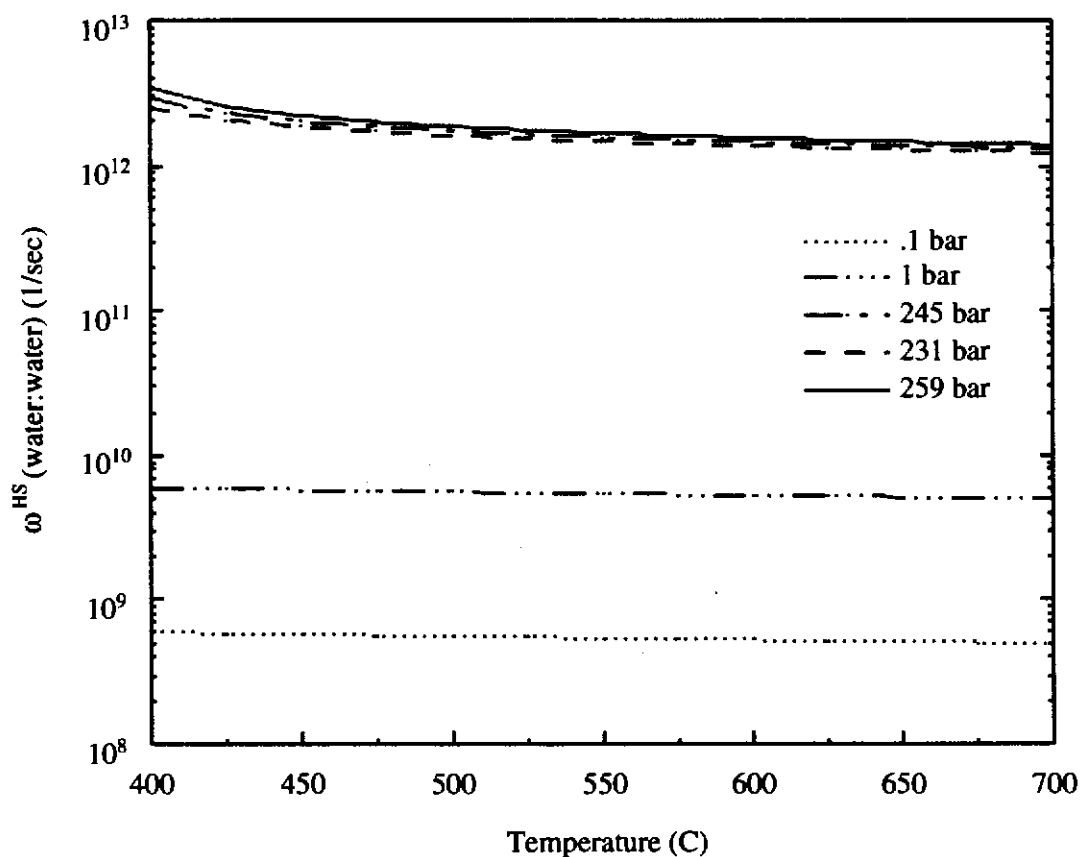
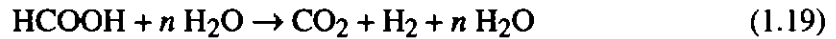
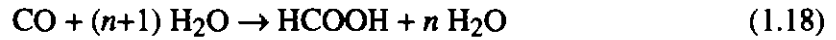


Figure 1.2
Hard-sphere collision frequency for water with itself as a function of temperature and pressure

magnitude) differences between the two values (Schroeder *et al.*, 1990). If deviations of this magnitude occur in supercritical water, current modeling approaches will be unable to predict SCWO rate behavior with any degree of certainty.

As a final note on modeling methodologies, a slightly more complicated extension of the modeling approach outlined above was used by Melius, *et al.*(1990) in the theoretical study of the water-gas shift reaction at high pressure. It deserves mention here because it is

occasionally cited in SCWO modeling research as an alternative approach to the methods discussed earlier in this section. In fact, it is actually quite similar to them and is subject to many of the same uncertainties and shortcomings. For the mechanism in question, the conversion of CO to CO₂ and H₂ in the presence of water at elevated pressure was postulated to proceed through two irreversible elementary reactions involving a formic acid intermediate:



Rates constants for these reactions were estimated using the thermodynamic formulation of conventional transition state theory (CTST) (Hynes, 1985):

$$k = (k_b T / h) v^{-\Delta v_i} \exp(-\Delta G_s^\ddagger / RT) \quad (1.20)$$

where k_b is Boltzmann's constant, h is Planck's constant, v is the molar volume of the mixture, and ΔG_s^\ddagger is the Gibbs free energy of activation of the reaction in solution. ΔG_s^\ddagger is defined as the difference between the chemical potential of the transition state and the chemical potentials of the reactants:

$$\Delta G_s^\ddagger = v^\ddagger \mu^\ddagger(T, P, x^\ddagger) + \sum_{\text{reactants}} \nu_i \mu_i(T, P, x_i) \quad (1.21)$$

The chemical potential of each species in the reaction, in turn, is calculated via:

$$\mu_i(T, P, x_i) = \mu_i^\circ(T, P^\circ, x_i = 1) + RT \ln \left(\frac{x_i \hat{\phi}_i P}{f_i^\circ} \right) \quad (1.22)$$

where each of the standard state and mixture terms have been defined previously. Insertion of equations (1.21) and (1.22) into the transition state relation results in an expression for the rate constant which is dependent of the concentrations of the reactants *and* the transition state. The required standard-state thermochemistry values ($\Delta H_{f,i}^\circ$, $\Delta S_{f,i}^\circ$, and $C_{p,i}^\circ = f(T)$) for stable

species and transition states were estimated via quantum chemistry. The geometry and vibrational frequencies were calculated at the Hartree-Fock level using a 6-31* basis set, while the electronic energies were calculated via Møller-Plesset fourth-order perturbation theory using a larger split valence plus polarization basis set (6-31**) (Szabo and Ostlund, 1989). Bond additivity corrections were applied to the *ab initio* electronic energies and the modified energies, geometries, and frequencies were used to calculate the standard-state enthalpies, entropies, and heat capacities. The resulting thermochemistry properties are appropriate for non-interacting molecules in an ideal gas standard state and are completely analogous to the standard state thermochemistry values normally supplied with a combustion mechanism.

Like the real-gas modeling approaches described earlier, deviations from ideal-gas behavior were addressed through the use of a classical equation of state. The mixture fugacity coefficients in equation (1.22) were calculated using the Peng-Robinson equation of state which yields the pressure as an explicit function of temperature, the molar volume of the mixture, species-specific parameters, and composition:

$$P = \frac{RT}{V_{mix} - b_{mix}(P_{c,i}, T_{c,i}, x_i)} - \frac{a_{mix}(T_{c,i}, P_{c,i}, \omega_i, x_i)}{V_{mix}(V_{mix} + b_{mix}) + b_{mix}(V_{mix} - b_{mix})} \quad (1.23)$$

Parameters for stable species were calculated using known values of the critical constants and accentric factors. Critical values for unstable species and transition states were calculated via the following relations:

$$V_c(\text{species}_j) = V_c(\text{species}_{j,\text{anhydrous}}) + 0.75nV_c(H_2O) \quad (1.24)$$

$$T_c(\text{species}_j) = T_c(H_2O) / n \sum_i (e_i / e_H)^2 \quad (1.25)$$

where e_i is the atomic charge (calculated via quantum chemistry) of the i th hydrogen in the molecule, e_H is the atomic charge of hydrogen in water (0.34), and n is the number of hydrogen atoms in the molecule. The rationale behind the development of these relations is

not discussed by the authors. In addition, no mention is made of the methods used to estimate the accentric factors for unstable species. The mixing rules employed were those proposed by Peng and Robinson and, due to the lack of data, the authors set the binary interaction parameters equal to zero. The resulting approach, then, bears considerable similarity to the real-gas approaches described earlier, and it suffers from many of the same uncertainties.

Chapter 2:

Research Objectives

The objective of this thesis is to further the understanding of the chemical and physical processes which govern waste destruction in the supercritical water oxidation process. Specifically, it examines the kinetics of methanol oxidation in supercritical water, the scalability of the resulting data, the effect of oxidant type and mixing on the rate of oxidation, and the predictive capability of detailed SCWO chemical kinetic mechanisms. Explicit research objectives are as follows:

1. Investigate the kinetics of methanol oxidation in supercritical water—including the effect of temperature, oxidant-to-fuel ratio, residence time, and feed concentration on the rate and extent of methanol destruction. Analyze the resulting product spectra and characterize the operative chemical kinetic pathways and the extent to which each contributes to the overall rate of destruction.
2. In addition to the methanol-specific objectives outlined above, this thesis addresses a number of broad research issues relevant to the SCWO community. They include:
 1. The use of hydrogen peroxide as an alternative oxidant.
 2. The effect of the rate and extent of feed mixing on oxidation rate.
 3. The direct comparison of kinetic rate data from two different scale reactor systems.
3. Examine the effect of parametric uncertainty on the predictive capability of a high-pressure elementary reaction hydrogen oxidation mechanism.

The experimental components of this thesis are described in Chapters 3 and 4. Chapter 3 describes the experimental apparatus, instruments, and methods used to acquire kinetic data and Chapter 4 details the results of the experimental work. The motivation and discussion of the kinetic modeling component alluded to in item 3 is provided in Chapter 5.

Chapter 3:

Experimental apparatus and methods

*“For the truth of the conclusions of physical science,
observation is the supreme Court of Appeal”*

Sir Arthur Eddington

3.1 DESCRIPTION OF EXPERIMENTAL APPARATUS

Experiments were conducted in a continuous flow, tubular reactor system which is similar in design to the apparatus used by Holgate (1993). During the course of this thesis work, however, a number of modifications were made to the equipment and associated instrumentation to improve the system's performance and operability. The modifications were made in three stages, resulting in three different system configurations which were used to collect the experimental data for this thesis. Schematics of these three systems are shown in Figures 3.1-3.3.

Each experimental system is comprised of four basic subsystems: a feed preparation/pressurization section, a preheating section, a reactor section, and a letdown section. The primary difference between the three system configurations is the design of the preheating section. Early experiments were conducted using a fluidized sandbath as the means of preheating the oxidant and organic feed streams. Later systems used (a) resistive heating elements in combination with electric heat tracing and (b) direct ohmic heating of the process line coupled with electric heat tracing. Each subsystem and their variants are described in detail in the paragraphs that follow. A chronological summary of the configuration and features of each system is provided in Table 3.1. Also shown are the laboratory notebook run numbers of the experiments associated with each system configuration.

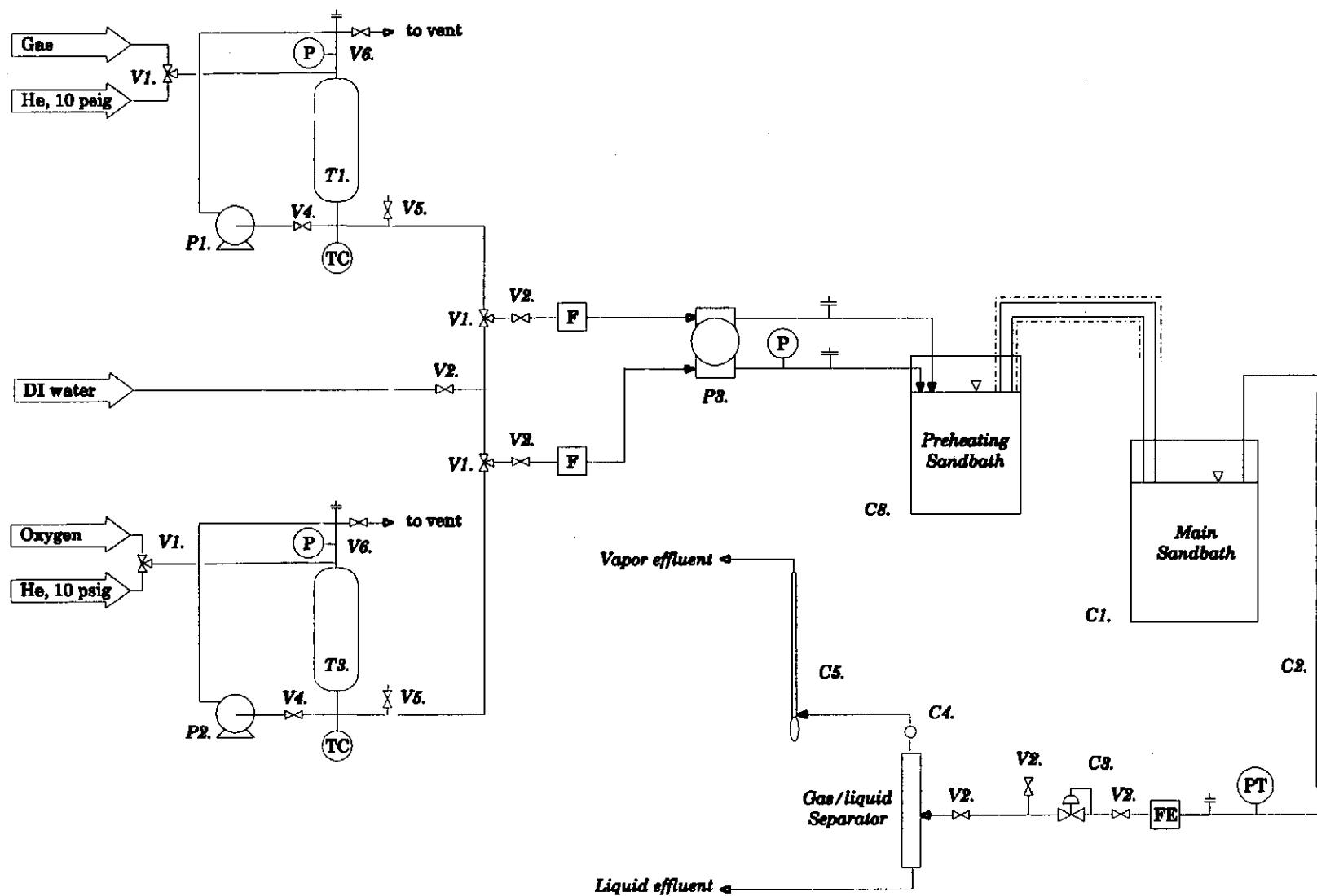


Figure 3.1
Schematic of bench-scale reactor apparatus with sandbath preheating system

Key

Vessels:

- T1: High-pressure organic saturator (Hoke, Model 8HD3000, 3 liters, 1800 psig rating)
- T3: High-pressure oxygen saturator (Hoke, Model 8HD3000, 3 liters, 1800 psig rating)

Pumps:

- P1: Organic saturator recirculation pump (LDC Analytical/Milton Roy minipump, Model 396)
- P2: Oxygen saturator recirculation pump (LDC Analytical/Milton Roy minipump, Model 396)
- P3: Organic and oxidant feed pump (Duplex LDC Analytical/Milton Roy minipump, Model 2396)

System Components:

- C1: Main sandbath (Techne FB-08, 700 °C maximum operating temperature)
- C2: Shell and tube heat exchanger (inner tube ¼ in. OD x 0.065 in. wall HC-276, outer tube ½ in. OD x 0.035 in. wall copper)
- C3: Manual backpressure regulator (Tescom, 26-3200 series, 5,000 psig max, $C_v = 0.04$)
- C4: Sampling port for vapor effluent line
- C5: Soap bubble flowmeter
- C8: Preheating sandbath (Techne SBL-2 or SBS-4)

Valves:

- V1: Whitey 3-way, ¼ in. ball valve (SS-43XS4, 2,500 psig max @ 100 °F)
- V2: Whitey 2-way, ¼ in. ball valve (SS-43S4, 3,000 psig max @ 100 °F)
- V4: Hoke 2-way, ¼ in. ball valve (7155G4Y, 6,000 psig max @ 300 °F)
- V5: Hoke 2-way, ¼ in. ball valve (7115G4Y, 6,000 psig max @ 300 °F)
- V6: Whitey metering valve (IRS4)

Figure 3.1
Schematic of bench-scale reactor apparatus with sandbath preheating system

Key, continued

Instrumentation and miscellaneous equipment:

- ⊙TC 1/16" Type K thermocouple (Omega)
- ⊙P Pressure gauge (Omega, 0-7,500 psig)
- ⊙PT Pressure transducer (Dynisco, Model 832, 0-7,500 psig, accuracy 0.1% FS)
- ⊠F Inline filter (Valco, ZUFR2, 10 μm (0.005") screen)
- ⊠FE Inline filter (Nupro, SS-4TF-7, 7μm fritted filter)
- ⊢ Rupture disk (HIP, 10-61AF4, fitted with Oseco angled seat disk, ¼" effective area, burst pressure 4,500 psig at 25 C (+6%, -3%))
- ⊗ Two-way valve (see valve key for manufacturer, type, and specifications)
- ⊗ Three-way valve (see valve key for manufacturer, type, and specifications)
- Metal tubing (see text for specifications and materials of construction)
- 1" wide wrapped insulation, approximately 1/8" thick (Zetex, 1,100 F max)

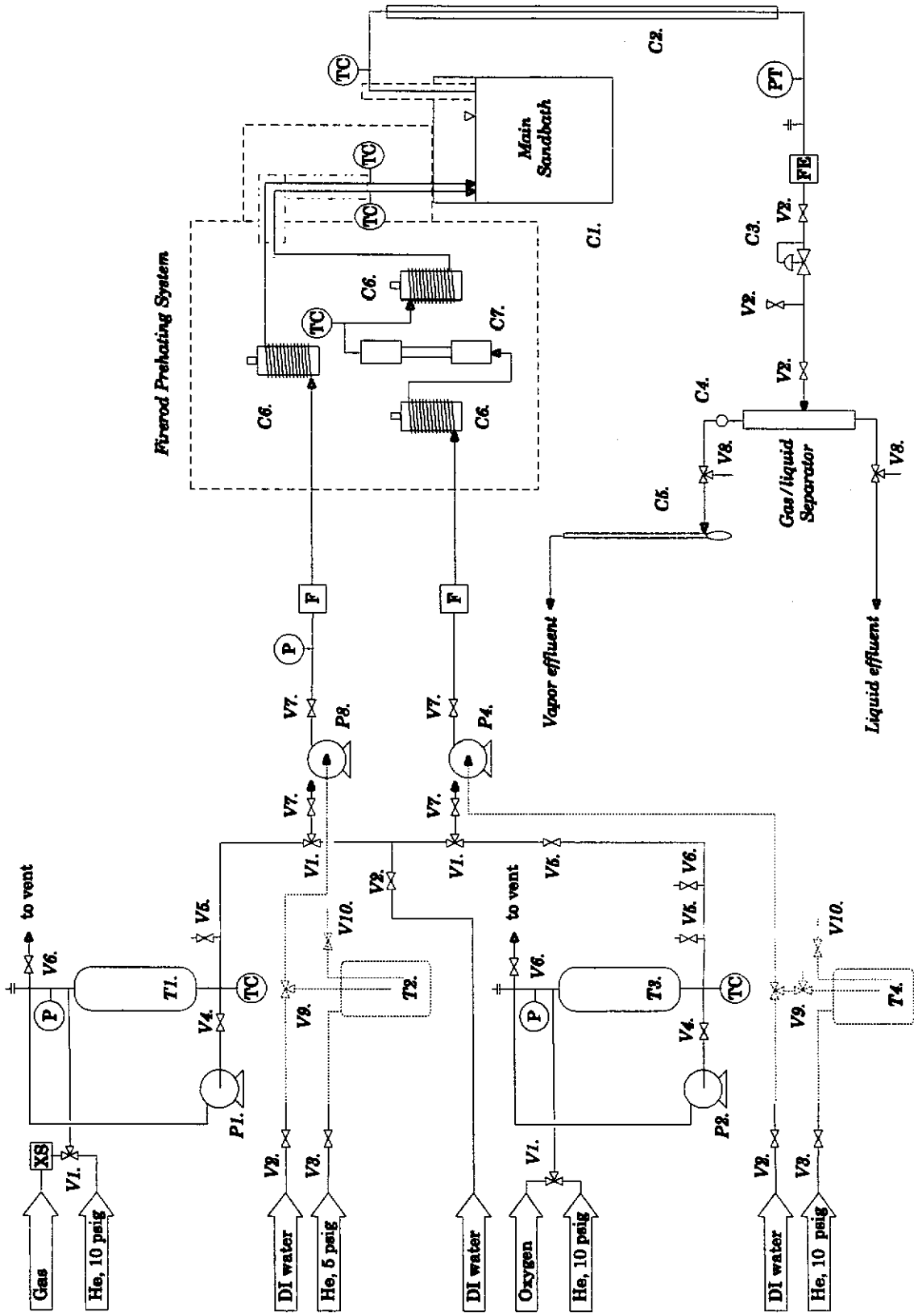


Figure 3.2
Schematic of bench-scale reactor apparatus with Firerod preheating system

Key

Vessels:

- T1: High-pressure organic saturator (Hoke, Model 8HD3000, 3-liters, 1800 psig rating)
- T2: Low-pressure organic feed vessel (Kontes, UltraWare, 5 liters, rated at 6 psig)
- T3: High-pressure oxygen saturator (Hoke, Model 8HD3000, 3 liters, 1800 psig rating)
- T4: Low-pressure peroxide feed vessel (Dionex, HDPE, 4 liters, PN 39164)

Pumps:

- P1: Organic saturator recirculation pump (LDC Analytical/Milton Roy minipump, Model 396)
- P2: Oxygen saturator recirculation pump (LDC Analytical/Milton Roy minipump, Model 396)
- P3: Organic feed pump (Rainin SD-200 HPLC pump, 25 mL/min, 4,600 psig max)
- P4: Oxygen feed pump (Rainin SD-200 HPLC pump, 25 mL/min, 4,600 psig max)

System Components:

- C1: Main sandbath (Techné FB-08, 700 °C maximum operating temperature)
- C2: Shell and tube heat exchanger (inner tube ¼ in. OD x 0.065 in. wall HC-276, outer tube ½ in. OD x 0.035 in. wall copper)
- C3: Manual backpressure regulator (Tescom, 26-3200 series, 5,000 psig max, $C_v = 0.04$)
- C4: Sampling port for vapor effluent line
- C5: Soap bubble flowmeter
- C6: Firerod/copper rod heating element (Watlow, Firerod, ¼ in. OD x 6.0 in. L, 240V, 1000W, max core temp 800 °C)
- C7: Packed bed reactor for H₂O₂ decomposition (see text for details of construction)

Valves:

- V1: Whitey 3-way, ¼ in. ball valve (SS-43XS4, 2,500 psig max @ 100 °F)
- V2: Whitey 2-way, ¼ in. ball valve (SS-43S4, 3,000 psig max @ 100 °F)
- V3: Whitey 2-way, 1/8 in. ball valve (SS-41S2, 2,500 psig max @ 100 °F)
- V4: Hoke 2-way, ¼ in. ball valve (7155G4Y, 6,000 psig max @ 300 °F)
- V5: Hoke 2-way, ¼ in. ball valve (7115G4Y, 6,000 psig max @ 300 °F)
- V6: Whitey metering valve (1RS4)
- V7: Hoke 2-way 1/8 in. ball valve (7155G2Y, 6,000 psig max @ 300 °F)
- V8: Whitey 3-way, 1/8 in. ball valve (SS-41SX2, 2,500 psig max @ 100 °F)

Figure 3.2
Schematic of bench-scale reactor apparatus with Firerod preheating system

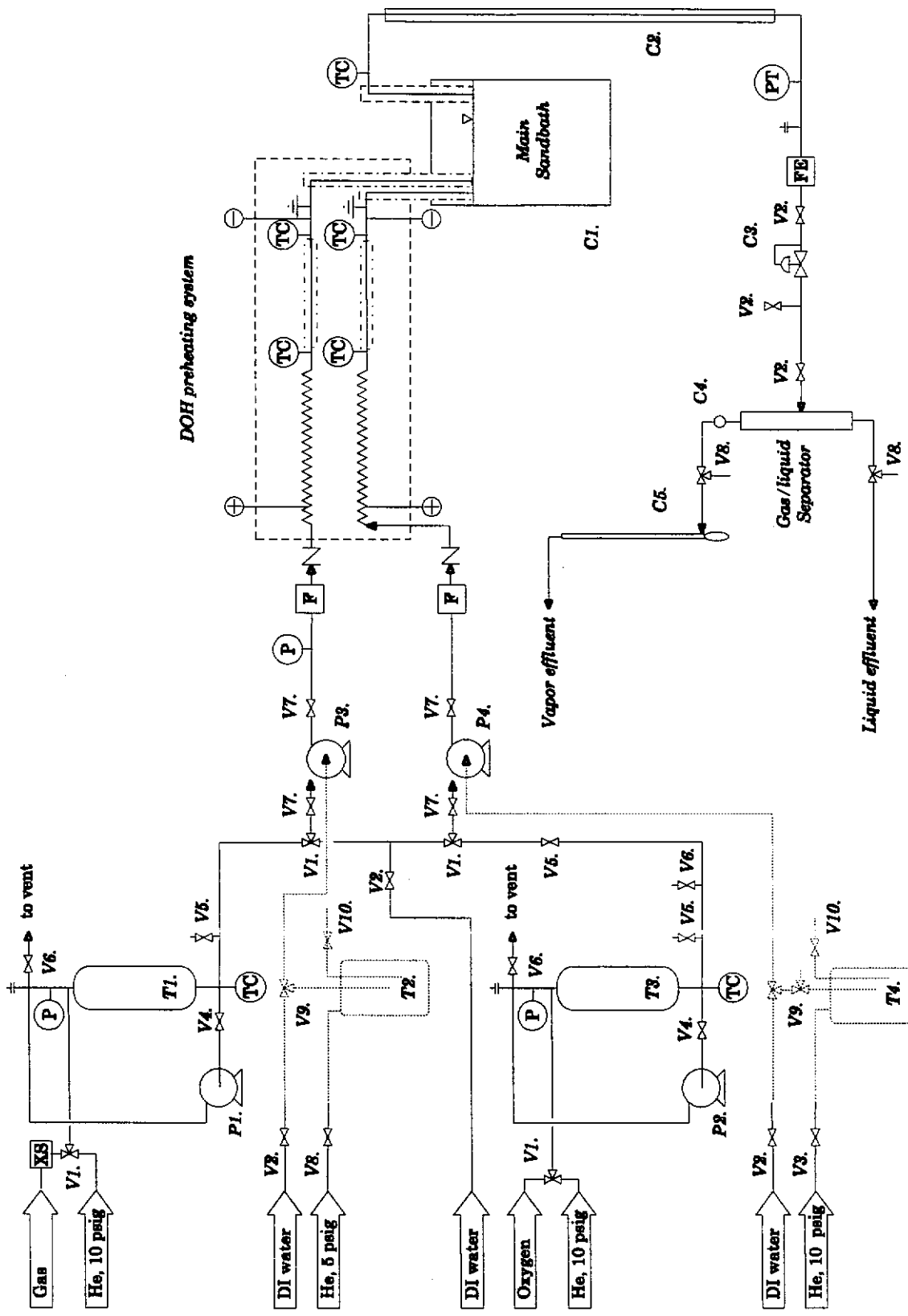
Key, continued

Valves, continued:

- V9: Omnifit 3-way, 1/8 in. single key ball valve (R0-00451109, 600 psig max, Teflon (PTFE) body and Tefzel key)
- V10: Upchurch 2-way, 1/8 in. ball valve (P-783, 1,000 psig max, Tefzel (ETFE) body and fittings)

Instrumentation and miscellaneous equipment:

- TC** 1/16" Type K thermocouple (Omega)
- P** Pressure gauge (Omega, 0-7,500 psig)
- PT** Pressure transducer (Dynisco, Model 832, 0-7,500 psig, accuracy 0.1% FS)
- F** Inline filter (Valco, ZUFR2, 10 μ m (0.005") screen)
- FE** Inline filter (Nupro, SS-4TF-7, 7 μ m fritted filter)
- XS** Excess flow valve (Autoclave engineering, SW K04400, o-ring type)
- \pm Rupture disk (HIP, 10-61AF4, fitted with Oseco angled seat disk,, 3/4" effective area, burst pressure 4,500 psig at 25 C (+6%, -3%))
- \bowtie Two-way valve (see valve key for manufacturer, type, and specifications)
- \boxtimes Three-way valve (see valve key for manufacturer, type, and specifications)
- Metal tubing (see text for specifications and materials of construction)
- Plastic tubing (PTFE, 1/8" x 0.062 ID)
- - - Heating tape (Thermolyne, Samox BWH102060, 1"W x 6'L, 940 watts max)
- - - 1-4" of insulation (Lynn Ceramics, Kowool alumina-silicate fiber blanket)



Experimental apparatus and methods

Figure 3.3
Schematic of bench-scale reactor apparatus with Direct Ohmic Heating (DOH) preheating system

Key*Vessels:*

- T1: High-pressure organic saturator (Hoke, Model 8HD3000, 3 liters, 1800 psig rating)
 T2: Low-pressure organic feed vessel (Kontes, UltraWare, 5 liters, rated at 6 psig)
 T3: High-pressure oxygen saturator (Hoke, Model 8HD3000, 3 liters, 1800 psig rating)
 T4: Low-pressure peroxide feed vessel (Dionex, HDPE, 4 liters, PN 39164)

Pumps:

- P1: Organic saturator recirculation pump (LDC Analytical/Milton Roy minipump, Model 396)
 P2: Oxygen saturator recirculation pump (LDC Analytical/Milton Roy minipump, Model 396)
 P3: Organic feed pump (Rainin SD-200 HPLC pump, 25 mL/min, 4,600 psig max)
 P4: Oxygen feed pump (Rainin SD-200 HPLC pump, 25 mL/min, 4,600 psig max)

System Components:

- C1: Main sandbath (Techné FB-08, 700 °C maximum operating temperature)
 C2: Shell and tube heat exchanger (inner tube ¼ in. OD x 0.065 in. wall HC-276, outer tube ½ in. OD x 0.035 in. wall copper)
 C3: Manual backpressure regulator (Tescum, 26-3200 series, 5,000 psig max, $C_v = 0.04$)
 C4: Sampling port for vapor effluent line
 C5: Soap bubble flowmeter

Valves:

- V1: Whitey 3-way, ¼ in. ball valve (SS-43XS4, 2,500 psig max @ 100 °F)
 V2: Whitey 2-way, ¼ in. ball valve (SS-43S4, 3,000 psig max @ 100 °F)
 V3: Whitey 2-way, 1/8 in. ball valve (SS-41S2, 2,500 psig max @ 100 °F)
 V4: Hoke 2-way, ¼ in. ball valve (7155G4Y, 6,000 psig max @ 300 °F)
 V5: Hoke 2-way, ¼ in. ball valve (7115G4Y, 6,000 psig max @ 300 °F)
 V6: Whitey metering valve (1RS4)
 V7: Hoke 2-way 1/8 in. ball valve (7155G2Y, 6,000 psig max @ 300 °F)
 V8: Whitey 3-way, 1/8 in. ball valve (SS-41SX2, 2,500 psig max @ 100 °F)
 V9: Omnifit 3-way, 1/8 in. single key ball valve (R0-00451109, 600 psig max, Teflon (PTFE) body and Tefzel key)
 V10: Upchurch 2-way, 1/8 in. ball valve (P-783, 1,000 psig max, Tefzel (ETFE) body and fittings)

Figure 3.3
Schematic of bench-scale reactor apparatus with Direct Ohmic Heating (DOH) preheating system

Key, continued

Instrumentation and miscellaneous equipment:

- ⊙ **TC** 1/16" Type K thermocouple (Omega)
- ⊙ **P** Pressure gauge (Omega, 0-7,500 psig)
- ⊙ **PT** Pressure transducer (Dynisco, Model 832, 0-7,500 psig, accuracy 0.1% FS)
- ▭ **P** Inline filter (Valco, ZUFR2, 10 μm (0.005") screen)
- ▭ **FE** Inline filter (Nupro, SS-4TF-7, 7μm fritted filter)
- ▭ **XS** Excess flow valve (Autoclave engineering, SW K04400, o-ring type)
- ± Rupture disk (HIP, 10-61AF4, fitted with Oseco angled seat disk, ¼" effective area, burst pressure 4,500 psig at 25 C (+6%, -3%))
- ∞ Two-way valve (see valve key for manufacturer, type, and specifications)
- ∞ Three-way valve (see valve key for manufacturer, type, and specifications)
- | Check valve (Nupro, SS-53S4, 6,000 psig max)
- Metal tubing (see text for specifications and materials of construction)
- Plastic tubing (PTFE, 1/8" x 0.062 ID)
- Cable heater (Watlow, 62H24A6X, 1/16" OD x 2'L, 120V, 240W max)
- Heating tape (Thermolyne, Samox BWH102060, 1"W x 6' L, 940 watts max)
- 1-4" of insulation (Lynn Ceramics, Kaowool alumina-silicate fiber blanket)

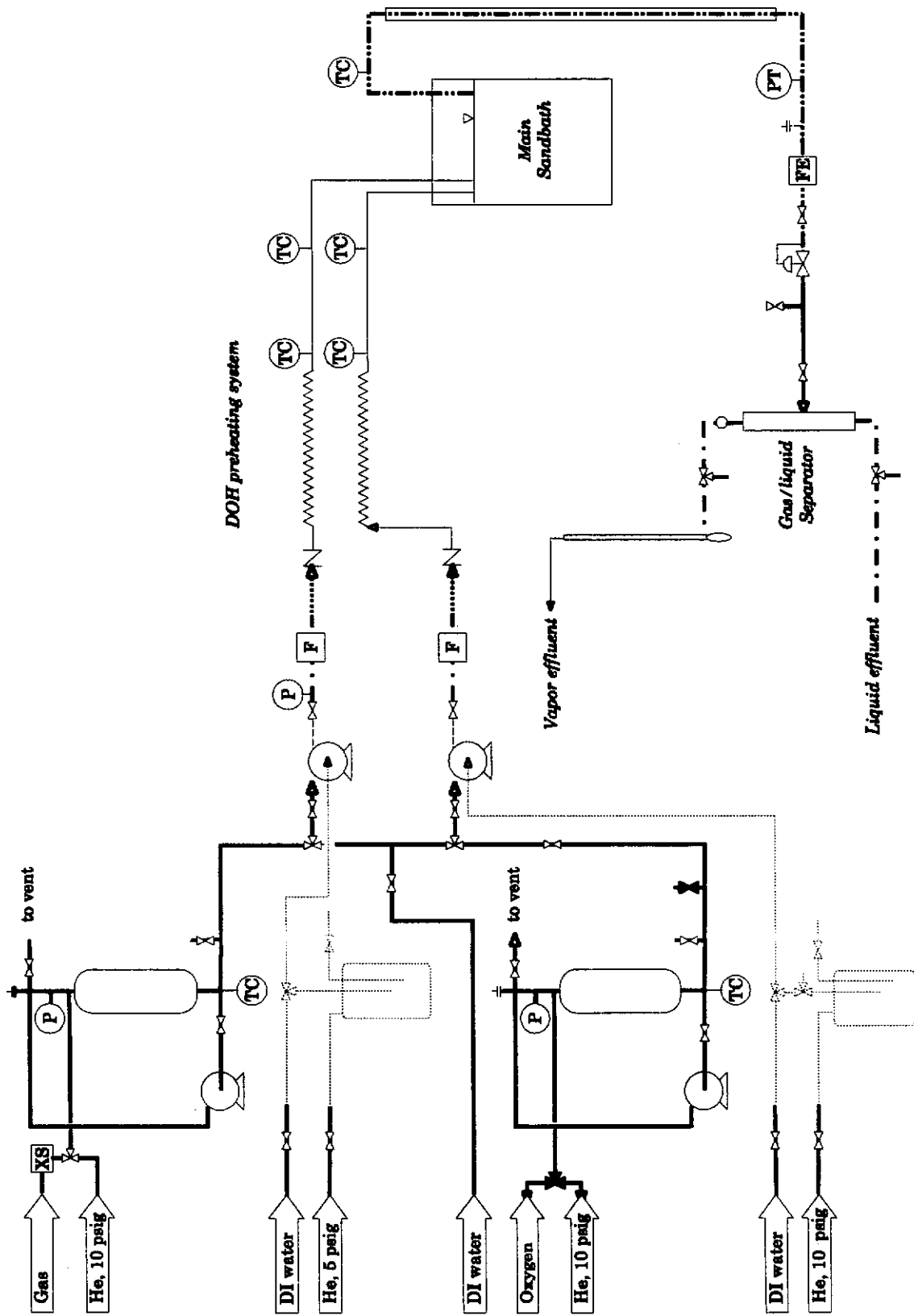


Figure 3.4
Piping and materials of construction diagram for bench-scale reactor apparatus

Materials Key

- 1/4" OD x 0.049" or 0.085" wall 316 or 316L stainless steel
- - - - - 1/4" OD x 0.065 wall Hastelloy C-276
- · - · - · 1/8" OD x 0.035" wall 316 or 304 stainless steel
- 1/8" OD x 0.062 ID" PEEK (polyetheretherketone), 4,000 psig max
- 1/8" x 0.060" ID PTFE (poly(tetrafluoroethylene))
- - - - - 1/16" OD x 0.040" ID seamless 316 stainless steel
- 1/16" OD x 0.01" wall #1 annealed, welded-and-drawn, Hastelloy C-276

TABLE 3.1
Chronology of Reactor System Configurations

System Configuration	Experimental Run Numbers					
	476- 488	530- 551	552- 606	606- 612	613- 648	649- 697
<i>Feed preparation and pressurization</i>						
Pumps						
LDC minipumps	x					
Rainin SD-200 HPLC pumps		x	x	x	x	x
<i>Preheating system</i>						
Primary heating method						
Sandbath	x	x				
Firerod system			x	x		
Direct ohmic heating (DOH)					x	x
Electric heat tracing on transfer line				x	x	x
Electric heat tracing on drop line to sandbath						x
<i>Main reactor</i>						
Old mixing tee design	x					
New mixing tee design		x	x	x	x	x
<i>Letdown system</i>						
Redesigned G/L separator to minimize holdup		x	x	x	x	x

Due the high-temperature, high-pressure environment of the SCWO process, much of the tubing and equipment in the experimental system is constructed of high-nickel alloys. These alloys possess the requisite material strength and corrosion resistance necessary to carry out experimental work safely and reliably. A piping and materials of construction diagram representative of the most recent system configuration is provided in Figure 3.4.

3.1.1 Feed system

The feed system consists of the vessels, equipment, tubing, and instrumentation needed to prepare and pump the oxidant and organic feed streams to the reactor. Its principal components are two high-pressure saturators, a low-pressure hydrogen peroxide feed tank, an low-pressure organic feed vessel, and two high-pressure preparative HPLC pumps.

The water used in feed preparation and all subsequent process and analytical work is obtained from a four cartridge Barnstead Nanopure-A water purification system (Model D2797). The water feed to the system is piped directly from the Bldg. 66 deionized (DI) water system. The purification system consists of one activated carbon cartridge, two mixed-bed anion/cation exchange cartridges, and one 0.2 μ m filtration cartridge. The resulting water has a specific resistance of greater than 18.1 MOhm-cm and is used without further treatment. All cartridges are replaced on an annual basis.

3.1.1.1 Organic feed system

Organic feed solutions are prepared in one of two ways, depending on whether the feed compound is a liquid or a gas. For gaseous reactants, feed preparation begins by filling a 3-liter, 304SS sampling cylinder (Hoke Model 8HD3000, 1800 psig rating) with approximately 2.5 liters of deionized water. The cylinder, or saturator, is then alternately pressurized and vented three times with the gas of interest to reduced the level of undesired gases (particularly oxygen) in the headspace and liquid. Reaction gases (*e.g.*, hydrogen, carbon monoxide) are supplied from regulated, compressed gas cylinders and have a purity of 99 wt% or greater. They are used without further purification. After the purging process, the saturator is pressurized to the desired equilibration pressure and closed off. Saturator pressure is monitored using a Heise precision pressure gauge (CM series, 0-3000 psig, accuracy 0.1% of span). The water in the saturator is allowed to equilibrate overnight (12-18 hours) with the pressurized gas source. Agitation of the saturator fluid during the equilibration process is provided by a recirculation pump (LDC Analytical/Milton Roy minipump Model 2396) which withdraws fluid from the bottom of the saturator and reintroduces it at the top of the saturator

above the vapor-liquid interface. The flowrate of the recirculation pump allows the liquid volume in the saturator to be turned over 2 to 3 times during a typical equilibration period. Inlet dissolved gas concentrations are calculated from published pressure-corrected Henry's law constants (Brelvi and O'Connell, 1972; Benson *et. al*, 1979) and are verified by measuring outlet gas flowrates and concentrations under cold-flow reactor conditions. A detailed discussion of equilibrium calculations and verification experiments can be found in the next section. The calculated concentrations and their estimated error are used in the data analysis program.

Liquid organic feeds (*e.g.*, methanol) are prepared volumetrically using Class A volumetric glassware and a 2.5-5 mL syringe (Hamilton). Anhydrous analytical-reagent grade methanol was obtained from Mallinckrodt and was used without further purification. As received, it contained less than 10 wppm of acetone, formaldehyde, and acetaldehyde. Feed solutions are analyzed via the analytical methods described in Section 3.2.1.1 prior to loading the solution into the organic feed vessel. Once prepared and analyzed, the feed solution is transferred to a 5-L plastic-coated, glass feed vessel (Kontes UltraWare). The vessel is capped and pressurized to 5 psig with helium from a regulated source. The feed line to the pump and the feed sampling line connected to the vessel are then flushed with the solution to remove any liquid from the last run and any air bubbles trapped in the line. Feed samples are taken at the beginning and end of each run using the subsurface feed sampling line to ensure that there is no change in feed composition. Each feed sample is analyzed in triplicate and the average and sample standard deviation of the resulting measurements are used in the data analysis program.

3.1.1.2 Oxidant feed system

Oxidant feed solutions are prepared in one of two ways, depending on whether oxygen or hydrogen peroxide is used as the oxidant. Feed preparation using oxygen is carried out using a 3-liter, high-pressure sampling cylinder (Hoke Model 8HD3000, 1800 psig rating) in a manner identical to that described for gaseous organics. Inlet dissolved oxygen concentrations are calculated using the following equilibrium relationship:

$$y_{O_2} \hat{\phi}_{O_2}(T, P, y_i) P = x_{O_2} H_{O_2, H_2O}(T, P) \quad (3.1)$$

which is valid for dilute solutions of oxygen in water where the activity coefficient of oxygen is independent of concentration.. Since a regulated pure oxygen supply is used to pressurize the saturator, the gas phase is assumed to be pure oxygen ($y_{O_2} = 1$ and $\hat{\phi}_{O_2}(T, P, y_i) \rightarrow \phi_{O_2}(T, P)$). The functional form of the pressure dependence of the Henry's law constant is given by

$$\left(\frac{\partial \ln H_{O_2}}{\partial P} \right)_T = \frac{\bar{v}_{O_2}^\infty}{RT} \quad (3.2)$$

For temperatures well below the critical point of the solvent ($T_c(H_2O) = 374 \text{ }^\circ\text{C}$), the partial molar volume of oxygen at infinite dilution can be assumed to be independent of pressure and Equation (3.2) can be integrated and substituted into Equation (3.1) to yield:

$$\phi_{O_2}(T, P) P = x_{O_2} H_{O_2, H_2O}(T, P^\circ) \exp\left(\frac{\bar{v}_{O_2}^\infty (P - P^\circ)}{RT} \right) \quad (3.3)$$

where P° is the reference pressure for the lower limit of integration. Implicit in the use of Equations (3.1) and (3.3) are two assumptions: a) that the water-oxygen mixture in the saturator is at thermodynamic equilibrium at the end of the saturation process and b) that the description of equilibrium given by Equation (3.3) is valid. The first assumption has been tested experimentally by varying the length of the equilibration time in the saturator. Equilibration periods of 1-3 days showed no measurable difference in the amount of evolved oxygen in the cold flow reactor tests described below. Practical use of Equation (3.3) also depends on accurate estimates of the ambient pressure Henry's law constant, the pure component oxygen fugacity coefficient, and the infinite dilution partial molar volume of oxygen in water. The value of $H_{O_2, H_2O}(T, P^\circ)$ at ambient temperature was calculated using the three-term power series correlation of Benson, *et al.* (1979) which is based on 37

measurements over a temperature range of 0-60 °C. The value of $\bar{v}_{O_2}^{\infty}$ was estimated using the corresponding states correlation of Brevli and O'Connell (1972), while values of $\phi_{O_2}(T,P)$ were calculated using the Peng-Robinson equation of state (1976). These quantities were used with Equation (3.3) to generate Figure 3.5 which shows the dissolved oxygen concentration in water at 25 °C as a function of pressure.

Because of the importance of accurately knowing the inlet oxygen concentration to the reactor, the oxygen solubility relationship shown in Figure 3.5 was tested experimentally. A series of five control experiments were conducted where water was equilibrated overnight in the saturator at headspace pressures of 600 and 1000 psig. The equilibrated solutions were then pumped at a known flowrate through the cold reactor system and allowed to flash into the gas/liquid separator. The flowrate and oxygen composition of the vapor effluent were measured using the methods described in Section 3.2.2.1 and the results were used to back-calculate the dissolved oxygen concentration in the saturator for each experiment. These back-calculated values are also shown in Figure 3.5 and demonstrate remarkable agreement with the calculated pressure-corrected Henry's law relation given by Equation (3.3).

Figure 3.5 also shows that the oxygen saturator system is fairly limited in terms of its ability to deliver high concentrations of dissolved oxygen in the oxidant feed stream. Since the maximum pressure rating of the saturator is 1,800 psig, the maximum dissolved oxygen concentration that can be attained in the feed at room temperature is 3930 wppm (parts per million by weight). This maximum limits the range of experimentally accessible oxygen feed concentrations and oxidant/organic ratios. An alternative approach explored during this thesis involves the use of hydrogen peroxide as the oxidant source. The method relies on the surface-catalyzed decomposition of hydrogen peroxide during preheating of the oxidant feedstream to produce oxygen and water. The method, first used at Sandia National Laboratory, is described in the following section.

Hydrogen peroxide decomposition has been studied extensively at temperatures of 100 to 280 °C by researchers investigating the water chemistry of BWR cooling loops (Takagi and Ishigure, 1985; Lin *et. al*, 1991; Lin, 1993). These investigators found decomposition to be

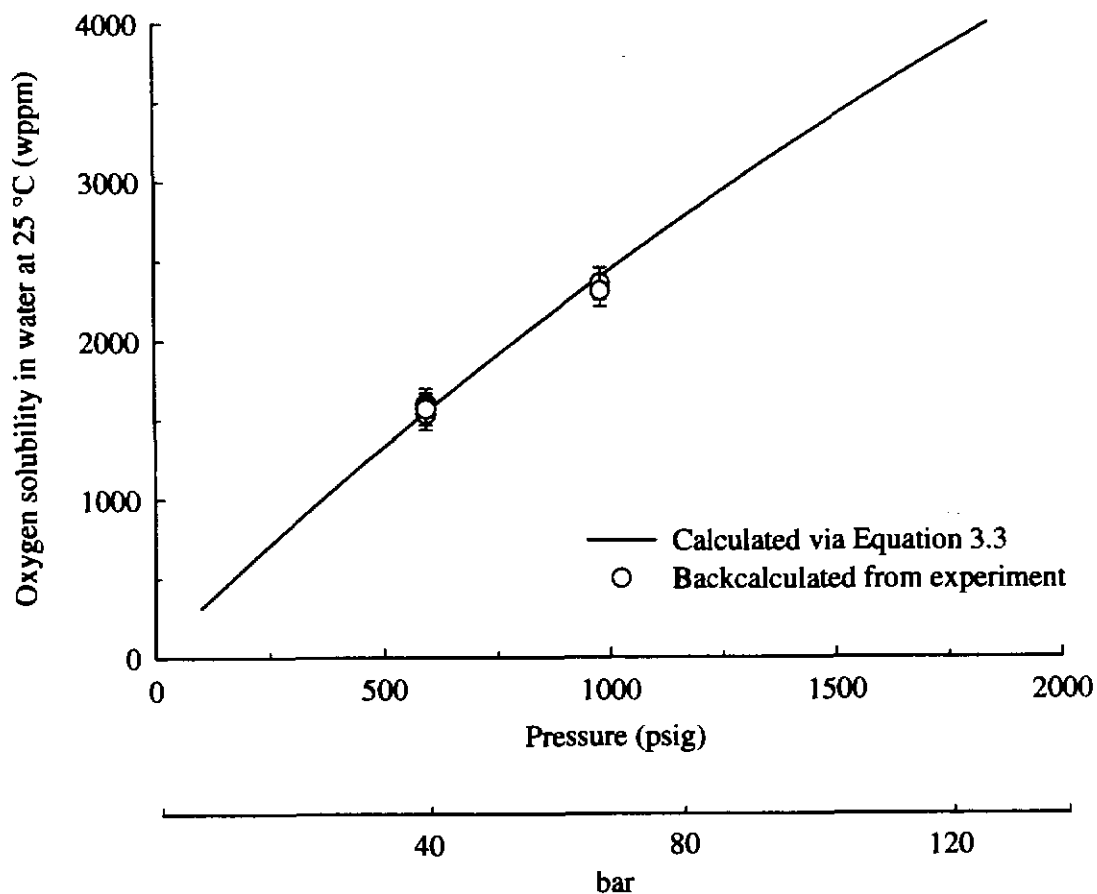


Figure 3.5
 Oxygen solubility in water as a function of pressure at 25 °C. Solid line represents values calculated using Equation 3.3 and point values are backcalculated from the saturator experiments described in Section 3.1.1.2.

surface-catalyzed and a strong function of the material of construction of the reactor and its surface-to-volume ratio. Over the dilute and limited concentration range of the BWR studies (1-10 wppb), peroxide decomposition kinetics were found to be first order in hydrogen peroxide concentration. Hydrogen peroxide decomposition can be described by the following global reaction wherein one mole of peroxide reacts through a series of elementary homogeneous and heterogeneous reactions to form ½ mole of oxygen and one mole of water:



Since the reacting peroxide/oxygen/water mixture is rapidly brought above the mixture critical point as it passes through the preheater, it quickly becomes a single fluid phase—thereby overcoming the room-temperature oxygen solubility constraint of the saturator system. The oxygen formed by the decomposition reaction then passes through the remaining preheater tubing and enters the mixing tee as molecular oxygen to serve as the oxidant. A key issue in this scheme is the timescale for peroxide decomposition relative to the residence time of the peroxide in the preheater. If the decomposition is incomplete, some peroxide could enter the mixing tee unreacted and serve as a potent source of OH radicals—thereby altering the rate of oxidation. A detailed discussion of this topic and of several control experiments which support the complete breakdown hypothesis can be found in Section 4.2 of Chapter 4.

Aqueous hydrogen peroxide feed solutions are prepared volumetrically using Class A volumetric glassware and a 25mL glass pipet. ACS Reagent Grade hydrogen peroxide (stannate stabilized) is obtained from Aldrich Chemical Co. (30wt%, PN 21,676-3) and is used without further purification. Hydrogen peroxide feed solutions are analyzed by the ceric ion titration method described in Section 3.2.1.2. Once prepared, the hydrogen peroxide feed solution is transferred to a 4-liter HDPE reservoir (Dionex, PN 39164). The reservoir is capped, pressurized to 10 psig with helium from a regulated source, and connected to the suction side of the oxidant pump with 1/8 in. x 0.062 in. ID PTFE tubing. The reservoir is equipped with a valved sampling line which is used to periodically draw off samples of the feed solution during a run for analysis. All of the tubing, valves, and fittings upstream of the

pump are plastic (HDPE, ETFE, or PTFE) to minimize the surface-catalyzed decomposition of hydrogen peroxide which would occur if these components were made of metal. Such decomposition would change the hydrogen peroxide feed concentration in the feed reservoir and could result in the formation of oxygen bubbles which would interfere with the correct operation of the pump check valves.

3.1.1.3 Oxidant and organic feed delivery

Organic and oxidant feed solutions are delivered to the preheating system via two digital, semi-preparative, HPLC pumps (Rainin, SD-200). Each pump is equipped with a 25 mL/min pump head (0.001 mL/min increment, rated for 4,600 psig at max. flow) and a pulse-dampening pressure module (rated for 6,000 psig). Due to the low-pulsing design of the Rainin pumps and the quality of the Tescom backpressure regulator (BPR) used downstream of the reactor, the system pressure varies by no more than ± 15 psig at operating pressures of 3,500-4,000 psig. The early version of the reactor system shown in Figure 3.1 used a duplex LDC Analytical/Milton Roy minipump to deliver the oxidant and organic feeds. The duplex configuration consisted of two pump bodies (hence, two liquid heads) mounted on either side of a drive motor. The motor rotated a pair of eccentric gears which caused the pistons to reciprocate within each liquid head. The oxidant and organic flowrates were adjusted via separate manual verniers which controlled the stroke length of each piston. System pressure varied by approximately ± 70 psig using the LDC feed pump in combination with the Tescom BPR.

When organic liquids and hydrogen peroxide solutions are used as the organic and oxidant feeds, each pump is supplied with approximately 5-10 psig of suction-side pressure. Pressure is provided by a regulated helium source and is applied to the headspace of the feed vessels. This head pressure ensures proper check valve action on the suction side of the pump and prevents the formation of air bubbles in the pump head on the intake stroke of the piston. In the low-pressure feed mode, the suction-side fitting on each pump is comprised of a Tefzel ferrule (Upchurch, P-300), a 1/8 in. Delrin nut (Upchurch, P-301), and plastic tubing (PTFE, 1/8 in. x 0.062 in. ID). When a high-pressure saturator feed is used, these plastic components

are replaced a 1/16 in. super flangeless ferrule and lock ring (Upchurch, P-250), a 316SS nut (Upchurch, F-160), and 1/16 in. x 0.0425 in. ID 316SS tubing. This ferrule/nut/tubing combination is rated for 7,000 psig and ensures a leak-free connection between the high-pressure saturator solution and the pump head inlet.

The extremely high suction-side pressures generated by the saturator system interfere with the internal volume/stroke calibration of the Rainin feed pumps. As a result, each pump is manually calibrated at a variety of flowrates and suction- and discharge-side pressures. These calibrations can be found in Appendix 8.4 and are used to calculate the true pump flowrate as a function of pump flow setpoint, saturator (suction-side) pressure, and reactor (discharge-side) pressure. During an experiment, the effluent flowrate (the sum of the organic and oxidant flowrates) is measured and compared to the sum of the calculated pump flowrates to ensure that the pumps are operating properly. The high suction-side pressures also result in abnormal wear on the primary piston seal and the upstream and downstream check-valves. These components are inspected periodically and are replaced approximately every 6 months during periods of heavy saturator use. The flowrate of the Duplex LCD minipump shown in Figure 3.1 was also manually calibrated for the small number of experiments in which it was used. The pump calibration performed by Holgate (1993) was used in these instances.

Each Rainin pump is equipped with a pressure transducer mounted in the pressure module located downstream of the pump head. The transducer signal serves to provide the pump computer with the current system pressure and as part of an electronic interlock system which can shut down the pump in event the system pressure exceeds a preset value. This interlock feature is present on both the organic and oxidant pumps and is the first of several engineering safety features designed to prevent system overpressure (see Section 3.4.2).

During heatup of the reactor and preheating systems, deionized water is pumped through the system using both feed pumps. Prior to starting up the system, the water in the DI water feed tank is degassed with helium from a regulated source through a pair of 5 μm fritted filters located at the bottom of the tank. The degassing procedure helps to remove dissolved oxygen and nitrogen in the DI water feed and minimizes the potential for bubble formation in

the pump heads. When the reactor system has reached the desired steady-state operating temperature, the feeds to the suction-side of the pumps are switched from water to the oxidant and organic feed reservoirs (or saturators). Upon exiting the feed pumps, each feed solution passes through a high-pressure valve (Hoke, 7155G2Y, 6000psig rating) and enters an 8 ft. length of 1/8 in. OD x 0.035 in. ID 316SS tubing leading to the preheating system. The valve allows the pump to be isolated from the system while it is at pressure for quick maintenance on the pump head. Just prior to entering the preheating system, each feed passes through a 2 μm in-line filter (Valco, ZUFR2) to minimize the passage of particulate matter into the narrow flowpath of the mixing tee located downstream.

3.1.2 Preheat system

The purpose of the preheating system is to raise the fluid temperatures of both the organic and oxidant feed solutions to reaction temperature prior to mixing them at the head of the reactor. During the course of this thesis three separate preheating systems were employed. Each system, its equipment, and associated instrumentation are described below.

3.1.2.1 Sandbath preheating system

The earliest preheating system consisted of a fluidized sandbath (Techne Model SBL-2 or SBS-4, maximum operating temperature 350 °C). A schematic of this system is shown in Figure 3.1. Each feed passes through a 5-7 ft. long coil of 1/16 in. OD x 0.01 in. wall HC-276 tubing immersed directly in the bath. The bath is normally operated at 300-350 °C, though a number of early experimental runs were conducted with the preheating sandbath off. Bath temperature is monitored using an immersed 1/16 in. Type K thermocouple (Omega). Upon exiting the bath, the feeds pass through approximately 1-2 ft. of insulated line (Zetex wrapped) and an additional 3 ft. of uninsulated line before dropping below the fluidized surface of the main sandbath (described in Section 3.1.3).

The sandbath preheating system was abandoned early in this thesis work for two reasons: a) its relatively low maximum operating temperature of 350 °C, and b) the long time (typically 2-3 hours) required for it to reach steady-state operation.

3.1.2.2 Firerod preheating system

In an effort to address the operational limitations of the sandbath preheating system, a new preheating system was designed and implemented in the Fall of 1995. The key element of the system, illustrated in Figure 3.2, consists of a 17 ft. length of 1/8 in. OD x 0.035 in. wall HC-276 tubing wound around a cylindrical copper rod (2 in. OD x 6 in. L). The center of each copper rod is drilled out and a close-fitting, resistive cylindrical heating element is inserted inside (Watlow, Firerod, 3/4 in. OD x 6.0 in. L, 240V, 1000W, max core temp 800 °C). Power input to the heating element is controlled by a zero-voltage-switched, silicon controlled rectifier (SCR) power controller (Omega, SCR71Z-230, 240V, 30 amps). The input signal to the SCR is provided by a PID temperature controller (Omega, CN9141A) which uses an 1/16 in. Type K thermocouple as the input sensing element. The thermocouple is mounted in a 1/8 in. tee (HIP, 15-23AF1) located approximately 6 in. downstream of the Firerod/copper-rod heating element. The tip of the thermocouple is centered in the flowstream passing through the tee. During operation, process feeds are pumped through the tubing and are raised to the controller setpoint temperature via heat conduction through the heating element and copper rod. The organic preheating section consists of one heating element and a control thermocouple. The oxygen-side section is comprised of two heating elements, a small packed-bed reactor positioned in between, and a control thermocouple located downstream of the second element. The packed-bed is used to promote the surface-catalyzed decomposition of hydrogen peroxide to oxygen and water (see Section 3.1.1.2). The reactor is constructed from a 9/16 in. OD x 5/16 in. ID x 15cm length of coned-and-threaded HC-276 tubing. The tube is packed with -60/+100 mesh Inconel-625 beads (Crucible Compaction Metals, Oakdale, PA). The beads are held in place by two 5/16 in. OD x 1/16 in. thick, 10 µm HC-276 frits (Newmet Krebsöge, Inc., Terreville, CT) which are press-fit into the end of the tube. The end fittings for the tube consist of two 316SS taper-seal 9/16 in. to 1/8 in. reducers (HIP, 15-21AF2HF9). Early pressure tests of the Firerod/packed reactor train showed that the taper-seal fittings did not seal properly upon repeated temperature cycling. As a result, all taper seal fittings were welded.

The packed-bed reactor, Firerod heating elements, and preheating tubing are placed in an 11 in. x 12 in. x 15 in. ceramic box constructed of 1 thick Kaowool fiber board and fiber bond cement (Lynn Ceramics). The interior of the box is filled with loose, bulk alumina-silicate ceramic fiber (Lynn Ceramics, 2,300 °F max) to provide additional insulation. In an effort to reduce heat loss in the transfer line between the box and the main sandbath, the transfer line is insulated with 1 in. thick ceramic fiber strips (Lynn Ceramics, 2,300 °F max) which are held in place by 2 in. wide insulating wrap (Zetex).

Initial trials of the Firerod preheating system revealed that it was capable of preheating both feed streams to a temperature of 580 °C at flowrates of 2-10 mL/min and higher. The time required to reach steady-state operation from a cold, room temperature start was approximately one and a half hours—a dramatic improvement of the 2-3 hour startup time of the sandbath preheating system. The Firerod system was used for a series of 54 benzene and methanol hydrolysis and oxidation experiments. Later, the transfer lines between the preheating box and the edge of the main sandbath were electrically heat traced with flexible Samox heat tape (Thermolyne, BWH102060, 1 in. W x 6 ft. L, 940 watts) and insulated with 1 in. thick ceramic fiber strips to further minimize heat loss in the transfer section. Power to the tape was provided by a Thermolyne Percentage Power Controller (Thermolyne, Type CN45500, 120V, 15 amp). The augmented configuration was used for an additional 6 methanol oxidation experiments.

Despite the improved performance of the Firerod system, the design suffered from several drawbacks. The original and heat-traced versions of the system were unable to achieve preheating temperatures in excess of 580°C. Early experience with benzene oxidation, however, suggested that temperatures in excess of 600°C would be necessary to achieve complete benzene destruction within experimentally accessible residence times. Unfortunately, operation at 580°C at the lower end of the flowrate range required the heating elements to operate at internal temperatures of 700-800°C. These temperatures are 100-200°C higher than the preheating setpoint of 580°C and are close to the operational limit of the heating elements. The system also suffered from control problems stemming from the large

time lag between when power was applied to the heating elements and when the resulting temperature increase would be sensed by the control thermocouple. This lag is attributable to the large thermal mass of the copper rods and resulted in severe integral windup of the PID controller.

3.1.2.3 Direct ohmic preheating (DOH) system

The DOH system was implemented in the Fall of 1996 in an effort to address the limitations of the existing Firerod system. The system design is a lab-scale adaptation of the DOH system employed at Los Alamos National Laboratories and is shown in Figure 3.3. It consists of two 31 ft. coiled lengths of 1/16 in. OD x 0.01 in. wall HC-276 tubing placed in a 8 in. x 14 in. x 26 in. insulated ceramic box constructed of Kaowool board and fiber bond cement (Lynn Ceramics). Each length of tubing is covered with two layers of high-temperature Nextel sleeving (Omega, XC-116 and XC-316, 2,200 °F max) to prevent inter- and intra-tube metal-to-metal contact. The void space in the box and between the tubing coils is filled with loose, bulk alumina-silicate ceramic fiber (Lynn Ceramics, 2,300 °F max). The positive lead of a 120V AC line is clamped securely to one end of the tubing and the negative lead to the other. A backup ground wire is placed 2 in. downstream of the negative lead to direct current to ground in the event of a failure of the negative lead connection. A short, six inch length of 1/8 in. OD x 0.062 in. ID PEEK (polyetheretherketone) tubing is located upstream of the positive lead. The PEEK tubing is electrically nonconductive and acts to electrically isolate the upstream tubing and instrumentation from the positive lead. The maximum service pressure of the PEEK tubing is 4,000 psig at 25 °C. However, its pressure rating drops dramatically with increasing temperature. In the event of a momentary upstream pressure drop, hot steam in the reactor section could backflow through the tubing, causing it to rupture. To prevent such backflow, a high-pressure check valve (Nupro, SS-53S4, 6,000 psig max) is located between the lead and the PEEK tubing on both feed lines.

Based on the reported electrical resistivity of Hastelloy C-276 at 500-600 °C (International, 1993), the total resistance of the previously described 31 ft. preheating line is approximately 11.1 ohms. Using an applied voltage of 120 V (rms), the resulting *maximum*

current draw is 15.3 amps. The corresponding maximum power input to the tube wall is 1.3 kW—a value several times larger than the calculated preheater duty required to raise a feed stream from ambient to process conditions. Power input to the preheating tubing is controlled by the same silicon controlled rectifiers (SCRs) used in the Firerod system. Power to the oxidant and organic feed lines is controlled separately using two SCRs. The input signal to an individual SCR is provided by a PID temperature controller (Omega, CN9141A) utilizing a 1/32 in. Type K thermocouple as the input sensing element. The thermocouple tip is centered in the feed flowstream, and the thermocouple itself is mounted in a 1/16 in. tee (Swagelok, SS-110-3) using a bored-through 1/16 in.-1/32 in. adapter (Valco, ZRU1.5T). The mounting tee for each feedstream is located 2 in. downstream of the negative lead and, as a result, is not ohmically heated. It is placed approximately 4-6 in. from the lip of the main sandbath in an effort to minimize the distance and heat loss between the preheating section and the sandbath. Both the organic and oxidant-side control temperatures are logged every 10 seconds by the HOTMUX™ data acquisition software (see Section 3.3).

The remaining length of tubing (~ 12-14 inches) between the end of the DOH system and the fluidized surface of the sandbath is actively heated by a resistive cable heater (Watlow, 62H24A6X, 1/16 in. OD x 2 ft. L, 120 V, 240 W max). Each length of feedstream tubing has its own separate heater and power supply. The cable heater is wound around the remaining preheating tubing beginning one inch downstream of the DOH grounding wire and extends below the surface of the sandbath. Power to each heater is controlled by a variable transformer (Powerstat, PN 3PN117C, 0-120 V, 12 amps). In the exposed section of tubing above the surface of the sandbath, Zetex insulating wrap is wound around the intertwined preheating tubing and cable heater to minimize heat loss.

The DOH system has been successfully tested at temperatures up to 625 °C at feed flowrates of 2-15 mL/min. Heatup time for the system varies from 30-45 minutes—a period far shorter than the time required by the main sandbath. In addition, the low thermal mass of the DOH preheating tubing enables the system to cool down rapidly from operating temperatures of 500-625 °C. One source of concern regarding the use of the DOH system is

the direct contact between the feed solutions and the current carrying wall of the preheating tubing. Due to the relatively high electric potentials and currents employed in the system, a series of experiments were conducted to determine if electrolytic reactions involving the feed were taking place. Experiments were performed by passing aqueous organic feed solutions through the DOH system during operation. The feed and effluent were then analyzed to determine if any change in organic concentration had taken place. For the compounds used in this thesis, particularly methanol, no reaction or degradation was observed. These experiments will have to be repeated, however, for other compounds which are part of future work involving the DOH preheating system. In addition, any planned kinetic experiments involving the presence of dissolved salts will have to be carefully examined to determine the current carrying capacity of the salt solution passing through the preheater.

3.1.3 Reactor system

After the preheating system, the organic and oxidant feedlines drop into the main sandbath (Techne, FB-08, 700 °C max). The sandbath consists of approximately 16 kg of fine, chromatographic-grade alumina supported by a porous metal plate and confined within an insulated, metal cylinder. Located around the periphery of the bath on the inside of the cylinder are four resistive heating elements. Power to the elements is provided by an internal 240V, 3 kW power supply controlled by a Eurotherm PID controller. The controller sensing element is a Type K thermocouple immersed in the sand bed. Fluidizing air to the bath is supplied from the Bldg. 66 high-pressure air supply (~80-100 psig). Prior to entering the sandbath, the air passes through a regulator and filter trap (Wilkerson, Model C04-02-B00, set to 60 psig) to remove condensed water and particulates. Airflow to the bath is controlled by a rotameter. The bath is also equipped with a dust extraction system to minimize the introduction of alumina fines into the surrounding lab environment. This reclamation system has been augmented by the construction of a Lexan hood around the entire preheating and main sandbath system. The hood completely encloses the top, bottom, and side of the bath and is vented to the Bldg. 66 hood exhaust.

Once in the main sandbath, the two feed solutions each pass through an additional 17 ft. coiled length of 1/16 in. OD x 0.01 in. wall HC-276 tubing. The additional tubing serves to ensure that the fluids are at the same temperature as the sandbath prior to entering the mixing tee. In an effort to detect any non-isothermality in the bath due to poor fluidization, two Type K thermocouples are placed in the bath at different heights. One is located at the bottom of the bath approximately 1-2 in. above the porous plate, and the other is at the top, approximately 3-4 in. below the fluidized surface of the sand. Temperature readings from these thermocouples are taken automatically every 10 seconds and are logged using the HOTMUX software (see Section 3.3).

3.1.3.1 Mixing tee and reactor design

Upon exiting the preheating tubing immersed in the sandbath, the two feedstreams are mixed in a high-pressure mixing tee located at the head of the tubular reactor. During the course of this work, the design of the tee underwent a number of refinements. As a consequence, several different tee designs were used to collect the data for this thesis. A summary of these designs along with relevant dimensions is provided in Table 3.2. The corresponding schematics are shown in Figure 3.7

For the purpose of this thesis, we are interested in the design of a tee suitable for rapid and complete mixing in a reactor application where the reaction rates are relatively high and the product composition may be affected by the degree of nonhomogeneity of the reactant concentrations. The design and performance of such devices has been the subject of considerable experimental and computational fluid dynamics (CFD) research. A survey of the relevant literature reveals that much of the early experimental work in this area focused on investigating the *macroscopic* homogeneity of mixed fluid streams by means of visually observing or measuring the downstream radial uniformity of a tracer or related quantity, such as thermal or electrical conductivity (Reed and Narayan, 1979; Maruyama *et. al*, 1981; Forney and Lee, 1982). Typically, the indicator of performance in these studies was the distance downstream of the mixing point at which a desired degree of uniformity was attained. In general, the studies concluded that the mixing distance was a function of the uniformity

criteria used, the flow configuration (opposed vs. side-entry flow), the ratio of side to mainstream velocities, the ratio of side to mainstream tube diameters, and the side and mainstream Reynolds numbers (Tosun, 1987). Using measurement points relatively far downstream of the mixing point ($15 < x/D < 120$), the authors found that optimal macromixing was achieved in 90° tees such as the one in Figure 3.6 by centering the sidestream jet along the pipeline axis of the main flow. The relevance of this finding to the design of a mixing tee for rapidly reacting mixtures is debatable, however. This is because the various measurement methods described above essentially look for uniform distribution of a property radially in the pipe by measuring the property averaged over many fluid elements. As a result, they provide no information about the *size* of the elements themselves and, hence, no information on the conditions that promote optimal micromixing. At the microscale, mixing takes place mainly by molecular diffusion between turbulent eddies, and the smaller the eddies, the faster the mixing process.

In an effort to address this limitation, a number of more recent investigations have explicitly focused on studying tee designs and flow conditions which promote micromixing at short distances ($x/D < 3$) downstream of the mixing point (Tosun, 1987; Cozewith and Busko, 1989; Forney and Gray, 1990). These studies utilize a well-characterized, rapid chemical reaction (or set of reactions) whose product composition or distribution is influenced by the degree of mixedness on the microscale. Examples include the diffusion-limited HCl/NaOH neutralization reaction used by Cozewith and Busko (1989) and the consecutive, competitive azo coupling reactions employed by Tosun (1987). The dependence of this latter example on mixing occurs because the rate of consumption of reactants is high relative to the rate of transport to and from the reaction zone. As a result, steep concentration gradients are formed between segregated, reactant-rich regions (eddies), and the formation of a detectable intermediate is promoted or depressed due to the overexposure of one reactant. Thus, tee and flow arrangements which result in small segregation lengths facilitate micromixing and, hence, detectable changes in the product composition.

The findings of the two studies cited above are summarized in the following paragraphs. The coordinate system and nomenclature for a tee mixer are shown in Figure 3.6. The sidestream diameter and velocity are represented by the variables d_j and v_j , while the mainstream diameter and velocity are represented by D_R and V_R . The distance downstream required for complete mixing is denoted by L . For the case considered here, the temperature, density, and viscosity of the two incoming streams will be treated as being equal.

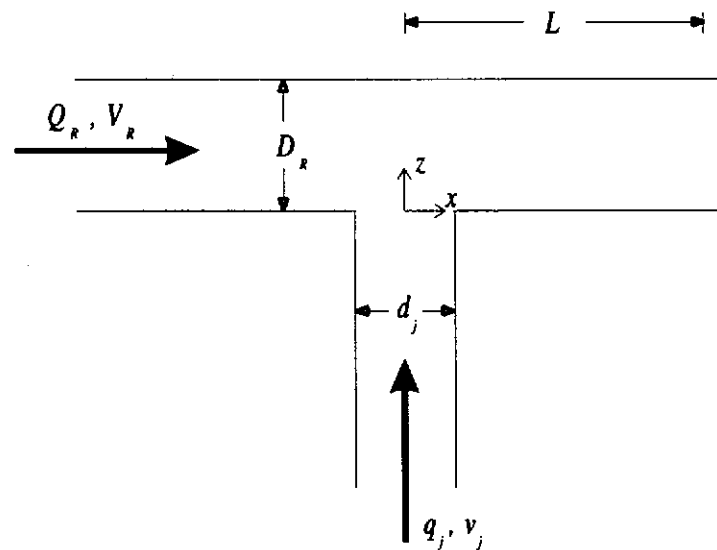


Figure 3.6
Schematic and nomenclature for 90° mixing tee

Effect of v_j/V_R and d_j/D_R ratios on mixing length

For a given d_j/D_R ratio, both studies found that there is a range of optimal v_j/V_R ratios which result in mixing in the shortest downstream distance. Starting at low v_j/V_R , the ratio of L/D decreases as v_j/V_R increases. At these low v_j/V_R ratios, the side jet is quickly bent over by the main flow and clings to the near wall of the main pipe. As v_j/V_R continues to increase, the side jet penetrates further into the main flow stream before being turned in the direction of the main flow. At the point where the side jet is centered in the main flow, a minimum in L/D is reached. At higher v_j/V_R , the jet impinges on the far wall of the pipe, and the impingement point moves further upstream as v_j/V_R is raised. The upper limit of the minimum L/D range occurs at a v_j/V_R ratio which causes the jet to strike the far wall at a x/D of $\sim 0.7-0.8$.

Ultimately, at higher v_j/V_R , the jet shoots directly across with pipe with little to no deflection. At this point, a portion of the fluid hitting the far wall spreads out around the circumference of the pipe and forms a thin layer near the wall that flows downstream along the pipe wall. The remainder of the side stream flows as a jet in the far wall half of the pipe.

The data of Cozewith (1989; 1991) and Tosun (1987) have been correlated by Forney and Gray (1990) in the form of:

$$\left(\frac{v_j}{V_R}\right)_{opt} = \frac{1}{(d_j / D_R)[1.6 - (d_j / D_R)]} \quad (3.5)$$

where $(v_j/V_R)_{opt}$ is the side-to-mainstream velocity ratio that gives mixing in the shortest downstream distance. Equation (3.5) was developed for data spanning a range of $0.047 \leq d_j/D_R \leq 0.25$ and $1.0 \leq v_j/V_R \leq 12$ and yields optimal velocity ratios within 20% of the experimental values. The corresponding mixing distance range is $1 \leq LD \leq 5$.

The use of the word “optimal” here deserves some discussion. While the initial trend of decreasing LD with increasing v_j/V_R is quite clear from all the data sets, the behavior at high v_j/V_R is somewhat contradictory. Tosun found well-defined optima in v_j/V_R , while Cozewith found that there was a relatively broad range of optimal v_j/V_R values. In some cases, no optimum was found to exist. In these instances, LD was found to monotonically decrease or level off as v_j/V_R increased beyond a critical value. The absence of a clearly defined upper bound on the optimal v_j/V_R is also supported by the data of Maruyama et al. (1981) and Gosman (1986) and is attributed to the switch from jet to impingement mixing. In the impingement regime, the jet strikes the far wall close to the tee inlet, and mixing continually improves as the jet flow increases. The presence or absence of clear minima is further obscured in all data sets by scatter in the experimental data and the lack of experimental replication. The latter would serve to indicate the degree of variability present in what are, admittedly, difficult experiments. In light of the contradictory findings regarding optimal v_j/V_R ratios, Equation (3.5) should probably be viewed as providing a suitable lower bound for v_j/V_R for a given d_j/D_R ratio.

Effect of jet and mainstream Reynolds numbers

Both the Tosun and Cozewith studies found that at the “optimal” v_j/V_R ratio, the mixing length, L , was independent of $N_{Re,R}$ for values greater than 10,000. Below this value, L increases approximately as $N_{Re,R}^{-0.8}$ for d_j/D_R ratios between 0.125 and 0.25. Over the range of diameter and velocity ratios explored in the Cozewith study, L/D varied from a value of 1.6 (at $N_{Re,R} > 10,000$) to a value of 16 (at $N_{Re,R} \cong 3,000$). For a given d_j/D_R and v_j/V_R ratio, $N_{Re,R}$ and $N_{Re,j}$ are related by:

$$N_{Re,j} = N_{Re,R} \left(\frac{v_j}{V_R} \right) \left(\frac{d_j}{D_R} \right) \quad (3.6)$$

Substitution of relevant values into Equation (3.6) reveals that $N_{Re,j}$ was maintained above 6,000 in all of the studies involving change in the mainstream Reynolds number.

Effect of d_j/D_R on L/D

The dependence of the downstream mixing distance on the ratio of the jet to mainstream diameter is unclear. Cozewith found a strong effect of d_j/D_R on mixing, with L/D varying as $(d_j/D_R)^2$. Thus, mixing occurs much more rapidly as d_j/D_R is reduced. In contrast, the data of Maruyama indicated no clear trend in mixing performance with d_j/D_R , while the Tosun study found that mixing was independent of it.

Mixing tees used in this study

Early data were taken using the mixing tee described by Holgate (1993). It consists of an unmodified HC-276 ¼ in. cross (High Pressure Equipment (HIP), 60-24HF4) with the oxidant and organic feeds entering from opposite sides of the tee. Placed in one of the arms, at an angle of 90° to the incoming flows, is a 1/16 in. Type K thermocouple with its tip centered in the flowstream. The flow conditions in the tee under typical operating conditions and the tee geometry are summarized in Table 3.2. Based on the discussion above, it is difficult to predict its performance since it is well outside the range of conditions and tee geometries explored in the literature. The data of Maruyama (1983) and Tosun (1987) suggest

that opposed-flow tees can be quite suitable for good micromixing. However, the range of d_j/D_R examined in the literature does not encompass the value of 1.0; nor are there data for sidestream Reynolds numbers as low as 1,200 to 2,800.

The reactor used with the ¼ in. HIP cross consisted of a 4.71 m coiled length of ¼ in. OD x 0.067 in. ID Inconel 625 tubing. The volume and surface area of the reactor can be found in Appendix 8.4. A HC-276 ¼ in. tee (HIP 60-23HF4) was located at the end of the reactor tubing and is fitted with an additional 1/16 in. Type K thermocouple in the side arm. The ¼ in. reactor/tee configuration was used for a total of 5 experiments.

The majority of the experiments in this thesis were conducted using a series of tubular reactors of varying diameter and length (see Appendix 8.4 for a complete listing). The new reactors were constructed of 1/8 in. OD tubing and had internal volumes ranging from 2.0 to 9.7 cm³. The change in tubing OD necessitated the construction of new mixing tees based on a 1/8 in. high-pressure cross (HIP 60-24HF2). Crosses were fabricated in both opposed-flow and side-entry configurations. In addition, in an effort to promote better mixing in the tee, a number of small inserts were fabricated and placed in the sidestream arms of several crosses to reduce the d_j/D_R ratio. The inserts consisted of piece of 0.01 in. ID x 1/16 in. OD 316SS tubing cut to a length of approximately 0.28 in.. The tubing was then press-fit into the arm of the cross with the front end flush with the interior wall of the cross (see Figure 3.7).

The resulting family of mixing tees are described in Table 3.2 and illustrated in Figure 3.7. As shown, the presence of the inserts dramatically increases the sidestream Reynolds number and the sidestream-to-mainstream velocity ratio in both the opposed-flow and side-entry tees. Under typical operating conditions, the v_j/V_R ratio in insert-fitted tees is approximately 22-24—a marked increase over the 0.5 value of unmodified tees. The d_j/D_R ratio reported in Table 3.2 is based on the ratio of the sidestream diameter and the diameter of the tee arm downstream of the mixing point. This latter diameter was chosen over the diameter of the reactor, since the length-to-diameter ratio of the arm is 4.5 (slightly larger than the reported L/D required for good mixing). Reported V_R and $N_{Re,R}$ values are also based on the arm diameter. Ideally, the arm diameter and the reactor diameter should be equal to use the

TABLE 3.2
Summary of Mixing Tee Configurations and Flow Conditions

No.	Manufacturer Part No. ^a	Type ^b	Tee ID inches (cm)	Reactor ID inches (cm)	d_j/D_R ^f	v_j/V_R	$N_{Re,j}$ ⁱ	$N_{Re,R}$ ^j	$N_{Re,R}$ ^k
1	HIP 60-24HF4	opposed	3/32 (.2381)	0.067 (.1702) ^d	1.0	~ 0.5 ^g	1200- 2800	3300- 7000	3100- 6800
2	HIP 60-24HF2	opposed	1/16 (.1588)	0.041 (.1041) ^e	1.0	~ 0.5 ^g	1500- 3400	3200- 7500	2900- 7300
3	HIP 60-24HF2	opposed	0.01 (.0254) ^c	0.041 (.1041) ^e	.16	22-24 ^h	3000- 11000	3200- 7500	3000- 7300
4	HIP 60-24HF2	side-entry	0.01 (.0254) ^c	0.041 (.1041) ^e	.16	22-24 ^h	3000- 11000	3200- 7500	3000- 7300
5	HIP 60-24HF2	side-entry	0.01 (.0254) ^c	0.067 (.1702) ^d	.16	22-24 ^h	6500- 24000	3300- 7700	3100- 7500

^a All tees from High-Pressure Equipment, Co. and constructed of HC-276.

^b In side-entry tees the angle of incidence, or branch angle, between the organic and oxidant feeds is 90°. In the opposed-flow design the angle is 180°.

^c Tees have a 1/16 in. OD x 0.01 in. ID x .28" L 316SS tube insert placed in both feed branches of the tee. Length to diameter ratio of the leg of tee downstream of mixing point is 4.5.

^d Original Holgate reactor (see Appendix 8.4 for details of geometry).

^e Any of a variety of 1/8 in. OD reactors used in this work (see Appendix 8.4 for a complete listing).

^f Values are for the tee given in each row. D_R based on diameter of empty arm of tee downstream of mixing point.

^g Based on equal volumetric flowrates of oxidant and organic feeds.

^h Based on typical operating conditions.

ⁱ Reynolds number in sidestream of mixing tee at typical operating conditions.

^j Reynolds number in leg of tee downstream of mixing point at typical operating conditions.

^k Reynolds number in reactor at typical operating conditions.

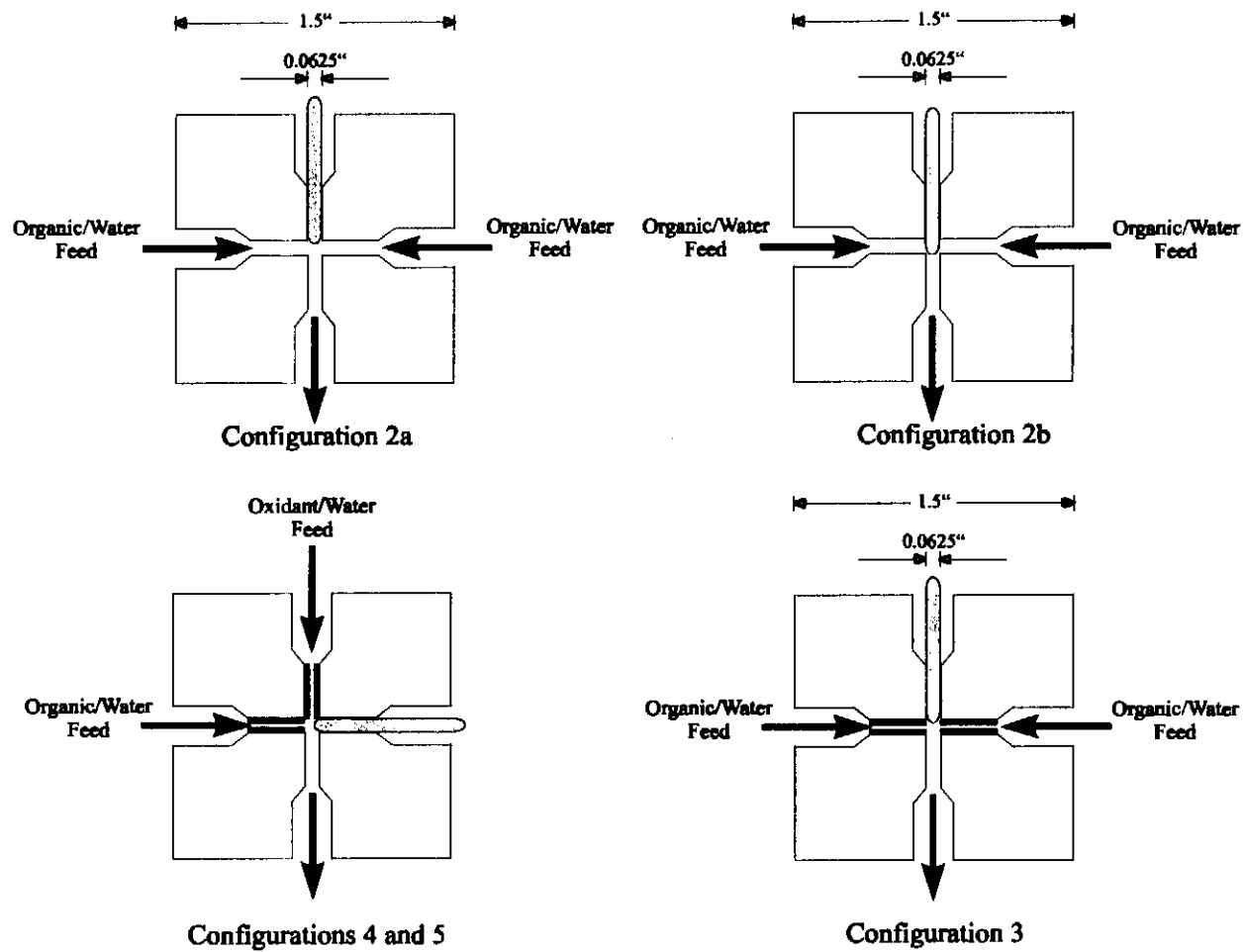


Figure 3.7
Schematics of opposed-flow and side-entry mixing tees described in Table 3.2

design rules given above with more confidence. In this work, however, the diameter of the reactor was either larger or smaller than the diameter of the downstream arm of the tee. As a result, the mixing fluid undergoes either an expansion or contraction as it passes from the tee to the reactor.

Using insert-fitted tees, $N_{Re,j}$ values under typical operating conditions exceed the reported critical value of 6,000 and can reach values as high as 11,000-24,000 in short residence time experiments. $N_{Re,R}$ values are unaffected by the design change and are still below the 10,000 value recommended for fully turbulent mainstream flow. Achieving high $N_{Re,R}$, over a broad range of reactor residence times is difficult in the current experimental system. In principle, high $N_{Re,R}$ could be achieved by decreasing the diameter of the reactor or increasing its length (at constant residence time). The latter option is problematic, however, given the cramped confines of the main sandbath and the need to maintain good fluidization within it. To the extent possible, the option of decreasing the reactor diameter was explored in this thesis, and the 0.041 in. ID tubing used for several of the reactors in Table 3.2 is the smallest, commercially available tubing that can be made with a 1/8 in. outer diameter. This decrease in the reactor inner diameter leads to an increase in the surface-to-volume ratio of the reactor—a potentially important issue for reactions which may be influenced by radical quenching at the reactor wall.

There are a number of small, but potentially important, differences between the idealized mixing tee shown in Figure 3.6 and the ones illustrated in Figure 3.7. As described in the discussion regarding the tee-to-reactor transition, the diameters of the downstream arms of the various mixing tees do not exactly match the diameters of the reactors to which they are connected. In addition, the insert-fitted tees have small, unswept volumes (or dead regions) to the sides of the inserts. In these unswept regions there is the potential for fluid recirculation. Lastly, each tee is fitted with a 1/16 in. thermocouple in the fourth arm of the tee. The tip of the thermocouple protrudes into the flowstream and disrupts the flow field that might otherwise be present.

In an effort to address the presence of unswept regions in the insert-fitted tees, several attempts were made to build a zero-dead-volume (ZDV) tee like the one illustrated in Figure 3.6. The initial effort attempted to use a 1/16 in. microvolume cross (Valco, ZX1C) which had 0.01 in. ID arms. Unfortunately, the 1/16 in. ferruled fittings on the cross were found to leak at high-temperature and pressure. An additional effort to have a cross fabricated out of a block of HC-276 failed due to the difficulty of boring a small diameter hole through alloy using conventional machine tools. An option which was left unexplored, due primarily to lead time and cost, involved fabricating the necessary small diameter holes via laser drilling (National Jet Company, LaVale, MD). The influence the various tee designs have on oxidation kinetics is discussed in Section 4.1.

3.1.4 Downstream processing

Upon exiting the reactor, the reactor effluent rises out of the sandbath through an insulated 26 cm x ¼ in. OD x 0.0625 in. ID HC-276 tube which connects the exit tee of the reactor to the inlet of the shell-and-tube heat exchanger. The connection between the riser and the heat exchanger is made using a ¼ in. HC-276 tee (Swagelok, HC-400-3) containing a 1/32 in. Type K thermocouple (Omega) mounted in the side arm of the tee. The inner tube of the heat exchanger is a 10 ft. long piece of ¼ in. OD x 0.065 in. wall HC-276 tubing. The outer shell is a 8 ft. length of ½ in. OD x 0.035 in. wall copper tubing. The end fittings of the heat exchanger are comprised of a ½ in. 316SS tee (Swagelok, SS-810-3) and a bored-through ¼ in.-½ in. reducer (Swagelok, SS-810-R-4). Cooling water is supplied to the shell-side of the heat exchanger from the Bldg. 66 cold water supply. Prior to entering the exchanger, the cooling water passes through a 10µm spiral-wound prefilter cartridge (VWR, 26303-052) to remove suspended particulates.

A pressure transducer (Dynisco, Model 832, 0-7,500 psig) downstream of the heat exchanger provides an measure of the system pressure at the exit of the reactor. Output from the transducer is displayed digitally and readings are taken approximately every 5-10 minutes during an experiment. At the end of a run, the readings are analyzed to yield a mean and sample standard deviation for use in the data analysis program. During a typical experimental

run at 3,500-4,000 psig, the pressure measured at this point varies by less than 30 psig. After the transducer, the reactor effluent passes through the housing of a high-pressure rupture disk (HIP, burst pressure 4,500 psig, +6%, -3%) which provides emergency pressure relief in the event of system overpressure. Following the rupture disk housing, the reactor effluent flows through a 7 μm in-line filter (Nupro, SS-4TF-7). The filter serves to remove any small particulates in the effluent stream prior to the entering the backpressure regulator (BPR). The BPR is a manually-adjusted, spring-loaded regulator (Tescom, 26-3200, 5,000 psig max) which is used to establish system backpressure when the feed pumps are in operation. On the low-pressure side of the BPR, the reactor effluent is flashed to atmospheric pressure and separates into a vapor and liquid phase. The two phases are separated in a gas-liquid separator comprised of a 1/2 in. OD x 8 in. L 316SS tube packed with 4mm borosilicate glass beads (Kimax). The early version of the gas-liquid separator used in the system shown in Figure 3.1 was constructed from a similar, but longer (12 in.) tube. The longer tube had a correspondingly larger holdup volume and, thus, more time was required to sweep out the separator headspace when changing from one set of run conditions to another. The separator was redesigned at the time shown in Table 3.1 to address the holdup issue.

Inside the gas-liquid separator the vapor phase passes overhead, through a septa-sealed sampling port, and on to a soap-bubble flowmeter. Upon exiting the flowmeter, the vapor is vented to a hood. The liquid phase exits the bottom of the separator and enters a 1/8 in. liquid sampling line. The sampling line allows for sample collection as well as flowrate measurement and is contained within a vented Lexan box to prevent volatile components in the effluent from entering the laboratory environment.

3.2 ANALYTICAL METHODS

3.2.1 Feed analysis

3.2.1.1 Organic feed analysis

During the course of an experimental run, two to three 3 mL feed samples are taken through the sample feed line on the organic feed reservoir. After being drawn, each sample is capped and placed in a refrigerated sample tray maintained at 10 °C to minimize sample volatilization into the headspace of the sample vial prior to analysis. Liquid feed analysis is carried out using a HP 5890 Series II gas chromatograph equipped with a flame ionization detector (FID). Splitless sample injection is performed via an automatic liquid sampler operating in fast injection mode. A 0.2 µL liquid sample is drawn through the septum cap of the sample vial and injected through a Merlin Microseal duckbill septa (HP 5182-3442) at the head of the inlet. The injection occurs over a period of approximately 100 ms into a single-taper, borosilicate glass liner with a total volume of 900 µL (HP 5181-3316). Between each injection, the autosampler syringe is washed out three times with deionized water and four times with the sample itself to minimize sample carry over.

Separation of the analytes in the sample is accomplished using a 30m x 530 µm x 5 µm film thickness DB-1 capillary column (J&W Scientific, 123-1035). The column is preceded by a 2.5 m x 530 µm polar Hydroguard retention gap (Restek, 10081) for solvent focusing. Helium is used as the carrier gas, and nitrogen is used as the makeup gas for the FID detector to maximize sensitivity. All carrier and detector support gases are grade 5.0 (>99.999% purity) and are passed through both activated carbon and molecular sieve traps to remove trace water, oxygen, and organic impurities. Using this method, the minimum detectable level of methanol in water is 1-2 wppm. Details of the method and a representative calibration table can be found in Appendix 8.3.1. Each sample is subjected to triplicate analyses and the mean and sample standard deviation of all feed samples are passed to the data analysis program.

3.2.1.2 Oxidant feed analysis

Dissolved oxygen concentration determination

The dissolved oxygen concentration in the saturator is calculated as described in Section 3.1.1.2. The concentration of oxygen at the *inlet* to the reactor is calculated based on the known organic and oxidant feed flowrates and the density change of the two feed solutions between ambient and experimental conditions. Due to the dilute nature of the oxygen/water and organic/water feeds, the density of both is assumed to be well approximated by that of pure water. Water density is calculated using the equation of state of Kestin, *et al.*(1984). The oxygen saturator temperature and pressure are monitored during the course of an experiment to ensure that significant changes do not occur in the dissolved oxygen concentration. The average and sample standard deviations of these measurements are passed to the data analysis program.

Hydrogen peroxide analysis

Hydrogen peroxide concentration is assayed via ceric ion titration using a Hach digital titrator (PN 16900-01) and Hach hydrogen peroxide reagents (PN 22928-00). In the assay, hydrogen peroxide is titrated with tetravalent cerium ion, a strong oxidant, in the presence of ferroin indicator. When all of the peroxide has been oxidized, the cerium oxidizes the indicator, causing a color change from orange to pale blue. Over the concentration range of the assay (2 to 35 g/L), the concentration of hydrogen peroxide is linearly proportional to the amount of titrant used. The assay procedure begins by adding 30mL of DI water and 2mL of 19.2N sulfuric acid to a clean 50mL erlenmeyer flask. 200 μ L of the hydrogen peroxide solution to be tested is added to the flask using an adjustable-volume digital pipette (Eppendorf Series 2000 Reference pipette, 50-200 μ L, PN 2247025-6). One drop of ferroin indicator solution is then added and the solution is titrated with 0.5N ceric ion solution until the solution changes from its original orange color to a very pale blue. A blank using 200 μ L of DI water is also run and the result is subtracted from the measured peroxide concentration. Samples of the hydrogen peroxide feed are taken at the beginning and end of an experimental run to ensure that no dramatic composition change occurs during the course of an experiment.

Each sample is subject to duplicate analyses and the average and sample standard deviation of these measurements are passed to the data analysis program.

3.2.2 Effluent analysis

3.2.2.1 Vapor effluent analysis

The flowrate of the effluent gas stream exiting the gas/liquid separator is measured using a soap-bubble flowmeter (Supelco, 2-0431) and a stopwatch. During a typical 1-2 hour run, the flowrate is measured 6 to 12 times. The averages and sample standard deviation of these values are used in the analysis program. The gas stream is sampled manually using a 200 μ L gas-tight syringe through a septum port located at the top of the gas/liquid separator. Gas stream composition is determined by injecting three vapor samples (a sample set) into three separate gas chromatographs. Each chromatograph is configured to detect a particular analyte or set of analytes. During a representative experimental run, 4 to 8 vapor-phase sample sets are analyzed. A brief description of the chromatographic configurations and methods used for each class of analytes is given below. A complete description of each method can be found in Appendices 8.1-8.4 .

Analysis of light gases

Analysis of oxygen, nitrogen, carbon monoxide, carbon dioxide, and methane is carried out using a Hewlett Packard 5890 Series II gas chromatograph equipped with a packed inlet and a thermal conductivity detector (TCD). Helium is used as the carrier gas and the method employs two packed columns connected in series through an air actuated switching valve (HP valving Option 404). The first column is a 5 ft. x 1/8 in. 60/80 mesh Carboxen 1000 column (Supelco) and the second is a 8 ft. x 1/8 in. 60/80 mesh Molsieve 5A column (Supelco). The Carboxen column effects the CO/CO₂ separation and the Molsieve 5A column carries out the H₂/O₂/N₂ separation. Upon injection, hydrogen, oxygen, and nitrogen pass through the Carboxen column relatively unretained and are separated on the Molsieve 5A column before entering the detector. Carbon monoxide is separated from CO₂ and methane in the Carboxen column, passes through the Molsieve 5A column, and elutes several minutes

after the N₂ peak. To prevent CO₂ from adsorbing irreversibly on the molecular sieve column, the switching valve is actuated 7.9 minutes into the method. The valve switch reverses the direction of carrier gas flow through the columns, preventing the entry of CO₂ and methane into the molecular sieve column, and causing them to pass back through the Carboxen column. The resulting analyte elution order through the detector is as follows: H₂, O₂, N₂, CO, CO₂, and CH₄. Details of the entire method can be found in Appendix 8.3.2.

The column and detector support gas flowrates for the 5890 were set and periodically checked using a portable mass flowmeter (Alltech). Calibration was done using known volumes of pure gas standards. Periodic injection of air and pure oxygen were used to determine if recalibration of the instrument was necessary. Recalibration was conducted approximately annually and, over the period of four years, resulted in very little change in the calibration curve of any analyte. During a run, effluent samples containing greater than 5-10 µL of nitrogen usually indicated a leak around the gas/liquid separator septum or at the inlet to the GC.

Analysis of hydrogen

Hydrogen analysis is conducted using a Perkin Elmer Sigma 1B gas chromatograph equipped with a thermal conductivity detector. The analysis employed the same columns and method used to analyze for the other light gases, but nitrogen was used as the carrier gas to maximize the thermal conductivity difference between the carrier and hydrogen, the analyte. Calibration was carried out using known volumes of pure hydrogen. A complete description of the method and a representative calibration curve can be found in Appendix 8.3.3.

3.2.2.2 Liquid effluent analysis

The flowrate of the liquid effluent is measured using a small (50-100mL) volumetric flask and a stopwatch. Flowrates significantly different (greater than +/- 0.1 mL/min) from the sum of the calculated feed pump flowrates (see Section 3.1.1.3) indicate a leak somewhere in the system, a leak around the pump piston seal, or the presence of air bubbles trapped in the pumphead. In these instances, the system is shutdown and repaired before acquiring data.

Flowrates are measured 6 to 12 times during an experiment and the resulting mean and sample standard deviation of the measurements are used in the analysis program described below.

Samples of the liquid effluent from the reactor are taken 4 to 6 times during the course of an experiment. Sampling begins approximately ½ hour after switching over to the organic and oxidant feeds and occurs approximately every 15-20 minutes thereafter. Each sample is analyzed in duplicate or triplicate via the same method used for feed analysis. Details of the method are given in Appendix 8.3.1.

3.3 DATA REDUCTION AND ANALYSIS

3.3.1 Temperature measurement and data logging

In addition to the flowrate and composition measurements described above, several other system parameters are monitored regularly during the course of an experiment. The reactor inlet and outlet temperatures, sandbath top and bottom temperatures, oxidant and organic control temperatures, and pre-heat exchanger temperature are logged every 10 seconds via HOTMUX™ software (DCC Corporation) residing on an Hewlett Packard Vectra 386 computer. At the end of a run, the temperature data log is transferred to Excel and the relevant, steady-state portion is subjected to statistical analysis to determine the mean and sample standard deviation of each measurement.

3.3.2 Carbon balance closure

One of the criteria used for accepting or rejecting the data from a given experimental run is the ability to sufficiently close an elemental carbon balance around the reactor system. That is to say, for a given mass flowrate of carbon entering the reactor, the same mass flowrate should be found exiting the reactor in the form of unreacted feed and carbon-containing oxidation products. For methanol experiments, these products include formaldehyde, carbon monoxide, and carbon dioxide. For the purpose of determining the total mass flowrate out of a given gas, each gas species in the vapor effluent is assumed to be in equilibrium with the liquid effluent. As a consequence, the total mass flowrate out of each

species is the sum of the *measured* mass flowrate in the vapor effluent and the *calculated* mass flowrate in the liquid effluent. The calculated mass flowrate is based on the measured liquid effluent flowrate and the calculated dissolved gas concentration. Dissolved concentrations of hydrogen, oxygen, nitrogen, carbon monoxide, and carbon dioxide at the ambient temperature and pressure conditions of the gas/liquid separator are calculated using Henry's law:

$$y_i \hat{\phi}_i(T, P, y_i) P = x_i H_{i, H_2O}(T, P) \quad (3.7)$$

with the vapor-phase species fugacity coefficients set equal to one. Ambient pressure Henry's law constants as a function of temperature were obtained from the literature for oxygen (Benson *et. al*, 1979), carbon monoxide (Rettich *et. al*, 1982), hydrogen, nitrogen, and carbon dioxide (corrected to account for the formation of HCO_3^- and CO_3^{2-}) (Wilhelm *et. al*, 1977). For gases other than carbon dioxide, the contribution of the dissolved gas species to the total molar effluent flowrate is less than 5%. The dissolved carbon dioxide contribution, however, is typically much higher due to its appreciable solubility in water. At the pH of the liquid effluent, typically 3.8 to 4.2, the concentrations of HCO_3^- and CO_3^{2-} contribute negligibly to the dissolved carbon content in the liquid. Thus, the strict vapor-liquid equilibrium relation between $\text{CO}_2(\text{g})$ and $\text{CO}_2(\text{l})$ implied by Equation (3.7) provides a good estimate of the carbon content of the liquid due to the presence of dissolved CO_2 .

3.3.3 Reported experimental uncertainties

All experimentally-measured quantities and associated confidence intervals reported in this thesis are calculated via:

$$\bar{x} \pm \frac{s \cdot t_{.025}((n_{obs} - 1) \text{ degrees of freedom})}{\sqrt{n_{obs}}} \quad (3.8)$$

where \bar{x} is the sample mean, s is the sample standard deviation, n_{obs} is the number of observations, and $t_{.025}((n_{obs} - 1) \text{ degrees of freedom})$ is the t -value providing an area of 0.025 in the upper and lower tails of a Student's t -distribution with $(n_{obs}-1)$ degrees of freedom.

Rigorously, the use of Equation (3.8) rests on the assumption that the observations are randomly drawn from a normally-distributed population. However, statistical research has shown that the *t*-statistic is applicable to non-normal populations provided the deviation from normality is not excessive (Mendenhall *et. al*, 1990). In either instance, the assumption of normal or near-normal population distributions seems appropriate for the type of measurements employed in this work. Examples of quantities calculated using Equation (3.8) include the reactor temperature and pressure, the vapor and liquid effluent flowrates, and the feed and effluent species concentrations.

Uncertainty in the derived quantities (*e.g.*, conversion, yield, etc.) reported in this thesis are calculated using standard propagation-of-error techniques (Taylor, 1982). In their standard form these techniques are based on the assumptions that the variables are independent and that their associated errors are small .

Table 3.3 summarizes a number of relevant system measurements and their associated uncertainty and observed experimental variability. For the experiments reported in Chapter 4, the temperatures at the top and bottom of the sandbath differed by less than 3 °C—indicating good fluidization within the bath. Over the course of a single experiment, the two quantities vary by less than 3°C from the sandbath setpoint. Since Type K thermocouples are only accurate within ± 3 to 4 °C over the temperature range of 500-600 °C, this variability is well within the reported measurement capabilities of the device. The reported reaction temperature is calculated as the average of the measured reactor inlet and outlet temperatures. For the experiments reported in this thesis, these two temperatures differed by less than 3 °C.

3.3.4 Data analysis program

Data analysis was carried out by a FORTRAN™ analysis program and later entirely within an Excel spreadsheet. In the latter case, FORTRAN™ subroutines for the thermodynamic properties of water (Kestin and Sengers, 1986), Henry's law constants, etc. were compiled as Dynamic Link Libraries (DLLs) and called directly as functions from within Microsoft Excel™. The resulting data workbook contained all relevant run information,

TABLE 3.3
Summary of Measurement Uncertainty and Observed Experimental Variability

Measurement	Accuracy	Maximum variability
Type K thermocouple	$\pm 3-4$ °C ^a	$\pm 1-2$ °C
Pressure transducer	± 7.5 psig ^b	± 15 psig ^d
Feed pump flowrate	± 0.05 mL/min ^c	± 0.1 mL/min

^a based on the reported accuracy of a Type K thermocouple over the temperature range of 500-600 °C (Omega Engineering, Inc.)

^b represents $\pm 0.1\%$ of the full scale range of a Dynisco Model 832 transducer (includes linearity, hysteresis, and repeatability).

^c value based on typical liquid flowrate of 5 mL/min at STP and reported accuracy of 1.0% of setpoint (Rainin Instrument, Co.).

^d value shown is representative of experiments using the Rainin feed pumps and the Tescom backpressure regulator. Experiments using the LDC Analytical/Milton Roy feed pumps exhibited pressure swings of ± 60 psig.

including worksheets containing experimental run sheets, analytical data, temperature measurements, and all calculated quantities.

3.4 SYSTEM SAFETY

3.4.1 Feed delivery of gaseous oxidants and organics

Extensive leak checking was performed on the high-pressure gas delivery system to ensure that it was free from organic and oxygen gas leaks. Periodic checks of the fittings and valves are conducted using soap solution (oxygen system) and a portable thermal conductivity detector (organic system).

Both the oxygen and organic saturator gas feed lines are fitted with excess-flow check valves (Autoclave Engineers, SWKO440) to prevent letdown of a gas cylinder in the event of a pressure loss in the saturator system during equilibration or system operation. The check valve consists of a non-spring-loaded poppet enclosed in a 316SS housing which is mounted vertically in the gas line. In the event of a pressure loss downstream, the increased gas velocity

in the housing raises the poppet and seats it against a Viton o-ring, thereby shutting off the gas flow to the system. The poppet is reset when the pressure across the check valve is equalized.

3.4.2 System overpressure

Two safety systems are employed to prevent system overpressure. The first is the electronic interlock on each of the Rainin SD-200 feed pumps. Each pump has a pressure transducer built into its pulse-dampening module (on the discharge side of the pumphead) and a keypad-entered maximum pressure limit (typically set at 4,400 psig). When the system pressure exceeds the preset limit, the pump drive mechanism automatically shuts off and an audible alarm is initiated to alert the operator. The success of this interlock system is dependent on the proper functioning and zeroing of the pressure transducers.

The second system used to prevent system overpressure is a single 316SS, angled-seat rupture disk (Oseco, ¼ in. effective area, burst pressure 4,500 psig at 25°C (+6%, -3%)) located upstream of the backpressure regulator. In the event of a buildup in system pressure in excess of the rated burst pressure, the disk provides rapid and complete depressurization of the entire reactor system. The blow-out side of the safety head containing the rupture disk is directed away from any area of operator activity and the entire reactor system is enclosed behind a ½ in. thick Lexan shield.

3.4.3 Saturator overpressure

Both the organic and oxygen saturators are fitted with a single, angled-seat rupture disk (Oseco, ¼ in. effective area, burst pressure 1,988 psig at 25°C (+6%, -3%)) to prevent overpressurization. Operation and placement are similar to the disk used on the main flow path.

3.4.4 Direct ohmic heating system

The direct ohmic heating system described in Section 3.1.2.3 is completely enclosed in within 2 to 4 in. of insulation. As a result, there are no exposed sections of electrically live tubing. A grounding wire is located downstream of the negative lead to direct current to

ground in the event the lead connection is compromised. During initial operation, a series of safety checks were carried out using a multimeter to ensure that the support structure and system components were electrically isolated from the DOH system.

3.4.5 Nuisance dust and vapor handling systems

The Techne sandbath is equipped with a cyclone-based, fines reclamation system and a particulate filter on the air exhaust from the cyclone. Despite these safeguards, the bath generates a fair amount of respirable ($<20\ \mu\text{m}$) dust. In an effort to minimize the amount of dust introduced into the laboratory environment, the main sandbath is enclosed within a Lexan hood which is vented to the building hood exhaust. Access to the front of the sandbath is provided by two Lexan doors which can be secured in place while the bath is in operation.

Efforts are also made to minimize operator exposure to the vapors from the reactor vapor and liquid effluents. The vapor effluent exiting the soap bubble flowmeter is directed to a nearby hood. Similarly, the liquid sampling line is enclosed within a small Lexan box which is vented to the building hood exhaust.

Chapter 4:

Experimental studies of methanol oxidation

“You can observe a lot just by watching.”

Yogi Berra

One-hundred and sixty-one methanol oxidation and hydrolysis experiments were conducted in the three tubular reactor systems described in Chapter 3. The experiments were performed at pressures of 246 to 269 bar over a temperature range of 420 to 550°C. Space times within the reactor ranged from 1.4 to 11.5 seconds. The concentration of methanol at the inlet to the reactor varied from 0.011 wt% to 0.39 wt%. The oxidant-to-organic molar feed ratios explored in the experiments encompassed both fuel-rich and fuel-lean conditions and varied from 1:3 to 3:1. Based on the global stoichiometry of the complete methanol oxidation reaction, the corresponding fuel-equivalence ratios varied from 0.5 to 4.5. Over the stated temperatures, pressure, and feed concentration ranges, the observed methanol conversion varied between 0.5 and 99.7%. Carbon mass-balance closures for the experiments ranged from 81 to 110% with an average value of 91%—indicating a relatively good ability to detect and quantify the complete and partial oxidation products of methanol.

Four separate series of experiments which were designed and implemented to address the experimental objectives outlined in Chapter 2. The first, presented in Section 4.1, examines the influence of mixing tee design on the rate and extent of methanol oxidation. The second focuses on the use of hydrogen peroxide as an alternative means of introducing oxygen into bench-scale SCWO reactors and is described in Section 4.2. The third series of experiments investigates the influence of fuel equivalence ratio on the rate of methanol oxidation and on the resulting distribution of complete and partial oxidation products. The results of these experiments are given in Section 4.3. Section 4.4 presents the results of a

collaborative effort between MIT and Sandia National Laboratory to compare methanol oxidation rate data taken in the reactor systems of the two groups. Lastly, preliminary data are presented in Section 4.5 which suggest that the reactor surface may play an important role in influencing the overall rate of methanol oxidation. Further discussion of this last topic can be found in Chapter 7 which details recommendations for future work.

4.1 MIXING STUDIES

In previous studies involving hydrogen, carbon monoxide, acetic acid, and methylene chloride, researchers at MIT observed pronounced induction periods prior to the onset of oxidation (Holgate, 1993; Meyer, 1993). The induction periods, or lag times, were approximately 1 to 3 seconds in length, were relatively compound-independent, and were estimated by extrapolating the normalized reactant concentration profiles back to the starting feed concentrations. In most instances, the induction periods were found to exhibit a slight temperature dependence with the lengths of the periods decreasing with increasing temperature. In an effort to better understand the observed time lags, the experimental induction times were compared to those predicted by high-pressure, combustion models (see Chapter 5). The models were found to exhibit induction behavior, but quantitative agreement between the model predictions and the data could not be achieved without significant adjustment of the model parameters. Based on their temperature dependency and the general agreement with the model predictions, the observed lag times were interpreted as being purely kinetic phenomena. Induction periods are characteristic of kinetic mechanisms which require the buildup of key intermediate species prior to reaching steady-state rates of reaction. They are frequently seen in oxidation and combustion systems and are attributable to the time required to buildup a steady-state free-radical pool (Moore and Pearson, 1981).

Much shorter induction times were observed by Rice, *et al.*(1996) in oxidation experiments at Sandia National Laboratory involving methanol. Using *in-situ* Raman spectroscopy to follow the progress of the reaction, they observed induction periods of 0.13 to 0.69 seconds over a temperature range of 440 to 500°C. As in the studies at MIT, the induction times were found to decrease with increasing temperature. A brief description of the

experimental system of Rice, *et al* can be found in Section 4.4. A more detailed description is given in the paper itself (Rice *et. al*, 1996) and in a report by Hanush, *et al.*(1996).

Early experimental work in this thesis at the upper end of the temperature range used the Sandia study yielded the methanol oxidation data shown in the upper graph of Figure 4.1. The data were taken using an 8.2m x 0.041 in. ID 316SS reactor (reactor 6 in Appendix 8.4) fitted with the opposed-flow mixing tee denoted as configuration 2a in Figure 3.7. For convenience, Figure 3.7 is reproduced in this Chapter as Figure 4.2. The data in Figure 4.1 were obtained at an operating temperature and pressure of 500°C and 246 bar using an initial methanol feed concentration of 0.069 wt% and a fuel-equivalence ratio of 1.5 (1:1 oxygen-to-methanol molar feed ratio). These conditions are comparable to those used in the study of Rice, *et al.*, yet the data in the figure clearly show a much longer induction period. Extrapolation of the conversion vs. time curve back to the x-axis reveals an apparent induction time of approximately 3 seconds. This value is approximately 23 times longer than the lag time seen in the *in-situ* Sandia data at the same temperature.

As a result of a seized fitting, the mixing tee used in the early MIT work (configuration 2a) was replaced with what was thought to be an identical one (configuration 2b). Replication of the early experiments in the same reactor using the latter tee, however, generated the data shown in the lower graph of Figure 4.1. Extrapolation of the newer data back to the x-axis yields an apparent induction time which is significantly shorter than the one seen previously. Also shown in the lower graph of Figure 4.1 are data taken using the newer tee and a shorter 2.5m x 0.041 in. ID 316SS reactor (reactor 9 of Appendix 8.4). The difference between the apparent induction periods is made clearer in Figure 4.3 which displays plots of $\ln(1-X)$ versus time for all three data sets. Assuming the data are well represented by a rate form which is first order in methanol, plots of $\ln(1-X)$ versus time should be linear and intercept the x-axis at zero. As shown, the plots are linear but do not pass through zero. Instead, they intersect the axis at positive values ranging from 0.7 to 3.2 seconds. In addition, the induction period for

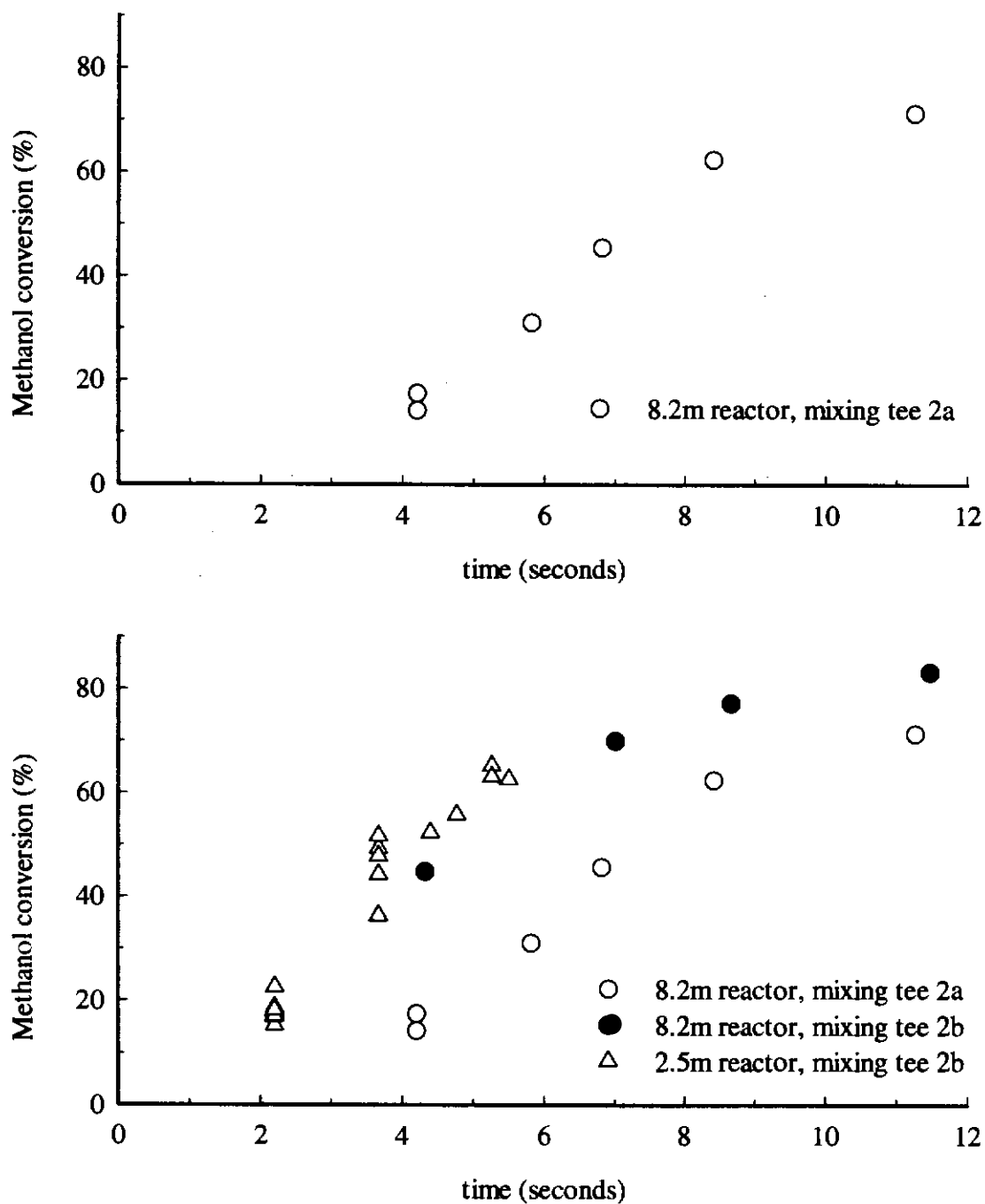


Figure 4.1
Methanol conversion as a function of time using mixing tees 2a and 2b of Figure 4.2.
Reactor conditions: $T=500^{\circ}\text{C}$, $P=246$ bar, $[\text{MeOH}]_0=0.069$ wt%, $\phi=1.5$.

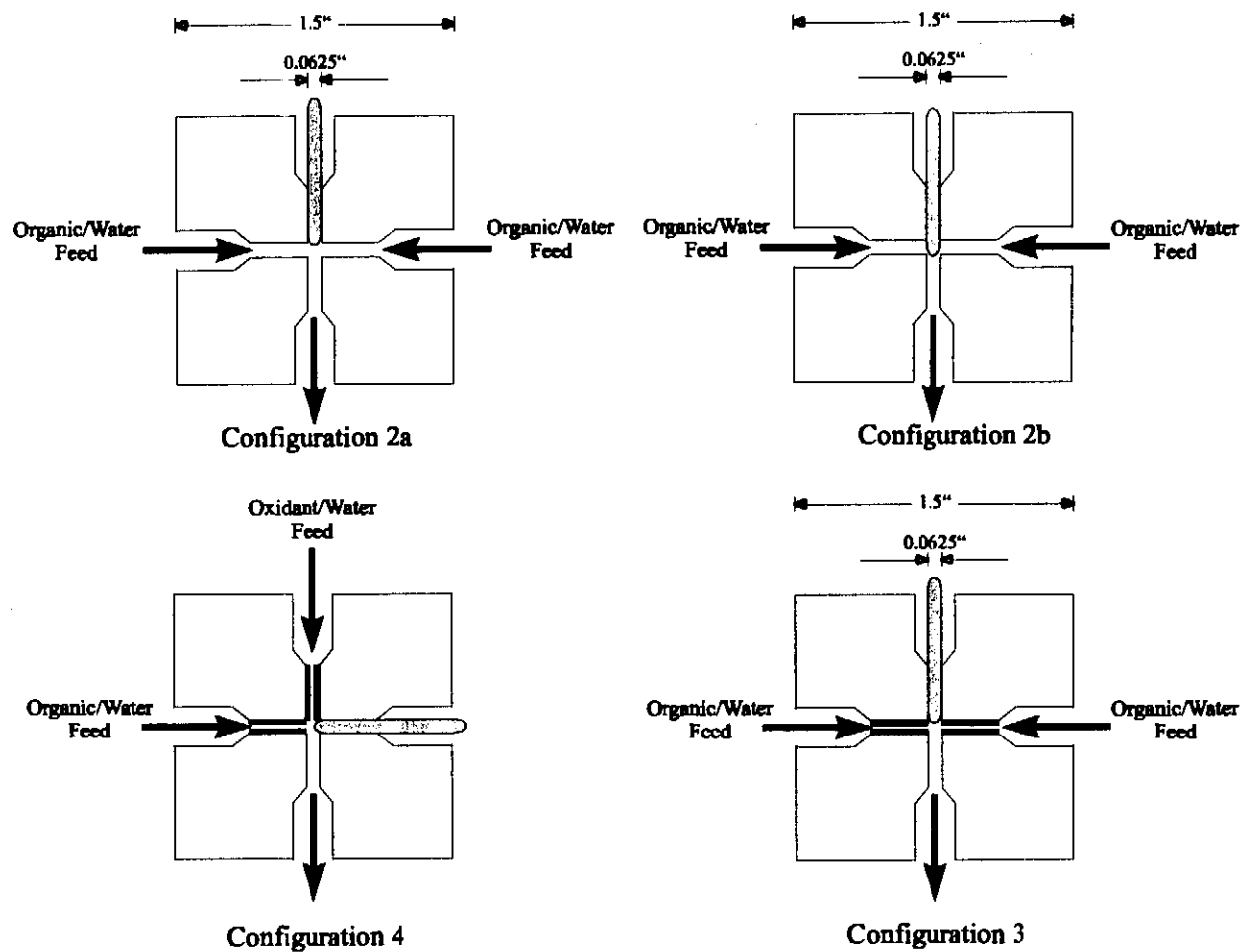


Figure 4.2
Schematics of opposed-flow and side-entry mixing tees described in Table 3.2

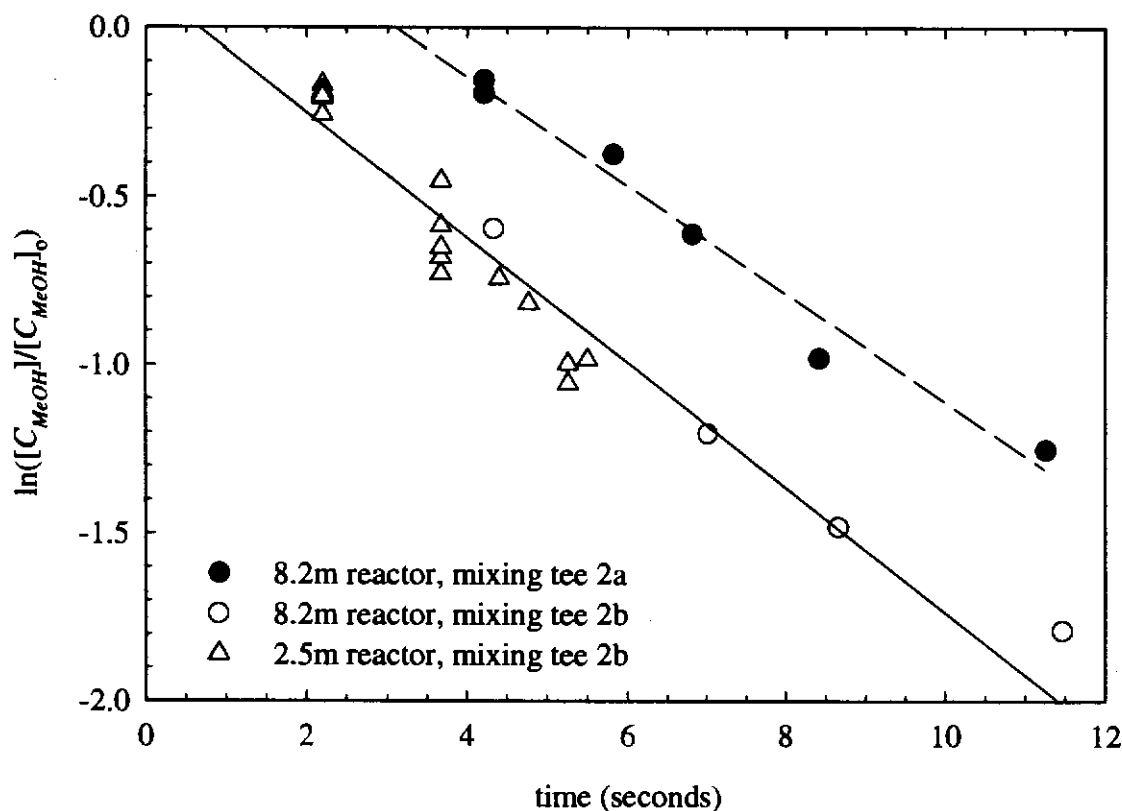


Figure 4.3

Assumed first-order plots of $\ln(1-X)$ vs. time for the methanol data taken using tees 2a and 2b of Figure 4.2. Conditions: $T=500^\circ\text{C}$, $P=246$ bar, $[\text{MeOH}]_0=0.069$ wt%, $\phi=1.5$.

tee 2b is approximately 2.5 seconds shorter than that of 2a. Disassembly and inspection of the mixing tees revealed that the only substantive difference between the two was the position of the 1/16 in. thermocouple in the side-arm of the tees. In tee 2b, the thermocouple was found to have traversed the entire diameter of the tee during tightening of the high-pressure fitting which surrounds the thermocouple sheath. As a result, the tip of the thermocouple was firmly embedded in the opening at the opposite side of the tee which led to the reactor. In tee 2a, the thermocouple tip was found to be approximately centered in the flow path of the tee. Schematics of both tees are provided in Figure 4.2. At the time the discovery was made, it was proposed that the restricted annular flow path around the thermocouple in tee 2b resulted in higher inlet velocities, and hence better mixing, of the oxidant and organic streams. This

hypothesis led to the investigation of mixing in pipeline tee mixers in the literature and the subsequent redesign of the mixing tee. A discussion of the literature findings and the details of the tee redesign are presented in Section 3.1.3.1.

Two new mixing tees were constructed as a result of the data shown in Figures 4.1 and 4.3. Based on the discussion in Chapter 3, both utilized 1/16 in. OD x 0.01 in. ID inserts to increase the jet-to-main-stream velocity ratios and jet Reynolds numbers for a given tee/reactor combination (see Table 3.2). Tees were constructed in both opposed-flow and side-entry configurations and are depicted in Figure 4.2 as configurations 3 and 4, respectively. In both tees, the thermocouple was positioned such that the tip was centered in the flow path. The tip positions were confirmed by disassembly of the tees and visual inspection of the thermocouple through the side arms. The two tees were used in conjunction with the 2.5m 316SS reactor described previously to generate the data shown in Figure 4.4. The experiments were conducted at 500°C and 246 bar with a methanol feed concentration at the inlet of the reactor of 0.069 wt%. The oxygen-to-methanol molar feed ratio was slightly fuel-rich at a value of 1:1 ($\phi=1.5$). As shown, the two tees yield similar conversion versus time profiles.

Using the redesigned tees, the apparent induction times begin to approach, but do not match, the 0.13 second value seen in the 500°C Sandia experiment. As is apparent in Figures 4.3 and 4.4, the resulting reduced induction periods are approximately 0.5 to 1 seconds and still represent a sizable fraction of the experimentally accessible space time in the reactor. Using the outermost 5.3 second data point in Figure 4.4 as a benchmark, a 1 second induction time represents 19% of the total reactor length. This induction length corresponds to approximately 450 tube diameters in a reactor with an L/D ratio of 2,400. Mixing lengths of this magnitude are outside the range of those observed in the mixing studies discussed in Chapter 3 which never exceeded 120 tube diameters. However, as discussed in Section 3.1.3.1, there are several important differences between the tees employed in the mixing literature and the tees which were feasible for use in this study. The presence of unswept dead

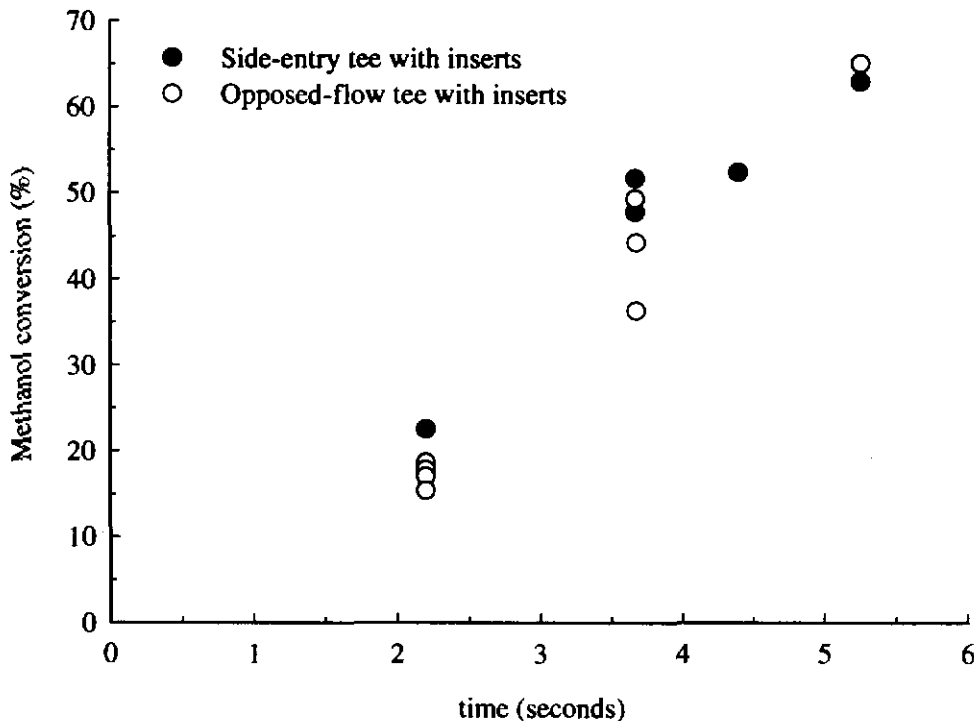


Figure 4.4

Comparison of the opposed-flow (configuration 3) and side-entry (configuration 4) mixing tees depicted in Figure 4.2. Both tees used 0.01 in. ID inserts. Conditions: $T=500^{\circ}\text{C}$, $P=246$ bar, $[\text{MeOH}]_0=0.069$ wt%, $\phi=1.5$.

volumes to the sides of the inserts, the protrusion of the thermocouple into the flow field, and the expansion and contractions in the flow path leading to the reactor all have the potential to influence the mixing process in ways which are difficult to predict. Furthermore, due to the constraints of the current reactor system, the reactor Reynolds numbers for the experiments depicted above range from 3,200 to 7,500—values below the fully-turbulent 10,000 minimum found to be required by the two studies cited in Chapter 3 for optimal mixing (Tosun, 1987; Cozewith and Busko, 1989). The remaining relevant mixing parameters (v_j/V_R , d_j/D_R , and $N_{Re,j}$) were within the range of values explored in these studies and are shown in Table 3.2. An additional influencing factor, that of the reactor surface, may also play a role in influencing the apparent induction times. This possibility is discussed in Section 4.5.

Based on the discussion in the preceding paragraph, it is not clear whether the 0.5 to 1 second induction periods seen using the new mixing tees could be further improved through changes to the tee geometry or increases in the reactor Reynolds number. Nor is it entirely clear to what extent the true kinetic induction period may contribute to the overall observed time lag. What is clear, however, is that a phenomenon originally thought to be purely kinetic in nature, was shown to be influenced by the geometry of the mixing tee and flow conditions within it. The influence of the rate and extent of mixing on oxidation rate should not be completely surprising, however, given the relatively short timescale over which the oxidation reaction occurs.

4.2 OXIDANT COMPARISON STUDIES

In an effort to overcome the limitations of the oxygen saturator system described in Chapter 3, alternative methods of introducing oxygen into the MIT reactor system were investigated as part of this thesis. At the time the investigation was undertaken, four methods were actively being used to deliver oxygen to bench- and pilot-scale SCWO reactors: high-pressure, oxygen booster pumps; liquid oxygen (LOX) injection; saturator-based delivery systems; and aqueous solutions of hydrogen peroxide. The first two methods deliver oxygen to the reactor inlet as a pure, high-pressure gas while the latter two result in a dilute feed mixture of oxygen in water. As discussed in Section 3.1.1.2, the fourth approach relies on the rapid, decomposition of hydrogen peroxide during feed preheating to form stoichiometric amounts of oxygen and water. The method was first used by the research group at Sandia National Laboratory in order to attain high feed concentrations of molecular oxygen in their tubular reactor system. It has since been adopted by other research groups (Brock *et. al*, 1996), including our own. Since the oxygen is generated under pressure and *in-situ* by the decomposition reaction, without the need for a high-pressure storage vessel, the method circumvents many of the design problems associated with the handling of pure oxygen, including adiabatic compression, particulate impact, materials selection, and system cleanliness. Thus, it serves as a convenient means of achieving industrially-relevant oxygen feed concentrations at the laboratory scale without the expense and design effort of a pure

oxygen delivery system. Its use, however, is based on the assumption that the hydrogen peroxide decomposition reaction goes to completion before the oxidant feed solution enters the reactor. Since this assumption was not tested experimentally at Sandia, one of the early objectives of this work was to validate the peroxide delivery system by comparing its performance to the oxygen saturator system used previously at MIT.

The use of hydrogen peroxide as a *primary* oxidant and rate enhancer has been discussed previously in the SCWO and wet oxidation literature. Lee and Gloyna (1990) compared the oxidation rate of 2,4-dichlorophenol and acetic acid using oxygen and hydrogen peroxide in a series of premixed, batch experiments at 400 to 500°C. At comparable operating conditions, they found that the conversion of both compounds was higher using peroxide. This finding is not surprising given the premixed nature of the experiments and the oxidizing power of hydrogen peroxide. A more recent study of the effect of hydrogen peroxide on SCWO oxidation rates was carried out by Bourhis, *et al.* (1995). Using a tubular flow reactor, the authors conducted experiments in which a cold water feedstream was spiked with hydrogen peroxide and mixed with a pure organic waste stream. The resulting peroxide/organic mixture was then brought into direct contact with a combined supercritical water/air stream and fed to the inlet of a 6.2m x 0.925cm ID tubular reactor. The peroxide feed concentration in the cold water feed was varied from 0.75 to 3 wt% and never exceeded 5% of the stoichiometric oxygen requirement. The organic concentration at the inlet of the reactor was approximately 12 wt%. No direct measurements of the organic concentration in the reactor effluent were made. Instead, the extent of reaction was inferred by measuring the axial temperature rise along the outer surface of the reactor due to the reaction exotherm and by monitoring the CO levels in the effluent gas. The addition of small amounts of hydrogen peroxide to the cold water feed were found to significantly raise the temperature profile down the length of the reactor, and, hence, the rate of oxidation. Since the organic and peroxide were premixed before being brought to reaction temperature, as they were in the batch experiments described above, the results have little bearing on the validation of the peroxide delivery system. The key validation issue is whether the kinetics of hydrogen peroxide

decomposition are rapid enough to ensure its complete breakdown to oxygen and water prior to entering the reactor. This issue is examined in greater detail in the following three sections. The first two sections attempt to quantify the rate and extent of peroxide breakdown in the preheating system while the third provides a direct, experimental comparison of methanol oxidation kinetics using both oxygen and hydrogen peroxide.

4.2.1 Kinetics of hydrogen peroxide decomposition

As discussed in Section 3.1.1.2, the kinetics of hydrogen peroxide decomposition in water have been examined in some detail in the boiling water reactor (BWR) literature (Takagi and Ishigure, 1985; Lin *et al.*, 1991; Lin, 1993). Unfortunately, the highest temperature used in these studies was 280°C. A more recent study within the SCWO community by Croiset, *et al.* (1997) at Sandia National Laboratory extended the temperature range to 420°C. As in the BWR work, decomposition was found to be first order in peroxide concentration and strongly surface-catalyzed. Experiments conducted at varying temperatures and surface-to-volume (S/V) ratios allowed the resulting rate data to be correlated in the form:

$$k_{overall} (s^{-1}) = k_h (s^{-1}) + k_w (cm / s^{-1}) * \left(\frac{S}{V} \right) (cm^{-1}) \quad (4.1)$$

where $k_{overall}$ is the overall, first-order rate constant for peroxide decomposition, k_h is the rate constant for homogeneous decomposition, k_w is the wall-catalyzed decomposition rate constant for an Inconel 625 surface, and S/V is the surface-to-volume ratio in units of cm^{-1} . Equation (4.1) was developed over a S/V ratio range of 8 to 55 cm^{-1} by inserting straight lengths of thin-walled 1/16 in. OD tubing into the 3/16 in. ID tubular reactor used at Sandia (see Section 4.4). Arrhenius expressions for the homogeneous and heterogeneous first-order, rate constants were developed over a temperature range of 300 to 420°C at pressures of 245 and 340 bar to yield:

$$k_h = 10^{13.7 \pm 1.2} \exp[-180 \pm 16(kJ / mol) / RT] \quad \text{for } T > 380^\circ C \quad (4.2)$$

$$k_w = 10^{3.3 \pm 0.3} \exp[-62.5 \pm 4.4(kJ / mol) / RT] \quad \text{for } T \geq T_c \quad (4.3)$$

In combination with information on the preheater residence time and geometry, Equations (4.1) to (4.3) can be used to estimate the conversion of hydrogen peroxide in the oxidant-side feedline of the MIT preheating system. As described previously, the preheating system is actually comprised of two preheating sections in series. The first section is based on one of the three preheating methods described in Section 3.1 and illustrated in Figures 3.1 to 3.3. It is used to raise the oxidant and organic feedstreams from ambient to process temperature. The second section consists of a 17 ft. coiled length of 1/16 in. OD x 0.0425 in. ID HC-276 tubing immersed in the main sandbath. Its function is to make up for any heat loss in the transfer line between the first preheating section and the main sandbath. Due to the addition of heat tracing and insulation on the transfer line, the immersed section of tubing is maintained at essentially at isothermal conditions. In an effort to arrive at a simple, conservative estimate of the peroxide conversion that can be achieved during preheating, only this latter section will be considered in the analysis which follows. Using the S/V ratio of the 0.0425 in. ID preheating tubing (37 cm^{-1}) and assuming the expressions above are equally valid for HC-276, Equations (4.1) to (4.3) were used to estimate the overall rate constants for peroxide decomposition at 400 and 500 °C. These values are representative of typical bench-scale operating temperatures for methanol oxidation. The residence time of the aqueous peroxide solution in the immersed section of the oxygen-side preheating line was calculated using the known volume of the line, the density change between ambient and operating temperatures, and a oxygen-side ambient flowrate of 7 mL/min. This flowrate is the maximum flowrate used during the methanol oxidation experiments conducted in this thesis. As such, it represents the minimum preheater residence time encountered experimentally.

The results of the hydrogen peroxide conversion calculations are presented below in Table 4.1. The results indicate the decomposition reaction will be 99.995% complete at 400°C and 100% complete (see table footnote) at 500°C. It is important to remember that these calculated values are conservative estimates based on residence times corresponding to only one-third of the actual heated length of the preheater tubing. The actual peroxide conversions will be substantially higher due to the decomposition occurring in the first section of the

preheater. Accordingly, the conversion values demonstrate that hydrogen peroxide can be expected to completely decompose within the oxidant-side feedline to yield a mixture of molecular oxygen in water. Additional experimental evidence for this hypothesis is provided in the following two sections.

TABLE 4.1
Estimate of hydrogen peroxide conversion in immersed section of oxidant preheating line based on kinetic data of Croiset, *et al.* (1997)
($P=246$ bar, oxidant-side ambient flowrate = 7 mL/min)

T (°C)	k_h (sec ⁻¹)	k_w (cm/sec)	$k_{overall}$ (sec ⁻¹)	τ (sec) ^a	Conversion (%)
400	0.536	0.028	1.57	6.3	99.995
500	34.4	0.119	38.8	3.1	100.000 ^b

^a Estimated residence time in immersed section of preheating tubing (assumed isothermal).

^b Actual value is $100 \cdot (1 - 5.79e-53)$.

4.2.2 Oxygen evolution control experiments

In Section 3.1.1.2, a series of control experiments were described in which oxygen-saturated water solutions from the saturator were pumped through the reactor system and allowed to flash into the gas/liquid saturator. Analysis of the resulting effluent vapor allowed an oxygen mass balance to be constructed around the reactor to verify the concentration of dissolved oxygen in the saturator at equilibrium. In preparation for the comparison of oxygen and hydrogen peroxide kinetics, a similar set of experiments were conducted to determine the extent of peroxide breakdown in the reactor preheating system.

Experiments were carried out by passing a prepared aqueous hydrogen peroxide solution through the reactor system at 500°C and 3,550 psig (246 bar) and by measuring the amount of evolved oxygen in the reactor effluent. Preparation and analysis of the feed solution were performed using the methods described in Section 3.2.1.2. During the experiments, the vapor and liquid effluent flowrates were measured periodically (see Section 3.2.2) and the oxygen concentration in the vapor effluent was determined by gas chromatography (see

Section 3.2.2.1). Based on effluent measurements and the global stoichiometry of the decomposition reaction,



the hydrogen peroxide concentration in the aqueous feed solution was back-calculated and compared to the value obtained by ceric ion titration of the feed (see Section 3.2.1.2). Flowrates through the reactor system were chosen to bound the range of oxidant-side flowrates used in typical reactor operation. At the time the experiments were conducted, the Firerod preheating system of Figure 3.2 was in place. Both runs used a 2.5m x 0.041 in. Inconel 625 reactor fitted with a side-entry tee with 0.01 in. inserts. The results of the experiments are presented in Table 4.2.

TABLE 4.2
Results of oxygen evolution experiments using hydrogen peroxide feed solutions
(500 ± 1°C, 246 ± 0.4 bar)

Run	Liquid effluent flowrate (ml/min)	Vapor effluent flowrate (ml/min)	Oxygen concn in vapor effluent (vol%)	Back-calculated H ₂ O ₂ concn in feed (wppm) ^a	Measured H ₂ O ₂ concn in feed (wppm) ^b
1	3.15 ± 0.01	3.7 ± 0.04	100	3175 ± 48	3450 ± 225
2	8.22 ± 0.02	9.86 ± 0.12	100	3241 ± 57	3450 ± 225

^a Based on measured flowrate and composition of effluent and stoichiometry of reaction (4.4)

^b Based on ceric ion titration method described in Section 3.2.1.2

Comparison of the measured and back-calculated H₂O₂ values show that they are in close, but not total, agreement. While the values at 500 °C are within the estimated uncertainties of the two measurements, the values at 400 °C lie just outside the estimated uncertainty bounds. However, the amounts of evolved oxygen in the reactor effluent are consistent with the concentration of hydrogen peroxide fed to the reactor. Since very little peroxide would have to survive the preheating process to have an influence on the rate of oxidation, the results of the

oxygen evolution experiments do not provide conclusive evidence of complete breakdown. As a result, a series of experiments were undertaken to directly compare oxygen and hydrogen peroxide kinetics using methanol as the candidate waste compound.

4.2.3 Direct comparison of oxidation kinetics using oxygen and hydrogen peroxide

The oxidant comparison experiments were conducted in a 2.5m x 0.041 in. ID Inconel 625 reactor (system 10 of Appendix 8.4) using both the Firerod and DOH preheating systems. The reactor was fitted with a side-entry mixing tee with 0.01 in. inserts (configuration 4 of Table 3.2). A total of 36 experiments were conducted, 21 of them using hydrogen peroxide, over a residence time range of 1.4 to 4.0 seconds. The operating temperature and pressure for the runs were 500°C and 3,550 psig (246 bar). In an effort to maximize the ability to discriminate between the two oxidants, experiments were conducted at fuel-rich conditions ($\phi=1.5$) where the oxidation rate is dependent on the oxygen feed concentration (see Section 4.3). The feed concentration of methanol at the inlet of the reactor was maintained at 1.9 mM (0.069 wt%) throughout all experiments. For runs employing dissolved oxygen, the oxygen saturator pressure was set at 600 psig (42 bar). For runs using hydrogen peroxide, the peroxide feed concentration was chosen to give a stoichiometrically-equivalent amount of dissolved oxygen (assuming complete decomposition).

Figure 4.5 shows the experimentally observed methanol conversion as a function of time using both dissolved oxygen and hydrogen peroxide. Also shown are the carbon balances (based on CO, CO₂, and methanol) for each of the runs displayed in the upper graph. Formaldehyde was not quantified in the effluent in these experiments. The data convincingly demonstrate that the rate of oxidation is equal for the two oxidants. Consequently, they also are in agreement with the calculations based on the kinetic work from Sandia (Table 4.2) which suggest that the breakdown of hydrogen peroxide should be complete at the conditions used for the comparison study.

Figures 4.6 and 4.7 show the complete and partial oxidation products (excluding formaldehyde) resulting from the oxygen and peroxide experiments shown in Figure 4.5. Both

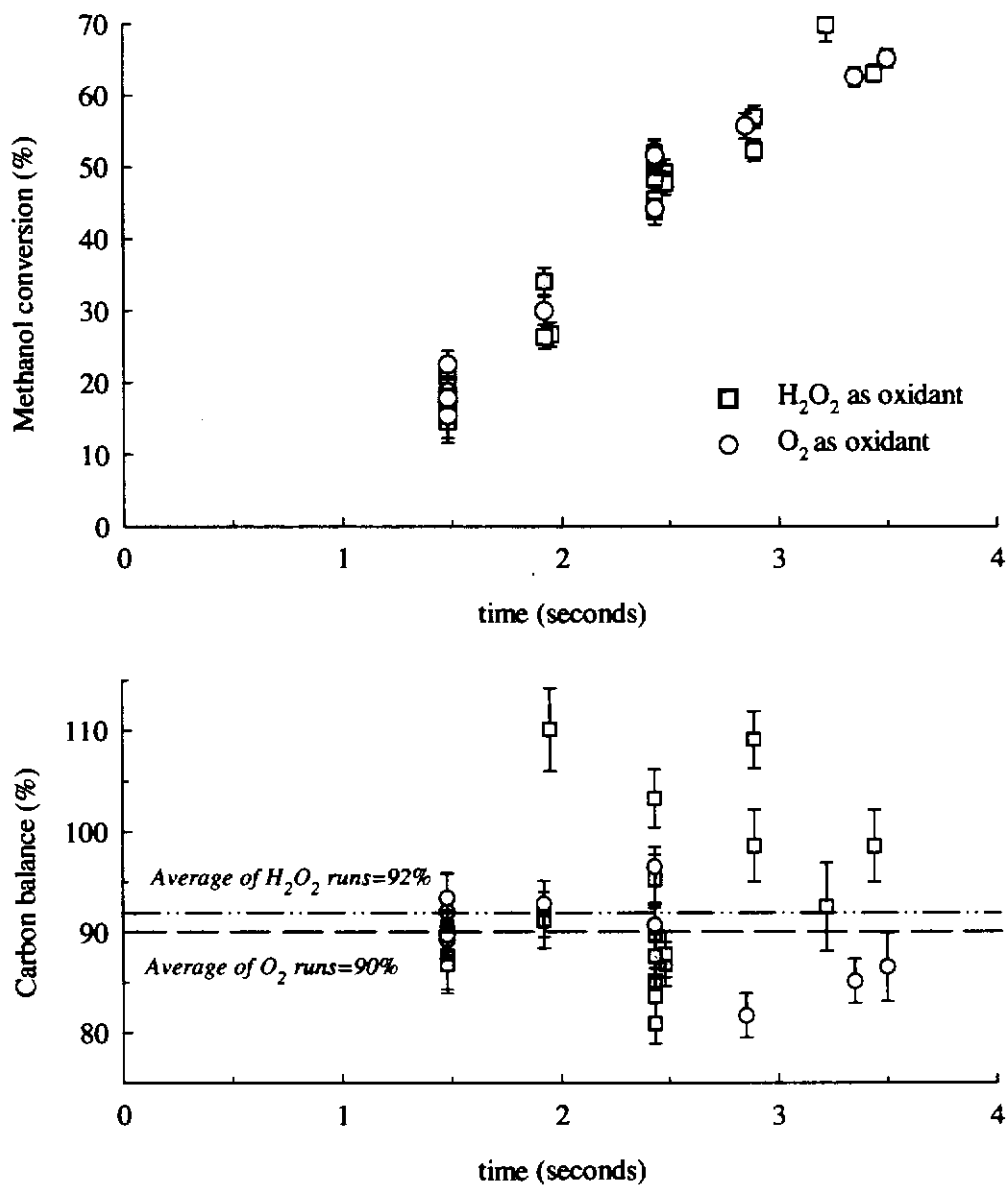


Figure 4.5
Comparison of methanol conversion as a function of time using dissolved oxygen and hydrogen peroxide as oxidants. Run conditions: $T=500^{\circ}\text{C}$, $P=246$ bar, $[\text{MeOH}]_0=0.069$ wt%, $\phi=1.5$.

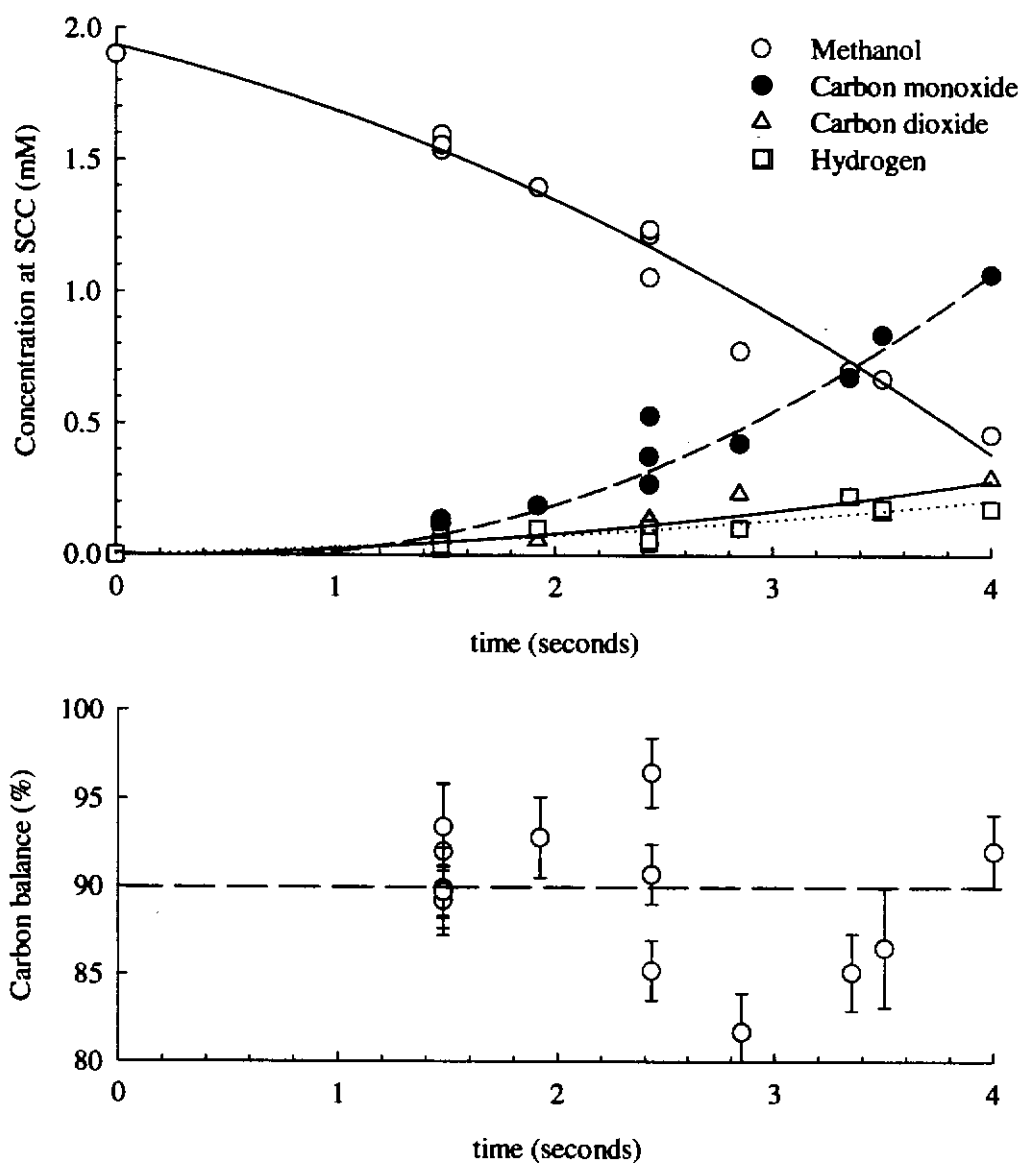


Figure 4.6
 Species concentrations as a function of time resulting from the oxidation of methanol using dissolved oxygen as the oxidant. Run conditions: $T=500^{\circ}\text{C}$, $P=246$ bar, $[\text{MeOH}]_0=0.069$ wt%, $\phi=1.5$.

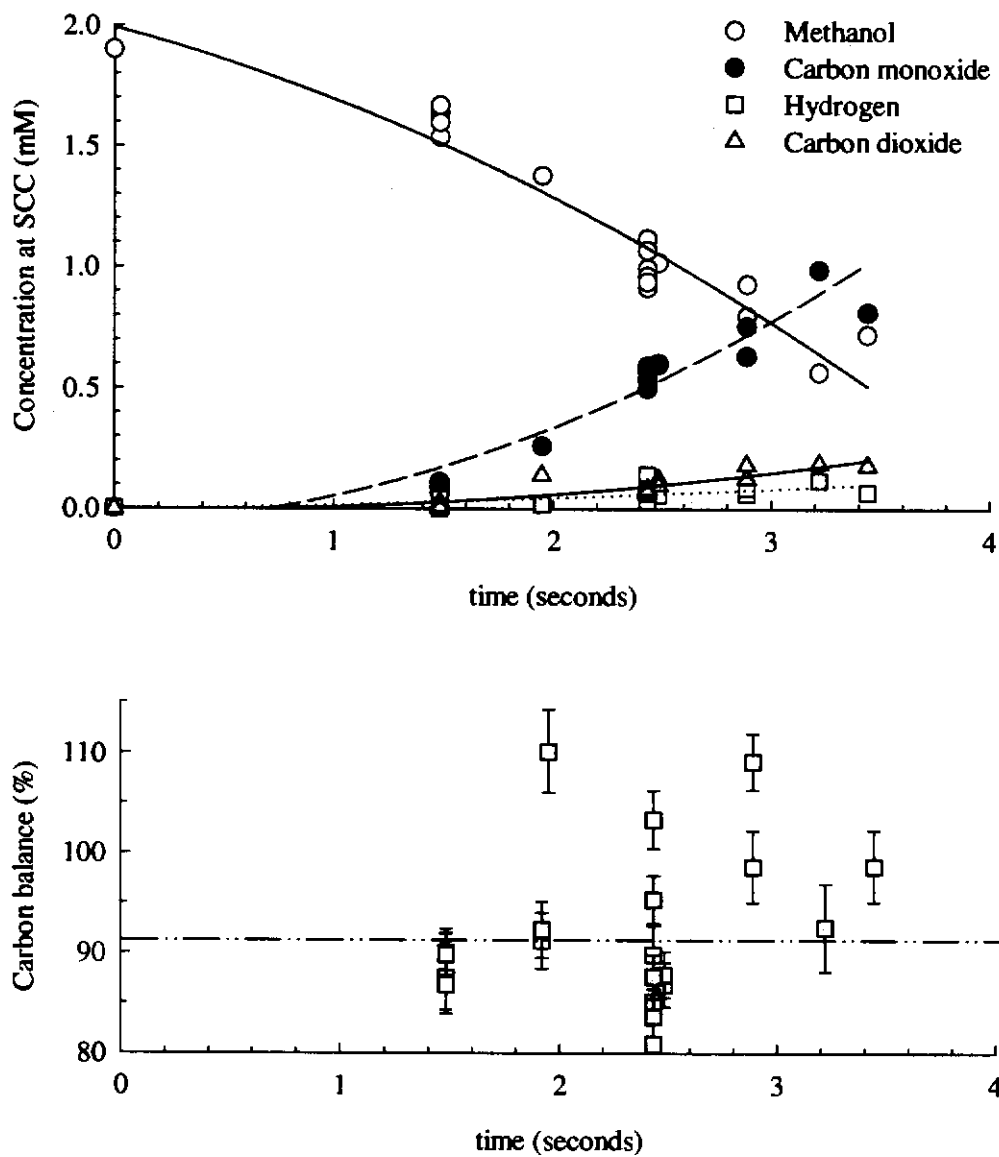


Figure 4.7

Species concentrations as a function of time resulting from the oxidation of methanol using hydrogen peroxide as the oxidant. Run conditions: $T=500^{\circ}\text{C}$, $P=246$ bar, $[\text{MeOH}]_0=0.069$ wt%, $\phi=1.5$.

figures exhibit a rapid decrease in methanol concentration over the 4 second time period shown. This decrease is accompanied by an increase in carbon monoxide concentration. At 4 seconds the carbon monoxide concentration reaches a value of 1mM (approximately half the starting methanol concentration). The subsequent conversion of carbon monoxide to carbon dioxide can be seen to occur at a much slower rate, with CO₂ concentrations never exceeding 0.4mM at the longest time investigated. Also seen in Figures 4.6 and 4.7 is the slow, gradual buildup of hydrogen in the effluent due to the influence of the water-gas shift reaction. The buildup is more pronounced than in typical fuel-lean experiments. This is due to the lack of available oxygen for direct hydrogen oxidation and to the relatively high CO concentrations present in the experiments.

A comparison of the product spectra resulting from the use of the two oxidants is provided in Figures 4.8 to 4.10. As is evident from the five graphs shown, the concentrations of methanol, oxygen, carbon monoxide, carbon dioxide, and hydrogen at supercritical conditions (SCC) are essentially identical for the two oxidants. The error bars shown in these figures were calculated using the methodology described in Section 3.3.3. Of the five graphs, the hydrogen graph displays the poorest agreement between the two oxidant data sets, with the peroxide data appearing to be systematically lower than that from the equivalent dissolved oxygen runs. However, the experiments shown were conducted over the period of one year, with intervening experiments involving other compounds. Given the age and condition of the gas chromatograph used for the hydrogen analysis method (see Appendix 8.3.3), the level of agreement is, nonetheless, fairly good.

Figure 4.5 through 4.10 demonstrate that the use of aqueous hydrogen peroxide solutions to generate molecular oxygen *in-situ* is a viable means of introducing oxygen into laboratory-scale SCWO reactor systems. However, the demonstration described above was made with peroxide solutions which yielded oxygen feed concentrations of only 0.069wt%. Additional methanol experiments, described in Section 4.4, employ peroxide solutions which produce 0.87 wt% oxygen at the reactor inlet. When compared with their dissolved oxygen counterparts, the 0.87 wt% runs exhibit no change in oxidation kinetics. While this latter data

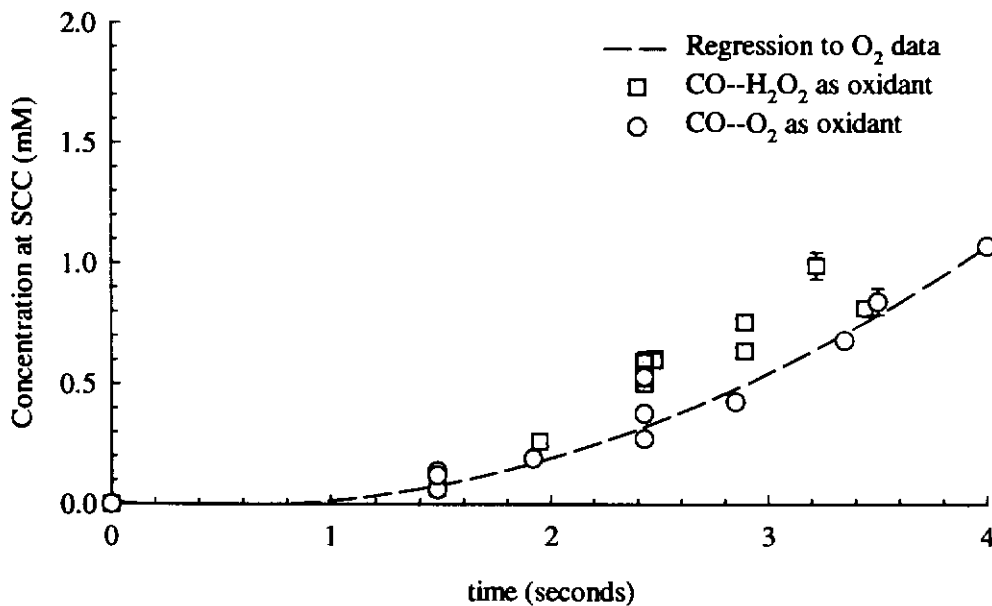
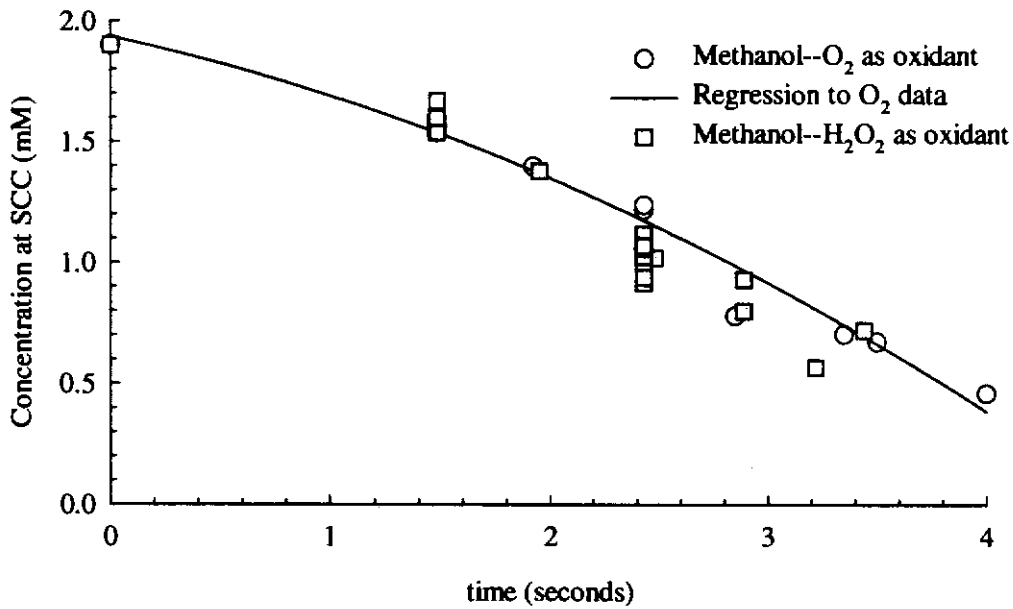


Figure 4.8

Comparison of methanol and carbon monoxide concentrations as a function of time using both dissolved oxygen and hydrogen peroxide as oxidants. Run conditions: $T=500^{\circ}\text{C}$, $P=246$ bar, $[\text{MeOH}]_0=0.069$ wt%, $\phi=1.5$.

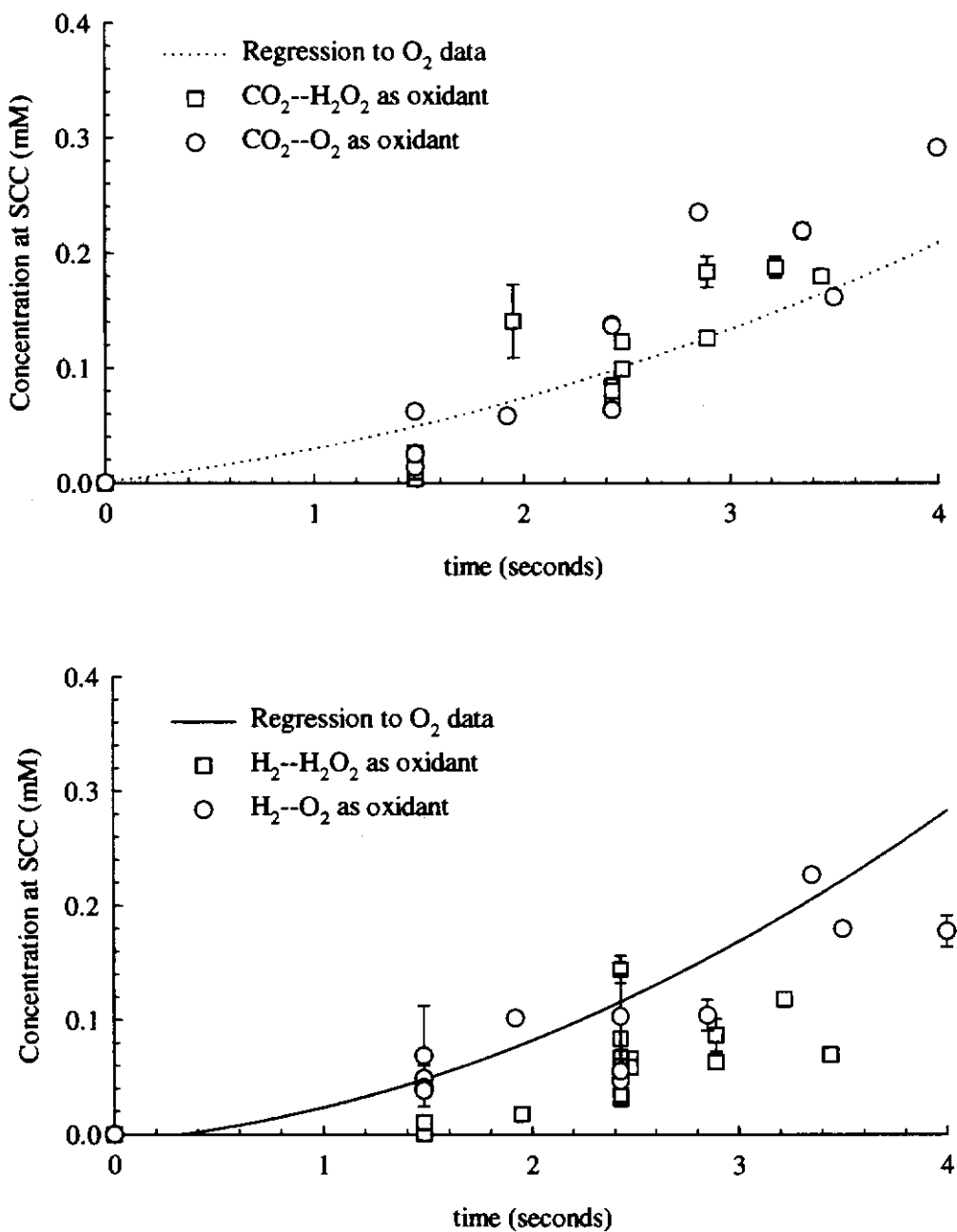


Figure 4.9

Comparison of carbon dioxide and hydrogen concentrations as a function of time using both dissolved oxygen and hydrogen peroxide as oxidants. Run conditions: $T=500^\circ\text{C}$, $P=246$ bar, $[\text{MeOH}]_0=0.069$ wt%, $\phi=1.5$.

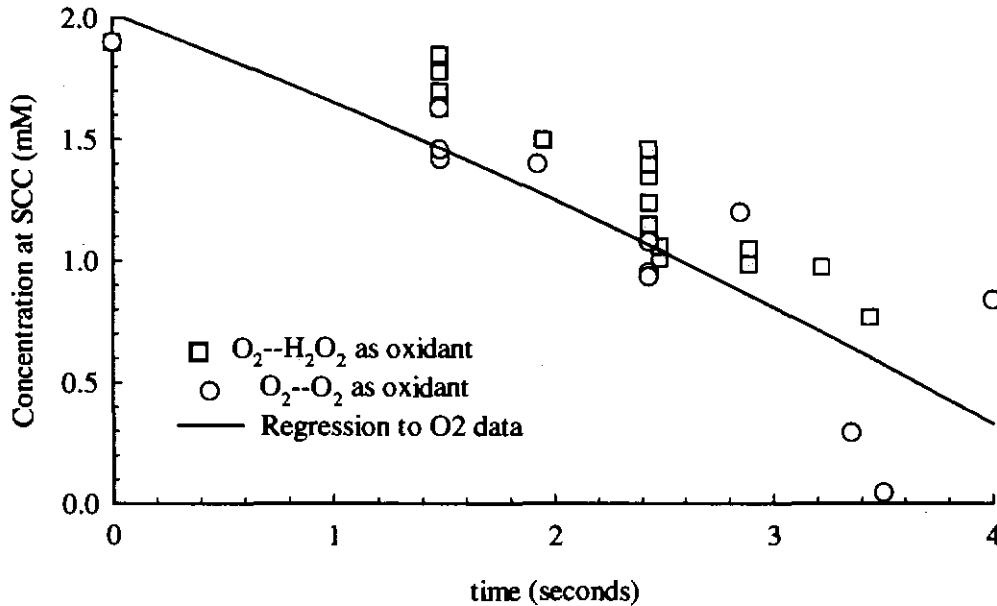


Figure 4.10

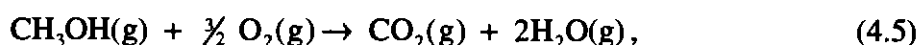
Comparison of oxygen concentrations as a function of time using both dissolved oxygen and hydrogen peroxide as oxidants. Run conditions: $T=500^{\circ}\text{C}$, $P=246$ bar, $[\text{MeOH}]_0=0.069$ wt%, $\phi=1.5$.

provides indirect evidence of the validity of the method at higher peroxide feed concentrations, extension to substantially higher concentrations (several wt%) should be supported with additional comparison experiments, perhaps using one of the other oxygen feed methods described above.

4.3 EFFECT OF FUEL-EQUIVALENCE RATIO

A series of ten experiments were conducted to determine the influence of fuel-equivalence ratio on the rate and extent of methanol oxidation. The experiments were conducted in a 7.3m x 0.041 in. ID Inconel 625 reactor (system 14 in Appendix 8.4) fitted with a side-entry tee with 0.01 in. inserts (configuration 4 of Table 3.2). The methanol concentration at the inlet of the reactor was fixed at 1.9mM (0.069 wt%), and the temperature

and pressure were held constant at 500°C and 3,550 psig (246 bar). Hydrogen peroxide was used as the oxidant in all runs, and the oxygen concentration at the inlet of the reactor was varied by changing the concentration of hydrogen peroxide in the oxidant feed solution. Experiments were conducted at oxygen-to-organic molar feed ratios of 3:1, 2:1, 1:1., 1:2, and 1:3. The corresponding inlet oxygen concentrations were 0.207, 0.138, 0.069, 0.035, and 0.023 wt%. Based on the global stoichiometry of the complete methanol oxidation reaction,



these feed ratios correspond to fuel equivalence ratios ranging from 0.5 (fuel-lean) to 4.5 (fuel-rich), where the fuel equivalence ratio, ϕ , is defined as

$$\phi = \frac{[\text{MeOH}]_o / [\text{O}_2]_o}{([\text{MeOH}]_o / [\text{O}_2]_o)_{\text{stoich}}}. \quad (4.6)$$

The results of the experiments are shown in Figures 4.11, 4.13, and 4.14. Figure 4.11 shows the measured methanol conversion at 5 and 7 seconds as a function of fuel-equivalence ratio. At both residence times, conversion increases with decreasing ϕ down to an equivalence ratio of approximately 1 to 1.5. Below this value, the methanol conversion levels off and remains relatively constant with further decreases in ϕ . Thus, the data, indicate that the rate of oxidation is independent of oxygen feed concentration above an oxygen-to-organic molar feed ratio of 1:1 to 1.5:1. This observation is consistent with the findings of previous MIT investigations of methanol oxidation in supercritical water (Webley and Tester, 1989; Tester *et. al.*, 1993). These investigations spanned a fuel-equivalence ratio range of 0.55 to 3.3 The observation is not consistent, however, with the data of Rice, *et al.* (1996) which are claimed to show that the oxidation rate of methanol at 480°C and 274 bar is independent of ϕ . The Rice, *et al.* data are shown in Figure 4.12. Over the range of fuel-equivalence ratios used in the study (0.85 to 3.4), there is no clear trend in conversion with ϕ . Closer inspection of Figure 4.12, however, reveals that there is a substantial amount of scatter in the data used for the comparison. For example, at a given residence time, the measured methanol conversions at

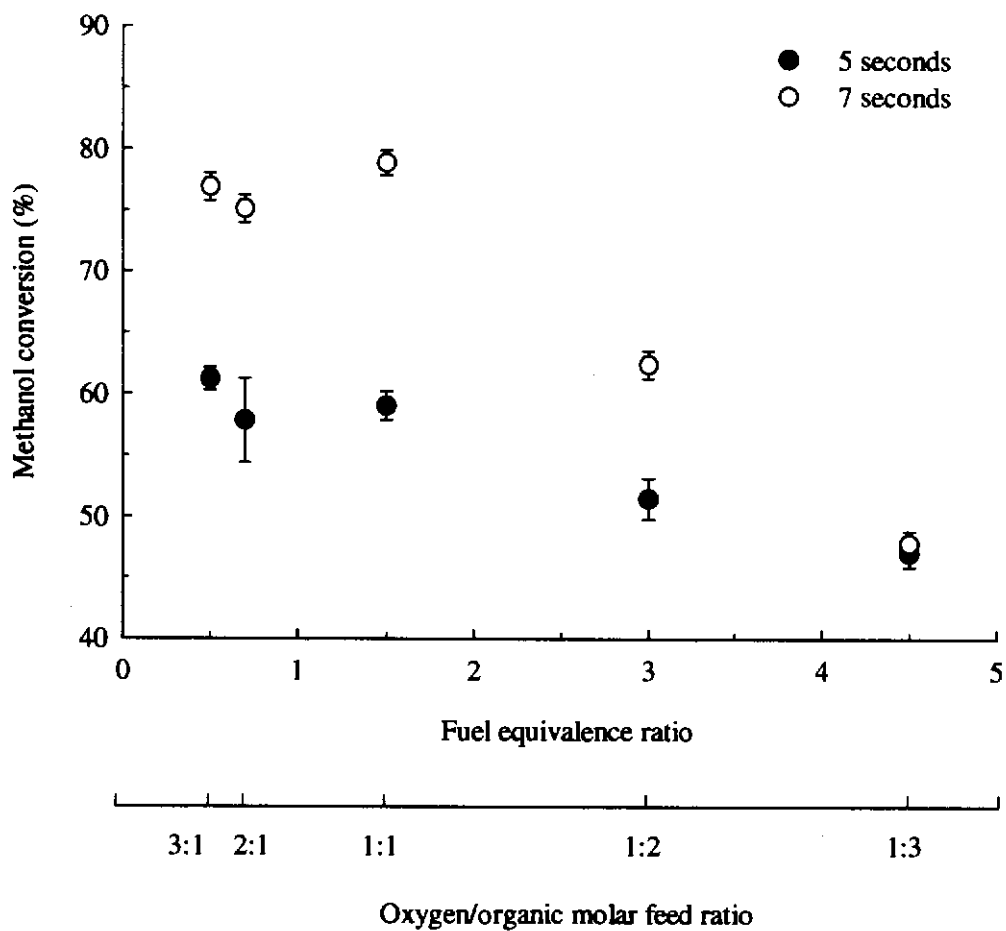


Figure 4.11
 Methanol conversion at 5 and 7 seconds as a function of fuel-equivalence ratio. Run conditions: $T=500^{\circ}\text{C}$, $P=246$ bar, $[\text{MeOH}]_0=0.069$ wt%.

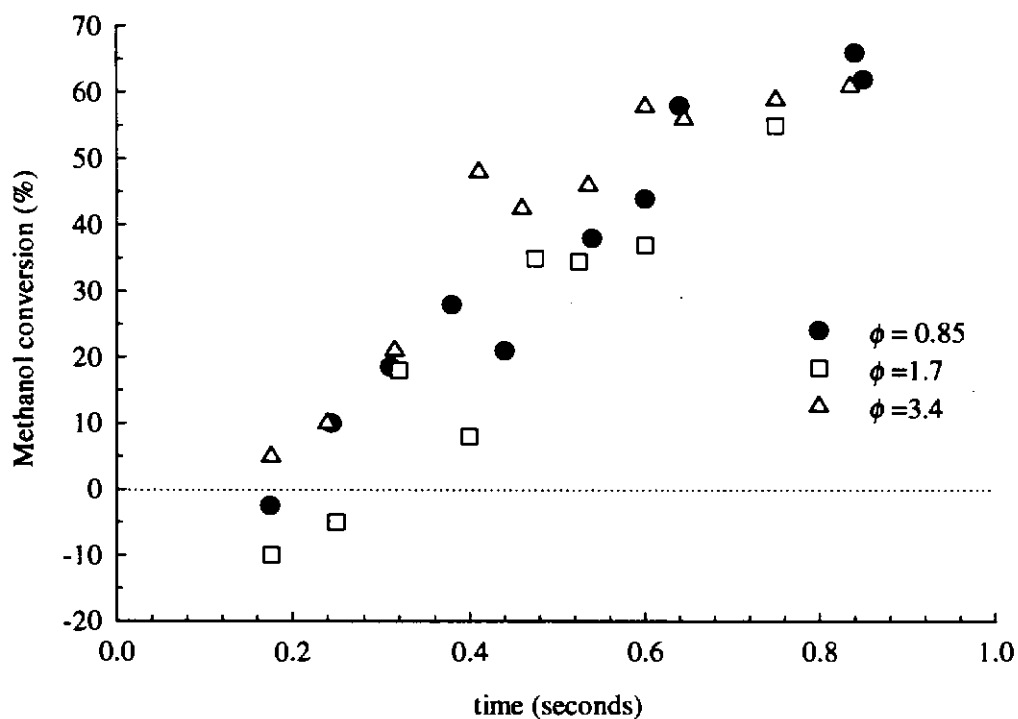


Figure 4.12
Methanol conversion as a function of time at fuel-equivalence ratios of 0.85, 1.7, and 3.4. Data taken from paper of Rice, *et al.* (Rice *et. al.*, 1996).

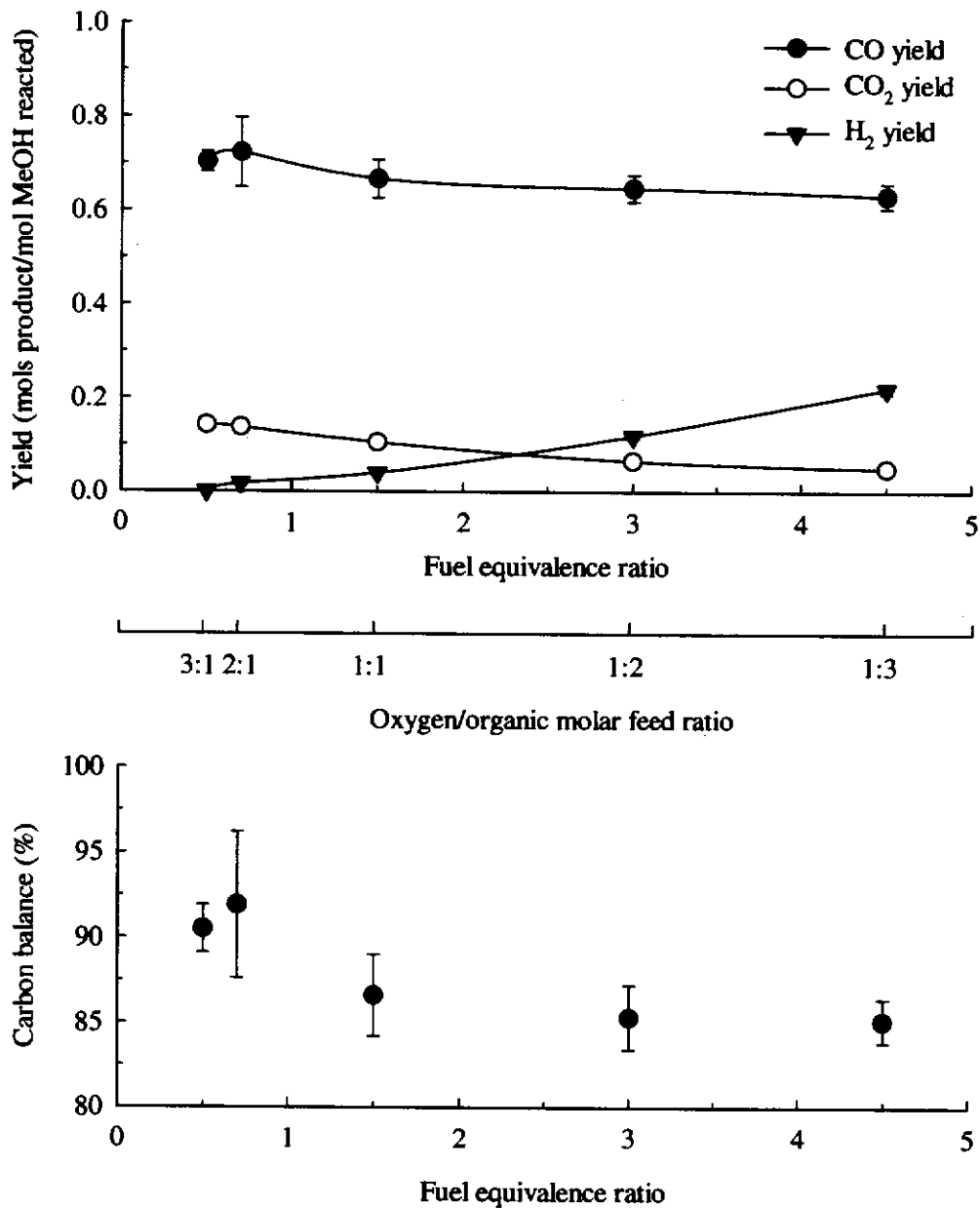


Figure 4.13

Carbon monoxide, carbon dioxide, and hydrogen molar yields as a function of fuel-equivalence ratio at 5 seconds. Run conditions: $T=500^{\circ}\text{C}$, $P=246$ bar, $[\text{MeOH}]_0=0.069$ wt%.

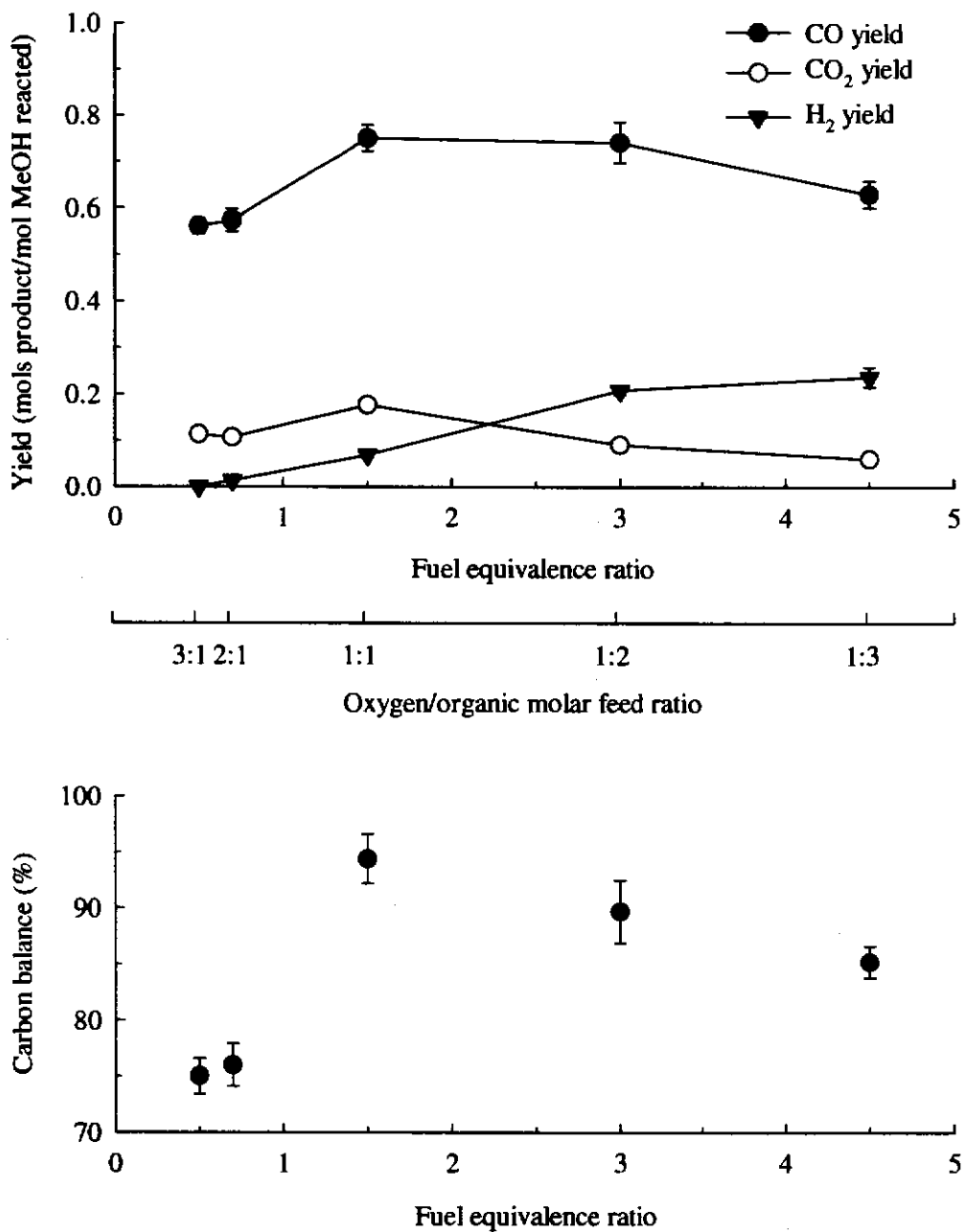


Figure 4.14
Carbon monoxide, carbon dioxide, and hydrogen molar yields as a function of fuel-equivalence ratio at 5 seconds. Run conditions: $T=500^{\circ}\text{C}$, $P=246$ bar, $[\text{MeOH}]_0=0.069$ wt%.

different values of ϕ vary by as much as 20 to 40%. Variations of this magnitude make it difficult to assess whether the oxidation rate is truly independent of ϕ since the scatter in the data prevent discriminating ϕ dependencies which lead to conversion differences of less than 20 to 40%. From a mechanistic viewpoint, the independence of oxidation rate on ϕ at fuel-lean conditions is consistent with existing elementary reaction models which indicate that OH and HO₂ radicals, not oxygen, participate in the rate-controlling, direct oxidation reactions with methanol (Webley and Tester, 1989; Brock *et. al*, 1996; Dagaut *et. al*, 1996; Rice *et. al*, 1996).

While the methanol oxidation rate is independent of oxygen at low ϕ , it is important to note that it is not independent over the entire oxygen concentration range explored in the experiments. As the data in Figure 4.11 clearly show, methanol conversion drops off by 10 to 30% as the oxygen-to-organic molar feed ratio decreases from 1:1 to 1:3. Based on replicate experiments at other conditions, a drop of this magnitude cannot be attributed to experimental error. It appears, therefore, that some minimum level of oxygen is required to maintain the steady-state concentrations of key species in the radical pool. This hypothesis is supported by the modeling work of Dagaut, *et al.* (1996) which indicates that 50% of the HO₂ net reaction rate during the steady-state portion of the oxidation is due to reactions involving molecular oxygen. Furthermore, 40% of the H₂O₂ net reaction rate is due to HO₂ recombination. Thus, the oxygen concentration has a significant role in maintaining the concentration of important OH radical precursors.

The dependence of oxidation rate on oxygen feed concentration is often lost in studies which determine the reaction order of oxygen by regressing a global rate expression to an entire oxidation data set. This is because these data sets are often weighted toward fuel-lean experiments, with little data at fuel-equivalence ratios significantly larger than one. Since the range of ϕ explored is relatively narrow, it is difficult to obtain a reliable estimate of the global reaction order with respect to oxygen. In addition, the estimated error associated with the regressed oxygen reaction order is often substantially larger than the point estimate of the order itself. This situation leads many investigators to the erroneous conclusion that the rate of

oxidation is independent of oxygen concentration, when clearly it cannot be for all values of ϕ since some level of oxygen is required for the reaction to proceed.

Not surprisingly, the fuel-equivalence ratio also has an impact on the spectrum of oxidation products generated during the oxidation process. Figures 4.13 and 4.14 show the influence of fuel-equivalence ratio on the molar yields of CO, CO₂, and H₂ at residence times of 5 and 7 seconds. As seen in the graph at 5 seconds, superstoichiometric oxygen-to-organic feed ratios lead to high yields of the primary carbon-containing oxidation products, CO and CO₂ (formaldehyde was not quantified in these experiments) and low yields of hydrogen (which presumably is being co-oxidized in the presence of excess oxygen). At the other end of the spectrum, substoichiometric molar feed ratios depress the direct oxidation of methanol and CO to CO₂ and promote the production of H₂ via the water-gas shift (WGS) reaction: $\text{CO} + \text{H}_2\text{O} \rightarrow \text{CO}_2 + \text{H}_2$. Based on the stoichiometry of the water-gas shift, one might expect the CO₂ yield to increase at high fuel-equivalence ratios. This, in fact, may be the case, but the overall CO₂ yield (as influenced by the WGS *and* direct oxidation) is seen to decrease monotonically with increasing fuel equivalence ratio. The graph at 7 seconds shown in Figure 4.x displays similar dependencies of the CO₂ and H₂ yields on fuel-equivalence ratio. The steep drop seen in CO yields at low fuel-equivalence ratios is most likely due to an analytical problem, as is evidenced by the sharp decrease in the corresponding carbon balances at these values of ϕ .

4.4 INTER-LABORATORY COMPARISON OF SCWO KINETICS

Chemical reactions in near-critical and supercritical water have been the subject of experimental investigation since the inception of the SCWO process in the late 1970's. As a result, a substantial body of kinetic information has accumulated describing hydrothermal transformation reactions. Surprisingly, however, there have been relatively few inter-laboratory comparisons of kinetic data on a given compound or class of reaction. This is due, in part, to the wide number of reactions which have been investigated and the disparate operating ranges of each experimental system. In addition, many of the near-critical studies

involved reactants which undergo substantial amounts of hydrolysis or pyrolysis. In this case, kinetic interpretation of the resulting data requires an accurate knowledge of the temperature-time history of the reactants. In the absence of such information, as is frequently the case, interpretation of the data and construction of a meaningful basis of comparison is oftentimes impossible.

In an effort to address the need for a well-characterized, inter-laboratory comparison of SCWO kinetic data, particularly at different scales, a joint research project was begun in 1995 between MIT and the Combustion Research Facility (CRF) at Sandia National Laboratory in Livermore, CA. One of the objectives of the project was to directly compare kinetic data from the bench-scale reactor system described in Chapter 3 with data taken in Sandia's larger, tubular flow reactor. This portion of the project was motivated, in part, by the assumed first-order Arrhenius plot shown in Figure 4.15 which compares previously published MIT methanol oxidation data (Tester *et. al*, 1993) with data taken under similar, though not identical, operating conditions at Sandia (Rice *et. al*, 1996). As shown in the figure, there is a significant difference in the apparent, first-order rate constants regressed from the two data sets. While the slopes, and hence apparent activation energies, appear to be similar, the values of the MIT rate constants are 4 to 5.5 natural log units lower than those obtained at Sandia. As a result of the dramatic differences between the two data sets, a series of experiments were undertaken by both groups using methanol as the model feed compound. Since the MIT data shown in Figure 4.15 were obtained using dissolved oxygen and the Sandia data were taken using hydrogen peroxide, initial work at MIT focused on the design and construction of a peroxide delivery system to allow a direct comparison of methanol oxidation kinetics using the two oxidants. This work led to the hydrogen peroxide and oxygen comparison experiments described in Section 4.2. Additional work examined mixing, preheating, and temperature measurement in the bench-scale reactor and resulted in the redesign of several key elements of the MIT reactor system. The redesign efforts are documented in Chapter 3 and in the preceding sections of this chapter.

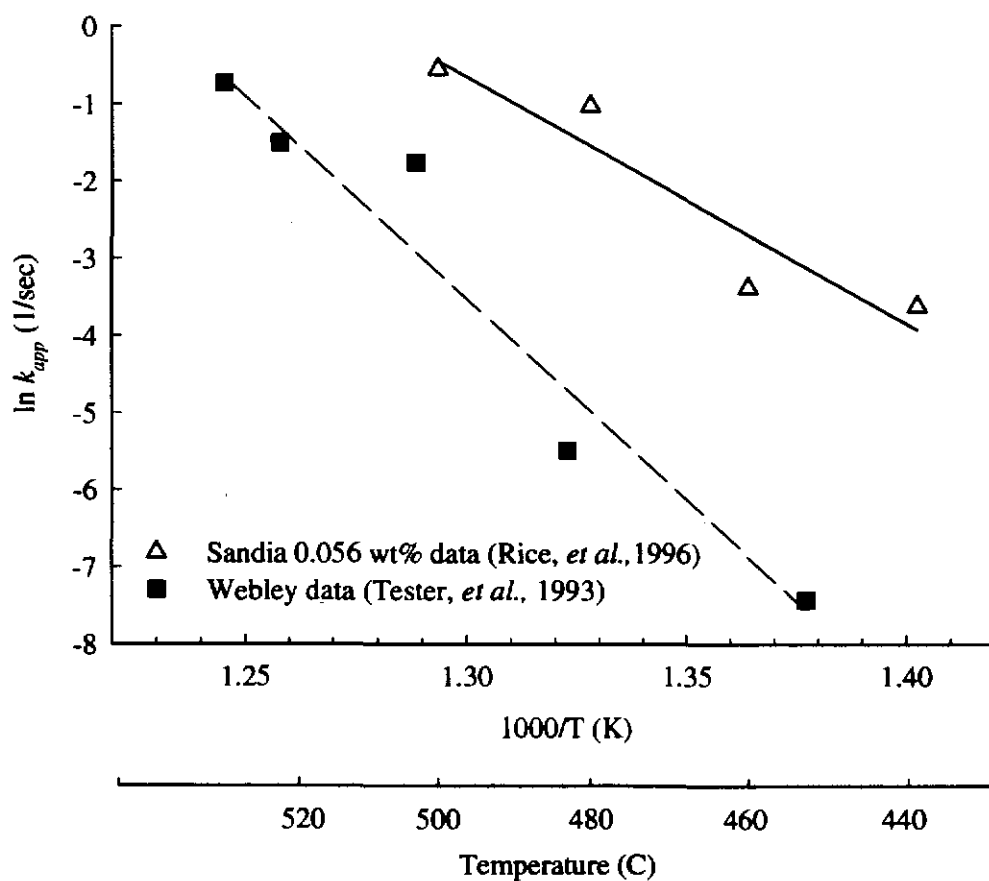


Figure 4.15

Comparison of MIT and Sandia apparent, first-order rate constants as a function of temperature for methanol oxidation. Data taken from published values of Rice, *et al.* (1996) and Tester, *et al.* (1993).

The MIT experiments conducted under the joint research program were undertaken after the redesign of the mixing tee (Sections 3.1.3.1 and 4.1), the installation of the DOH preheating system (Section 3.1.2.3), and the hydrogen peroxide decomposition experiments (Section 4.2). As such, they reflect the majority of design changes made to the reactor system during the course of this thesis. The reactor used was comprised of a side-entry mixing tee with 0.01 in. inserts and the tubular reactor originally used by Holgate (configuration 5 of Table 3.2). Experiments were conducted using both dissolved oxygen and hydrogen peroxide as the oxidants.

The Sandia SCWO reactor system is illustrated in Figure 4.16. The reactor section is comprised of six 61 cm heat-traced and insulated, straight sections of 9/16 in. OD x 3/16 in. ID Inconel 625 tubing connected by insulated Autoclave Engineers 9/16 in. tees. Type K thermocouples are inserted in each of the tees and their tips are centered in the reactor flow. The thermocouples provide the input signal to six independent controllers which provide power to each section of heat tracing. The total length of the reactor is 3.8 meters and it has a surface-to-volume ratio of 8.4 cm^{-1} . A complete description of the apparatus, including the feed, reactor, and letdown subsystems, can be found in the report by Hanush (1996). For the experiments described below, effluent analysis at Sandia was performed using a gas chromatograph equipped with an FID detector (Rice *et. al*, 1996).

4.4.1 Methanol hydrolysis/pyrolysis experiments

Prior to undertaking the main body of experiments, two control experiments were performed at MIT to measure the extent of methanol destruction in the absence of added oxygen. The experiments were performed by flowing a prepared methanol feed solution through the organic-side of the system and helium-sparged, deionized water through the oxygen-side. For both experiments, the system pressure was 269 bar and the residence time was fixed at 7 seconds. The temperatures of the two runs (420 and 480°C) were chosen to bracket the temperature range of the proposed joint experiments. The results of the experiments are presented in Table 4.3. As shown, very little methanol conversion occurred at

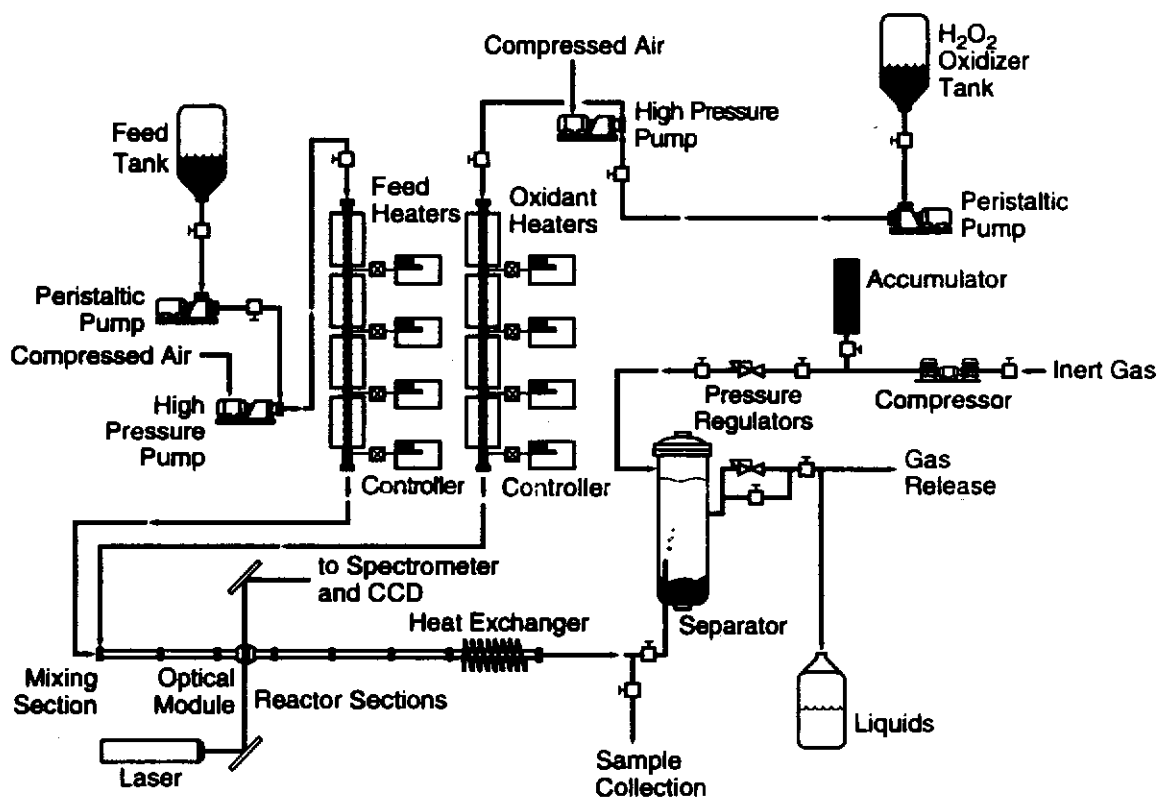


Figure 4.16
Schematic of Sandia supercritical water oxidation flow reactor. Diagram taken from (Rice, et al., 1996).

either set of conditions, and the corresponding carbon balances indicate that the majority of the methanol in the feed was recovered in the effluent. During both runs, no vapor effluent flowrate was observed in the soap-bubble flowmeter, and periodic analysis of the gas/liquid separator headspace revealed no detectable CO or CO₂.

TABLE 4.3
Hydrolysis/pyrolysis control experiments for joint MIT/Sandia kinetic study
($C_{MeOH,o} = 0.059$ wt%, $\tau = 8$ seconds)

Run No.	Pressure (bar)	Temperature (°C)	Conversion (%)	Carbon balance (%)
679	269 ± 1	422 ± 4	0.5 ± 2.6	99.5 ± 2.6
680	269 ± 1	483 ± 4	3.8 ± 3.2	96.2 ± 3.2

As a result of the findings presented in Table 4.3, it is apparent that methanol does not react to a significant degree over the timescales of interest to this work by either a hydrolytic or pyrolytic pathway. Thus, the direct comparison of the MIT and Sandia data sets which follows is simplified by not having to consider the contribution of these kinetic pathways to the rate of methanol destruction.

4.4.2 Joint MIT/Sandia methanol oxidation experiments

The dependence of methanol oxidation rate on temperature and methanol feed concentration was explored by both groups through a series of jointly-planned experiments at 420 to 520°C. For these experiments, the system pressure was set at either 269 or 274 bar and the oxidant-to-fuel molar feed ratio was fixed at a value of 2.25 ($\phi = 0.667$). Methanol feed concentrations of 0.011, 0.056, 0.15, and 0.39 wt% were chosen to match the previously published values of Rice, *et al.* (1996). A summary of the experiments conducted by the two groups is given in Table 4.4.

TABLE 4.4
Summary of MIT/Sandia methanol oxidation experiments

	MIT	Sandia
Number of experiments:	22 ^a	21 ^b
Temperature range:	420-520 °C	430-500 °C
Pressure:	269 ± 1.5 bar	274 bar
Residence time:	7-8 seconds	7 seconds
Fuel-equivalence ratio:	0.67	0.67
Methanol feed concentrations:	0.011 wt% (3) ^c	0.011 wt% (5) ^c
	0.056 wt% (12) ^{c,d}	0.056 wt% (6) ^c
	0.15 wt% (4) ^c	--
	0.39 wt% (3) ^c	0.39 wt% (6) ^c
	-- ^e	1.2 wt% (4)
Range of experimental methanol conversion:	32.2-99.7 %	5-99.85 %

^a Three experiments resulted in methanol effluent concentrations below the minimum detectable level (MDL) of the GC method (see Section 3.2.2.2). Two occurred in 0.056wt% experiments at temperatures of 500 and 520°C. The third occurred in an 0.15wt% experiment at 500°C. These experiments are not included in the comparison.

^b Nineteen of these experiments are reported in Rice, *et al.* (1996). The results of two additional experiments were provided in private communication.

^c Numbers in parentheses indicate the number of experiments conducted at a given feed concentration.

^d Nine experiments were conducted using hydrogen peroxide and three using dissolved oxygen.

^e No experiments at 1.2 wt% were conducted at MIT. Detailed heat transfer calculations for the reactor section immersed in the main sandbath indicated that the resulting experiments would not be isothermal due to the substantial reaction exotherm at this feed concentration.

4.4.2.1 Temperature dependence of oxidation

Figures 4.17-4.19 shown the apparent first-order rate constants, k_{app} , obtained from the MIT and Sandia experiments described in Table 4.4. While the scatter in the Sandia data makes it difficult to assess the degree of agreement in all of the figures, the data at 0.011,

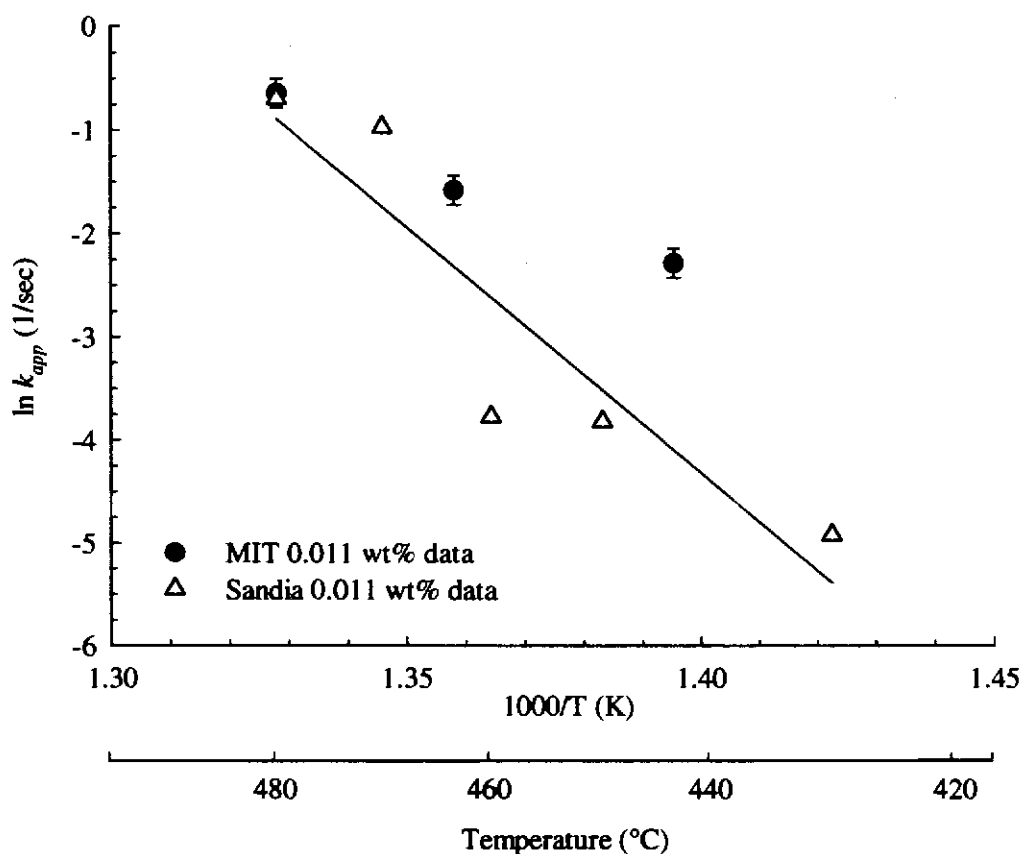


Figure 4.17

Comparison of MIT and Sandia apparent, first-order rate constants as a function of temperature at a methanol feed concentration of 0.011 wt%. Run conditions: $P=269$ bar (MIT) and 274 bar (Sandia). Space time fixed at 7 seconds and $\phi=0.67$ for all runs. Hydrogen peroxide was used as the oxidant.

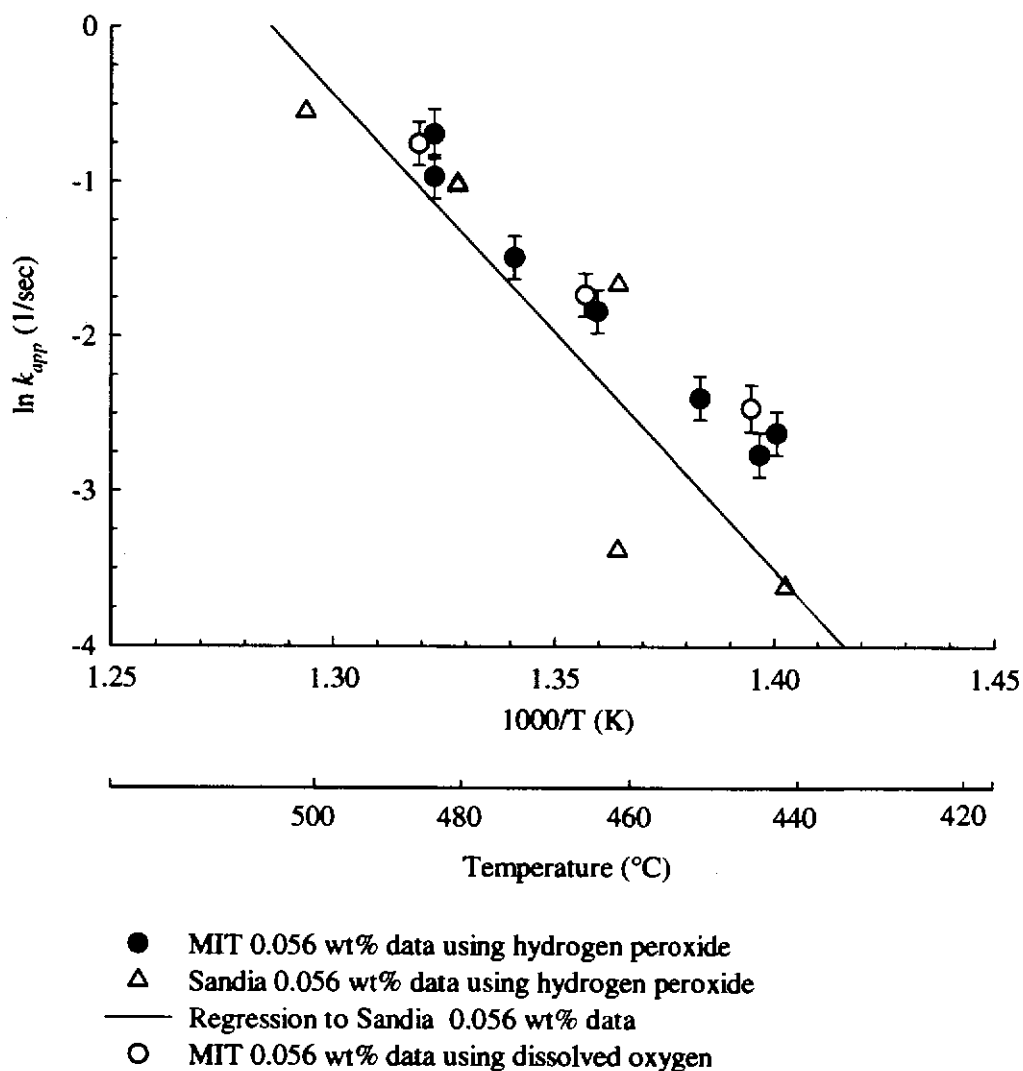


Figure 4.18

Comparison of MIT and Sandia apparent, first-order rate constants as a function of temperature at a methanol feed concentration of 0.056 wt%. Run conditions: $P=269$ bar (MIT) and 274 bar (Sandia). Space time fixed at 7 seconds and $\phi=0.67$ for all runs. Both hydrogen peroxide and dissolve oxygen were used in the MIT experiments.

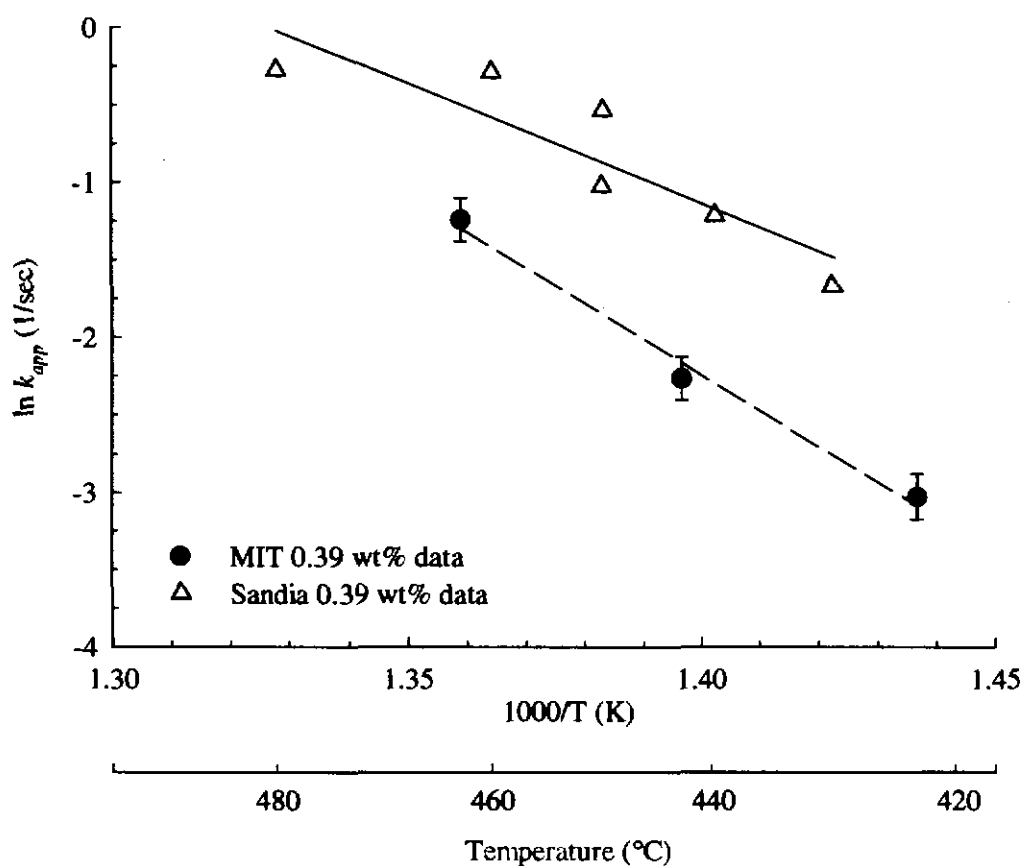


Figure 4.19

Comparison of MIT and Sandia apparent, first-order rate constants as a function of temperature at a methanol feed concentration of 0.39 wt%. Run conditions: $P=269$ bar (MIT) and 274 bar (Sandia). Space time fixed at 7 seconds and $\phi=0.67$ for all runs.

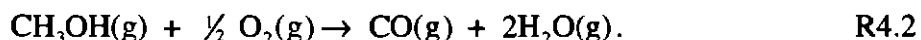
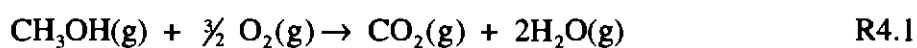
0.056, and 0.39 wt% methanol show much better agreement than the data in the original Webley/Sandia comparison. This is particularly true of the 0.056 wt% data shown in Figure 4.18, which include both oxygen- and hydrogen peroxide-based runs. Here, the MIT rate constants fall within 0.25 to 1.0 natural log units of the line fit to the Sandia rate constant data via least squares regression. However, the point-to-point agreement between the two data sets is much better than a comparison based on the fitted line would suggest. This is because the Sandia data also exhibit considerable scatter above and below the fitted line. The deviation of the Sandia data from the fit line varies from 0.3 to 1.0 log units—a range comparable to that seen in the MIT data. As can be seen from the graph, the point-to-point agreement between the two 0.056 wt% data sets is excellent at temperatures above 450 °C. Below 450°C, the data sets appear to diverge, with the MIT rate constants assuming values of 0.8 to 1.0 log units higher than the line fitted to the Sandia values. Nonetheless, the level of agreement is remarkable given the differences in the reactor systems, their scales, and the operational and analytical methods used to acquire the data.

A similar situation is found in the 0.011 wt% data sets depicted in Figure 4.17. Here, the agreement between the MIT and Sandia values is excellent at high temperatures and poorer at low temperatures. At the upper end of the experimental temperature range the data are essentially indistinguishable. At temperatures below 450 to 460 °C, however, the level of agreement diminishes, and the outermost MIT datum lies approximately 2.0 natural log units above the line fitted to the Sandia data. As was the case with the analysis of the 0.056 wt% data, however, deviation of the 0.011 wt% data from the fitted line may not be the best basis for comparison to use. While the 0.011 and 0.056 wt% data from both groups are in relatively good agreement, the same cannot be said of the 0.39 wt% data set. As shown in Figure 4.19, the Sandia 0.39 wt% rate constants lie along a straight line with a relatively constant displacement of 0.75 to 1.25 natural log units above the MIT data. The discussion of this difference will be deferred until the next section.

4.4.2.2 Feed concentration dependence of oxidation

The design of the joint experiments also allowed the dependence of the oxidation rate on methanol feed concentration to be determined. Figure 4.20 shows the apparent, first-order rate constants from the MIT data set as a function of temperature and initial feed concentration. Since all feed concentrations lie on approximately the same straight line, the data are consistent with a global rate expression which is first order in methanol concentration. In contrast, a similar graph of the Sandia data shows a marked increase in rate at the highest feed concentration (0.39 wt%). This graph is shown in Figure 4.21. The increase seen in the Sandia data at high methanol feed concentration could be indicative of a reaction which is not truly first order in methanol or one in which there is a substantial reaction exotherm at high methanol feed concentrations. Given that the MIT methanol data appear to exhibit first-order behavior over the entire feed concentration and temperature range, the latter possibility was examined in greater detail. Specifically, calculations were performed to estimate the adiabatic temperature rise (ATR) associated with each of the feed concentrations shown in Table 4.4. Details of the calculations are presented in the following paragraphs.

The temperature rise calculations were carried out by estimating the heats of reaction of the following global oxidation reactions in the ideal-gas state:



The first reaction depicts the complete oxidation of methanol to yield carbon dioxide and water. At the conditions of Figure 4.19, however, only 30 to 50% of the carbon in the reacted methanol is converted to carbon dioxide. The remainder is in the form of carbon monoxide and, to a much lesser extent, formaldehyde. The carbon monoxide partial oxidation reaction is shown in global form in reaction R4.2. Since the true heat release due to oxidation is somewhere between the bounds established by the two reactions, separate ATR calculations were carried out using the heat of reaction of each. The calculations were performed at a representative operating temperature of 460°C (733 K) and a pressure of 269 bar. The heats of

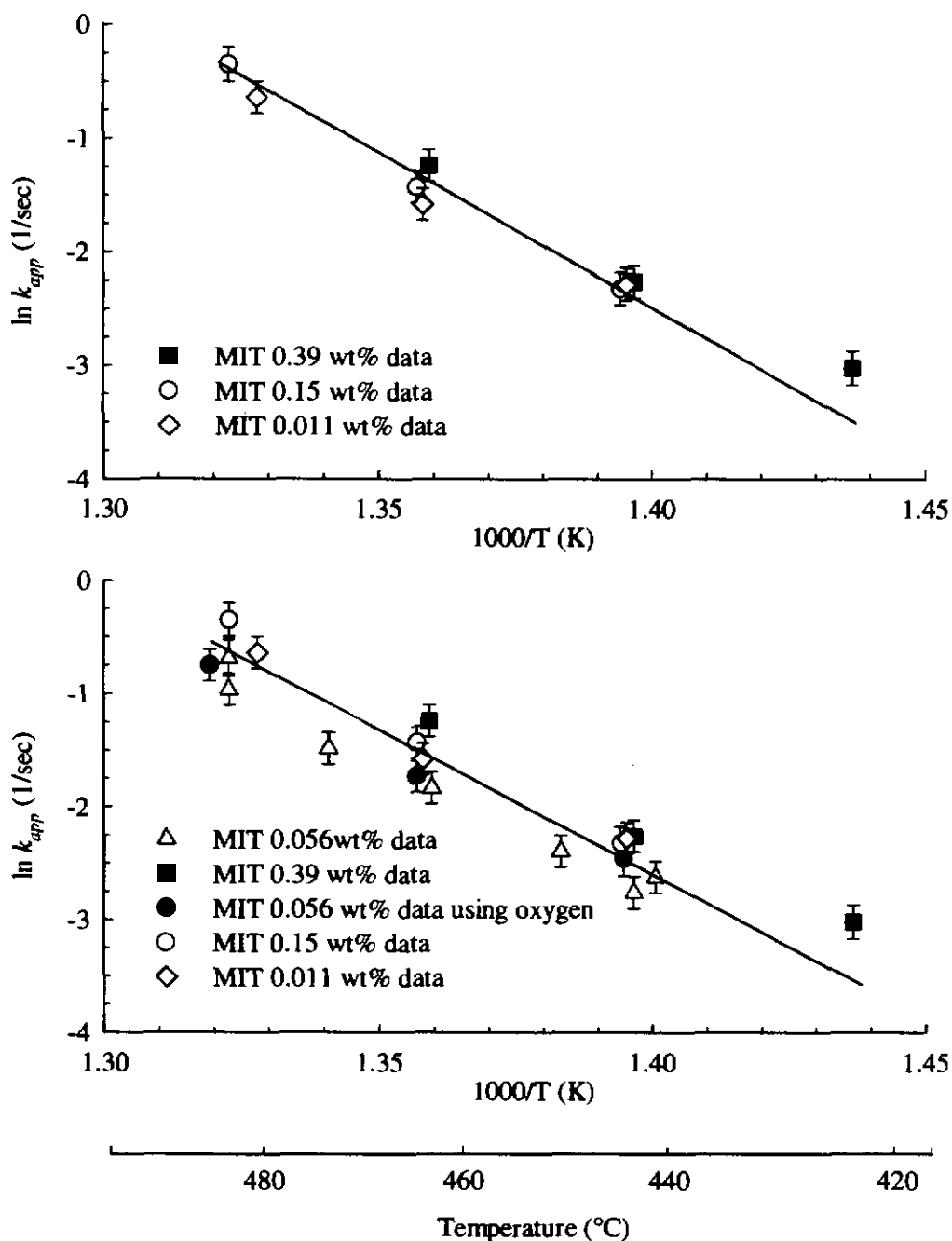


Figure 4.20
MIT apparent, first-order rate constants as a function of temperature and methanol feed concentration. Lower graph shows the entire MIT data set, including feed concentrations not used in the joint MIT/Sandia study and runs using dissolved oxygen. Run conditions: $P=269$ bar, space time fixed at 7 seconds, and $\phi=0.67$ for all runs.

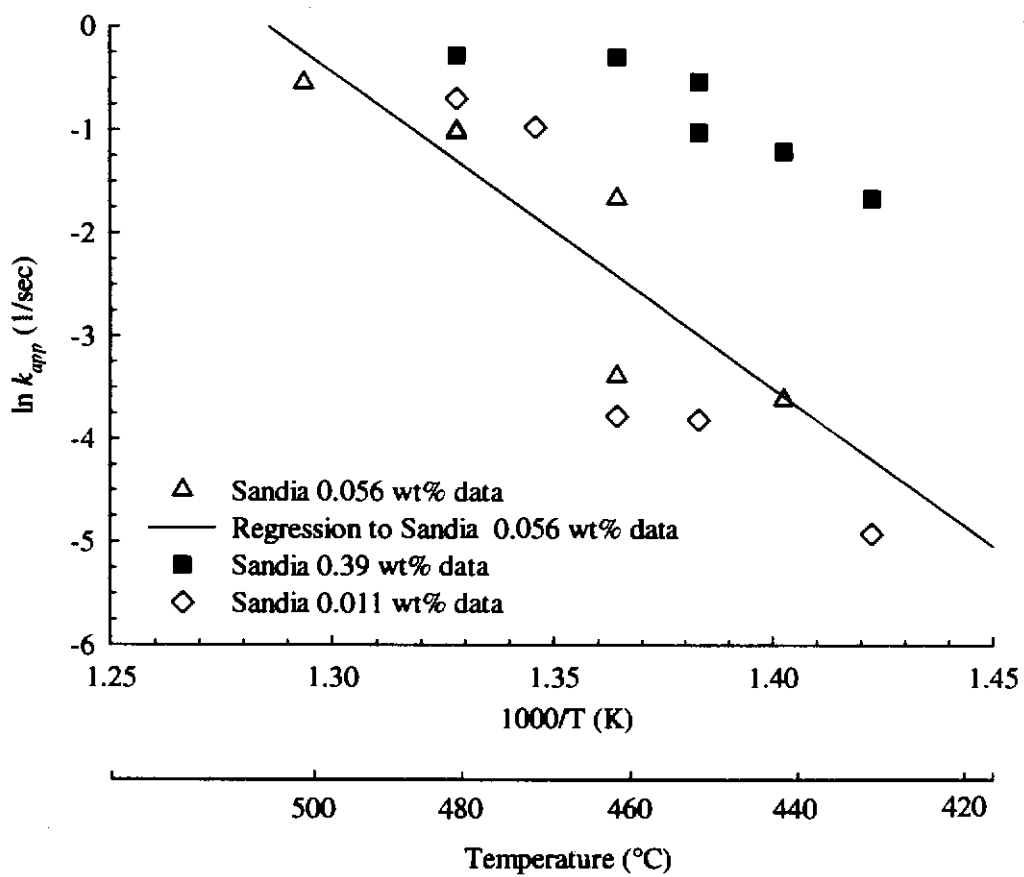


Figure 4.21
 Sandia apparent, first-order rate constants as a function of temperature and methanol feed concentration. Run conditions: $P=274$ bar, space time fixed at 7 seconds, and $\phi=0.67$ for all runs.

reaction of were estimated using published values of the heats of formation and heat capacities of each species in an ideal-gas standard state (Chase *et. al.*, 1985). The temperature dependence of the heat of reaction was determined using the following relation:

$$\Delta H_R^\circ(733 \text{ K}) = \Delta H_R^\circ(298 \text{ K}) + \int_{298}^{733} \Delta C_p^\circ(T) dT \quad (4.7)$$

where $\Delta C_p^\circ(T)$ is the ideal-gas, constant-pressure, heat capacity change of reaction. The resulting estimated heats of reaction for R4.1 and R4.2 are presented in Table 4.5.

The adiabatic temperature rise associated with each methanol feed concentration was estimated using the heats of reaction calculated above and the heat capacity of the reaction medium. Given the dilute nature of the medium, the heat capacity of pure water at 460 °C and 269 bar was used to approximate the heat capacity of reacting mixture. Since the calculated temperature rises were found to be relatively modest (~0.3 to 18°C), a single mean value of the heat capacity was used in the analysis (Kestin *et. al.*, 1984). The true heat capacity of water at these conditions decreases with increasing temperature, making the estimated values a conservative lower bound on the actual temperature rise. However, use of the heat capacity of water at 478°C (460 + 18°C) in the ATR analysis changes the estimated temperature rises by less than 3°C. As shown in Table 4.5, the estimated adiabatic temperature rise for reaction R4.1 varies from 0.5 to 17.5 °C for methanol feed concentrations of 0.011wt% to 0.39 wt%. Similar calculations for the less exothermic reaction R4.2 produce estimated temperature rises of 0.3 to 10.5 °C over the same feed concentration range. Temperature deviations of this magnitude would have a significant impact on the apparent, first-order rate constants. However, inspection of Figure 4.19 reveals that the MIT rate constants at 0.39 wt% are displaced from their Sandia counterparts by about 22 °C. This temperature deviation exceeds the 17.5 °C upper limit established by the ATR calculation for R4.1. Since it is unlikely that (a) the Sandia reactor is truly adiabatic and (b) the full heat of reaction of R4.1 is released, the

TABLE 4.5
Estimated adiabatic temperature rise for reactions R4.1 and R4.2 as a function of
methanol feed concentration
($T_o = 460\text{ }^\circ\text{C}$, $C_{p, \text{water}}(460\text{ }^\circ\text{C}, 269\text{ bar}) = 5\text{ J/g K}$)

MeOH feed concentration (wt%)	Reaction R4.1 $\Delta H_R^\circ(733\text{ K}) = -716.1\text{ kJ/mol}$	Reaction R4.2 $\Delta H_R^\circ(733\text{ K}) = -432.8\text{ kJ/mol}$
0.011	0.5 °C	0.3 °C
0.056	2.5 °C	1.5 °C
0.15	6.7 °C	4.0 °C
0.39	17.5 °C	10.5 °C

the exotherm hypothesis alone cannot account for the differences in the two 0.39 wt% data sets. It could, however, be a contributing factor. The exotherm hypothesis is further complicated by the fact that no axial temperature rise was observed in the Sandia reactor during operation. As mentioned above, the Sandia reactor is comprised of six separate tubular sections connected by high-pressure tees. Each tee contains a 1/16 in. OD Type K thermocouple which is held in place by a high-pressure fitting. Each reactor section is actively heated by a 375W cable heater and is insulated to minimize heat loss to the environment. The tees connecting the sections are insulated, but are not actively heated. Since heat loss at SCWO operating temperatures (500 to 625°C) can be quite high, particularly in bench-scale systems, it is not unfeasible that the bodies of the connecting tees are at a lower temperature than the reactor sections and the reacting fluid passing through them. If this is the case, heat loss down the sheath of the thermocouple due to conduction could be adversely affecting the junction temperature at the thermocouple tip. This situation is quite common when thermocouples are passed through piping or vessel walls where the wall temperature is significantly different than the internal fluid temperature. For the scenario described above, the resulting temperature measurements would systematically underestimate the true fluid temperature, thereby making it difficult to detect a rise in temperature due to a reaction

exotherm. In the absence of a detailed description of the tee geometry, thermocouple position, and flow conditions within the tee (or, better yet, a direct measurement of the tee body temperature), further productive analysis of the potential temperature measurement problem is not possible. At the time of the writing of this thesis, experiments are underway at Sandia to determine investigate the exotherm and temperature measurement hypothesis.

4.5 EFFECT OF SURFACE-TO-VOLUME RATIO

In contrast to oxidation and other well-documented homogeneous transformation reactions, little is known about reactions which may occur at the reactor surface in SCWO systems. Determining the role surface effects play, if any, is important to both the experimental and modeling components of this thesis. It is important because surface effects, like hydrolysis and pyrolysis, have the potential to contribute to the observed rate of reaction in an oxidation experiment. The presence of significant surface contributions to the overall reaction rate would result in kinetic observations and regressed rate parameters which are geometry dependent and of limited utility for engineering design or for comparison with homogeneous kinetic models. In general, reactor surface effects may be catalytic or non-catalytic in nature. Non-catalytic surface effects are well-known phenomena in gas-phase reactors used in the atmospheric and combustion communities. In these systems, the reactor surface inhibits the rate of reaction by acting as a termination site for highly-reactive free-radicals (Moore and Pearson, 1981; Lewis and von Elbe, 1987). The gas-phase oxidation of hydrogen (Yetter *et. al.*, 1991), methane (Gardiner and Olson, 1980) and other compounds have been found to be dramatically influenced by the quenching of radical species at the surface of the reactor vessel. The net effect of such an interaction is the depletion of key intermediate species in the radical pool and a decrease in the overall rate of oxidation.

A limited study of the role of surface effects on the SCW oxidation of hydrogen and carbon monoxide was conducted by Holgate (1993). Experiments were carried out using both packed and open, tubular reactors at temperatures of 550 to 560°C, 246 bar, and a fuel-equivalence ratio of one. The packed-bed reactor was filled with 150 to 250 μm Inconel 625 beads, resulting in a surface-to-volume (S/V) ratio of approximately 480 cm^{-1} . The open

tubular reactor consisted of a 4.71m x 0.067 in. ID Inconel 625 tube with a S/V ratio of 24 cm^{-1} (reactor 5 of Appendix 8.4). Experiments were carried out in both reactors over space times ranging from 3 to 10 seconds. In the case of hydrogen, the additional surface area was found to decrease the apparent, first-order rate constant for oxidation from 0.44 s^{-1} to 0.074 s^{-1} . Thus, the apparent rate was reduced by approximately a factor of 6. Similar experiments with carbon monoxide resulted in a 7-fold reduction in the apparent, first-order rate constant in the presence of the added surface area. In addition, all of the stable species concentration profiles displayed temporal behavior indicative of a much slower rate of reaction.

The study of surface reactions in SCWO reactor systems is not one of the primary objectives of this thesis. However, data taken during the course of this work support the earlier findings of Holgate and suggest that the reactor surface may have a pronounced effect on the rate of oxidation in SCWO systems. The results of methanol oxidation experiments in two open, tubular reactors with different inner diameters are presented in the Arrhenius plot shown in Figure 4.22. Experiments were conducted at 269 bar, a fuel-equivalence ratio of 0.67, and a fixed residence time of seven seconds. The methanol feed concentration for all runs was 0.056 wt%. The data set exhibiting the lower reaction rate in Figure 4.22 was taken in a 7.3m x 0.041 in. ID Inconel 625 reactor (reactor 12 of Appendix 8.4) fitted with a side-entry mixing tee with inserts. The faster data were obtained using the original 4.71m x 0.067 in. ID Inconel 625 reactor (reactor 5 of Appendix 8.4) of Holgate fitted with the same tee. The surface-to-volume ratios of the 7.3 and 4.71m reactors were 39 and 24 cm^{-1} , respectively.

As shown, the lower S/V ratio reactor exhibits a markedly faster rate of oxidation at the same set of operating conditions. At a temperature of $480 \text{ }^\circ\text{C}$, the larger ID reactor results in an apparent, first-order rate constant which is approximately three log-units higher than that seen in the smaller ID reactor. It is also evident that much higher temperatures must be used in the high S/V ratio reactor to achieve comparable rates of reaction. It should be emphasized, however, that the data set shown is rather limited and is not the result of a systematic study of surface reactions. However, the behavior seen is consistent with surface-mediated free-radical

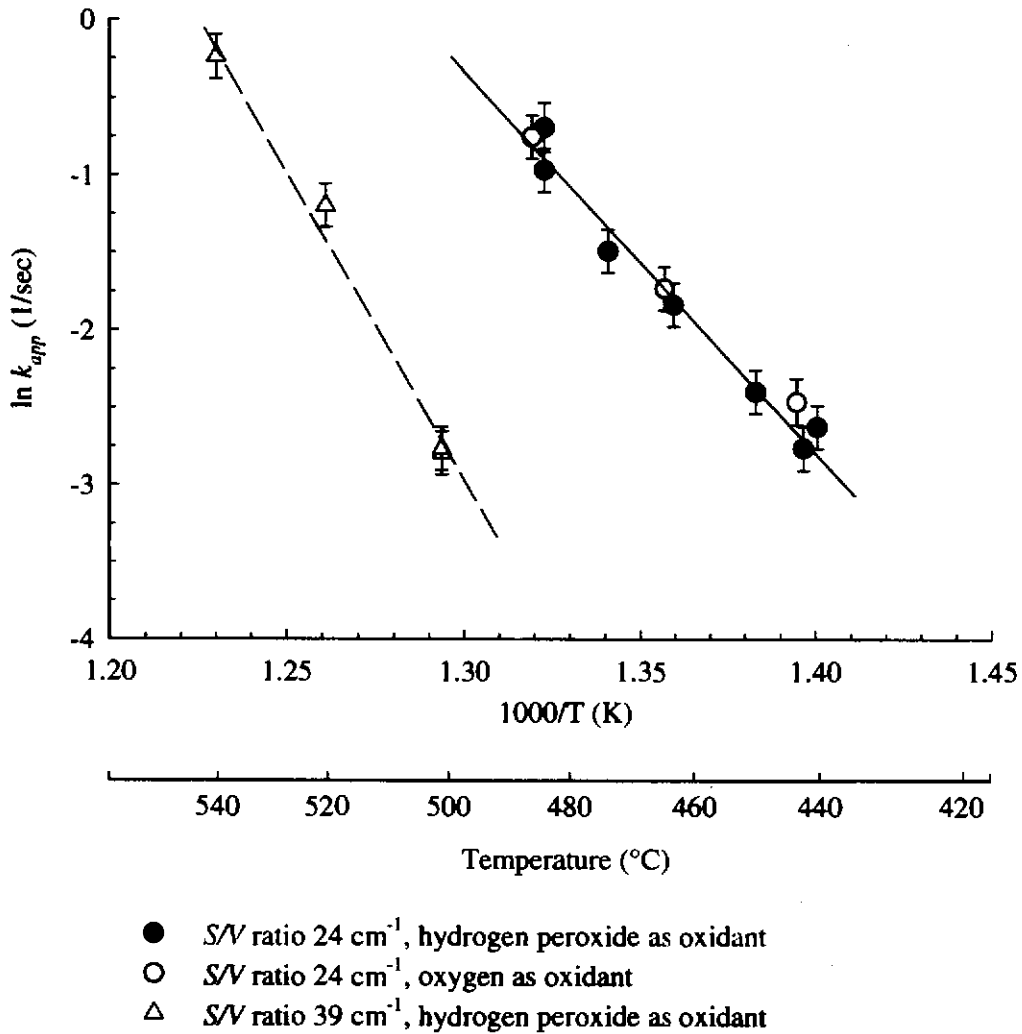


Figure 4.22

Comparison of apparent, first-order rate constants for methanol oxidation using two different surface-to-volume ratio reactors. Conditions: 246 bar, 7 seconds residence time, $\phi=0.67$, $[\text{MeOH}]_0=0.056 \text{ wt } \%$.

quenching at the wall of the reactor. Clearly, though, further investigation of this phenomenon is warranted and should be of great interest to the SCWO community. Chapter 7 provides additional details of proposed research along these lines.

Chapter 5:

Kinetic modeling of supercritical water oxidation

*“If a man will begin with certainties, he shall end in doubt,
but if he will be content to begin with doubts,
he shall end in certainties.”*

Francis Bacon (1605)

5.1 BACKGROUND AND MOTIVATION

As discussed in Section 1.3, interest in the SCWO process has led to the development of combustion chemistry models which describe supercritical water oxidation at the elementary reaction level. Past modeling efforts have yielded kinetic mechanisms describing the oxidation of simple fuels such as hydrogen (Holgate and Tester, 1993; Paterson *et. al.*, 1993; Holgate and Tester, 1994; Brock and Savage, 1995; Dagaut *et. al.*, 1995; Alkam *et. al.*, 1996), carbon monoxide (Holgate and Tester, 1994; Brock and Savage, 1995; Dagaut *et. al.*, 1995), methane (Webley and Tester, 1991; Brock and Savage, 1995; Dagaut *et. al.*, 1995) and methanol (Webley and Tester, 1989; Butler *et. al.*, 1991; Butler *et. al.*, 1991; Schmitt *et. al.*, 1991; Brock and Savage, 1995; Alkam *et. al.*, 1996; Dagaut *et. al.*, 1996). These mechanisms have been incorporated into one-dimensional, isobaric flow models with either isothermal or imposed axial temperature profiles, and the resulting plug-flow reactor models have been compared, with varying degrees of success, to experimentally-measured, stable species concentration profiles.

In the early stages of this research project, we intended to build upon past modeling efforts and extend the high-pressure modeling approach outlined in Section 1.3 to higher molecular weight hydrocarbons, heteroatom-containing compounds (*e.g.*, HD mustard), and, ultimately, mixtures. The resulting model predictions were then to be compared with laboratory data. This approach was abandoned in this research for several reasons. First, the

number of reactions required to describe the oxidation process at the elementary reaction level grows dramatically as the molecular weight and functional complexity of the molecule increase. Each new chemical species introduces three additional thermochemical parameters to the model and each new chemical reaction introduces one forward rate constant. This increase in mechanism size is illustrated in Table 5.1 which shows the number of reactions, chemical species, and parameters associated with the oxidation mechanisms of four relatively simple fuels.

TABLE 5.1
Size Comparison of Several Representative Low-Pressure Oxidation Mechanisms

Mechanism	Number of Elementary Reactions	Number of Chemical Species	Number of Kinetic and Thermochemical Parameters	Source
Hydrogen	19	8	43	(Yetter <i>et. al.</i> , 1991)
Carbon Monoxide	28	12	64	(Yetter <i>et. al.</i> , 1991)
Methanol	89	20	149	(Held, 1993)
Benzene	451	87	712	(Lindstedt and Skevis, 1994)

Modeling of large heteroatom-containing compounds is further complicated by the introduction of heteroatom thermochemistry and kinetics. Few, if any, experimental values exist for the thermodynamic and rate parameters of heteroatom-containing stable species and intermediates; nor are there particularly reliable means of estimating them. Because of the increase in complexity associated with modeling higher molecular weight compounds and the difficulty in extending the modeling approach to compounds of direct interest to SCWO waste destruction, a shift in modeling focus occurred. Rather than concentrating on parameter estimation, model development, and comparing model results to data, we focused on understanding the predictive capability of the existing oxidation models and their utility as design tools. Specifically, an interest developed in understanding how uncertainty in the model's kinetic and thermochemical parameters influenced the predicted species concentration profiles. This interest was motivated, in part, by the desire to identify the key

differences in the published SCWO mechanisms listed above and to understand how these differences affect model behavior. Another important question that arose at this stage was whether disagreements between model predictions and experimental data were a consequence of inadequate adaptation of combustion kinetics to SCWO conditions or were attributable to the uncertainties inherent in the model itself. The work in this chapter was motivated largely by the latter issue as well as by the general need to address the role that parametric uncertainty plays in modeling other coupled transport and reaction processes, such as atmospheric chemistry and combustion.

Uncertainty always exists in engineering models and systems because many of the model input quantities cannot be measured or calculated exactly. In SCWO and combustion modeling, some of the potential sources of uncertainty include reaction rate constants, species thermochemistry, initial conditions, and transport properties. The uncertainties in these quantities need to be explicitly addressed in the modeling process in order to determine their impact on the model outputs and to establish the likely limits to the predictive performance of the model. Uncertainty analysis provides the means to carry out this investigation and is comprised of two principal elements: sensitivity analysis and uncertainty propagation. Sensitivity analysis examines the dependence of model outputs to changes in model inputs and is routinely employed in the analysis of chemical kinetic mechanisms as a means of identifying dominant reaction rate parameters. Examples of uncertainty propagation in the chemical kinetic literature, however, are relatively rare. Its primary aim is the *computation* of the uncertainty in the model outputs induced by uncertainty or error in the model inputs. Uncertainty analysis also helps to identify the inputs which contribute the most to the uncertainty in the model predictions, highlighting those where a reduction in uncertainty would best improve the predictive capability of the model.

The atmospheric chemistry community has examined in some detail the role of uncertainty in coupled transport and reaction modeling. Gas-phase chemical mechanisms have been identified as one of the most important components in photochemical and air quality models, and it is recognized that uncertainties in these mechanisms can introduce significant

uncertainties into the calculated species concentrations (Gao *et. al*, 1996). Previous applications of uncertainty analysis in atmospheric modeling have employed Monte Carlo (MC) simulation with either simple or stratified sampling methods and have been applied to regional air quality models (Gao *et. al*, 1996), aerosol formation and growth (Raes *et. al*, 1992), and photochemical ozone models (Stolarski *et. al*, 1978; Ehhalt *et. al*, 1979; Derwent and Øystein, 1988). Alternative approximation methods have also been used to calculate the expected values and variances of response variables in atmospheric models (Atherton *et. al*, 1975).

In the Monte Carlo approach, each uncertain model parameter is treated as a random variable and assigned a suitable probability representation. Values are drawn from the probability distribution of each random variable and the coupled transport/kinetic model is solved to yield the complete time evolution of the response variables of interest (typically species concentrations). The solution process is repeated until stable statistics are achieved for the response distributions in the model. By necessity, the number of random variables in these studies is small due to the fact that the computational tractability of Monte Carlo methods is heavily dependent on the number of random variables, the complexity of the model, and the sampling method used. In cases where reaction mechanisms are coupled with detailed transport models, the number of random variables ranges from four (Raes *et. al*, 1992) to ten (Derwent and Øystein, 1988). Larger numbers of random variables have been incorporated into Monte Carlo simulations of complex reaction mechanisms, though usually at the expense of realistic transport modeling and through the use of sophisticated sampling techniques (Ehhalt *et. al*, 1979; Gao *et. al*, 1996). As an example, consider the work of Gao *et al.* (1996) who employed Latin-hypercube sampling to simulate a regional acid-deposition model with 59 uncertain rate parameters and 17 uncertain stoichiometric coefficients. Although the authors were successfully able to calculate the uncertainties in predicted species concentrations and identify the key controlling model parameters, they acknowledged that inclusion of this mechanism in a more comprehensive air quality model--taking detailed account of transport, mixing and surface removal, meteorology, and boundary and initial

conditions--would require a reduction of the number of uncertain parameters in the mechanism.

The remainder of this chapter is divided into two parts. In the first part, a new, computationally-efficient means of carrying out uncertainty propagation called the Deterministic Equivalent Modeling Method (DEMM) is introduced and compared to Monte Carlo simulation. The DEMM methodology was developed by Tatang (1995) for the propagation of parametric uncertainty in complex chemical and environmental systems. The second part of this chapter utilizes both DEMM and MC to investigate the effects of parametric uncertainty on a hydrogen oxidation mechanism adapted to SCWO conditions.

5.2 THEORETICAL TREATMENT OF SCWO KINETICS

As described in Section 1.3, the key assumptions made in modeling SCW oxidation kinetics are (1) that reactions at the conditions of interest (240-260 bar, 500-650 °C) can be treated as gas-phase, free-radical reactions and (2) that the water medium, which participates in reactions both as a reactant and as a third-body collider, does not interfere with reaction events through solvation effects. The free radical assumption is supported by evidence showing that the physical and transport properties of water above 500 °C and 250 bar (typical SCWO operating conditions) closely resemble those of a non-polar, dense gas (Holgate and Tester, 1993; Brock and Savage, 1995; Dagaut *et. al*, 1995; Dagaut *et. al*, 1996). At typical reaction conditions for commercial SCWO applications, densities range from 0.07 to 0.1 g/cm³ and the viscosity of the reaction medium is about a factor of 25 lower than at ambient conditions (Kestin and Sengers, 1986; Sengers and Watson, 1986). In addition, the static dielectric constant at 250 bar decreases from its room temperature value of 78 to a value of 1 to 2 at 500 °C (Uematsu and Franck, 1980). As a consequence the ion product of water at 250 bar decreases with increasing temperature from its subcritical value of 10⁻¹⁴ to approximately 10⁻²³ in the range of 723-873 K (Marshall and Franck, 1981) indicating that water only weakly dissociates and poorly solvates ions in its supercritical state. While the free-radical assumption is well supported circumstantially by this experimental evidence and by experimentally-obtained product spectra, direct experimental verification is still necessary to justify the

assumption that water does not act as a solvent by influencing individual reaction events. This information is likely to come from spectroscopic work involving flash photolysis of compounds that are well understood in the gas phase. To date, these efforts have been confined to the dense, sub-critical region and have not been successfully extended to the more commercially relevant, low-density supercritical regime.

As discussed in Section 1.3, the adaptation of combustion mechanisms to the much higher pressures and relatively low temperatures of the SCWO process typically involves two modifications. The first is the proper treatment of the pressure-dependence/fall-off behavior of unimolecular and recombination reactions. The second modification is the inclusion of nonideal or real-gas effects in the calculation of the reverse rate constant (Melius *et. al.*, 1990; Butler *et. al.*, 1991; Butler *et. al.*, 1991; Schmitt *et. al.*, 1993; Alkam *et. al.*, 1996). As mentioned in the introduction, this modification requires estimation of the mixture compressibility factor and the mixture fugacity coefficients for all species in the reaction medium and is typically carried out with a classical thermodynamic (*PVTN*) equation of state (Tester and Modell, 1997). However, an accurate thermodynamic description of the multi-component, supercritical reaction medium requires data to specify the pure-component and interaction parameters for stable *and* unstable species. Given the limited mixture data available for stable species in supercritical water and the complete absence of such data for unstable, free-radical intermediates, accounting for solution-phase non-idealities via a classical equation of state is a questionable practice. In principle, critical parameters for unstable, free-radical intermediates and binary interaction parameters for stable and unstable species are needed. In practice, pure component radical species critical properties are estimated using group contribution methods, while binary interaction parameters are frequently set to zero because of the lack of data available for estimating them.

Accepting the inherent and systematic uncertainties introduced by the basic SCWO modeling assumptions, this chapter is concerned with exploring the additional uncertainty arising from the kinetic mechanism parameters themselves, *i.e.*, the reaction rate constants and species thermochemistry. In many cases, the uncertainty in rate constants and the

thermochemistry can be quite large, with many rate constant values known only to within a factor of two to three. In addition, the values of important thermochemical parameters, most notably standard-state heats of formation, are continually being updated to reflect recent experimental and computational efforts to improve the accuracy of their reported values.

5.3 APPLICATION OF UNCERTAINTY ANALYSIS TO KINETIC MODELING

In this work, the forward rate constants, $k_{f,j}$'s, and species standard-state heats of formation, $\Delta H_{f,i}^{\circ}$'s, were treated as random variables and were assumed to be the sole sources of uncertainty in the kinetic mechanism. The standard-state heat capacities and entropies, initial concentrations, and all remaining model parameters and inputs were treated as deterministic ("exact") quantities. The standard-state condition for all species was taken to be that of an ideal gas at 298.15 K and 1 bar. Each forward rate constant was assigned a log-normal probability distribution, thereby limiting $k_{f,j}$ to positive values, and was parameterized by a median value, computed from the parameters in Table 5.2, and a multiplicative uncertainty factor, UF_j . The uncertainty factors were either drawn from Baulch *et al.* (1992) or estimated from other literature sources. This simple parameterization procedure was chosen because the available kinetic data for the majority of elementary reactions rarely warrant the assignment of a sophisticated, data-based probability distribution. If sufficient data were available to construct an empirically-based probability distribution, the resulting rate constant distribution could readily be incorporated into the analysis. Using the log-normal formalism, the bounds on a given rate constant can be defined in terms of its median value and uncertainty factor, where the upper bound is given by:

$$\text{Median}(k_{f,j}) \times UF_j \quad (5.1)$$

and the lower bound by:

$$\text{Median}(k_{f,j}) + UF_j \quad (5.2)$$

The upper and lower bounds were interpreted as encompassing 95% of all possible values of the rate constant. The consequences of this interpretation and its impact on the uncertainty in the model outputs are discussed in Section 5.5.

TABLE 5.2
Chemical Kinetic Mechanism for the High-Pressure Oxidation of Hydrogen^a

No	Elementary Reaction		A^b	n	E_a/R	Ref
1	OH + H	\leftrightarrow H ₂ O	1.620E+14	0	75	(Cobos and Troe, 1985)
2	H ₂ + OH	\leftrightarrow H ₂ O + H	1.024E+08	1.6	1660	(Baulch <i>et. al.</i> , 1992)
3	H + O ₂	\leftrightarrow HO ₂	1.481E+12	0.6	0	(Atkinson <i>et. al.</i> , 1989)
4	HO ₂ + HO ₂	\leftrightarrow H ₂ O ₂ + O ₂	1.867E+12	0	775	(Baulch <i>et. al.</i> , 1992)
5	H ₂ O ₂ + OH	\leftrightarrow H ₂ O + HO ₂	7.829E+12	0	670	(Baulch <i>et. al.</i> , 1992)
6	H ₂ O ₂ + H	\leftrightarrow HO ₂ + H ₂	1.686E+12	0	1890	(Baulch <i>et. al.</i> , 1992)
7	H ₂ O ₂	\leftrightarrow OH + OH	3.000E+14	0	24400	(Baulch <i>et. al.</i> , 1992)
8	OH + HO ₂	\leftrightarrow H ₂ O + O ₂	2.891E+13	0	-250	(Baulch <i>et. al.</i> , 1992)
9	H + O ₂	\leftrightarrow OH + O	1.990E+14	0	8460	(Baulch <i>et. al.</i> , 1992)
10	O + H ₂	\leftrightarrow OH + H	5.126E+04	2.67	3160	(Baulch <i>et. al.</i> , 1992)
11	OH + OH	\leftrightarrow O + H ₂ O	1.504E+09	0	50	(Baulch <i>et. al.</i> , 1992)
12	H ₂ + M	\leftrightarrow H + H + M	2.230E+14	0	48350	(Tsang and Hampson, 1986)
13	H + HO ₂	\leftrightarrow OH + OH	1.690E+14	0	440	(Baulch <i>et. al.</i> , 1992)
14	H + HO ₂	\leftrightarrow H ₂ + O ₂	4.280E+13	0	710	(Baulch <i>et. al.</i> , 1992)
15	O + HO ₂	\leftrightarrow OH + O ₂	3.250E+13	0	0	(Baulch <i>et. al.</i> , 1992)
16	H ₂ O ₂ + H	\leftrightarrow H ₂ O + OH	1.020E+13	0	1800	(Baulch <i>et. al.</i> , 1992)
17	O + H + M	\leftrightarrow OH + M	4.708E+18	-1	0	(Tsang and Hampson, 1986)
18	O + O + M	\leftrightarrow O ₂ + M	1.890E+13	0	-900	(Tsang and Hampson, 1986)
19	H ₂ O ₂ + O	\leftrightarrow OH + HO ₂	6.620E+11	0	2000	(Baulch <i>et. al.</i> , 1992)

The standard-state heats of formation, $\Delta H_{f,i}^o$, for each species were assigned normal (Gaussian) probability distributions and were parameterized by their mean values and standard deviations. The standard deviations were estimated based on reported experimental error limits (Shum and Benson, 1983; Chase *et. al.*, 1985; Kee *et. al.*, 1988; Fisher and Armentrout, 1990; DeMore *et. al.*, 1992; Bauschlicher and Partridge, 1993; Leung and Lindstedt, 1995) and are shown, along with their mean values, in Table 5.3. While not the only possible choice, the selection of normally-distributed $\Delta H_{f,i}^o$'s naturally leads to reverse rate constants which, like their forward counterparts, are log-normally distributed. This is evident from the equation relating the forward and reverse rate constants to the concentration-based equilibrium constant $K_{c,j}$:

$$k_{r,j} = k_{f,j} K_{c,j}^{-1} \quad (5.3)$$

$K_{c,j}$, in turn, is related to the activity-based equilibrium constant, $K_{a,j}$, by:

$$K_{c,j}^{-1} = K_{a,j}^{-1} \left[\frac{ZRT}{f_i^o} \right]^{\sum_i \nu_{i,j}} \prod_i \hat{\phi}_i^{\nu_{i,j}} \quad (5.4)$$

where $K_{a,j}$ can be expressed in terms of the standard-state Gibbs-free-energy change for reaction j :

$$\ln K_{a,j} = \frac{-\Delta G_{rx,j}^o(T)}{RT} \quad (5.5)$$

Substitution of Eq. (5.5) into Eq. (5.4) yields the following expression for $K_{c,j}^{-1}$:

$$K_{c,j}^{-1} = \exp(\Delta G_{rx,j}^o(T) / RT) \left[\frac{ZRT}{f_i^o} \right]^{\sum_i \nu_{i,j}} \prod_i \hat{\phi}_i^{\nu_{i,j}} \quad (5.6)$$

The relationship between $\Delta G_{rx,j}^o$ and the individual species thermochemical parameters is given by the integrated form of the Gibbs-Helmholtz equation (Tester and Modell, 1997). Inspection of the equation reveals that $\Delta G_{rx,j}^o$ is linearly dependent on the species standard-state heats of formation:

TABLE 5.3
Mean Values and Standard Deviations for Species Standard-State^a
Enthalpies of Formation ΔH_f° in kcal/mol

	H ^d	O ^d	OH ^d	H ₂ O ^d	H ₂ O ₂ ^d	HO ₂ ^e
μ^b	52.10	59.56	9.3	-57.80	-32.53	3.0
$2\sigma^c$	0.01	0.02	0.2	0.01	0.07	0.5

^aStandard state: ideal gas at 1 bar, 298.15 K

^b μ =mean

^c σ =standard deviation

^d(Kee *et. al.*, 1988)

^eEstimate based on evaluation of recently reported values from (Benson *et. al.*, 1979; Chase *et. al.*, 1985; Kee *et. al.*, 1988; Fisher and Armentrout, 1990; Bauschlicher and Partridge, 1993; Leung and Lindstedt, 1995).

TABLE 5.4
Reduced High-Pressure Hydrogen Oxidation Mechanism
with Reported Uncertainty Factors

No.	Elementary Reaction	UF^a
1	<i>Initiation</i> OH + H \leftrightarrow H ₂ O	3.16 ^b
2	<i>Propagation</i> H ₂ + OH \leftrightarrow H ₂ O + H	1.26 ^c
3	H + O ₂ \leftrightarrow HO ₂	1.58 ^d
4	HO ₂ + HO ₂ \leftrightarrow H ₂ O ₂ + O ₂	1.41 ^c
5	H ₂ O ₂ + OH \leftrightarrow H ₂ O + HO ₂	1.58 ^c
6	H ₂ O ₂ + H \leftrightarrow HO ₂ + H ₂	2.00 ^c
7	H ₂ O ₂ \leftrightarrow OH + OH	3.16 ^c
8	<i>Termination</i> OH + HO ₂ \leftrightarrow H ₂ O + O ₂	3.16 ^c

^a UF =multiplicative uncertainty factor (see Eqtns (5.1) and (5.2) for definition).

^bEstimated.

^c(Baulch *et. al.*, 1992)

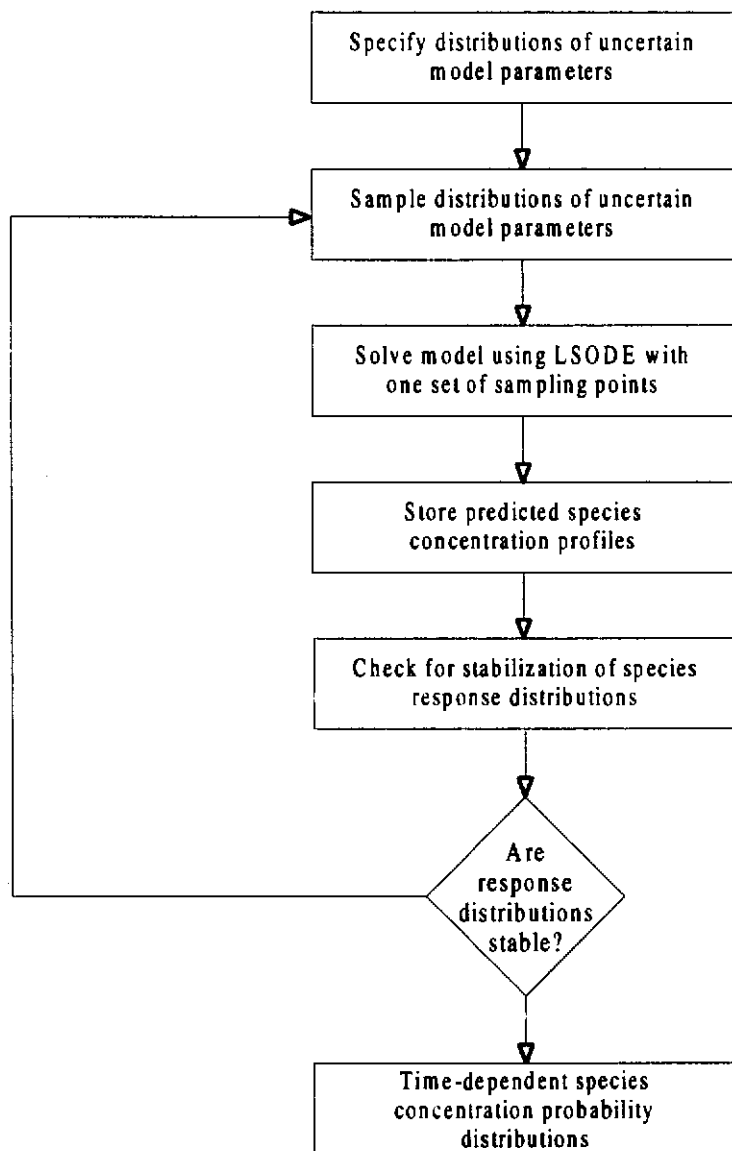
^d(Atkinson *et. al.*, 1989)

$$\Delta G_{rx,j}^{\circ}(T) = \sum_i v_{i,j} \Delta H_{f,i}^{\circ}(T^{\circ}) - T \sum_i v_{i,j} S_i^{\circ}(T^{\circ}) - \int_{T^{\circ}}^T \frac{1}{T^2} \left\{ \int_{T^{\circ}}^T \sum_i C_{p,i}^{\circ} dT \right\} dT \quad (5.7)$$

Since $\Delta G_{rx,j}^{\circ}$ is a linear function of the independent, normally-distributed $\Delta H_{f,i}^{\circ}$'s, it is also normally distributed. By definition, the corresponding inverse equilibrium constant, $K_{c,j}^{-1}$, is log-normally distributed because of its exponential dependence on $\Delta G_{rx,j}^{\circ}$. As shown by Eq. (5.3), the reverse rate constant is then a product of two independent, log-normally distributed random variables ($K_{c,j}^{-1}$ and k_{fj}) and, therefore, is log-normal as well. Thus, the selection of normal $\Delta H_{f,i}^{\circ}$'s and log-normal k_{fj} 's naturally leads to a self-consistent form of the probability representation for the reverse rate constants.

The uncertainty analysis was carried out using the two solution methodologies mentioned previously. The first was a straightforward Monte Carlo simulation employing pseudo-random sampling. The second was the Deterministic Equivalent Modeling Method (DEMM). Using the two procedures to perform the same uncertainty analysis serves to illustrate the features of each method and to demonstrate the computational advantage of DEMM, particularly when applied to larger kinetic mechanisms. The isothermal, tubular reactor modeled in this study was assumed to be well approximated by the plug-flow idealization. As a result, the governing species conservation equations reduce to a set of coupled, nonlinear, first-order, ordinary differential equations. Both solution methods employed the deterministic stiff ODE solver LSODE (Hindmarsh, 1983) for the solution of these equations.

Figure 5.1 outlines the approach used for the Monte Carlo simulation. For each run, the log-normal distributions of the k_{fj} 's and $K_{c,j}^{-1}$'s are sampled randomly, the k_{rj} 's are calculated as the product of the sampled k_{fj} 's and $K_{c,j}^{-1}$'s, and the resulting set of rate constants are passed to LSODE for solution of the species conservation equations. The predicted species concentrations and their associated residence times are then stored, and the sampling and solution process is repeated until the response distributions are statistically stable. At the end

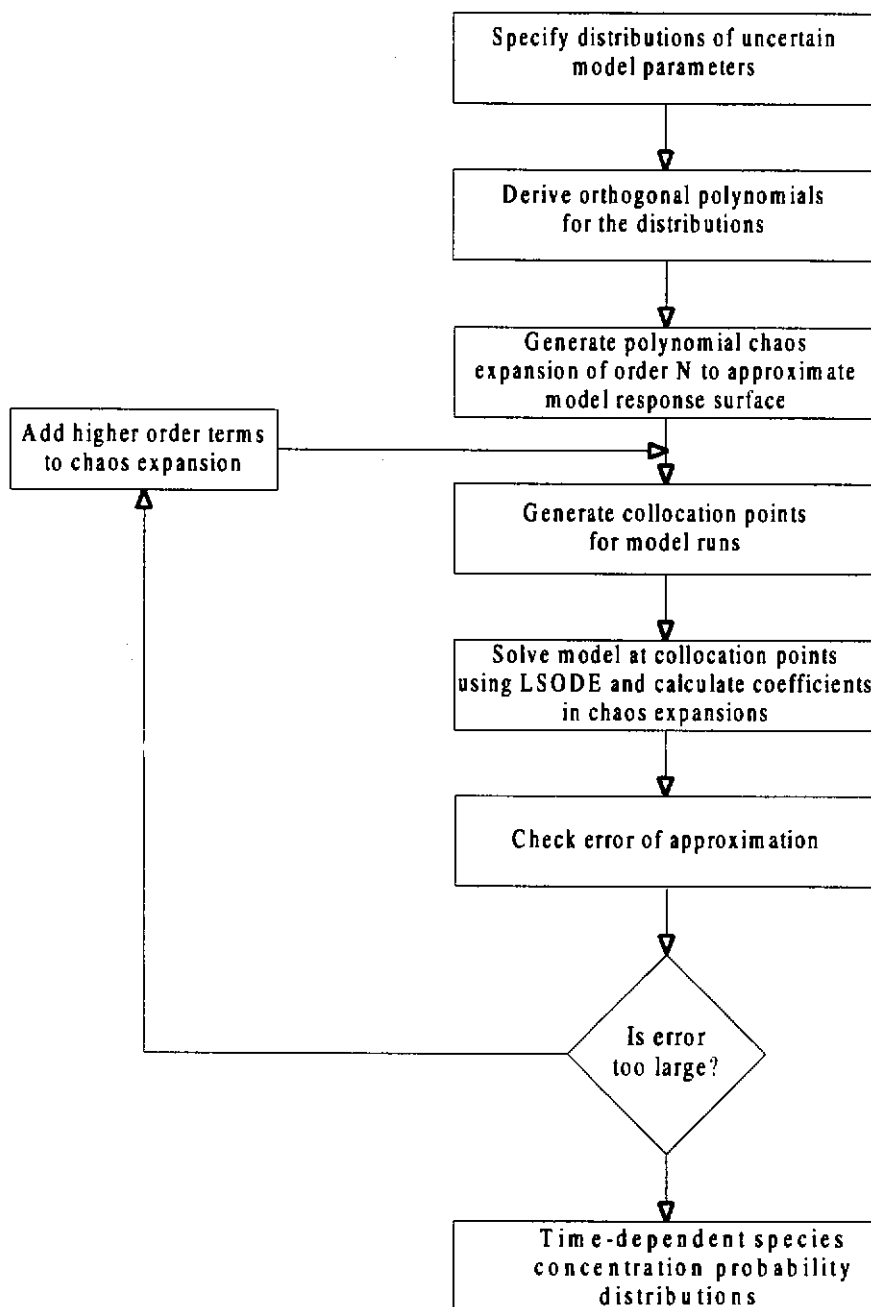
**FIGURE 5.1**

Flowsheet illustrating the computational steps used in the Monte Carlo simulation of the reduced hydrogen oxidation mechanism of Table 5.4. The FORTRAN code for the simulation is provided in Appendix 8.6.

of the sampling/solution process, the individual response distributions at each point in time are sorted and analyzed to determine their means, medians, and upper and lower 2.5% tail regions. For the hydrogen oxidation mechanism shown in Table 5.4 with 16 random variables, 15,000 sampling points were sufficient to achieve stable response statistics.

Even when sophisticated sampling techniques are used, Monte Carlo methods can become computationally intractable for complex models with large numbers of random variables. DEMM provides an attractive alternative approach to Monte Carlo simulation by reducing the number of model solutions needed to establish the probability distributions of the response variables. The basic concept of the DEMM methodology is to approximate the response variables of the model as probabilistically-weighted polynomial functions of the uncertain model parameters. DEMM relies on the direct representation of parametric uncertainty via polynomial chaos expansions and utilizes orthogonal collocation to calculate the response distributions of the model outputs. For the uncertainty analysis presented in this paper, second-order polynomials were sufficient to adequately approximate the species response distributions in the model. The number collocation points needed to calculate the response distributions is a function of the number of random variables and the number of terms used in the polynomial chaos expansions (the order of the approximation). In this case, with 16 random variables and a second order approximation, 153 collocation points, and therefore 153 calls to the LSODE solver, were needed to generate the desired response distributions. A summary of the key steps in the DEMM solution process is shown in Figure 5.2. For a detailed discussion of the DEMM methodology and examples of its application in air quality and atmospheric modeling see Tatang (1995).

Two key features of the DEMM methodology are the use of symbolic manipulation and compiler technology, and the ability to solve models with uncertainties using the same algorithms employed for the corresponding deterministic problems. Like Monte Carlo, DEMM has the capability to predict the time evolution of the probability distributions of each species in the mechanism. DEMM also provides a systematic means of identifying the

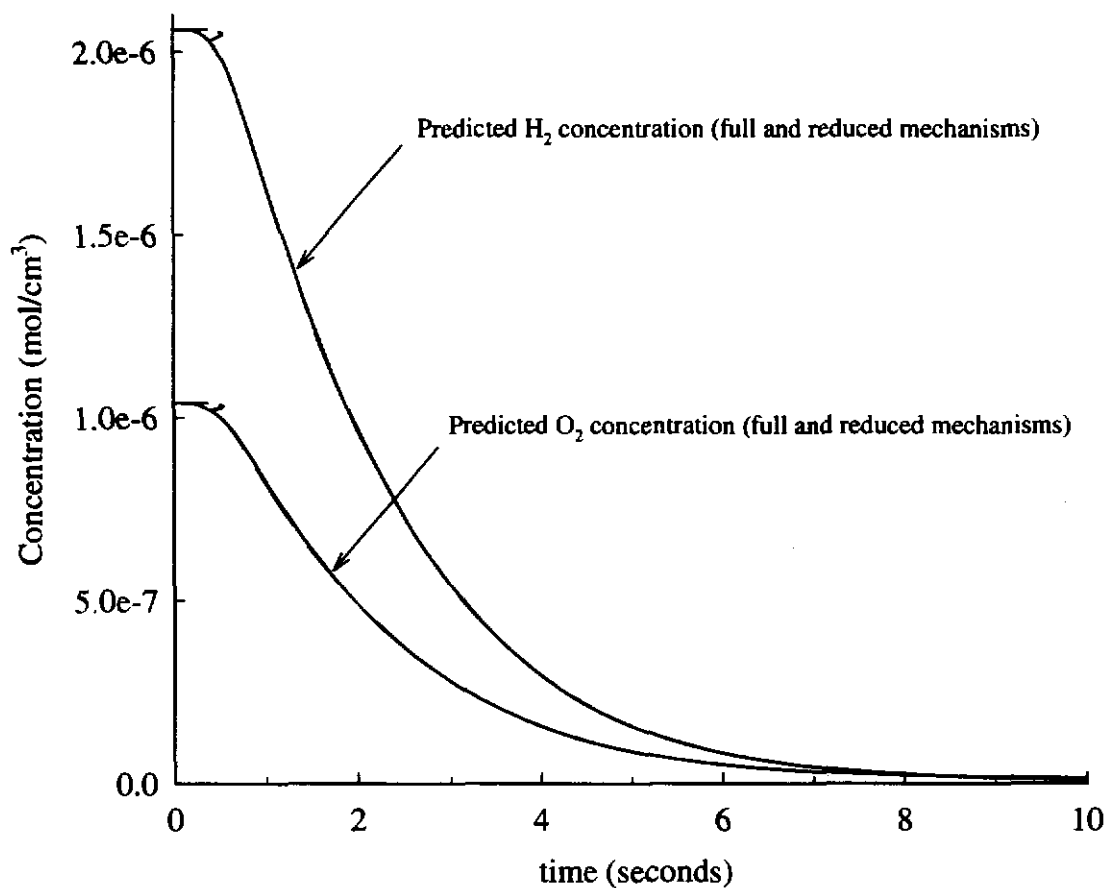
**FIGURE 5.2**

Flowsheet illustrating the computational steps used in the Deterministically Equivalent Modeling Method (DEMM) analysis of the reduced hydrogen oxidation mechanism of Table 5.4.

variables to which the model output is most sensitive, highlighting those where a reduction in uncertainty would best improve the predictive performance of the model. As will be demonstrated, DEMM also offers the advantage of a significant decrease in the computational time required to solve the model--often two to three orders of magnitude--while closely approximating the results from a full Monte Carlo simulation.

5.4 MODELING RESULTS

The hydrogen oxidation mechanism of Yetter *et al.* (1991) was used with rate constants updated, where applicable, from recent literature sources (Cobos and Troe, 1985; Tsang and Hampson, 1986; Atkinson *et al.*, 1989; Yetter *et al.*, 1991; Baulch *et al.*, 1992). This is the same mechanism originally used by Holgate and Tester (1993) to model the supercritical water oxidation of hydrogen. Species thermochemical data were taken from the CHEMKIN database (Kee *et al.*, 1988), except for the standard-state heat of formation for HO₂ radical which was updated from the JANAF value of 0.5 kcal/mol to 3.0 kcal/mol (Shum and Benson, 1983; Fisher and Armentrout, 1990; DeMore *et al.*, 1992; Bauschlicher and Partridge, 1993; Leung and Lindstedt, 1995). The full high-pressure, hydrogen oxidation mechanism was reduced by a combined first-order sensitivity/uncertainty and reaction path analysis before carrying out the uncertainty study. As shown in Figure 5.3, the resulting reduced mechanism (Table 5.4) predicts species concentration profiles identical to those of the full model. With their emphasis on HO₂ and H₂O₂ chemistry, both the full and reduced mechanisms are similar to the low-temperature (850-1200K), high-pressure (1-15.7 atm) hydrogen oxidation mechanism developed by Kim (1994). In terms of dealing with potential nonideal solution effects, the mixture compressibility factor, Z , was set to its pure water value (at reaction T and P) due to the dilute nature of the reaction medium. Mixture fugacity coefficients, $\hat{\phi}_i$, were set equal to unity. As will be shown in the discussion section, the magnitude of the real-gas correction to the model predictions through the inclusion of the mixture compressibility factor and mixture fugacity coefficients is minor compared to the parametric uncertainty present in the mechanism itself.

**FIGURE 5.3**

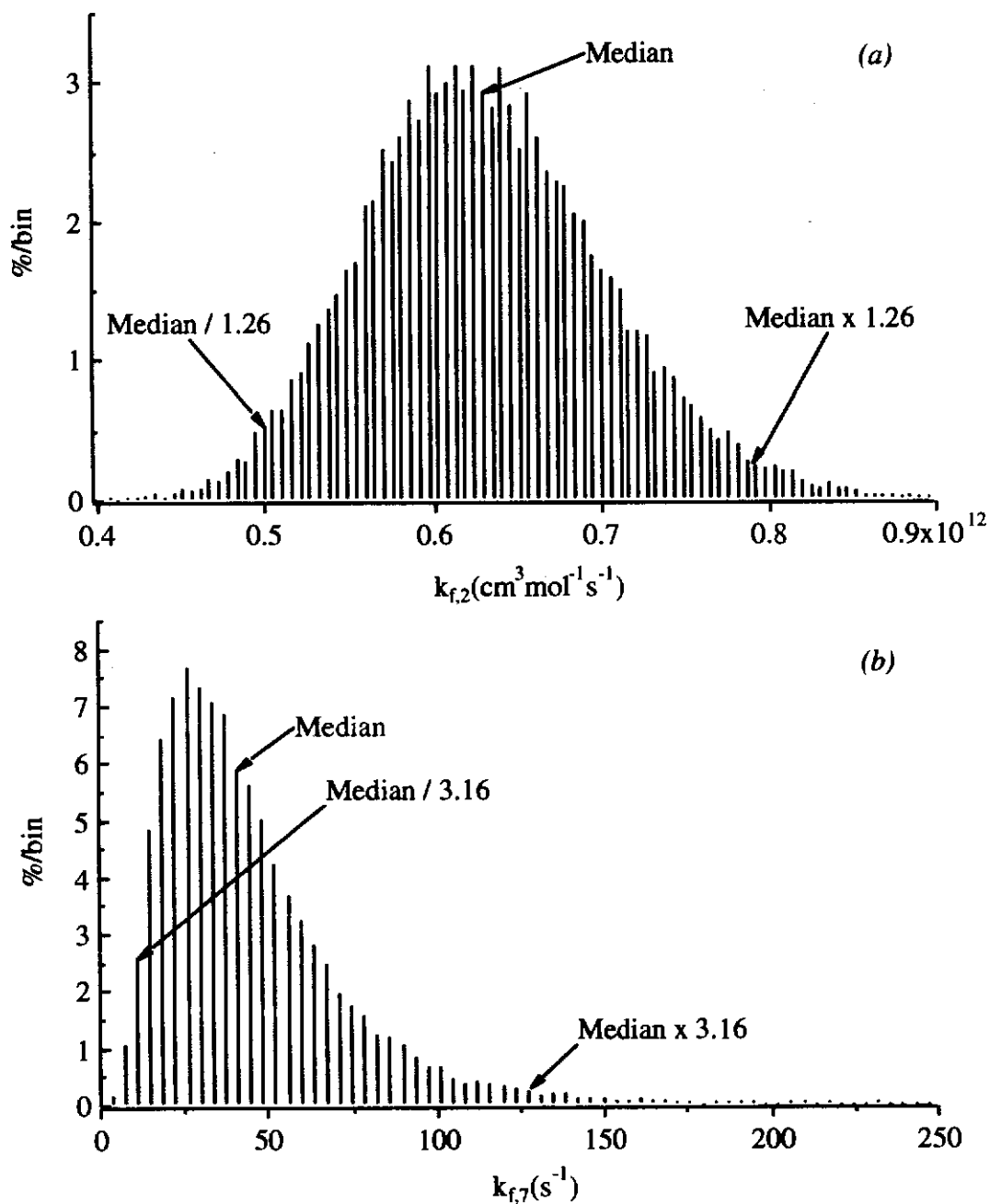
Comparison of predicted H₂ and O₂ species concentrations from the full (Table 5.2) and reduced (Table 5.4) reaction mechanisms. Reaction conditions: $T= 550\text{ }^{\circ}\text{C}$, $P= 246\text{ bar}$, $[\text{H}_2]_0= 2.06 \times 10^{-6}$, $[\text{O}_2]_0= 1.04 \times 10^{-6}$, $[\text{H}_2\text{O}]_0= 4.218 \times 10^{-3}\text{ mol/cm}^3$.

5.5 DISCUSSION OF MODELING RESULTS

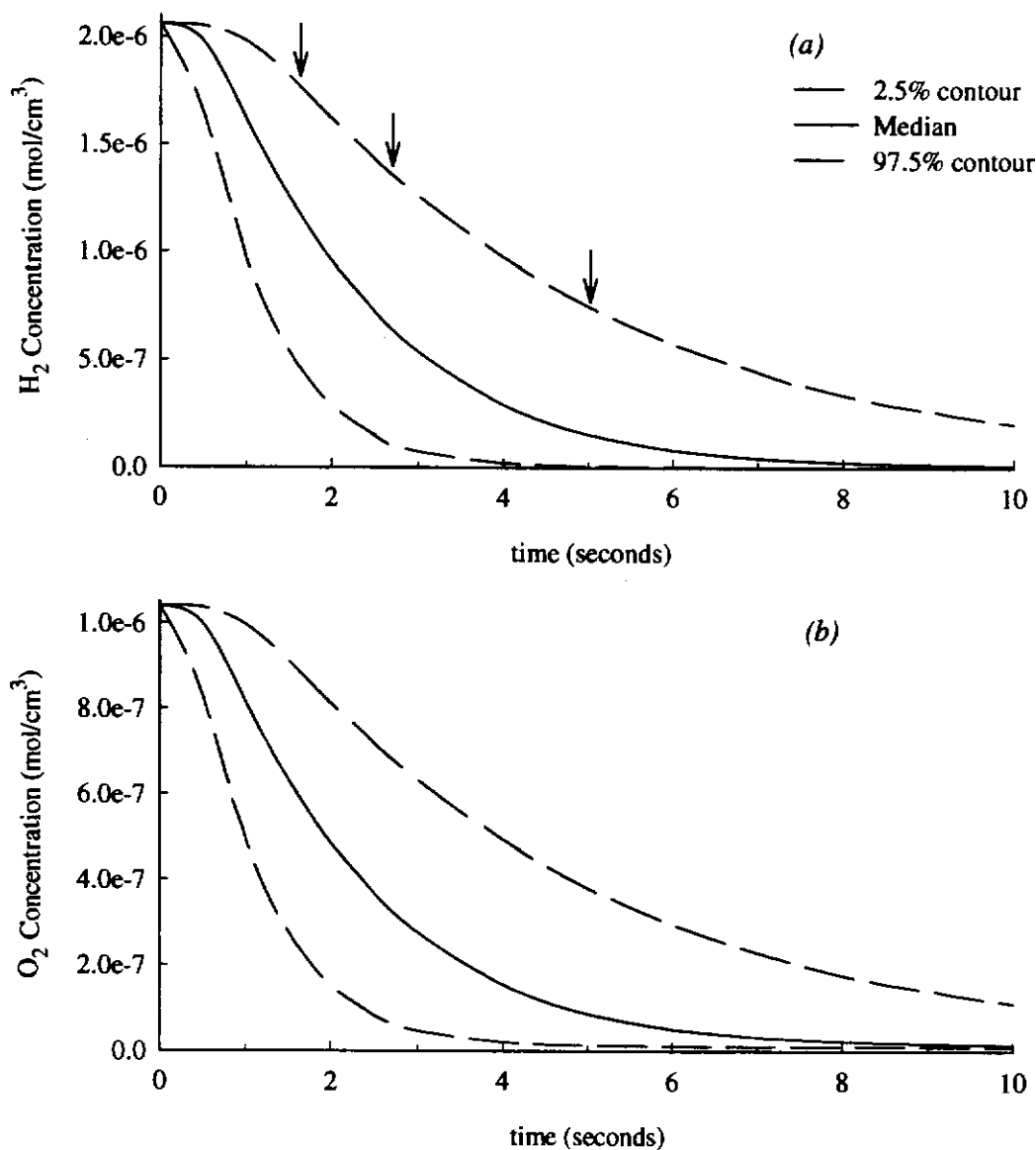
Figure 5.4 shows the sampled distributions of two representative forward rate constants used in the Monte Carlo simulation of the H₂ oxidation mechanism. Both histograms are the result of 15,000 pseudo-random sampling points and serve to demonstrate that the sampled distributions are representative of the parameterized log-normal distributions from which they were drawn (Table 5.4). The x-axes of the histograms display the range of sampled values for each rate constant, while the y-axis shows the percentage of the runs in which each value was used. Also indicated on each diagram are the upper and lower uncertainty bounds as defined by Eqs. (5.1) and (5.2). As intended, 95% of the sampled values of each rate constant lie within these bounds.

Both Monte Carlo and DEMM methods were applied to the reduced hydrogen oxidation model. Both methods predict nearly identical median species concentrations and time-dependent probability distributions. Figure 5.5 shows the predicted median concentrations for the species H₂, O₂, H₂O₂, and HO₂, over a simulated ten-second reaction time interval. The median concentration, or the 50% probability contour, represents the species concentration above and below which fifty percent of the model predictions lie. Also shown in each panel of Fig. 5.5 are the MC-derived upper 97.5% and lower 2.5% probability contours of the species concentration distributions. The probability contours predicted by DEMM are virtually identical to those predicted by MC, but are not shown to simplify the figure. Ninety-five percent of the model predictions lie within the shaded area bounded by the 97.5% and 2.5% probability contours, with 2.5% lying above and below these bounds.

Figure 5.5 shows that the uncertainty in each predicted species concentration is not constant but varies with time. At the start of the reaction, there is no uncertainty in the predicted concentrations since the initial concentrations of all species were treated as deterministic quantities. As the reaction proceeds, the uncertainty in each species concentration increases and reaches a maximum at approximately 2 seconds. At these maxima, the uncertainties in the predicted species distributions are quite large. The upper and lower 2.5%

**FIGURE 5.4**

Sampled log-normal forward rate constant distributions for the reaction: $\text{H}_2 + \text{OH} = \text{H}_2\text{O} + \text{H}$ (a), and $\text{H}_2\text{O}_2 = 2\text{OH}$ (b), based on the median values and uncertainty factors presented in Tables 5.2 and 5.4. The upper and lower bounds indicated on both panels are calculated by Equations (5.1) and (5.2), respectively.

**FIGURE 5.5**

H₂ (a) and O₂ (b) concentration probability distributions as a function of time resulting from Monte Carlo simulation of the reduced hydrogen oxidation mechanism given in Table 5.4 with 15,000 pseudo-random sampling points. Reaction conditions: $T= 550\text{ }^{\circ}\text{C}$, $P= 246\text{ bar}$, $[\text{H}_2]_0= 2.06\times 10^{-6}$, $[\text{O}_2]_0= 1.04\times 10^{-6}$, $[\text{H}_2\text{O}]_0=4.218\times 10^{-3}\text{ mol/cm}^3$. Solid lines represent the median values of the probability distributions while the upper and lower dashed lines represent the 2.5% and 97.5% probability contours. The arrows in panel (a) indicate the times of the three cross-sections of the hydrogen concentration probability distribution shown in Figure 5.6.

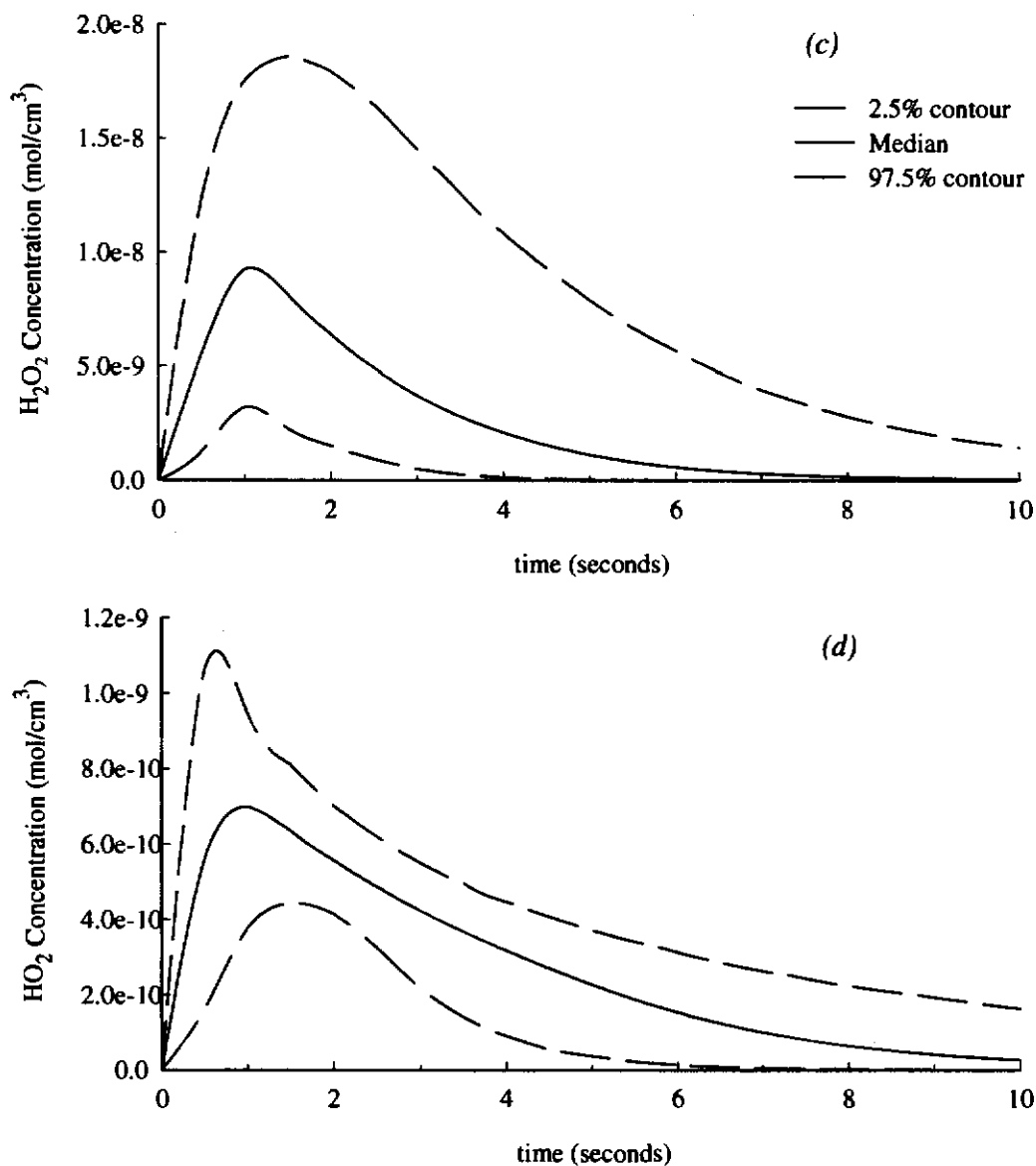


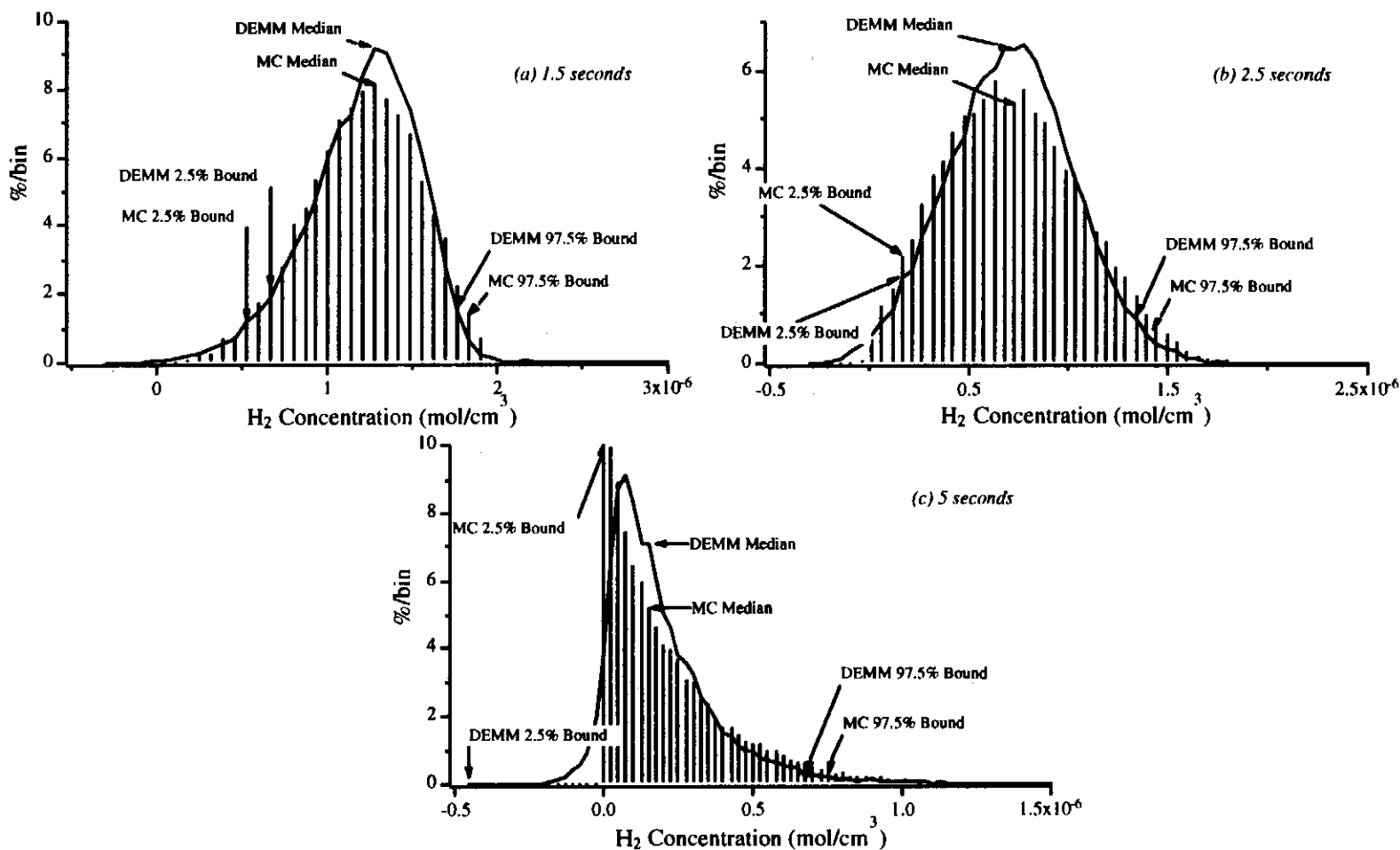
FIGURE 5.5, continued.

H₂O₂ (c) and HO₂ (d) concentration probability distributions as a function of time resulting from Monte Carlo simulation of the reduced hydrogen oxidation mechanism given in Table 5.4 with 15,000 pseudo-random sampling points. Reaction conditions: $T=550\text{ }^{\circ}\text{C}$, $P=246\text{ bar}$, $[\text{H}_2]_0=2.06\times 10^{-6}$, $[\text{O}_2]_0=1.04\times 10^{-6}$, $[\text{H}_2\text{O}]_0=4.218\times 10^{-3}\text{ mol/cm}^3$. Solid lines represent the median values of the probability distributions while the upper and lower dashed lines represent the 2.5% and 97.5% probability contours.

bounds for the H_2 and O_2 concentrations vary by $\pm 70\%$ from their median values. More dramatically, the predicted HO_2 and H_2O_2 concentrations vary by $+90\%$ to -70% and $+180\%$ to -80% from their respective medians. Past the 2 second mark, the uncertainty in all species concentrations decreases and eventually goes to zero since the model, with virtually any probable combination of rate constants, predicts the completion of the reaction at long residence times. The shape of the concentration probability distributions can also be deduced from Fig. 5.5. For example, with increasing time the $[H_2]$ probability distribution shifts from being skewed downwards to being skewed upwards. This shift is seen more clearly in Fig. 5.6 which shows the $[H_2]$ probability distribution at three points in time: 1.5; 2.5; and 5.0 seconds. These times are indicated by the arrows in Fig. 5.5a. The vertical lines are the response histograms generated by MC simulation while the solid lines represent the DEMM approximation to the response using the same set of sampling points. Both methods show that with increasing time the probability distribution shifts from being skewed to the right at 1.5 seconds, to an almost normal distribution at 2.5 seconds and finally skewed to the left at times greater than 5 seconds.

Figure 5.6 also serves to illustrate the remarkable agreement between the two methods. The agreement between MC and DEMM could be improved by increasing the order of the polynomials beyond the second-order approximation used in this study. However, as is evident from the comparison, the use of the second-order polynomial already shows excellent agreement with the MC results and produces nearly identical median and 2.5% and 97.5% probability contour predictions as MC in a fraction of the time required to perform the MC simulation. More remarkably, for the 8 reversible reaction mechanism shown in Table 5.3, DEMM required 153 calls to the LSODE solver routine, compared with 15,000 for the Monte Carlo simulation--resulting in approximately a 100-fold reduction in the computational time required to carry out the analysis.

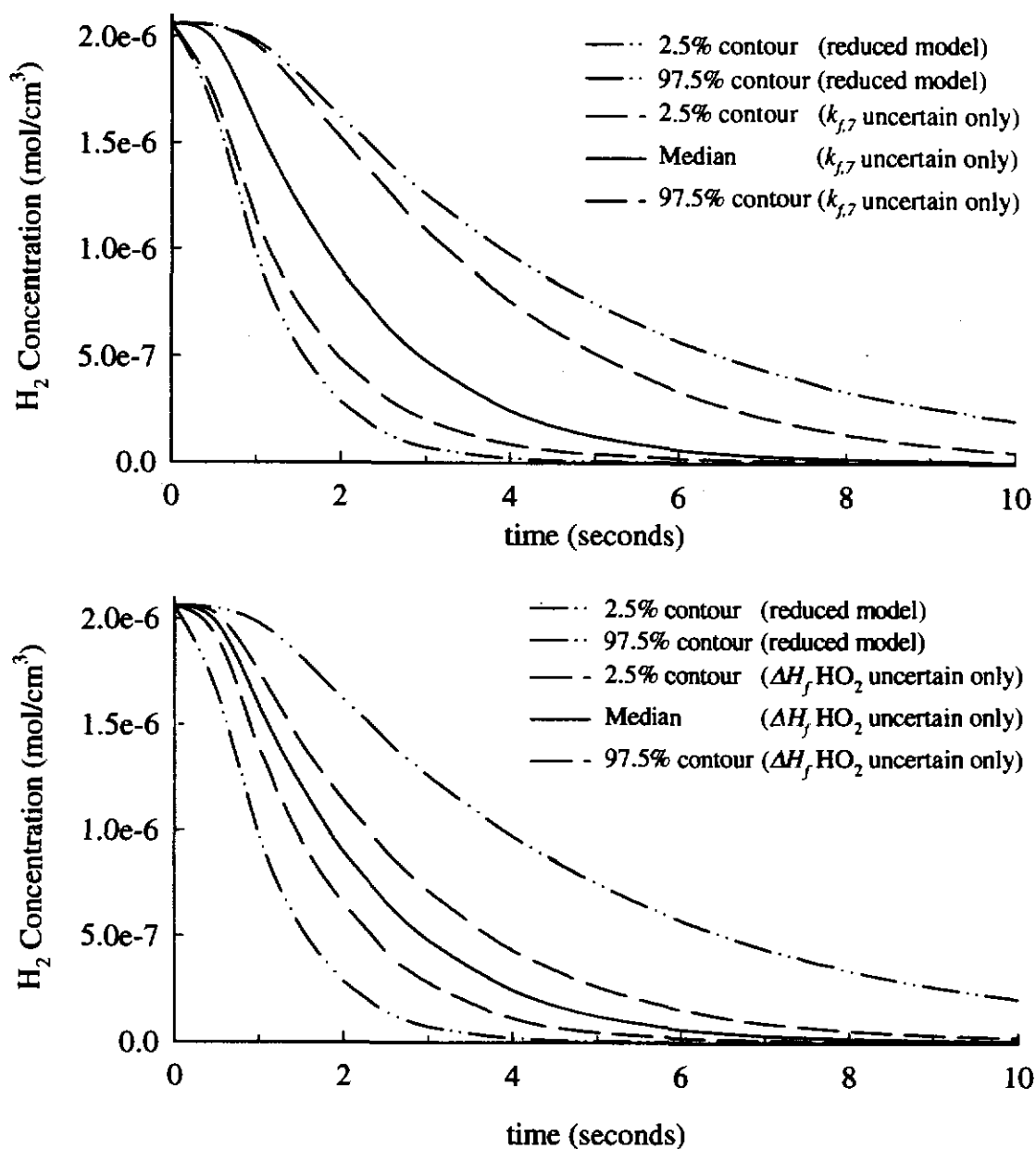
Figures 5.5 and 5.6 also demonstrate that significant uncertainty exists in the predicted species concentrations for even the relatively simple hydrogen oxidation mechanism

**FIGURE 5.6**

Hydrogen concentration probability distribution at the three points in time, 1.5 (a); 2.5 (b), and 5.0 (c) seconds indicated by the arrows in Figure 5.5a. Reaction conditions are the same as in Figure 5.5. Vertical lines represent the empirical distributions resulting from Monte Carlo simulation with 15,000 pseudo-random sampling points: solid lines are the polynomial approximations of the distributions obtained via DEMM using the same 15,000 sampling points.

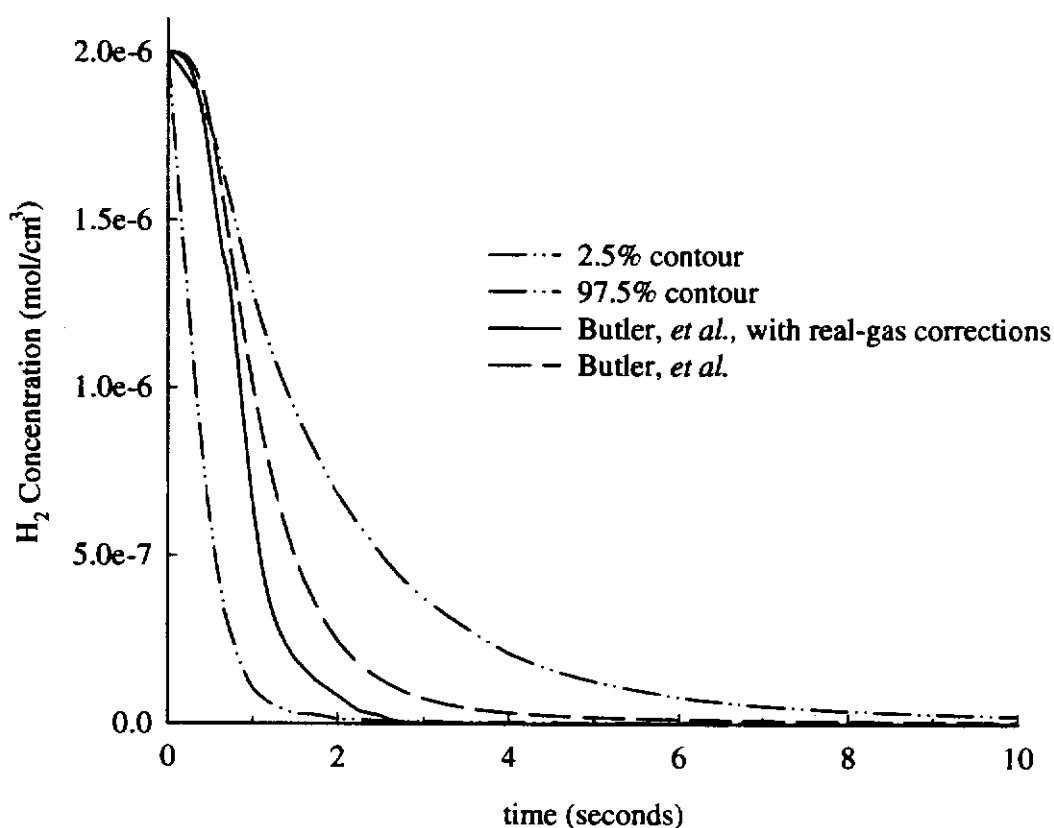
employed in this study. However, not all of the uncertain model parameters contribute equally to the uncertainty in the model output. For example, the model is quite sensitive to the highly uncertain value of the rate constant for H_2O_2 dissociation (Table 5.4, reaction 7). This is not surprising given its importance as the primary chain branching reaction in the mechanism. Restricting the uncertainty analysis to treat $k_{7,7}$ as the only uncertain parameter, with all other $k_{f,j}$'s and the $\Delta H_{f,i}^\circ$'s treated as deterministic quantities, reveals the range of the concentration predictions achievable by only varying $k_{7,7}$. Figure 5.7a shows the result of such an analysis and compares the range of predicted H_2 concentrations due to uncertainty in $k_{7,7}$ alone with the range resulting from the reduced model given in Table 5.3. The dashed lines in Fig. 5.7a represent the 2.5% and the 97.5% probability contours of the predicted $[\text{H}_2]$ when $k_{7,7}$ is treated as the only uncertain parameter. The dotted-and-dashed lines represent the 2.5% and 97.5% contours of the reduced model of Table 5.3.

The uncertainty in the standard-state heat of formation of HO_2 radical, whose reported mean value has varied between 0.5 (Chase *et. al*, 1985) and 3.8 kcal/mol (Bauschlicher and Partridge, 1993) in recent years, also has considerable impact on the uncertainty in the predicted H_2 concentration. This is consistent with its important role in the formation of H_2O_2 through disproportionation (reaction 4, Table 5.4) and its reaction with water (reverse of reaction 5, Table 5.4). The 95% probability interval bounded by the dashed lines in Fig. 7b results from restricting the MC simulation to treat $\Delta H_f^\circ(\text{HO}_2)$ as the only uncertain parameter and indicates the variability in the predicted $[\text{H}_2]$ profile by adjusting the value of the $\Delta H_f^\circ(\text{HO}_2)$ alone. As shown in Table 5.3, the mean value and error estimate for the $\Delta H_f^\circ(\text{HO}_2)$ were taken to be 3.0 ± 0.5 kcal/mol. Both the $\Delta H_f^\circ(\text{HO}_2)$ and the forward rate constant for reaction (7) were identified as the key contributors to the H_2 uncertainty through examination of the magnitudes of the coefficients in the series approximation for the hydrogen response distribution. Thus, in addition to carrying out the uncertainty computation itself, the DEMM-based methodology also provides a straightforward and systematic means of identifying important random variables in the model.

**FIGURE 5.7**

Uncertainty in predicted H_2 concentrations resulting from: uncertainty in the k_f of the H_2O_2 dissociation reaction (a); and uncertainty in the standard-state heat of formation of HO_2 radical (b). All remaining rate constants and heats of formation are treated as deterministic quantities. Middle solid lines are the median values of the predicted $[\text{H}_2]$ values; regions bounded by dashed lines show the range of H_2 concentration predictions due to uncertainty in $k_{f,7}$ alone (a), and the heat of formation of HO_2 alone (b). Also shown for comparison are the upper and lower bounds for the reduced model (Table 5.4)

Identifying those model parameters with the greatest influence on the uncertainty in the predicted concentration profiles reveals which parameters need to be known more precisely in order to reduce the overall uncertainty of the model output. If the concentration predictions are highly uncertain, model refinements such as real-gas corrections may be unwarranted given the uncertainty in the rate parameters of the base mechanism. In the case studied, a large improvement to the predictive capability of the model would result when uncertainties in the aforementioned key model parameters are reduced. To make this point more emphatically, consider the work of Alkam *et al.* (1996) who applied real-gas corrections to a mechanism similar to that given in Table 5.2. Predictions from their mechanism with and without real-gas corrections are presented in Fig. 5.8 along with uncertainty estimates from the present reduced mechanism with no real-gas corrections. Real-gas corrections are seen to change the $[H_2]$ predictions by 57% at most. However, both the $[H_2]$ predictions with and without real-gas corrections are well within the 95% probability interval of the MC analysis. These observations indicate that the Alkam *et al.* model is not significantly different from the one in Table 5.4 given the uncertainties assigned to the k_{fj} 's and ΔH_{fj}^o 's. Thus, the incorporation of real-gas effects is overshadowed by the variability in the predicted hydrogen concentration caused by parametric uncertainties inherent in the model.

**FIGURE 5.8**

The effect of real-gas corrections on the H_2 concentration predicted by the mechanism of Alkam *et al.* (1996) compared with the $[H_2]$ probability distribution calculated from the Monte Carlo simulation of the mechanism in Table 5.3. Reaction conditions: $T=582\text{ }^\circ\text{C}$, $P=246\text{ bar}$, $[H_2]_0=2.06\times 10^{-6}$, $[O_2]_0=1.04\times 10^{-6}$, $[H_2O]_0=4.218\times 10^{-3}\text{ mol/cm}^3$. Upper and lower dashed lines represent the 97.5% and 2.5% probability contours resulting from the MC simulation.

Chapter 6:

Conclusions

1. Mixing studies. As in previous studies involving hydrogen, carbon monoxide, acetic acid, and methylene chloride, kinetic data from the oxidation of methanol in supercritical water were found to exhibit a pronounced apparent induction time. However, the apparent induction time was shown to be influenced by the geometry and flow conditions within the mixing tee. By reducing the inner diameter of the tee to increase the sidestream Reynolds number and the side-to-mainstream velocity ratio, the apparent time lag was reduced from approximately 3.2 to 0.7 seconds. Comparison of side-entry and opposed-flow mixing tees with the inserts revealed no difference in the observed rate of methanol oxidation. The final tee design has a sidestream-to-mainstream diameter ratio of 0.16 and operates at sidestream Reynolds numbers of 6,500 to 24,000.

2. Oxidant comparison studies. A direct comparison of methanol oxidation kinetics was made using dissolved oxygen and hydrogen peroxide as oxidants. Using hydrogen peroxide feed concentrations which yielded stoichiometrically-equivalent amounts of dissolved oxygen upon decomposition, the rates of methanol conversion were found to be identical using the two oxidants. Moreover, the time-dependent concentrations of carbon monoxide, carbon dioxide, and hydrogen resulting from the oxidation process were demonstrated to be the same for both oxidants. The findings validate the use of hydrogen peroxide feed solutions as a viable means of attaining industrially-relevant oxygen feed concentrations at the bench-scale without the use of more sophisticated oxygen delivery methods.

3. Effect of fuel-equivalence ratio on rate of oxidation and product spectra. The rate of methanol oxidation was found to be independent of oxygen feed concentration above an oxygen-to-organic molar feed ratio of 1:1 to 1.5:1. Below this range, the rate of conversion

was found to drop off significantly. The entire study spanned a fuel-equivalence ratio range of 0.5 to 4.5. In addition, the distribution of products resulting from the oxidation reaction was found to be dependent on ϕ . Substoichiometric oxygen-to-organic molar feed ratios depress the direct oxidation of methanol and CO to CO₂ and promote the production of H₂ via the water-gas shift reaction. Reaction at fuel-lean conditions results in higher conversion of CO to CO₂ and a reduction in H₂ formation due to its direct oxidation in the presence of excess oxygen.

4. Interlaboratory comparison of methanol oxidation kinetics. With the redesign of several key elements of the MIT apparatus, the rates of methanol oxidation in the MIT and Sandia reactor systems were found to be comparable. The best agreement was found at low methanol feed concentrations (0.011 and 0.056 wt%). Comparison of rate data at higher feed concentrations was complicated by the scatter in the Sandia data and the possibility of non-isothermal operation due to the reaction exotherm. The MIT data set exhibited no dependence of rate on the methanol feed concentration. In contrast, the Sandia data were seen to display a significant increase in apparent rate at the highest feed concentration explored (0.39 wt%). In addition, the reaction of methanol due to hydrolysis or pyrolysis pathways was found to be negligible at the conditions studied.

5. Influence of reactor surface on rate of oxidation. Preliminary experiments utilizing reactors with high surface-to-volume ratios were seen to exhibit a marked decrease in oxidation rate when compared to those conducted in low S/V reactors. The data are consistent with a kinetic interpretation wherein the rate of oxidation is influenced by radical quenching at the wall of the reactor.

6. Uncertainty analysis. DEMM and Monte Carlo simulation were used to assess the uncertainty in the predictions of a reduced, SCWO hydrogen mechanism. Both methods produced identical predictions of species concentration profiles and their time-dependent

probability distributions. Further, both analyses reveal that there is considerable uncertainty in the predicted species concentration profiles arising from the reported uncertainties in the forward rate constants and species standard-state enthalpies of formation. Model predictions were found to be highly sensitive to two relatively uncertain parameters: the ΔH_f° of HO₂ radical and the rate constant for H₂O₂ dissociation. The MC simulation work also demonstrated that the impact of real-gas corrections on the predicted species profiles is minimal when compared to the uncertainty in the mechanism itself. Both DEMM and Monte Carlo simulation proved to be computationally tractable means of conducting parametric uncertainty analysis. However, the two methods differed substantially in the amount of computation time necessary to perform the analysis. To adequately develop the time-dependent response distributions of the model, Monte Carlo required 15,000 calls to the LSODE solver routine. By comparison, DEMM required 153 calls. This two order of magnitude reduction in the required number of model solutions makes DEMM an attractive tool for the analysis of more complex mechanisms where the computational time and memory requirements of Monte Carlo may become prohibitive.

Chapter 7:

Recommendations

The findings and observations reported in this thesis raise a number of basic research issues which seem appropriate for further investigation. Foremost among them is the need to better understand the role the reactor surface plays in influencing oxidation kinetics. This issue is critical to the interpretation of bench-scale rate data and to the application of such data in the design of larger scale reactors. Specific recommendations for future work are made in the paragraphs that follow.

7.1 EXAMINATION OF REACTOR SURFACE EFFECTS

During the course of the MIT-Sandia National Laboratory collaboration, it became apparent that oxidation experiments conducted in reactors with high S/V ratios exhibited markedly slower reaction rates than those conducted in reactors with lower S/V ratios. Preliminary findings for methanol oxidation were described in Section 4.5, but recent unpublished experiments with benzene show similar behavior. Given the free radical nature of the oxidation mechanism, the rate decrease is consistent with surface-mediated, radical quenching at the reactor wall. Radical quenching is a well-known phenomena in the low-pressure environment of atmospheric and combustion chemistry research—an environment characterized by a relatively high ratio of wall to bulk collision rates. Several experimental strategies have been developed for minimizing the influence of quenching at ambient and sub-ambient pressures. They include careful selection of the wall material (*e.g.*, quartz) and use of wall passivation procedures. In the SCWO environment, however, such strategies are difficult to implement. Since the wall of the reactor must be pressure-bearing and also able to withstand high-temperatures, the range of suitable construction materials is limited to closely-related families of high-nickel alloys with relatively narrow compositional ranges. This experimental material limitation could be overcome by the use of a pressure-balanced, tubular

reactor similar to the one used at Los Alamos National Laboratory for materials evaluation. In the pressure-balanced system, a non-pressure-bearing tube constructed of the material of interest is placed within a larger, pressure-bearing tube. The pressure on both sides of the inner tube is equalized by having its end open to the same fluid that is passing through in the annular space around it. Alternatively, and perhaps more simply, surface composition effects could be investigated through the use of the packed-bed reactor that already exists within the MIT research group by packing it with a suitable material. Materials of interest might include high-nickel alloys, nickel, chrome, platinum, gold, and various ceramics—some of which are being considered as potential linings for commercial SCWO reactors. The effect of surface-to-volume (S/V) ratio on the rate and extent of oxidation could be explored by varying the diameter of open tubular reactors or the particle size of the material in the packed bed. A further extension of these ideas would be to utilize the group's new high-pressure, stirred tank reactor. Experiments could be conducted with and without the presence of fine metal or ceramic powders suspended in the SCW medium. In this instance, efforts would have to be made to ensure that the powder material is retained within the reactor and is suspended and evenly dispersed throughout the reactor volume.

7.2 EXTENSION OF FEED MIXING STUDIES

As discussed in Section 4.1, the changes made to the mixing tee design had a significant impact on methanol oxidation kinetics. The question remains, however, whether additional changes to the design could further improve mixing and thereby reduce the remaining observed lag time. As pointed out in the review of the mixing literature in Chapter 3, current mainstream Reynolds numbers in the tee fall well short of being fully turbulent ($N_{Re,R} > 10,000$). Mainstream Reynolds numbers below this value have been shown to increase the downstream distance required for complete mixing. The most straightforward and easily implemented solutions to this problem are to reduce the diameter of the reactor and downstream leg of the tee and to increase the mainstream flowrate. Unfortunately, the former approach also increases the surface-to-volume ratio of the reactor and runs the risk of slowing down the overall rate of oxidation through surface quenching. The latter approach would

require the use of longer reactors in order to maintain access to the same range of residence times. This is certainly feasible but care must be exercised to ensure that good fluidization is maintained within the main sandbath.

7.3 IN-SITU SPECTROSCOPIC INVESTIGATION OF ELEMENTARY REACTION EVENTS IN SUPERCRITICAL WATER

There is a growing body of experimental and theoretical evidence suggesting that the local density of solvent around a solute in a supercritical fluid is greater than the bulk density. This has resulted in speculation about the whether the solvent plays a role in influencing reaction rates through clustering or cage effects. Such a role would undermine the basic “gas-phase” modeling assumption typically made in modeling SCWO oxidation processes at the elementary reaction level. Experimental work in this area has been carried out in the physical chemistry community and has focused on the study of elementary kinetic phenomena such as thermal unimolecular decomposition and radical recombination reactions, unimolecular isomerizations, and photolysis. To date, these studies have been limited to fluids such as carbon dioxide, ethane, fluoroform, and others with relatively low critical temperatures and pressures. In what would be a dramatic, but valuable, departure from previous reactor engineering studies in the group, it is proposed that a basic science effort be made to examine the role of water on elementary reaction events at conditions relevant to commercial SCWO operation. There are two barriers to such a line of investigation. The first is the design of a reliable, optically-accessible pressure vessel. Largely due to the efforts of the individuals in the SCWO salt phase-equilibrium work, this has been and continues to be a strength of the MIT research program. In addition, there are a number of well-tested, cell designs from other SCWO research groups, particularly those at Sandia and Los Alamos National Laboratories. The second, and more challenging, aspect of the work is the selection of an appropriate kinetic system or phenomena and the development of the means to study it *in-situ*. The recent collaboration with individuals from the Harrison spectroscopy lab in the Department of Chemistry holds the promise for success in this area.

Chapter 8:

Appendices

“The devil’s in the details.”

CONTENTS:

8.1 Operating instructions for bench-scale tubular reactor

8.2 Feed pump calibrations

8.3 Details of analytical methods

8.3.1 Liquid feed and effluent analysis

8.3.2 Vapor effluent analysis of light gases

8.3.3 Vapor effluent analysis of hydrogen

8.4 Summary of tubular reactor geometries

8.5 Summary of design changes to bench-scale reactor system

8.6 Program for Monte Carlo simulation of hydrogen oxidation

8.1 OPERATING INSTRUCTIONS FOR BENCH-SCALE TUBULAR REACTOR

Day prior to run (if using oxygen saturator system)

1. **Empty oxygen saturator** (if not done at end of previous run) to drain by pressurizing saturator from He manifold.
 - Check oxygen saturator pressure gauge to ensure that saturator is not pressurized. If tank is pressurized, close off oxygen supply and vent saturator.
 - Close valve on oxygen supply tank and turn regulator valve fully counterclockwise to prevent possibility of accidental overpressure.
 - Close vent line on saturator and switch oxygen saturator feed valve to "Helium"
 - Empty saturator to drain through valve at bottom of saturator.
 - Switch oxygen saturator feed valve to "Oxygen" and vent saturator.
 2. **Empty organic saturator** to labelled waste container by pressurizing saturator from He manifold.
 3. **Charge 2,500ml DI water to oxygen saturator** valve at bottom of saturator.
 - Fill 2 liter transfer flask with 2 liters of > 18.1 MOhm-cm water from DI system.
 - Make sure vent line to oxygen saturator is open.
 - Pressure transfer water from flask to saturator through valve at bottom of saturator using He manifold as pressure source.
 - Repeat to complete 2.5 liter charge.
 4. **Open valve on oxygen saturator recirculation loop.**
 5. **Purge oxygen saturator head space three times.**
 - Closing vent line and pressurizing with about 100 psig of oxygen.
 - Allow saturator to sit at pressure for 10-15 min.
 - Close oxygen supply line and vent saturator to atmosphere.
 - Repeat pressurization/vent procedure a total of three times.
- NOTE: When using combustible gases as organic source, do not vent oxygen and organic saturators at the same time.*
6. **Pressurize oxygen saturator to desired pressure.**
 - Close vent line on saturator tightly.
 - Slowly increase saturator pressure by turning oxygen regulator valve clockwise until desired pressure is reached (usually 5-10 psig higher than target value).

- Turn on oxygen recirculation pump.

NOTE: Check oil level in pump and add additional pump oil if needed.

- Lower Lexan shield, secure with wing-nut, and post "High Pressure" sign.

Day of run*Water tank and pump preparation***1. Top off water feed tank.**

- Close He supply to water tank and open top of tank to check level.
- If level is too low, start up DI water system with DI flow into sink. Once DI water quality has risen to 18.1 MOhm-cm or greater, open system DI supply valves (one on DI system and one on top of water tank) to direct flow to water feed tank.
- After filling, close both DI supply valves (2) and cap water feed tank tightly.
- Open water tank vent valve.
- Open He sparge valve at bottom of water tank and slowly open He sparge needle valve until He can be heard bubbling into tank.
- Let water tank sparge for 5-10 minutes.
- Close He sparge and needle valves and close water tank vent valve.
- Open He supply to water tank to pressurize to 5 psig with He.

2. Zero all system pressure transducers.

- Zero Dynisco pressure transducer. With no flow through system, press and hold in "calc" button and then press "func" button; release both "calc" and "func" buttons. When transducer display alternately displays "lo scale" and "0", press "calc" and release. When display alternately displays "hi scale" and "10000", press "calc" and release. Finally, when displays alternates between "tare" and "0", press "calc" and release.
- Zero pressure transducers on both Rainin feed pumps and check high-pressure interlock settings. Interlocks should be set to shutdown pumps at 4600 psig.

3. Turn on and degas oxygen and organic feed pumps. (NOTE: Degassing pump heads is only necessary if previous run used the oxygen saturator)

- Switch feed lines to both pumps to "water feed."
- Open isolation valves upstream and downstream of both feed pumps.
- Turn on both Rainin SD-200 pumps.
- Carefully crack the suction side fitting on both pump heads to flush out any trapped bubbles which might have formed during shutdown procedure.

NOTE: Carefully retighten fittings, making sure they go in straight and do not strip.

- Set desired flow setpoints on both pumps and hit "Run" on each keypad.

- Visually confirm flow at outlet of G/L separator and measure flowrate if desired.

NOTE: From time to time, the EPROMs in the feed pumps will reset the pump parameters (head size, etc.) to their default values. If the measured flowrate is not what you expect, check to see if the pump parameters are correct. EPROM failure can be easily recognized by looking at the flow setting on the pump's digital display. Using the 25ml pump heads, the flow setting should have three significant digits after the decimal point. If it has two, the EPROMs have reset to the 200ml default setting.

System pressurization

4. **Establish desired system pressure by slowly turning the back-pressure regulator (BPR) knob clockwise.**

- System pressure will build up slowly at first (especially at low flowrates) so it may be necessary to wait a minute after the first few turns of the BPR.
- Once system pressure has risen to several hundred psig, system pressure can be raised more rapidly.

NOTE: Once system pressure is established, visually inspect suction-side fittings on both feed pumps and all other fittings downstream for leaks (particularly the fittings on the 1/16" preheater lines).

- Check flowrate using volumetric flask and stopwatch. If flowrate is low, depressurize system and repeat degassing procedure. Alternatively, start looking for leaks.

System heat-up

5. **Create temperature data log file in HOTMUX software (on Vectra computer)**

- Turning on power switch to line printer and positioning printer head after a perforated page break.
- Enter HOTMUX software and select "Data storage" from the main menu. Type in a filename for the run and follow prompts from software.

6. **Return any sand collected via the extraction air system to the main sandbath.**

- Sandbath level should be approximately 1 in. below top bend of heater elements with fluidization air OFF.

7. ESTABLISH COOLING WATER FLOW TO HEAT EXCHANGER

- Turn black arrow knob after heat-exchanger water filter upwards toward plastic line leading to heat exchanger.
- **Visually confirm** water flow at end of line coming from outlet of heat exchanger.
- Periodically check plastic tube fitting at utility outlet of heat exchanger for leaks.

NOTE: FAILURE TO TURN ON COOLING WATER FLOW IS A BAD THING. IF YOU TURN IT ON AFTER THE SYSTEM IS AT TEMPERATURE, YOU WILL EXPERIENCE STEAM HAMMER THE LIKES OF WHICH YOU WILL NEVER WISH TO SEE AGAIN.

8. Turn on fluidization air and power to sandbath.

Main sandbath:

- Open valve from building HP air supply (main sandbath supply pressure should be set at 60 psig).
- Purge any condensed water from regulator trap by briefly depressing valve stem at bottom of regulator.
- Set main sandbath air flowrate to 20 ml/min using rotameter on front of sandbath and turn on extraction air switch.
- Visually check main sandbath for fluidization level.
- Turn on power to main sandbath and enter desired setpoint.
- Check to see that air extraction light is illuminated on front of main sandbath. If not, lower the fluidization flow to the preheater sandbath (if used) until light comes on.
- As main sandbath heats up, lower fluidization air flow periodically. The final airflow value at operating temperature should be 12 ml/min.

9. Turn on DOH preheaters and heat tracing for transfer line

- Turn off power to DOH preheaters at circuit breaker box.
- Turn on power to DOH and heat tracing controllers by flipping switch on power strip on right side of sandbath table.
- Set setpoints on both DOH controllers to 25 °C.
- Turn power setting to "HI" on both heat tracing controllers. Check for "power" and "cycle" lights to come on.
- Let heat tracing carry out initial heatup. Once DOH controllers read 200 °C, turn on power to DOH SCRs, raise the DOH controller setpoints to 200 °C and gradually increase until desired preheating temperature is attained.

*GC preparation***10. Prepare GC's for gas and liquid sample analyses:**

- a. While GC carrier gas flowrates are still at their low standby setting, replace inlet septa on all GC's and on gas sampling line. Use SGE white septa for purged/packed inlets on HP 5890 and 6890 GCs and Supelco Thermogreen septa on lower PE GC and on G/L separator sampling port.
- b. Establish normal carrier gas flows to HP GC's by turning valves (labeled "1" and "2") from their low-flow standby positions to their high-flow operating positions.

c. HP 5890 GC TCD preparation:

- For TCD operation on HP 5890 GC #1, turn on reference gas at left front of GC *before* turning on the detector or starting up HP chemstation software.

NOTE: FAILURE TO TURN ON REFERENCE GAS BEFORE TURNING ON THE TCD WILL DAMAGE THE DETECTOR.

- Open the HP chemstation software for the HP 5890 FID/TCD by selecting the online copy from the "Start" menu on the Gateway 486 computer.

d. HP 5890 GC FID preparation:

- Open the HP chemstation software for the GC of interest by selecting the online copy from the "Start" menu on the Gateway 486 computer.
- Assign SIG1 to the FID by pressing "SIG1"-"A"-(enter)-"SIG1". GC panel display should rapidly drop to 0.0 after a short time.
- Open H₂ and Air detector support gas lines by turning valves located to left of H₂ and air manifold regulators. Open instrument H₂ and Air lines to detector by turning on/off knobs on upper left front of GC counterclockwise to their full open positions.
- Ignite FID flame by briefly depressing FID ignition button. GC display should increase to some number between 10 and 100 and then slowly fall off to approx. 9 to 11 over a period of several minutes. If the display rapidly returns to 0.0, the detector failed to ignite and the ignition button needs to be depressed and released again. Once the flame is lit, open the Aux nitrogen flow by turning the

Aux knob on the upper left front of the GC counterclockwise to its full open position.

NOTE: The FID on HP 5890 GC #1 is most easily by using the following modified procedure: open air and hydrogen support gas valves, then close the hydrogen valve. While holding down the ignition button, reopen the hydrogen valve. This should result in a working flame. Now open the Aux nitrogen valve and proceed with the remainder of the GC startup.

- If there's a question as to whether the flame is lit on any GC, hold a mirror or other shiny metal object over the FID detector outlet. Water condensation on the surface of the object indicates that the flame is lit.

e. HP 6890 FID and TCD operation

- Detector support gases and flame ignition are all automatically controlled on the 6890 and occur when the method is loaded into the HP ChemStation software.

f. Autoinjector tray and tower preparation

- Turn on cooling water to sample trays by depressing "power" and then "cool" buttons on front of VWR refrigerated bath. Setpoint should be set to 15 °C.
- Turn on autosampler control module(s) and (if using automatic injection) position autoinjector over desired inlet.
- Open autoinjector door and remove syringe. Remove syringe plunger and wet with water or appropriate solvent. Replace plunger in syringe barrel and check to see that plunger moves freely. Reinstall syringe in autoinjector and make sure that the syringe needle is in the needle guide and that syringe assembly moves easily up and down.
- Empty autoinjector waste vials into appropriate, labelled waste containers.
- Flush and refill autoinjector wash vials with desired solvent (usually water).

g. Calibrate Perkin-Elmer GC for H₂ if needed.

10. Prepare, analyze, and load organic feed solution

- Prepare organic feed solution in hood using clean volumetric flask and digital pipette.

- Analyze solution via GC or other appropriate analytical technique to ensure correct concentration before loading solution into organic saturator.
- If using the 5-liter glass feed vessel, close He pressurization valve to vessel headspace. Slowly uncap vessel to relieve internal pressure and empty contents into labelled waste container. Transfer organic feed solution from flask to vessel. Recap vessel snugly and open He pressurization valve.

NOTE: HELIUM PRESSURE TO ORGANIC FEED VESSEL SHOULD NOT EXCEED 5 psig. IF IT DOES, THE VESSEL MAY SHATTER.

Flush feed solution through sampling line and through to the water/organic feed switching valve.

- (If using the metal organic saturator, pressurize it from He manifold and drain any contents to labelled waste container. Open organic-side sample valve to flush out line between saturator and sample valve. Vent saturator and transfer feed solution from flask to saturator by pressurization.

Pressurize saturator from He manifold and briefly open organic-side sample valve to flush feed line with new feed solution.)

11. Prepare, analyze, and load oxidant feed solution

- Prepare hydrogen peroxide feed solution using clean volumetric flask and pipet.
- Confirm H₂O₂ concentration using Hach ceric ion titration kit (see instructions).
- Close He pressurization line to peroxide feed vessel. Slowly open cap on vessel to relieve internal pressure. Disconnect lines to and from feed vessel and empty contents into drain.
- Load oxidant feed solution into Dionex plastic reservoir and close cap snugly.
- Reattach He supply line to Dionex feed vessel and place (but don't completely tighten) line leading from vessel into the switching valve. Open supply pressure to vessel and let liquid flow out of feed line to remove any air in the line (this will ensure proper pump action).
- Tighten fitting on water/oxidant feed switching valve.

12. Begin run

- When system is at steady-state and desired temperature and pressure, turn off saturator recirculation pump (if used) and flip over from water feeds to organic and oxygen feeds.

Shutdown

1. **Turn off power to sandbath, all heat tracing and DOH preheat system. Leave fluidization air ON during cooldown.**

NOTE: FAILURE TO LEAVE FLUIDIZATION AIR ON DURING COOLDOWN WILL RESULT IN BUCKLING OF THE AIR DISTRIBUTION PLATE IN THE BOTTOM OF THE MAIN SANDBATH. DO NOT TURN OFF FLUIDIZATION AIR UNTIL SANDBATH TEMPERATURE IS BELOW 200 °C.

2. **Leave oxidant and organic pumps ON.**
3. **If using the oxygen saturator, shutdown oxygen feed to system.**

If using the oxygen saturator:

- Simultaneously close suction side valve to oxygen-side pump and press “stop” on pump console.
- Close oxygen supply to saturator by closing valve near oxygen cylinder.
- Slowly vent oxygen saturator.
- When saturator pressure is about 10 psig, switch oxygen and organic-side feeds to water.

NOTE: Flow from exit of G/L separator should continue. Stoppage of flow usually indicates trapped vapor in the pump head(s). If using an organic gas, do not vent both saturators at the same time.

3. **Once system pressure is below 300 °C, depressurize system by slowly turning the BPR counterclockwise.**
4. **While sandbath temperatures are still above 200°, leave on water feed flow to system and maintain cooling water flow to heat exchanger.**

8.2 FEED PUMP CALIBRATIONS

8.2.1 High suction-side pressure calibration of organic-side Rainin SD-200 pump

3/12/96 Organic saturator equilibrated with H₂ at 410 psig overnight prior to measurements below
Pump suction side fitted with 1/16" OD superflangeless compression fitting

Oxygen-side Pump					Organic-side Pump					
Discharge Pressure	Suction Pressure	Flow Setting	Minutes	Seconds	Flask Size (ml)	Measured Flowrate	Suction Pressure	Flow Setting	Calculated Flowrate**	Delta
3550	5	0	5	22.15	50	9.312	386	9	9.312	0.312
3550	5	0	5	14.89	50	9.527	386	9	9.527	0.527
3550	5	0	5	25.95	50	9.204	386	9	9.204	0.204
3540	5	0	5	24.2	50	9.254	386	9	9.254	0.254
3540	5	0	5	29.55	50	9.103	386	9	9.103	0.103
3540	5	0	5	29.29	50	9.111	386	9	9.111	0.111
3510	5	0	8	7.47	50	6.154	389	6	6.154	0.154
3510	5	0	8	11.09	50	6.109	389	6	6.109	0.109
3510	5	0	8	5.44	50	6.180	389	6	6.180	0.180
3520	5	0	8	6.8	50	6.163	389	6	6.163	0.163
3530	5	0	8	5.67	50	6.177	389	6	6.177	0.177
3530	5	0	8	5.51	50	6.179	389	6	6.179	0.179

Oxygen-side Pump						Organic-side Pump				
Discharge Pressure	Suction Pressure	Flow Setting	Minutes	Seconds	Flask Size (ml)	Measured Flowrate	Suction Pressure	Flow Setting	Calculated Flowrate**	Delta
3550	5	0	5	43.17	50	8.742	5	9	8.742	-0.258
3690	5	0	5	16.81	50	9.469	794	9	9.469	0.469
3570	5	0	5	22.39	50	9.305	796	9	9.305	0.305
3570	5	0	5	19.78	50	9.381	790	9	9.381	0.381
3590	5	0	5	24.31	50	9.250	788	9	9.250	0.250
3600	5	0	5	20.59	50	9.358	785	9	9.358	0.358
3590	5	0	8	7.3	25	3.078	800	3	3.078	0.078
3600	5	0	8	3.36	25	3.103	810	3	3.103	0.103
3610	5	0	8	4.59	25	3.095	817	3	3.095	0.095
3560	5	0	8	4.26	25	3.098	817	3	3.098	0.098
3580	5	0	8	4.34	25	3.097	818	3	3.097	0.097
3560	5	0	4	3.58	25	6.158	812	6	6.158	0.158
3560	5	0	4	3.04	25	6.172	806	6	6.172	0.172
3560	5	0	4	2.88	25	6.176	803	6	6.176	0.176
3570	5	0	4	2.33	25	6.190	800	6	6.190	0.190
3570	5	0	4	3.47	25	6.161	798	6	6.161	0.161

3/13/96 Organic saturator equilibrated with H2 at 1200 psig for 1.5 hrs. prior to measurements below

Oxygen-side Pump					Organic-side Pump					
Discharge Pressure	Suction Pressure	Flow Setting	Minutes	Seconds	Flask Size (ml)	Measured Flowrate	Suction Pressure	Flow Setting	Calculated Flowrate**	Delta
3580	5	0	5	29.62	50	9.101	5	9	9.101	0.101
3560	5	0	5	19.89	50	9.378	1139	9	9.378	0.378
3570	5	0	5	19.59	50	9.387	1139	9	9.387	0.387
3580	5	0	5	20.4	50	9.363	1139	9	9.363	0.363
3580	5	0	5	20.53	50	9.359	1139	9	9.359	0.359
3580	5	0	5	21.95	50	9.318	1139	9	9.318	0.318
3570	5	0	7	59.64	50	6.255	1145	6	6.255	0.255
3580	5	0	4	0.2	25	6.245	1144	6	6.245	0.245
3580	5	0	4	1.66	25	6.207	1140	6	6.207	0.207
3590	5	0	4	2.62	25	6.183	1139	6	6.183	0.183
3590	5	0	4	2.77	25	6.179	1139	6	6.179	0.179
3560	5	0	8	14.94	25	3.031	1156	3	3.031	0.031
3570	5	0	8	20.86	25	2.995	1158	3	2.995	-0.005
3580	5	0	7	52.8	25	3.173	1158	3	3.173	0.173
3570	5	0	8	1.4	25	3.116	1154	3	3.116	0.116
3570	5	0	8	13.19	25	3.041	1149	3	3.041	0.041

Regression Output for High Suction-Side Pressure Organic Pump Calibration

<i>Regression Statistics</i>	
Multiple R	0.9991
R Square	0.9983
Adjusted R Square	0.9982
Standard Error	0.1028
Observations	46

<i>ANOVA</i>					
	<i>df</i>	<i>SS</i>	<i>MS</i>	<i>F</i>	<i>Significance F</i>
Regression	2	264.27	132.13	12505.13	3.50E-60
Residual	43	0.45	0.01		
Total	45	264.72			

	<i>Coefficients</i>	<i>Standard Error</i>	<i>t Stat</i>	<i>P-value</i>	<i>Lower 95%</i>	<i>Upper 95%</i>	<i>Lower 95.0%</i>	<i>Upper 95.0%</i>
Intercept	-0.2461295	0.06927	-3.55316	9.389E-04	-0.38583	-0.10643	-0.38583	-0.10643
Flow Setpoint (ml/min)	1.0406451	0.00708	146.96664	9.856E-60	1.02637	1.05492	1.02637	1.05492
Suction Pressure (psig)	0.00022247	0.00005	4.93206	1.264E-05	0.00013	0.00031	0.00013	0.00031

8.2.2 Low suction-side pressure calibration of organic-side Rainin SD-200 pump

Date: 8/9/95

Suction-side pressure (psig He)	Discharge pressure (psig)*	Time reqd to fill 100ml flask		Displayed flowrate (ml/min)	Measured flowrate (ml/min)	Difference (ml/min)
		Minutes	Seconds			
5	3500	19	34.91	5	5.107	0.107
5	3500	19	40.81	5	5.081	0.081
5	3500	19	38.67	5	5.090	0.090
5	3500	19	32.5	5	5.117	0.117
5	3500	19	30.29	5	5.127	0.127
5	3500	19	35.86	5	5.103	0.103
5	3500	19	36.86	5	5.098	0.098
5	3500	19	30.94	5	5.124	0.124
5	3500	19	32.51	5	5.117	0.117

* As measured by Dynisco transducer

Date: 8/10/95

Suction-side pressure (psig He)	Discharge pressure (psig)*	Time reqd to fill 100ml flask		Displayed flowrate (ml/min)	Measured flowrate (ml/min)	Difference (ml/min)
		Minutes	Seconds			
5	3500	19	31.86	2.5	2.560	0.060
5	3500	19	28.73	2.5	2.567	0.067
5	3500	19	24.88	2.5	2.575	0.075
5	3500	19	26.97	2.5	2.571	0.071
5	3500	19	24.61	2.5	2.576	0.076
5	3500	19	24.8	2.5	2.576	0.076
5	3500	19	40.23	2.5	2.542	0.042

Date: 8/16/95

Suction-side pressure (psig He)	Discharge pressure (psig)*	Time reqd to fill 100ml flask Minutes	Seconds	Displayed flowrate (ml/min)	Measured flowrate (ml/min)	Difference (ml/min)
5	3500	9	54.09	10	10.099	0.099
5	3500	9	51.78	10	10.139	0.139
5	3500	9	48.7	10	10.192	0.192
5	3500	9	53.86	10	10.103	0.103
5	3500	9	51.66	10	10.141	0.141
5	3500	9	50.69	10	10.158	0.158
5	3500	9	50.73	10	10.157	0.157
5	3500	9	48.77	10	10.191	0.191

Date: 8/16/95

Suction-side pressure (psig He)	Discharge pressure (psig)*	Time reqd to fill 100ml flask Minutes	Seconds	Displayed flowrate (ml/min)	Measured flowrate (ml/min)	Delta (ml/min)
5	3820	9	47.97	10	10.205	0.205
5	3820	9	50.12	10	10.167	0.167
5	3820	9	51.59	10	10.142	0.142
5	3820	9	50.5	10	10.161	0.161
5	3820	9	48.51	10	10.195	0.195
5	3820	9	49.09	10	10.185	0.185
5	3820	9	51.29	10	10.147	0.147

Date: 8/16/95

Suction-side pressure (psig He)	Discharge pressure (psig)*	Time reqd to fill 100ml flask Minutes	Seconds	Displayed flowrate (ml/min)	Measured flowrate (ml/min)	Delta (ml/min)
5	4000	9	47.97	10	10.205	0.205
5	4000	9	51.84	10	10.138	0.138
5	4000	9	51.51	10	10.144	0.144
5	4000	9	47.14	10	10.219	0.219
5	4000	9	48.66	10	10.193	0.193

Date: 8/17/95

Suction-side pressure (psig He)	Discharge pressure (psig)*	Time reqd to fill 100ml flask Minutes	Seconds	Displayed flowrate (ml/min)	Measured flowrate (ml/min)	Delta (ml/min)
5	3500	13	2.14	7.5	7.671	0.171
5	3500	13	3.22	7.5	7.661	0.161
5	3500	13	2.99	7.5	7.663	0.163
5	3500	13	4.94	7.5	7.644	0.144
5	3500	13	4.15	7.5	7.652	0.152

Regression Output for Low Suction-Side Pressure Organic Pump Calibration

Regression Statistics	
Multiple R	0.999964
R Square	0.999929
Adjusted R Square	0.999925
Standard Error	0.026091
Observations	41

ANOVA					
	df	SS	MS	F	Significance F
Regression	2	363.8613932	181.9306966	267251.9168	1.5284E-79
Residual	38	0.025868351	0.000680746		
Total	40	363.8872615			

	Coefficients	Standard Error	t Stat	P-value	Lower 95%	Upper 95%	Lower 95.0%	Upper 95.0%
Intercept	-0.089069	0.089821	-9.91627E-01	3.27652E-01	-0.27090	0.09276	-0.27090	0.09276
Flow Setpoint (ml/min)	1.011173	0.001681	6.01512E+02	3.25794E-77	1.00777	1.01458	1.00777	1.01458
Discharge pressure (psig)	0.000039	0.000027	1.47219E+00	1.49204E-01	-0.00001	0.00009	-0.00001	0.00009

8.2.3 High suction-side pressure calibration of oxygen-side Rainin SD-200 pump

Organic-side Pump						Oxygen-side Pump				
Discharge Pressure	Suction Pressure	Flow Setting	Calculated Flowrate*	Minutes	Seconds	Flask Size (ml)	Measured Flowrate	Suction Pressure	Flow Setting	Calculated Flowrate**
3540	5	7.5	7.633	13	6.31	100	7.631	5	0	-0.003
3540	5	7.5	7.633	13	5.94	100	7.634	5	0	0.001
3540	5	7.5	7.633	13	5.51	100	7.638	5	0	0.005
3540	5	5.5	5.611	13	3.14	100	7.661	196	2	2.050
3540	5	5.5	5.611	13	2.94	100	7.663	194	2	2.052
3540	5	5.5	5.611	13	3.75	100	7.656	194	2	2.045
3540	5	1.5	1.566	13	3.56	100	7.657	195	6	6.091
3540	5	1.5	1.566	13	3.75	100	7.656	194	6	6.089
3540	5	1.5	1.566	13	3.17	100	7.661	193	6	6.095
3540	5	1.5	1.566	12	59.31	100	7.699	591	6	6.133
3540	5	1.5	1.566	13	9.32	100	7.601	594	6	6.035
3540	5	1.5	1.566	13	2	100	7.673	600	6	6.106
3540	5	1.5	1.566	12	58.55	100	7.707	602	6	6.140
3550	5	1.5	1.567	12	58.45	100	7.708	596	6	6.141
3550	5	1.5	1.567	12	54.67	100	7.745	591	6	6.179
3560	5	5.5	5.612	12	58.69	100	7.705	600	2	2.093

Organic-side Pump						Oxygen-side Pump				
Discharge Pressure	Suction Pressure	Flow Setting	Calculated Flowrate*	Minutes	Seconds	Flask Size (ml)	Measured Flowrate	Suction Pressure	Flow Setting	Calculated Flowrate**
18-Sep	Deaerated water tank contents for 10 min									
3510	5	5.5	5.610	13	3.73	100	7.656	599	2	2.046
3500	5	5.5	5.609	13	1.25	100	7.680	600	2	2.071
3500	5	5.5	5.609	13	5.97	100	7.634	602	2	2.024
3500	5	5.5	5.609	13	7.23	100	7.622	605	2	2.012
3500	5	5.5	5.609	13	7.89	100	7.615	599	2	2.006
3500	5	5.5	5.609	13	2.06	100	7.672	605	2	2.063
3500	5	5.5	5.609	13	3.05	100	7.662	605	2	2.053
3510	5	5.5	5.610	13	3.15	100	7.661	998	2	2.052
3510	5	5.5	5.610	12	58.33	100	7.709	1005	2	2.099
3510	5	5.5	5.610	13	0.01	100	7.692	995	2	2.082
3510	5	5.5	5.610	12	58.17	100	7.710	1010	2	2.101
3510	5	5.5	5.610	13	0.42	100	7.688	1000	2	2.078
3510	5	5.5	5.610	12	59.2	100	7.700	995	2	2.090

9/25/95 Oxygen saturator equilibrated at 1000 psig overnight prior to measurements below

Organic-side Pump						Oxygen-side Pump				
Discharge Pressure	Suction Pressure	Flow Setting	Calculated Flowrate*	Minutes	Seconds	Flask Size (ml)	Measured Flowrate	Suction Pressure	Flow Setting	Calculated Flowrate**
3500	5	1.5	1.565	13	10.59	100	7.589	5	6	6.025
3510	5	1.5	1.565	12	34.03	100	7.957	1005	6	6.392
3510	5	1.5	1.565	12	57.23	100	7.720	1010	6	6.155
3510	5	1.5	1.565	12	53.97	100	7.752	1000	6	6.187
3520	5	1.5	1.566	12	59.45	100	7.698	998	6	6.132
3520	5	1.5	1.566	12	57.33	100	7.719	1010	6	6.153
3520	5	1.5	1.566	13	2.06	100	7.672	1005	6	6.107
3510	5	3.5	3.587	13	10.78	100	7.587	1005	4	4.000
3510	5	3.5	3.587	12	57.62	100	7.716	998	4	4.128
3520	5	3.5	3.588	12	57.42	100	7.718	1015	4	4.130
3520	5	3.5	3.588	13	5.11	100	7.642	1005	4	4.054
3530	5	3.5	3.588	12	54.94	100	7.743	1000	4	4.154
3520	5	3.5	3.588	13	3.86	100	7.654	1005	4	4.067
3520	5	5.5	5.610	12	57.4	100	7.718	1010	2	2.108
3520	5	5.5	5.610	12	55.45	100	7.737	1005	2	2.127
3530	5	5.5	5.611	12	50.23	100	7.790	995	2	2.179
3520	5	5.5	5.610	13	2	100	7.673	1005	2	2.062

9/26/95 Oxygen saturator equilibrated at 1400 psig overnight prior to measurements below
 Pumps heads cleared of vapor prior to runs

Organic-side Pump						Oxygen-side Pump				
Discharge Pressure	Suction Pressure	Flow Setting	Calculated Flowrate*	Minutes	Seconds	Flask Size (ml)	Measured Flowrate	Suction Pressure	Flow Setting	Calculated Flowrate**
3500	5	5.5	5.609	13	3.56	100	7.657	5	2	2.048
3500	5	5.5	5.609	12	52.47	100	7.767	1410	2	2.158
3500	5	5.5	5.609	12	50.81	100	7.784	1405	2	2.175
3500	5	5.5	5.609	13	3.99	100	7.653	1405	2	2.044
3500	5	5.5	5.609	12	55.34	100	7.739	1405	2	2.129
3500	5	5.5	5.609	12	57.22	100	7.720	1405	2	2.110
3500	5	1.5	1.565	12	53.88	100	7.753	1410	6	6.188
3500	5	1.5	1.565	12	58.5	100	7.707	1410	6	6.142
3500	5	1.5	1.565	12	54.8	100	7.744	1415	6	6.179
3500	5	1.5	1.565	12	53.98	100	7.752	1400	6	6.187
3500	5	1.5	1.565	12	52.42	100	7.768	1400	6	6.203
3500	5	3.5	3.587	12	49.17	100	7.801	1420	4	4.214
3500	5	3.5	3.587	12	56.61	100	7.726	1420	4	4.139
3500	5	3.5	3.587	12	55.01	100	7.742	1430	4	4.155
3500	5	3.5	3.587	13	0.62	100	7.686	1430	4	4.099
3500	5	3.5	3.587	12	53.15	100	7.760	1430	4	4.173
3500	5	3.5	3.587	12	52.04	100	7.772	1430	4	4.185
3500	5	3.5	3.587	12	48.86	100	7.804	1430	4	4.217
3500	5	5.5	5.609	13	4.31	100	7.650	1435	2	2.041
3500	5	5.5	5.609	12	56.2	100	7.730	1435	2	2.121
3500	5	5.5	5.609	13	5.56	100	7.638	1435	2	2.028
3510	5	5.5	5.610	13	3.61	100	7.657	1435	2	2.047
3510	5	5.5	5.610	12	54.67	100	7.745	1435	2	2.135

<i>Regression Statistics</i>	
Multiple R	0.999611
R Square	0.999222
Adjusted R Square	0.999184
Standard Error	0.051364
Observations	65

ANOVA

	<i>df</i>	<i>SS</i>	<i>MS</i>	<i>F</i>	<i>Significance F</i>
Regression	3	206.651497	68.883832	26109.076	9.49801E-95
Residual	61	0.1609369	0.0026383		
Total	64	206.812434			

	<i>Coefficients</i>	<i>Standard Error</i>	<i>t Stat</i>	<i>P-value</i>	<i>Lower 95%</i>	<i>Upper 95%</i>	<i>Lower 95.0%</i>	<i>Upper 95.0%</i>
Intercept	-1.107219	1.916E+00	-5.779E-01	5.654E-01	-4.938E+00	2.72365	-4.93809	2.72365
Flow setpoint (ml/min)	1.018293	3.914E-03	2.602E+02	1.308E-94	1.010E+00	1.02612	1.01047	1.02612
Suction pressure (psig)	0.000075	2.089E-05	3.572E+00	6.976E-04	3.286E-05	0.00012	0.00003	0.00012
Discharge Pressure (psig)	0.000307	5.427E-04	5.665E-01	5.731E-01	-7.778E-04	0.00139	-0.00078	0.00139

8.2.4 Low suction-side pressure calibration of oxygen-side Rainin SD-200 pump

11/20/95

Flow Setting	Suction	Discharge	Time to Fill 50ml Flask		Flow (ml/min)	Delta
	Pressure (psig)	Pressure (psig)	Min	Sec		
6	5	3550	8	12.23	6.095	0.095
6	5	3540	8	8.37	6.143	0.143
6	5	3540	8	19.12	6.011	0.011
6	5	3550	8	9.39	6.130	0.130
6	5	3550	8	11.14	6.108	0.108
8	5	3550	6	14.69	8.007	0.007
8	5	3540	6	7.75	8.158	0.158
8	5	3550	6	7.83	8.156	0.156
8	5	3540	6	9.42	8.121	0.121
8	5	3560	6	9.28	8.124	0.124
4	5	3560	12	14.19	4.086	0.086
4	5	3560	12	15.03	4.081	0.081
4	5	3570	12	23.51	4.035	0.035
4	5	3570	12	23.66	4.034	0.034
4	5	3570	12	26.56	4.018	0.018
2	5	3570	24	49.84	2.014	0.014
2	5	3570	12	21.86	2.022	0.022
2	5	3580	12	9.51	2.056	0.056
2	5	3580	12	23.59	2.017	0.017
2	5	3580	12	22.94	2.019	0.019

<i>Regression Statistics</i>	
Multiple R	0.99985
R Square	0.99969
Adjusted R Square	0.99967
Standard Error	0.04209
Observations	20

ANOVA

	<i>df</i>	<i>SS</i>	<i>MS</i>	<i>F</i>	<i>Significance F</i>
Regression	1	103.1088357	103.108836	58194.4579	4.79341E-33
Residual	18	0.031892368	0.0017718		
Total	19	103.140728			

	<i>Coefficients</i>	<i>Standard Error</i>	<i>t Stat</i>	<i>P-value</i>	<i>Lower 95%</i>	<i>Upper 95%</i>	<i>Lower 95.0%</i>	<i>Upper 95.0%</i>
Intercept	-0.005397	0.023055	-2.341E-01	8.176E-01	-0.05383	0.04304	-0.05383	0.04304
Flow setpoint (ml/min)	1.015425	0.004209	2.412E+02	4.793E-33	1.00658	1.02427	1.00658	1.02427

8.3 DETAILS OF ANALYTICAL METHODS

8.3.1 Liquid feed and effluent analysis

Splitless/autosampler analysis of methanol in an aqueous matrix. Method employs a 2.5m Hydroguard (Restek) retention gap and uses an HP Nanoliter adapter for controlling the injection volume. Method developed by B. Phenix/J. DiNaro 9/12/95. Recalibrated 6/14/96 for new HP Chemstation software.

Column information: 530 μ m x 30m x 5 μ m DB-1 column

Method Change History

Operator	Date	Change Information
bd/jd	6/14/96 4:58:10 PM	
bd/jd	6/18/96 7:06:37 PM	
bp/jd	8/9/96 10:45:15 AM	
bp/jd	10/4/96 11:03:34 AM	
bp/jd	7/14/97 10:40:30 PM	
bp/jd	7/14/97 10:51:29 PM	Confirmed 7/14/97 BP

Run Time Checklist

Pre-Run Cmd/Macro: off
Data Acquisition: on
Standard Data Analysis: on
Customized Data Analysis: off
Save GLP Data: off
Post-Run Cmd/Macro: off
Save Method with Data: off

Injection Source and Location

Injection Source: HP GC Injector
Injection Location: Front

HP GC Injector

Front Injector:
Sample Washes 4
Sample Pumps 3
Injection Volume 0.2 microliters
Syringe Size 10.0 microliters
On Column Off
Nanoliter Adapter On
PostInj Solvent A Washes 3

PostInj Solvent B Washes 0
 Viscosity Delay 2 seconds
 Plunger Speed Fast

Back Injector:
 No parameters specified

OVEN/DET

Runtime (min): 3.0

Zone Temperatures:

	State	Setpoint
Inl. A	ON	200 C.
Inl. B	ON	110 C.
Det. A	ON	110 C.
Det. B	ON	200 C.
Aux.	ON	110 C.

Oven Zone:

Oven max 220 C.
 Equib Time 1.00 Min.
 Oven State ON
 Cryo State OFF
 Ambient 25 C.
 Cryo Blast OFF

Oven Program:

Setpoint
 Initial Temp.: 70 C.
 Initial Time: 3.00 Min.

Level	Rate (C/min.)	Final Temp.(C)	Final Time (min)
1	0.00	0	0.00

Purge Valve Settings

Purge A/B

	Init Value	On Time (Min.)	Off Time (Min.)
A (Valve 3)	Off	0.50	2.50
B (Valve 4)	Off	0.00	0.00

A - Splitless Injection: Yes
 B - Splitless Injection: No

Valves/Relays Information**Initial Setpoints:****5890 Valves:**

Valve 1: Off
Valve 2: Off
Valve 3 (Purge A): Off
Valve 4 (Purge B): Off

Detector Information**Detector A:**

Type TCD
State OFF

Detector B:

Type FID
State ON

Timed Events:

Events:	Value:	Time:
Initial TCD A Sensitivity	Low	Initial
Initial TCD A Polarity	+	Initial

Signal Information

Save Data: Signal 1

Signal 1:**SignalDet. B**

Data rate 20.000 Hz.
Peakwidth 0.013 min.
Start Time 0.00 min.
Stop Time 650.00 min.

Signal 2:**SignalDet. B**

Data rate 10.000 Hz.
Peakwidth 0.027 min.
Start Time 0.00 min.
Stop Time 650.00 min.

Integration Events

Results will be produced with the enhanced integrator.

Signal Specific Integration Event Table "Event_FID1B"

Event	Value	Time	
Initial Area Reject	200.000	Initial	
Initial Slope Sensitivity	1364.521	Initial	
Initial Peak Width	0.004	Initial	
Initial Peak Height	1.000	Initial	
Initial Shoulders	OFF	Initial	
Area Sum ON	1.800		
Area Sum OFF	2.300		

Apply Manual Integration Events: No

Calibration Table

Calibration for methanol 6/9/96

Calib. Data Modified: Sunday, June 09, 1996 5:10:55 PM

Calculate: External Standard

Based on: Peak Area

Rel. Reference Window : 10.000 %
 Abs. Reference Window : 0.000 min
 Rel. Non-ref. Window : 10.000 %
 Abs. Non-ref. Window : 0.000 min
 Uncalibrated Peaks : compound name not specified
 Partial Calibration : Yes, identified peaks are recalibrated
 Correct All Ret. Times: No, only for identified peaks

Curve Type: Linear
 Origin: Ignored
 Weight: Equal

Recalibration Settings:
 Average Response : No Update
 Average Retention Time: No Update

Calibration Report Options :
 Printout of recalibrations within a sequence:
 Calibration Table after Recalibration

Normal Report after Recalibration

Signal 1: FID1 B,

RetTime [min]	Lvl Sig	Amount [wppm]	Area	Amt/Area	Ref Grp	Name
2.100	1 1	102.88000	6.30482e4	1.63177e-3		Methanol
	6	303.73000	1.81226e5	1.67597e-3		
	5	601.46000	3.68264e5	1.63323e-3		
	4	902.20000	5.51161e5	1.63691e-3		
	3	1202.93000	7.26621e5	1.65551e-3		
	2	1503.66000	9.10887e5	1.65076e-3		

Gas flowrates for Liquid Feed and Effluent Method:

Method Info: Splitless; autosampler
 Method Filename: MEOHAUTO
 Method Location: HP 5890 Series II TCD/FID
 Comments: Calibrated for methanol, benzene and phenol
 Date of Initial Method Development: 3/13/95
 Current Date: 6/18/96

Gas Pressures and Flowrates (@ zone temperatures specified above):

Gas	Cylinder Pressure (psia)	Local Regulator Pressure (psia)	Carrier*	Flowrate (ml/min) Carrier+Gas**	Gas***
Helium Carrier	65	N/A	4.5	N/A	4.50
FID Hydrogen	60	17	4	33.9	29.90
FID Air	80	35	1.6	302	300.40
FID Aux	60	N/A	1.7	37.6	35.90

	Flowrate (ml/min)
Purge:	3.2
Split:	50.5
Carrier:	4.5

Column Headpressure (psia): 3.2

Summary Info:

Carrier + Aux: 40.40

(Carrier+Aux)/H2 1.35

:

Split ratio: 11.22

* Carrier (He) flowrate measured at detector outlet as either He, H2, Air, or N2

** Combined carrier (He) and support gas (H2, Air, or N2) flowrate measured as support gas of interest.

*** Difference between (carrier+gas) and (carrier)

8.3.2 Vapor effluent analysis of light gases

New (8/95) method for analyzing light gases (H₂,O₂,N₂,CO,CO₂,CH₄) with maximum oven temperature of 225 C (for FID operation). Method employs column switching between 5'x1/8" 60/80 Carboxen 1000 and 8'x1/8" 60/80 Molecular Sieve 5A columns using 10-port switching valve. Developed by bp/jd based on original Holgate Porapak-T/Mol Sieve 5A method.

Column information: 5' x 1/8" 60/80 Carboxen 1000 (w/ retaining screens at both ends)

8' x 1/8" 60/80 Molecular Sieve 5A (w/ retaining screens at both ends)

SAMPLE IN/OUT LINES ON 10-PORT VALVE ARE CAPPED.

Order of elution: H₂,O₂,N₂,CO,CO₂,CH₄

Method Change History

Operator	Date	Change Information
bp/jd	8/22/96 11:35:13 AM	changed n2 RT
bp/jd	12/9/96 12:59:16 PM	
bp/jd	2/19/97 1:26:13 PM	
bp/jd	7/14/97 11:47:04 PM	Confirmed 7/14/97 BP

Run Time Checklist

Pre-Run Cmd/Macro: off
Data Acquisition: on
Standard Data Analysis: on
Customized Data Analysis: off
Save GLP Data: off
Post-Run Cmd/Macro: off
Save Method with Data: off

Injection Source and Location

Injection Source: Manual
Injection Location: Back

HP GC Injector

Front Injector:
Sample Washes 4
Sample Pumps 3
Injection Volume 0.2 microliters
Syringe Size 10.0 microliters
On Column Off
Nanoliter Adapter On
PostInj Solvent A Washes 3
PostInj Solvent B Washes 0

Viscosity Delay 2 seconds
 Plunger Speed Fast

Back Injector:
 No parameters specified

OVEN\DET

Runtime (min): 12.8

Zone Temperatures:

	State	Setpoint
Inl. A	ON	200 C.
Inl. B	ON	110 C.
Det. A	ON	110 C.
Det. B	ON	200 C.
Aux.	ON	110 C.

Oven Zone:

Oven max 220 C.
 Equib Time 2.00 Min.
 Oven State ON
 Cryo State OFF
 Ambient 25 C.
 Cryo Blast OFF

Oven Program:

	Setpoint		
Initial Temp.:	80 C.		
Initial Time:	4.00 Min.		
Level	Rate (C/min.)	Final Temp.(C)	Final Time (min)
1	40.0	110	8.00

Purge Valve Settings

Purge A/B

	Init Value	On Time (Min.)	Off Time (Min.)
A (Valve 3)	Off	0.00	0.00
B (Valve 4)	Off	0.00	0.00

A - Splitless Injection: No
 B - Splitless Injection: No

Valves/Relays Information

Initial Setpoints:

5890 Valves:

Valve 1: On
 Valve 2: Off
 Valve 3 (Purge A): Off
 Valve 4 (Purge B): Off

Valve/Relay Time Table:

Time	Name	State	Comment
7.90	Valve 1	Off	Switch column order

Detector Information

Detector A:

Type TCD
 State ON

Detector B:

Type FID
 State OFF

Timed Events:

Events:	Value:	Time:
Initial TCD A Sensitivity	Low	Initial
Initial TCD A Polarity	+	Initial

Signal Information

Save Data: Signal 1
 Signal 1:
 Signal Det. A
 Data rate 10.000 Hz.
 Peakwidth 0.027 min.
 Start Time 0.00 min.
 Stop Time 650.00 min.

Signal 2:
 Signal Det. A
 Data rate 10.000 Hz.
 Peakwidth 0.027 min.
 Start Time 0.00 min.
 Stop Time 650.00 min.

Integration Events

Results will be produced with the standard integrator.

Signal Specific Integration Event Table "Event_TCD1A"

Event	Value	Time
Initial Area Reject	1000.000	Initial
Initial Threshold	-2.000	Initial
Initial Peak Width	0.040	Initial
Initial Shoulders	OFF	Initial
Baseline Now	0.000	7.872
Negative Peak	ON	7.890
Negative Peak	OFF	8.116

Apply Manual Integration Events: No

Calibration Table

Calibration for Permanent Gases, Method NEWGAS

Calib. Data Modified : Monday, December 09, 1996 12:35:05 PM

Calculate : External Standard

Based on : Peak Area

Rel. Reference Window : 8.000 %
 Abs. Reference Window : 0.000 min
 Rel. Non-ref. Window : 15.000 %
 Abs. Non-ref. Window : 0.000 min
 Uncalibrated peaks RF : 2.50000e-4
 Partial Calibration : Yes, identified peaks are recalibrated
 Correct All Ret. Times: No, only for identified peaks

Curve Type: Linear
 Origin: Included
 Weight: Equal

Recalibration Settings:
 Average Response : Average all calibrations
 Average Retention Time: Floating Average New 75

Calibration Report Options :

Printout of recalibrations within a sequence:

Calibration Table after Recalibration

Normal Report after Recalibration

If the sequence is done with bracketing:

Results of first cycle (ending previous bracket)

Signal 1: TCD1 A,

RetTime [min]	Lvl Sig	Amount [uL]	Area	Amt/Area	Ref Grp Name
3.600	1 6	10.00000	1.91069e4	5.23370e-4	Oxygen
	3	30.00000	6.00444e4	4.99630e-4	
	1	50.00000	9.95223e4	5.02400e-4	
	2	70.00000	1.34365e5	5.20970e-4	
	4	100.00000	2.00489e5	4.98780e-4	
4.510	1 2	10.00000	2.16389e4	4.62130e-4	Nitrogen
	4	30.00000	6.16219e4	4.86840e-4	
	1	50.00000	1.00817e5	4.95950e-4	
	3	70.00000	1.42175e5	4.92350e-4	
	5	100.00000	2.08325e5	4.80020e-4	
7.200	1 2	10.00000	2.03645e4	4.91050e-4	Carbon Monoxide
	4	30.00000	5.96528e4	5.02910e-4	
	1	50.00000	9.98403e4	5.00800e-4	
	3	70.00000	1.46242e5	4.78660e-4	
	6	100.00000	2.07508e5	4.81910e-4	
	7	150.00000	3.15670e5	4.75180e-4	
	8	200.00000	4.16502e5	4.80190e-4	
9.300	1 2	10.00000	2.42254e4	4.12790e-4	Carbon Dioxide
	6	30.00000	7.29643e4	4.11160e-4	
	1	50.00000	1.21803e5	4.10500e-4	
	5	70.00000	1.72473e5	4.05860e-4	
	3	100.00000	2.44894e5	4.08340e-4	
11.527	1 2	10.00000	1.59916e4	6.25330e-4	Methane

4	30.00000	4.99459e4	6.00650e-4
1	50.00000	8.77855e4	5.69570e-4
3	70.00000	1.20232e5	5.82210e-4
5	100.00000	1.64185e5	6.09070e-4

Gas flowrates for analysis of light gases:

Method Info: Manual injection
 Method Filename: NEWGAS
 Method Location: HP 5890 Series II TCD/FID and HP 6890 TCD/FID
 Comments: Calibrated for oxygen, nitrogen, carbon monoxide, carbon dioxide, methane
 Date of Initial Development: 8/95
 Current Date: 8/95

Gas Pressures and Flowrates (@ zone temperatures specified above):

Gas	Cylinder Pressure (psia)	Local Regulator Pressure (psia)	Flowrate (ml/min)		
			Carrier*	Carrier+Gas**	Gas***
Helium Carrier	65		28.5	-	-
Helium Reference	65		28.5	64.6	36.1
FID Hydrogen	NA	NA	-	-	-
FID Air	NA	NA	-	-	-
FID Aux	NA	N/A	-	-	-

Column Headpressure (psia): 50

ATTN•CHART•DELAY: 3 (Enter) 10 (Enter) 0.08 (Enter)
Time Device Function Name: 0.00 (Enter) EXT (SHIFT X)X_7 (Enter) (NEXT LINE)
(ACCEPT SECTN)

The printer should print out the conditions that were just entered. If the conditions are wrong, turn the power off to clear the memory, then turn the power back on and start again.

Next, hit: (SETUP)
Analyzer: 1 (Enter)
Detector: 2 (Enter)
Method: 1 (Enter)
(Enter)
(Enter)
(Enter)
(Enter)

At this point, the GC needs to heat up. To view the current values and setpoints, hit:
(DISPLAY ACTUAL) 1 (Enter)

When all the light go out, analyzer 1 is ready. Now the plotter needs to be reconnected, push:
(PLOT) "0" (0 should be showing)
press the spacebar

Analyzer: 1 (Enter)
Detector: 2 (Enter)
Mode: 0 (Enter)

When the analyzer is ready (10-15 min.) it prints:
ANAL...1...DET...2...METH...1...1...FILE..._
RUN..._
SENSITIVITIES...200...20

To Modify a Method:

The analyzer needs to be voided before modification, hit:
VOID (V) 1 (Enter)
MOD (SHIFT M) 1 (Enter)
ACCPT SECTN or use NEXT LINE to get to the line you want to modify (see manual)

After making any changes, connect the method to the analyzer, hit:
SETUP
Analyzer: 1 (Enter)

Detector: 1 (Enter)
 Method: 1 (Enter)
 (Enter)
 (Enter)
 (Enter)
 (Enter)

To Change the Nitrogen Cylinder:

Note: Do not let the cylinder run out of gas. Pressure control switch turns the GC off. To replace the cylinder before it is empty, make sure all buttons on the analyzer are out (this disconnects the power to the filament). After the new cylinder is installed, push in the N1 button to reestablish the current to the bridge without losing the programmed method.

<SHIFT> <:> A : all bulbs will light in sections (press enter to see each set)

Gas flowrates for analysis of hydrogen:

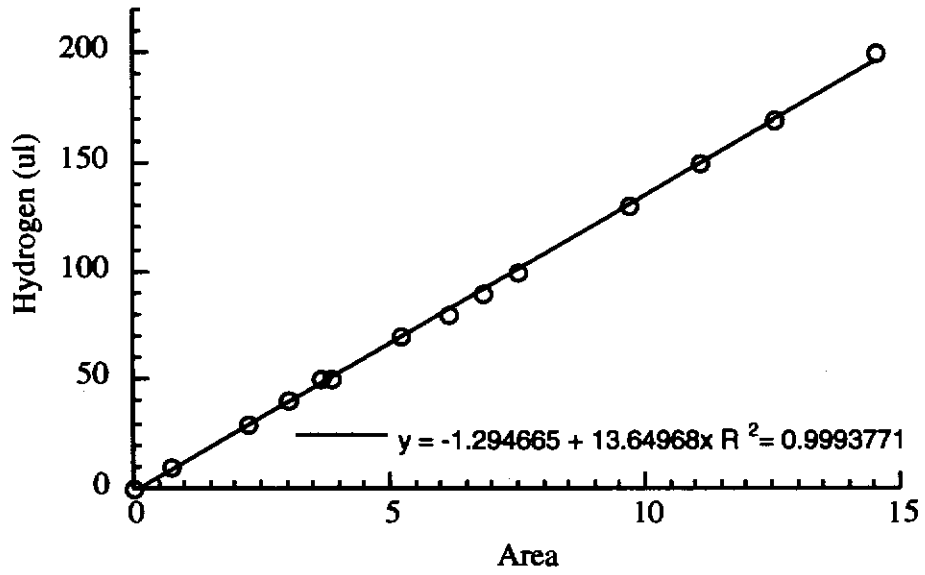
Method Info: Manual injection
 Method Filename: NA
 Method Location: Perkin Elmer Sigma 1B
 Comments: Calibrated for hydrogen
 Date of Initial Development: -
 Current Date: 3/19/96

Gas Pressures and Flowrates (@ zone temperatures specified above):

Gas	Cylinder Pressure (psia)	Local Regulator Pressure (psia)	Flowrate (ml/min)		
			Carrier*	Carrier+Gas**	Gas***
Nitrogen Carrier	70		40	-	-
Nitrogen Ref	70		-	-	-
FID Hydrogen	NA	NA	-	-	-
FID Air	NA	NA	-	-	-
FID Aux	NA	N/A	-	-	-

Column Headpressure (psia): 65

Hydrogen Calibration for Perkin Elmer Sigma 1B
3/19/96



8.4 SUMMARY OF TUBULAR REACTOR GEOMETRIES

Number	Matl	Length (m)	ID-calc (in)	Volume-measured (ml)	Volume-calc (ml)	Vol. Error (%)	ID (backcalcd) (in)	Surface Area (cm ²)	S/V (cm ⁻¹)	Status
5	Inc625	4.71	0.067	10.674	10.7134	0.370	0.067	251.8	23.5	Original Holgate reactor OK
6	316SS	8.176	0.041	8.5922 8.6173 8.6383 8.616 0.046	6.9638 6.9638 6.9638	-23.4 -23.7 -24.0 -23.72 0.66	0.046 0.046 0.046 0.046 0.00	297.1 297.5 297.9 297.5 0.80	34.6 34.5 34.5 34.5 0.09	Siezed into 316SS end fittings; Cone removed to try with Valco cross
7	316SS	2.499								Siezed into 316SS end fittings
8	316SS	8.175	0.041	8.8779 8.8318 8.9032 8.871 0.072	6.9633 6.9633 6.9633	-27.5 -26.8 -27.9 -27.40 1.04	0.046 0.046 0.046 0.046 0.000	302.0 301.2 302.4 301.88 1.23	34.0 34.1 34.0 34.03 0.14	Cone removed to try with Valco cross
9	316SS	2.499	0.041	2.603 2.602 2.605 2.603 0.003	2.1286 2.1286 2.1286	-22.3 -22.2 -22.4 -22.30 0.14	0.045 0.045 0.045 0.045 0.000	90.4 90.4 90.4 90.42 0.05	34.7 34.7 34.7 34.73 0.02	Cone fitting replaced with taper seal

Summary of tubular reactor geometries, continued.

Number	Matl	Length (m)	ID-calc (in)	Volume-measured (ml)	Volume-calc (ml)	Vol. Error (%)	ID (backcalcd) (in)	Surface Area (cm ²)	S/V (cm ⁻¹)	Status
10	Inc625	2.499	0.041	2.0698	2.1286	2.8	0.040	80.6	39.0	OK
				2.0179	2.1286	5.2	0.040	79.6	39.4	
				2.0218	2.1286	5.0	0.040	79.7	39.4	
				2.036		4.33	0.040	79.97	39.27	
				0.058		2.71	0.001	1.13	0.55	
11	316SS	6.067	0.055	9.7926	9.3000	-5.3	0.056	273.2	27.9	OK
				9.6840	9.3000	-4.1	0.056	271.7	28.1	
				9.8384	9.3000	-5.8	0.057	273.9	27.8	
				9.772		-5.07	0.056	272.95	27.93	
				0.159		1.70	0.000	2.22	0.23	
12	Inc625	7.368	0.041	6.2286	6.2759	0.75	0.041	240.1	38.6	OK
				6.1977	6.2759	1.25	0.041	239.5	38.7	
				6.2387	6.2759	0.59	0.041	240.3	38.5	
				6.222		0.86	0.041	240.01	38.58	
				0.043		0.68	0.000	0.82	0.13	
13	Inc625	11.227	0.041	9.1874	9.5629	3.93	0.040	360.0	39.2	OK
				9.3588	9.5629	2.13	0.041	363.4	38.8	
				9.2492	9.5629	3.28	0.040	361.2	39.1	
				9.265		3.11	0.040	361.54	39.02	
				0.174		1.81	0.000	3.38	0.36	
14	Inc625	7.3	0.041	5.2531	6.2180	15.52	0.038	219.5	41.8	Newly Constructed 4/14/97 Machine shop added spacer
				5.3055	6.2180	14.67	0.038	220.6	41.6	
				5.3292	6.2180	14.29	0.038	221.1	41.5	
				5.296		14.83	0.038	220.41	41.62	
				0.078		1.25	0.000	1.62	0.31	

8.5 SUMMARY OF DESIGN CHANGES TO BENCH-SCALE REACTOR SYSTEM

The following is a summary of the changes made to the original Holgate reactor system when the bench-scale reactor and analytical instrumentation were relocated to 66-053:

1. Duplex LDC Analytical/Milton Roy feed pump was replaced with two Rainin SD-200 semi-preparative HPLC pumps.
2. Sandbath preheating system was redesigned as detailed in Section 3.1.2.
3. Porapak-T column used in light gas analysis (Section 3.2.2.1) was replaced with a Carboxen 1000 column. This modification raised the maximum working temperature of the GC oven from 190 °C to 225 °C.
4. Rupture disk on effluent feed line replaced with one rated for 4,500 psig burst pressure.
5. Air supply to main sandbath rerouted from Bldg 66 low- to high-pressure air supply. Air supply regulator pressure set to 60 psig as recommended by Techne.
6. The ¼" x 0.049" wall feed lines connecting the saturators and feed pumps were replaced with ¼" x 0.085" wall lines to decrease holdup volume upstream of the pumps and to shorten the length of time required to attain steady-state operation.
7. All Cajon tees and crosses were removed from the system and replaced with equivalent Swagelok components. Cajon components were found to be prone to leakage at elevated pressures.
8. Each gas chromatograph was placed on a separate, dedicated electrical circuit to reduce the possibility of electrical overload.
9. Pressure gauge on helium line leading to water feed tank replaced.

8.6 FORTRAN PROGRAM FOR MONTE CARLO SIMULATION

```

    program h2o2mccol2
c
c   Date:           12/11/95
c   Developed by:   B. Phenix and J. DiNaro
c   Version:        2.0   -- final version used in paper (8 rev rxns, 7 species)
c                   1.0   -- 8 rxns (2 rev), 7 species (5/95)
c   Summary:
c   This program accepts pseudo-random, log-normal rate constants
c   generated by the DEMM driver program and passes them to LSODE
c   for repetitive solution of the species conservation equations.
c
c   Required files and routines:
c   LSODE           stiff ODE solver (Hindmarsh)
c   h2o2mccol.in   input file containing initial conditions, rate constant central
c                   values and uncertainty factors, and LSODE flag variables
c   rtecnsts.pnt   DEMM-generated file containing sampling points
c   fex            user-supplied subroutine containing species ODEs
c
c   implicit double precision (a-h,o-z)
c   external fex, jdum
c   parameter(neq=7)
c   double precision yh2(13,15000)
c   double precision k1,k2,k3,k4,k5,k6,k7,k8,km1,km2,km3,km4,km5,
c   1 km6,km7,km8,keq1,keq2,keq3,keq4,keq5,keq6,keq7,keq8
c   dimension y(neq),rwork(134),iwork(27),yout(neq,100),yinit(neq)
c   common /rates/ k1,k2,k3,k4,k5,k6,k7,k8,km1,km2,km3,km4,km5,
c   1 km6,km7,km8
c
c   Open user-supplied h2o2mccol.in, rtecnsts.pnt, and output files
c   open(unit=15,file='h2o2mccol.in',status='old')
c   open(unit=12,file='rtecnsts.pnt',status='old')
c   open(unit=10,file='h2o2mccol.out',status='unknown')
c   open(unit=6,file='mcerr.out',status='unknown')
c
c   Read in initial conditions in from h2o2mccol.in
c   read(15,*)(yinit(i),i=1,neq)
c
c   Read and set time steps and flag variables for LSODE
c   read(15,*)tout
c   read(15,*)tfinal

```

```
read(15,*)itol
read(15,*)rtol
read(15,*)atol
read(15,*)itask
read(15,*)istate
read(15,*)iopt
read(15,*)lrw
read(15,*)liw
read(15,*)mf
read(15,*)itmax
c
rwork(5)=0.0d0
rwork(6)=0.0d0
rwork(7)=0.0d0
iwork(5)=0
iwork(6)=10000
iwork(7)=0
nerr=0
dnerr=0.0d0
delt=tout
istep=tfinal/tout
ditmax=itmax

c Begin Monte Carlo iteration (outer loop), itmax = number of sampling sets
do 60 i=1,itmax

c Read in one set of sampled rate constants and equilibrium constants which were
c generated by DEMM from reported central values and uncertainty factors
c
  read(12,*)km1,keq1,k2,keq2,k3,keq3,k4,keq4,km5,keq5,km6,keq6,
  1 k7,keq7,k8,keq8
c
c Calculate reverse rate constants from sampled equilibrium and forward rate constants
k1=km1*keq1
km2=k2*keq2
km3=k3*keq3
km4=k4*keq4
k5=km5*keq5
k6=km6*keq6
km7=k7*keq7
km8=k8*keq8
```

```
c   Define initial species concentrations for LSODE at each new iteration
      do 22 k=1,neq
        y(k)=yinit(k)
22  continue

c   Set starting time and time step size at each new iteration
      t=0.0d0
      tout=delt

c   Set istate variable to 1 for initial LSODE pass
      istate=1

c   Begin LSODE loop (inner loop)
      do 40 iout = 1,istep
        call lsode(fex,neq,y,t,tout,itol,rtol,atol,itask,istate,
1       iopt,rwork,lrw,iwork,liw,jdum,mf)

c   Skip to next set of random variates if LSODE doesn't converge
      if(istate.lt.0) then
        nerr=nerr+1
        dnerr=nerr
        write(6,*)i,iout
        write(6,27)istate
27      format(///22h error halt.. istate=,i3)
        istate=1
        go to 60
      endif

c
c   Store output concentration for species 2 at desired time intervals
      if(iout.eq.1)then
        yh2(1,i)=y(2)
      else if (iout.eq.2)then
        yh2(2,i)=y(2)
      else if (iout.eq.3)then
        yh2(3,i)=y(2)
      else if (iout.eq.4)then
        yh2(4,i)=y(2)
      else if (iout.eq.5)then
        yh2(5,i)=y(2)
      else if (iout.eq.6)then
        yh2(6,i)=y(2)
      else if (iout.eq.8)then
```

```
      yh2(7,i)=y(2)
    else if (iout.eq.10)then
      yh2(8,i)=y(2)
    else if (iout.eq.12)then
      yh2(9,i)=y(2)
    else if (iout.eq.14)then
      yh2(10,i)=y(2)
    else if (iout.eq.16)then
      yh2(11,i)=y(2)
    else if (iout.eq.18)then
      yh2(12,i)=y(2)
    else if (iout.eq.20)then
      yh2(13,i)=y(2)
    end if

c    Increment time step
      t = tout
      tout = tout+delt
40  continue
60  continue

c    Write output species concentrations as a function of time to file
      do 80 j=1,itmax
        write(10,75)yh2(1,j),yh2(2,j),yh2(3,j),yh2(4,j),yh2(5,j),
1    yh2(6,j),yh2(7,j),yh2(8,j),yh2(9,j),yh2(10,j),yh2(11,j),
1    yh2(12,j),yh2(13,j)
75  format(13(e11.4,3X))
80  continue

      stop
      end

c    Reaction mechanism subroutine
      subroutine fex (neq, t, y, ydot)
      implicit double precision (a-h,o-z)
      dimension y(7), ydot(7)
      double precision k1,k2,k3,k4,k5,k6,k7,k8,km1,km2,km3,km4,
1 km5,km6,km7,km8
      common /rates/ k1,k2,k3,k4,k5,k6,k7,k8,km1,km2,km3,km4,km5,
1 km6,km7,km8

c    Define species conservation equations
```

```

ydot(1) = k1*y(5)-km1*y(4)*y(1)+k2*y(2)*y(4)-km2*y(5)*y(1)-
+ k3*y(1)*y(3)+km3*y(6)+k6*y(2)*y(6)-km6*y(7)*y(1)
ydot(2) = -k2*y(2)*y(4)+km2*y(5)*y(1)-k6*y(2)*y(6)+
+ km6*y(7)*y(1)
ydot(3) = -k3*y(1)*y(3)+km3*y(6)+k4*y(6)**2-km4*y(7)*y(3)+
+ k8*y(6)*y(4)-km8*y(5)*y(3)
ydot(4) = k1*y(5)-km1*y(1)*y(4)-k2*y(2)*y(4)+km2*y(5)*y(1)+
+ k5*y(6)*y(5)-km5*y(7)*y(4)+2.0d0*k7*y(7)-
+ 2.0d0*km7*y(4)**2-k8*y(6)*y(4)+km8*y(5)*y(3)
ydot(5) = -k1*y(5)+km1*y(4)*y(1)+k2*y(2)*y(4)-km2*y(5)*y(1)
+ -k5*y(6)*y(5)+km5*y(7)*y(4)+k8*y(6)*y(4)
+ -km8*y(5)*y(3)
ydot(6) = k3*y(1)*y(3)-km3*y(6)-2.0d0*k4*y(6)**2
+ +2.0d0*km4*y(7)*y(3)-k5*y(6)*y(5)+km5*y(7)*y(4)
+ -k6*y(2)*y(6)+km6*y(7)*y(1)-k8*y(6)*y(4)
+ +km8*y(5)*y(3)
ydot(7) = k4*y(6)**2-km4*y(7)*y(3)+k5*y(6)*y(5)
+ -km5*y(7)*y(4)+k6*y(2)*y(6)-km6*y(7)*y(1)
+ -k7*y(7)+km7*y(4)**2

```

```

return
end

```

c Dummy JDUM subroutine
subroutine jdum(neq,t,y,ml,mu,pd,nrpd)
return
end

```

include 'lsode.f'

```

Chapter 9:

References

Abraham, M.A. and Klein, M.T. (1985) "Pyrolysis of benzylphenylamine neat and with tetralin, methanol, and water solvents." *Ind. Eng. Chem. Proc. Des. Dev.* **24**: 300-306.

Abraham, M.A. and Klein, M.T. (1987) "Solvent effects during the reaction of coal model compounds." in *ACS Symposium Series 329: Supercritical Fluids: Chemical and Engineering Principles and Applications*. T.G. Squires and M.E. Paulaitis, Eds., Washington, D.C., American Chemical Society: 67-76.

Alkam, M.K., Pai, V.M., Butler, P.B., and Pitz, W.J. (1996) "Methanol and hydrogen oxidation kinetics in water at supercritical states." *Combust. Flame* **106**: 110-130.

Amin, S., Reid, R.C., and Modell, M. (1975) "Reforming and decomposition of glucose in an aqueous phase." Intersociety Conference on Environmental Systems, San Francisco, CA.

Armellini, F.J. (1993) "Phase equilibria and precipitation phenomena of sodium chloride and sodium sulfate in sub- and supercritical water." PhD. thesis, Department of Chemical Engineering, Massachusetts Institute of Technology, Cambridge, MA.

Atherton, R.W., Schainker, R.B., and Ducot, E.R. (1975) "On the statistical sensitivity analysis of models for chemical kinetics." *AIChE Journal* **21**(2): 441-448.

Atkinson, R., Baulch, D.L., Cox, R.A., Hampson, R.F., Kerr, J.A., and Troe, J. (1989) *J. Phys. Chem. Ref. Data* **18**: 881.

Barnes, C.M., Marshall, R.W., Jr., Mizia, R.E., Herring, J.S., and Peterson, E.S. (1993) "Identification of technical constraints for treatment of DOE mixed waste by supercritical water oxidation." Idaho National Engineering Laboratory, INEL/EG&G, EGG-WTD-10768.

Baulch, D.L., Cobos, C.J., Cox, R.A., Esser, C., Frank, P., Just, T., Kerr, J.A., et al. (1992) "Evaluated kinetic data for combustion modelling." *J. Phys. Chem. Ref. Data* **21**(411-737).

Baur, H.C.L. (1991) "A novel approach to the hydrolysis of ethers with added salts in supercritical aqueous solution." M.S. thesis, Department of Chemical Engineering, Eindhoven University of Technology, Eindhoven, The Netherlands.

- Bauschlicher, C.W. and Partridge, H. (1993) "An accurate determination of the HO₂ heat of formation." *Chem. Phys. Lett.* **208**(3,4): 241-246.
- Benson, B.B., Krause, D., and Peterson, M.A. (1979) "The solubility and isotopic fractionation of gases in dilute aqueous solution. I. Oxygen." *J. Sol. Chem.* **8**(9): 655-690.
- Beulow, S.J. (1990) "Destruction of propellant components in supercritical water." Los Alamos National Laboratory, LA-UR-90-1338.
- Beulow, S.J. (1992) "Chemical reactions of nitrogen containing compounds in supercritical water." Workshop on Federal Programs Involving Supercritical Water Oxidation, Gaithersburg, MD.
- Bourhis, A.L., Swallow, K.C., Hong, G.T., and Killilea, W.R. (1995) "The use of rate enhancers in supercritical water oxidation." in *ACS Symposium Series, 608 (Innovations in supercritical fluids)*. K.W. Hutchenson and N.R. Foster, Eds., Washington, D.C., American Chemical Society: 338-347.
- Bramlette, T.T., Mills, B.E., and Kencken, K.R. (1990) "Destruction of DOE/DP surrogate wastes with supercritical water oxidation technology." Sandia National Laboratory, SAND90-8229.
- Brelvi, S.W. and O'Connell, J.P. (1972) "Corresponding states correlations for liquid compressibility and partial molar volumes of gases at infinite dilution in liquids." *AIChE Journal* **18**(6): 1239-1243.
- Brennecke, J.F. (1993) "Spectroscopic investigations of reactions in supercritical fluids." in *ACS Symposium Series 514*. E. Kiran and J.F. Brennecke, Eds., Washington, D.C., American Chemical Society.
- Brock, E., Oshima, Y., Savage, P., and Barker, J. (1996) "Kinetics and mechanism of methanol oxidation in supercritical water." *J. Phys. Chem.* **100**: 15834-15842.
- Brock, E.E. and Savage, P.E. (1995) "Detailed chemical kinetics model for supercritical water oxidation of C₁ compounds and H₂." *AIChE Journal* **41**(8): 1874-1888.
- Butler, P.B., Bergan, N.E., Bramlette, T.T., Pitz, W.J., and Westbrook, C.K. (1991) "Oxidation of hazardous waste in supercritical water: A comparison of modeling and experimental results for methanol destruction." U.S. Department of Energy Report, DE91-017097.

Butler, P.B., Bergan, N.E., Bramlette, T.T., Westbrook, C.K., and Pitz, W.J. (1991) "Oxidation of hazardous waste in supercritical water Part I: A comparison of modeling and experimental results for methanol destruction." U.S. Department of Energy Report, DE92-008565.

Chase, M.W., Davies, C.A., Downey, J.R., Frurip, D.J., McDonald, R.A., and Syverud, A.N. (1985) *JANAF Thermochemical Tables.*, American Chemical Society, American Institute for Physics, National Bureau of Standards.

Christoforakos, M. and Franck, E.U. (1986) "An equation of state for binary fluid mixtures to high temperatures and pressures." *Ber. Bunsenges. Phys. Chem.* **90**: 780-789.

Cobos, C.J. and Troe, J. (1985) "The influence of potential energy parameters on the reaction $H + CH_3 \rightleftharpoons CH_4$." *Chem. Phys. Lett.* **113**(5): 419-424.

Cozewith, C. and Busko, M. (1989) "Design correlations for mixing tees." *Ind. Eng. Chem. Res.* **28**: 1521-1530.

Cozewith, C., Ver Strate, G., Dalton, T.J., Frederick, J.W., and Ponzi, P.R. (1991) "Computer simulation of tee mixers for nonreactive and reactive flows." *Ind. Eng. Chem. Res.* **30**: 270-275.

Croiset, E., Rice, S.F., and Hanush, R.G. (1997) "Hydrogen peroxide decomposition in supercritical water." *AIChE Journal*: submitted.

Dagaut, P., Cathonnet, M., and Boettner, J.-C. (1996) "Chemical kinetic modeling of the supercritical water oxidation of methanol." *J. Supercrit. Fluids* **98**: 33-42.

Dagaut, P., Daney de Marcillac, B., Tan, Y., Cathonnet, M., and Boettner, J.-C. (1995) "Chemical kinetic modeling of the supercritical water oxidation of simple fuels: H_2 , CO , CH_4 ." *J. Chim. Phys.* **92**: 1124-1141.

DeMore, W.B., Sander, S.P., Golden, D.M., Hampson, R.F., Kurylo, M.J., Howard, C.J., Ravishankara, A.R., et al. (1992) "Chemical kinetics and photochemical data for use in stratospheric modeling." NASA/Jet Propulsion Laboratory, Pasadena, JPL 92-20.

Derwent, R. and Øystein, H. (1988) "Application of sensitivity and uncertainty analysis techniques to a photochemical ozone model." *J. of Geophys. Res.* **93**(D3): 5185-5199.

Downey, K.W., Snow, R.H., Hazlebeck, D.A., and Roberts, A.J. (1995) "Corrosion and chemical agent destruction. Research on supercritical water oxidation of hazardous military

wastes." in *ACS Symposium Series 608 (Innovations in Supercritical Fluids)*. K.W. Hutchenson and N.R. Foster, Eds., Washington, D.C., American Chemical Society: 313-326.

Ehhalt, D.H., Chang, J.S., and Butler, D.M. (1979) "The probability distribution of the predicted CFM-induced ozone depletion." *J. of Geophys. Res.* **84**(C12): 7889-7894.

Fisher, E.R. and Armentrout, P.B. (1990) "Heat of formation of HO₂. A direct determination from guided ion beam studies of O₂⁺(²Π_g, v=0) + CH₄." *J. Phys. Chem.* **94**(11): 4396-4398.

Forney, L.J. and Gray, G.E. (1990) "Optimum design of a tee mixer for fast reactions." *AIChE Journal* **36**(11): 1773-1776.

Forney, L.J. and Lee, H.C. (1982) "Optimum dimensions for pipeline mixing at a T-junction." *AIChE Journal* **28**(6): 980-987.

Franck, E.U. (1970) "Water and aqueous solutions at high pressures and temperatures." *Pure Appl. Chem.* **24**: 13-30.

Franck, E.U. (1976) "Properties of water." in *High temperature , high pressure electrochemistry in aqueous solutions*. D. de G. Jones and R.W. Staehle, Eds., Houston, TX, National Association of Corrosion Engineers: 109-116.

Franck, E.U. (1983) "Thermophysical properties of supercritical fluids with special consideration of aqueous systems." *Fluid Phase Equil.* **10**: 211-222.

Franck, E.U. (1987) "Fluids at high temperatures and pressures." *J. Chem. Thermodynam.* **19**(225-242).

Gao, D., Stockwell, W.R., and Milford, J.B. (1996) "Global uncertainty analysis of a regional-scale gas-phase chemical mechanism." *J. of Geophys. Res.* **101**(C4): 9107-9119.

Gardiner, W.C. and Olson, D.B. (1980) "Chemical kinetics for high-temperature combustion." *Ann. Rev. Phys. Chem.* **31**: 377.

Gehrke, C., Schroeder, J., Schwarzer, D., Troe, J., and Voss, F. (1990) "Photoisomerizations of diphenylbutadiene in low-viscosity non-polar solvents: experimental manifestations of multidimensional Kramers behavior and cluster effects." *J. Chem. Phys.* **92**(8): 4805-4816.

Gilbert, R.G. and Smith, S.C. (1990) *Theory of unimolecular and recombination reactions*. Cambridge, MA, Blackwell Scientific Publications.

- Gloyna, E.F. and Li, L. (1995) "Supercritical water oxidation research." *Environ. Prog.* **14**(3): 182-192.
- Gorbaty, Y.E. and Kalinichev, A.G. (1995) "Hydrogen bonding in supercritical water. 1. Experimental results." *J. Phys. Chem.* **99**: 5336-5340.
- Gosman, A.D. and Simitovic, R. (1986) "An experimental study of confined jet mixing." *Chem. Eng. Sci.* **41**: 1853.
- Haar, L., Gallagher, J.S., and Kell, G.S. (1984) *NBS/NRC Steam Tables*. New York, NY, Hemisphere Publishing Corp.
- Hanush, R.G., Rice, S.F., Hunter, T.B., and Aiken, J.D. (1996) "Operation and performance of the supercritical fluids reactor (SFR)." Sandia National Laboratories, Livermore, CA, SAND96-8203.
- Held, T.J. (1993) "The oxidation of methanol, isobutene, and methyl tertiary-butyl ether." PhD. thesis, Mechanical and Aerospace Engineering, Princeton University, Princeton.
- Hindmarsh, A.C. (1983) "ODEPACK, a systematized collection of ODE solvers." in *Scientific Computing*. R.S. Stepleman, et al., Ed., Amsterdam, North-Holland: 55-64.
- Holgate, H.R. (1993) "Oxidation chemistry and kinetics in supercritical water: hydrogen, carbon monoxide, and glucose." PhD. thesis, Department of Chemical Engineering, Massachusetts Institute of Technology, Cambridge, MA.
- Holgate, H.R. and Tester, J.W. (1993) "Fundamental kinetics and mechanisms of hydrogen oxidation in supercritical water." *Combust. Sci. Technol.* **88**: 369-397.
- Holgate, H.R. and Tester, J.W. (1994) "Oxidation of hydrogen and carbon monoxide in sub- and supercritical water: Reaction kinetics, pathways, and water-density effects. 2. Elementary reaction modeling." *J. Phys. Chem.* **98**: 810-822.
- Hong, G.T., Fowler, P.K., Killilea, W.R., and Swallow, K.C. (1987) "Supercritical water oxidation: treatment of human waste and system configuration tradeoff study." 17th Intersociety Conference on Environmental Systems, Seattle, WA.
- Huppert, G.L., Wu, B.C., Townsend, S.H., Klein, M.T., and Paspek, S.C. (1989) "Hydrolysis in supercritical water: identification and implications of a polar transition state." *Ind. Eng. Chem. Res.* **28**: 161-165.

- Hynes, J.T. (1985) "Chemical reaction dynamics in solution." *Ann. Rev. Phys. Chem.* **36**: 573-597.
- Hynes, J.T. (1985) "The theory of reactions in solution." in *Theory of Chemical Reaction Dynamics, Vol. IV*. M. Baer, Ed., Boca Raton, FL, CRC Press, Inc.
- International, I.A. (1993) "INCO alloy C-276." Huntington, WV, IAI-23-1.
- Johnston, J.B., Hannah, R.E., Cunningham, V.L., Daggy, B.P., Sturm, F.J., and Kelly, R.M. (1988) "Destruction of pharmaceutical and biopharmaceutical wastes by the MODAR supercritical water oxidation process." *Biotechnology* **6**: 1423-1427.
- Kee, R.J., Grcar, J.F., Smooke, M.D., and Miller, J.A. (1988) Sandia National Laboratory, 85-8240/UC-2.
- Kee, R.J., Rupley, F.M., and Miller, J.A. (1989) "CHEMKIN II: A Fortran chemical kinetics package for the analysis of gas-phase chemical kinetics." Sandia National Laboratory, SAND89-8009.
- Kersten, R.J.A. (1991) "Hydrolysis of diphenylether in supercritical water." M.S. thesis, Department of Chemical Engineering, Eindhoven University of Technology, Eindhoven, The Netherlands.
- Kestin, J. and Sengers, J.V. (1986) "New international formulations for the thermodynamic properties of light and heavy water." *J. Phys. Chem. Ref. Data* **15**(1): 305-320.
- Kestin, J., Sengers, J.V., Kamgar-Parsi, B., and Levelt Sengers, J.M.H. (1984) "Thermodynamic properties of fluid water." *J. Phys. Chem. Ref. Data* **13**(16): 175-183.
- Killilea, W.R. and Swallow, K.C. (1992) "The fate of nitrogen in supercritical water oxidation." *J. Supercrit. Fluids* **5**(1): 72-78.
- Kim, T.J. (1994) "Gas-phase kinetic studies of the hydrogen-oxygen and carbon monoxide-hydrogen-oxygen systems." PhD thesis, Department of Mechanical Engineering, Princeton University, Princeton.
- Kirts, R.E. (1995) "Destruction of Navy hazardous wastes by supercritical water oxidation." Annual Meeting--Air Waste Management Association, 9.
- Klein, M.T., Torry, L.A., Wu, B.C., Townsend, S.H., and Paspek, S.C. (1990) "Hydrolysis in supercritical water: solvent effects as a probe of the reaction mechanism." *J. Supercrit. Fluids* **3**(4): 228-232.

- Ladanyi, B.M. and Hynes, J.T. (1986) "Transition-state solvent effects on atom transfer rates in solution." *J. Am. Chem. Soc.* **108**: 585-593.
- Lawson, J.R. and Klein, M.T. (1985) "Influence of water on guaiacol pyrolysis." *Ind. Eng. Chem. Fundam.* **24**: 203-208.
- Lee, D.S., Gloyna, E.F., and Li, L. (1990) "Efficiency of H₂O₂ and O₂ in supercritical water oxidation of 2,4-dichlorophenol and acetic acid." *J. Supercrit. Fluids* **3**: 249-255.
- Leung, K.M. and Lindstedt, R.P. (1995) "Detailed kinetic modeling of C1-C3 alkene diffusion flames." *Combust. Flame* **102**(N1): 129.
- Lewis, B. and von Elbe, G. (1987) *Combustion, flames, and detonations of gases, 3rd edition*. Orlando, FL, Academic Press, Inc.
- Lin, C.C. (1993) "Estimation of hydrogen peroxide decomposition rates in the boiling water reactor primary coolant circuit." *Nuc. Tech.* **103**: 257-261.
- Lin, C.C., Smith, F.R., Ichikawa, N., Baba, T., and Itow, M. (1991) "Decomposition of hydrogen peroxide in aqueous solutions at elevated temperatures." *Int. J. Chem. Kin.* **23**: 971-987.
- Lindemann, F.A. (1922) *Trans. Faraday Soc.* **17**: 598.
- Lindstedt, R.P. and Skevis, G. (1994) *Combust. Flame* **99**: 551.
- Marshall, W.L. and Franck, E.U. (1981) "Ion product of water substance, 0-1000 °C, 1-10,000 bars. New international formulation and its background." *J. Phys. Chem. Ref. Data* **10**(2): 295-304.
- Maruyama, T., Mizushima, T., and Hayashiguchi, S. (1983) "Optimum jet mixing in turbulent pipe flow." *Int. Chem. Eng.* **23**: 707.
- Maruyama, T., Suzuki, S., and Mizushima, T. (1981) "Pipeline mixing between two fluid streams meeting at a tee junction." *Int. Chem. Eng.* **21**(2): 205.
- Melius, C.F., Bergan, N.E., and Shepherd, J.E. (1990) "Effects of water on combustion kinetics at high pressure." Twenty-Third Symposium (International) on Combustion, Orleans, France.

Mendenhall, W., Wackerly, D.D., and Scheaffer, R.L. (1990) *Mathematical statistics with applications*. Belmont, CA, Duxbury Press.

Meyer, J.C. (1993) "Oxidation chemistry and kinetics of model compounds in supercritical water: glucose, acetic acid, and methylene chloride." M.S. thesis, Department of Chemical Engineering, Massachusetts Institute of Technology, Cambridge, MA.

Modell, M. (1989) "Supercritical water oxidation." in *Standard Handbook of Hazardous Waste Treatment and Disposal*. H.M. Freeman, Ed., New York, NY, McGraw-Hill: 8.153-8.168.

Modell, M. (1990) "Treatment of pulp mill sludges by supercritical water oxidation." Final Report, DOE Contract No. FG05-90CE40914.

Modell, M., Larson, J., and Sobczynski, S.F. (1992) "Supercritical water oxidation of pulp mill sludges." *Tappi. J.*(June): 195-202.

Moore, J.W. and Pearson, R.G. (1981) *Kinetics and mechanism*. New York, NY, John Wiley and Sons.

Moore, J.W. and Simpson, J.M. (1993) "A review of supercritical water oxidation research and technology." Oak Ridge National Laboratory, ORNL/CF-93139.

NRC (1993) "Alternative technologies for the destruction of chemical agents and munitions." National Research Council, Washington, D.C., .

Paterson, C., Breshears, D., and Foy, B. (1993) "Steady state combustion of hydrogen and oxygen in supercritical water." *Combust. Sci. Technol.* **89**(411-423).

Peng, D.Y. and Robinson, D.B. (1976) "New two-constant equation of state." *Ind. Eng. Chem. Fundam.* **15**: 59-64.

Raes, F., Saltelli, A., and Van Dingenen, R. (1992) "Modelling formation and growth of H₂SO₄-H₂O aerosols: Uncertainty analysis and experimental evaluation." *J. Aerosol Sci.* **23**(7): 759-771.

Reed, R.D. and Narayan, B.C. (1979) "Mixing fluids under turbulent flow conditions." *Chem. Eng.* **86**(131): 131.

Reid, R.C., Prausnitz, J.M., and Poling, B.E. (1987) *The properties of gases and liquids*. New York, NY, McGraw Hill.

- Rettich, T.R., Battino, R., and Wilhelm, E. (1982) "Solubility of gases in liquids. 15. High-precision determination of Henry's coefficients for carbon monoxide in water at 278 to 323K." *Ber. Bunsenges. Phys. Chem.* **86**: 1128-1132.
- Rice, S.F., Hunter, T.B., and Rydén, Å.C. (1996) "Raman spectroscopic measurement of oxidation in supercritical water. 1. Conversion of methanol to formaldehyde." *Ind. Eng. Chem. Res.* **35**: 2161-2171.
- Rice, S.F., LaJeunesse, C.A., Hanush, R.G., Aiken, J.D., and Johnston, S.C. (1994) "Supercritical water oxidation of colored smoke, dye, and pyrotechnic compositions." Sandia National Laboratory, SAND94-8209.
- Robinson, C. (1992) "Demilitarization R&D technology for conventional munitions via SCWO of colored smokes, dyes, and pyrotechnics." Workshop on Federal Programs Involving Supercritical Water Oxidation, Gaithersburg, MD.
- Schmitt, R.G., Butler, P.B., and French, N.B. (1993) "Chemkin real gas: A Fortran package for analysis of thermodynamic properties and chemical kinetics in nonideal systems." University of Iowa, Iowa City, UIME PBB 93-006.
- Schmitt, R.G., Butler, P.B., Westbrook, C.K., and Pitz, W.J. (1991) "Destruction of hazardous waste in supercritical water. Part II: A study of high pressure methanol oxidation kinetics." U.S. Department of Energy Report, DE92-008559.
- Schroeder, J., Schwarzer, D., Troe, J., and Voss, F. (1990) "Cluster and barrier effects in the temperature and pressure dependence of the photoisomerization of *trans*-stilbene." *J. Chem. Phys.* **93**(4): 2393-2404.
- Sengers, J.V. and Watson, J.T.R. (1986) "Improved international formulations for the viscosity and thermal conductivity of water substance." *J. Phys. Chem. Ref. Data* **15**(4): 1291-1314.
- Shum, L.G.S. and Benson, S.W. (1983) "Review of the heat of formation of the hydroperoxyl radical." *J. Phys. Chem.* **87**(18): 3479-3482.
- Simmrock, K.H., Janowsky, R., and Ohnsorge, A. (1986) *Critical Data of Pure Substances, Vol. II, Part 2.*, Dechema Chemistry Data Series.
- Spritzer, M.H., Hazlebeck, D.A., and Downey, K.W. (1995) "Supercritical water oxidation of chemical agents and solid propellants." *J. Energ. Mater.* **12**(3&4): 185-212.

- Staszak, C.N., Malinowski, K.C., and Killilea, W.R. (1987) "The pilot-scale demonstration of the MODAR oxidation process for the destruction of hazardous waste materials." *Environ. Prog.* **6**(1): 39-43.
- Steinfeld, J.I., Francisco, J.S., and Hase, W.L. (1989) *Chemical kinetics and dynamics*. Englewood Cliffs, NJ, Prentice Hall.
- Stolarski, R.S., Butler, D.M., and Rundel, R.D. (1978) "Uncertainty propagation in a stratospheric model 2. Monte Carlo analysis of imprecisions due to reaction rates." *J. of Geophys. Res.* **83**(6): 3074-3078.
- Swallow, K.C., Killilea, W.R., Malinowski, K.C., and Staszak, C. (1989) "The MODAR process for the destruction of hazardous organics wastes--field test of a pilot-scale unit." *Waste Mgmt.* **9**: 19-26.
- Szabo, A. and Ostlund, N.S. (1989) *Modern quantum chemistry*. New York, NY, McGraw Hill.
- Takagi, J. and Ishigure, K. (1985) "Thermal decomposition of hydrogen peroxide and its effect on reactor water monitoring of boiling water reactors." *Nuc. Sci. Eng.* **89**: 177-186.
- Tatang, M.A. (1995) "Direct incorporation of uncertainty into chemical and environmental engineering systems." PhD. thesis, Departement of Chemical Engineering, Massachusetts Institute of Technology, Cambridge, MA.
- Taylor, J.R. (1982) *An introduction to error analysis: The study of uncertainties in physical measurements*. Mill Valley, CA, University Science Books.
- Tester, J.W., Holgate, H.R., Armellini, F.J., Webley, P.A., Killilea, W.R., Hong, G.T., and Barner, H.E. (1991) "Oxidation of hazardous organic wastes in supercritical water: A review of process development and fundamental research." in *ACS Symposium Series 518: Emerging Technologies for Hazardous Waste Management III*. D.W. Tedder and F.G. Pohland, Eds., Washington, D.C., American Chemical Society: 35-76.
- Tester, J.W. and Modell, M. (1997) *Thermodynamics and its applications*. Upper Saddle River, NJ, Prentice Hall.
- Tester, J.W., Webley, P.A., and Holgate, H.R. (1993) "Revised global kinetic measurements of methanol oxidation in supercritical water." *Ind. Eng. Chem. Res.* **32**(1): 236-239.
- Thomason, T.B., Hong, G.T., Swallow, K.C., and Killilea, W.R. (1990) "The MODAR supercritical water oxidation process." in *Innovative Hazardous Waste Treatment Technology*

Series, Volume 1: Thermal Processes. H.M. Freeman, Ed., Lancaster, PA, Technomic Publishing: 31-42.

Thomason, T.B. and Modell, M. (1984) "Supercritical water destruction of aqueous wastes." *Haz. Waste* **1**(1): 453-467.

Timberlake, S.H., Hong, G.T., Simson, M., and Modell, M. (1982) "Supercritical water oxidation for wastewater treatment: preliminary study of urea destruction." 12th Intersociety Conference on Environmental Systems, San Diego, CA.

Tosun, G. (1987) "A study of micromixing in tee mixers." *Ind. Eng. Chem. Res.* **26**: 1184-1193.

Townsend, S.H., Abraham, M.A., Huppert, G.L., Klein, M.T., and Paspek, S.C. (1988) "Solvent effects during reactions in supercritical water." *Ind. Eng. Chem. Res.* **27**: 143-149.

Townsend, S.H. and Klein, M.T. (1985) "Dibenzylether as a probe into the supercritical fluid solvent extraction of volatiles from coal with water." *Fuel* **64**: 635-638.

Truhlar, D.G., Hase, W.L., and Hynes, J.T. (1983) "Current status of transition state theory." *J. Phys. Chem.* **87**(15): 2664-2678.

Tsang, W. and Hampson, R.F. (1986) "Chemical kinetic data base for combustion chemistry. Part I. Methane and related compounds." *J. Phys. Chem. Ref. Data* **15**(3): 1087-1112.

Uematsu, M. and Franck, E.U. (1980) "Static dielectric constant of water and steam." *J. Phys. Chem. Ref. Data* **9**(4): 1291-1306.

Webley, P.A. (1989) "Fundamental oxidation kinetics of simple compounds in supercritical water." PhD. thesis, Department of Chemical Engineering, Massachusetts Institute of Technology, Cambridge, MA.

Webley, P.A. and Tester, J.W. (1989) "Fundamental kinetics of methanol oxidation in supercritical water." in *Supercritical Fluid Science and Technology*. K.P. Johnston and J.M.L. Penninger, Eds., Washington, D.C., American Chemical Society. **406**: 259-275.

Webley, P.A. and Tester, J.W. (1991) "Fundamental kinetics of methane oxidation in supercritical water." *Energy and Fuels* **5**: 411-419.

Whitlock, D.R. (1978) "Organic reactions in supercritical water." M.S. thesis, Department of Chemical Engineering, Massachusetts Institute of Technology, Cambridge, MA.

Wilhelm, E., Battino, R., and Wilcock, R.J. (1977) "Low-pressure solubility of gases in liquid water." *Chem. Rev.* **77**(2): 219-262.

Woerner, G.A. (1976) "Thermal decomposition and reforming of glucose and wood at critical conditions of water." M.S. thesis, Department of Chemical Engineering, Massachusetts Institute of Technology, Cambridge, MA.

Yetter, R.A., Dryer, F.L., and Rabitz, H. (1991) "A comprehensive reaction mechanism for carbon monoxide/hydrogen/oxygen kinetics."

Yetter, R.A., Dryer, F.L., and Rabitz, H. (1991) "A comprehensive reaction mechanism for carbon monoxide/hydrogen/oxygen kinetics." *Combust. Sci. Technol.* **79**: 97-128.